Development of Dermally Absorbed Copper(II) Complexes as Potential Anti-Inflammatory Drugs

A thesis submitted to the

University of Cape Town

In fulfilment of the requirements for the degree of

DOCTOR OF PHILOSOPHY

By

Giselle Marianthi Vicatos

Supervisors:

Prof. Graham E. Jackson

Prof. Susan A. Bourne

Department of Chemistry
University of Cape Town
Rondebosch 7701
South Africa

June 2020

University of Cape Town

The copyright of this thesis vests in the author. No quotation from it or information derived from it is to be published without full acknowledgement of the source. The thesis is to be used for private study or non-commercial research purposes only.

Published by the University of Cape Town (UCT) in terms of the non-exclusive license granted to UCT by the author.

University of Cape Town

Acknowledgements

- I wish to thank my supervisor, Professor Graham Jackson, for his constant guidance and support throughout this thesis. He has taught me such invaluable knowledge and skills that I feel without his supervision, the depth of my understanding for many techniques and topics would not be as vast. I also feel that if I continue with an academic career, the skills and depth of topics that he has taught me has prepared me and made me feel ready enough to take that next step. His patience and constant advice throughout this thesis were also greatly appreciated since many challenges were met throughout the study, and just being able to contact him at any time of the day and on any day of the week helped immensely. I truly could not have imagined a better supervisor!

- I wish to thank my supervisor, Professor Susan Bourne, for her guidance in the X-ray crystallography section. Even though I was not able to explore this section of chemistry fully, since my complexes could not diffract properly and so a full structural elucidation was not possible, I know that she would have continued to guide me through this section with top professional supervision.

- I wish to thank Ahmed Hammouda for his constant advice and help throughout this thesis. There were many times where I needed technical help and Ahmed was always available and happy to help no matter what the situation was.

- I wish to thank Radwan Alnajjar for teaching and guiding me through the computational section. Out of pure kindness he volunteered to show me how to perform and analyse computational calculations, as well as proofread the section so that I had all the technical terms correctly worded.

- I wish to thank Raffaele Bonomo for collecting the EPR spectroscopy data and giving insight into the analysis.

- I also wish to thank my family and friends for all the emotional support during this dissertation; without them my mental state would not be as good as it is now.

Plagiarism Declaration

I, Giselle Vicatos, hereby declare that the work on which this thesis is based is my original work (except where acknowledgements indicate otherwise) and that neither the whole work nor any part of it has been, is being, or is to be submitted for another degree in this or any other university. I authorise the University to reproduce for the purpose of research either the whole or any portion of the contents in any manner whatsoever.

Signed by candidate

Giselle Vicatos

12th June 2020

Abstract

Rheumatoid arthritis (RA) is a debilitating disease affecting 5% of the world's population and there is no cure. Copper(II) complexes have been reported to have anti-inflammatory activity and alleviate the symptoms associated with the disease. The present study focuses on the design of new drugs that could be used to change the bioavailability of copper(II) and hence alleviate the inflammation. The tripeptides, glycyl-L-leucyl-L-histidine (GLH), sarcosyl-L-leucyl-L-histidine (Sar-LH), glycyl-L-phenylalanyl-L-histidine (GFH) and sarcosyl-L-phenylalanyl-L-histidine (Sar-FH) were designed to resemble the natural *in vivo* copper(II) transporter, human serum albumin, so that they could be selective for copper(II). The preferred route of administration is dermal absorption and so sarcosine was added to improve the lipophilicity of the drug. This administration method was chosen since it is both nonharmful and convenient for patients.

The stability of the complexes was measured using glass electrode potentiometry and their solution structure studied using UV-Vis spectrophotometry, CW-EPR spectroscopy, ^{1}H NMR, ESI-MS and molecular modelling calculations. The presence of sarcosine did not significantly affect the stability of the complexes. Several species were found to exist in solution depending on the pH, but at pH 7, the $CuLH_{-2}$ species predominated for all four tripeptides. In this species, the ligand was found to coordinate to copper(II) via the terminal amine-N, the two amide-Ns and imidazole-N, in a square planar geometry.

Using a computer model of blood plasma, all four ligands were found to mobilise copper(II), without disrupting the homeostasis of nickel(II), zinc(II) or calcium(II) in the order of GFH > Sar-FH > GLH > Sar-LH. GFH increased the low molecular mass copper(II) species by 40.7 times at 0.1 mM. The lipophilicity of the complexes was estimated by measuring their octanol/water partition coefficients. All the complexes were found to be hydrophilic with log $P_{oct/aq}$ ranging from -3 to -2. Dermal absorption was estimated using an artificial membrane and a Franz cell. Only a moderate increase in membrane permeability of copper(II) was found.

The stability of the copper(II) complexes, their ability to mobilise copper(II) from endogenous sources and their improved dermal absorption, justifies further testing of this class of ligand as potential, dermally absorbable, anti-inflammatory drugs.

Table of Contents

Abbreviations

RA	- rheumatoid arthritis
NSAIDs	- non-steroidal anti-inflammatory drugs
DMARDs	- disease modifying anti-rheumatic drugs
L.M.W	- low molecular weight
ttda	- 3,6,9,12-tetra-azatetradecanedioate
dtda	- 3,6,9-triazaundecanedioate
cageL	- 3,5-diaminodiamido-4- oxahexacyclododecane
L1	- N,N′ -di(aminoethylene)-2,6-pyridinedicarbonylamine
L2	- bis-(N,N-dimethylethyl)- 2,6-pyridinedicarboxamide
L3	- N,N′-bis[2(2-pyridyl)-methyl]pyridine-2,6-dicarboxamide
[555-N]	- N^1-(2-aminoethyl)-N^2-(pyridin-2-ylmethyl)ethane-1,2-diamine
[H(555)-N]	- N-(2-(2-aminoethylamino)ethyl)picolinamide
[H_2(556)–N]	- 2-amino-N-(2-oxo-2-(2-(pyridin-2-yl)ethyl amino)ethyl)acetamide
[H_2(5555)-N]	- N,N′-(2,2′-azanediylbis(ethane-2,1-diyl))dipicolinamide
HSA	- human serum albumin
GLH	- glycyl-L-leucyl-L-histidine
Sar-LH	- sarcosyl-L-leucyl-L-histidine
GFH	- glycyl-L-phenylalanyl-L-histidine
Sar-FH	- sarcosyl-L-phenylalanyl-L-histidine
GGG	- triglycine
Gly-Leu-Phe	- glycyl-L-leucyl-phenylalanine
Sar-Leu-Phe	- sarcosyl-L-leucyl-phenylalanine
Gly-His-Lys	- glycyl-L-histidyl-L-lysine
Sar-His-Lys	- sarcosyl-L-histidyl-L-lysine
Sar-Lys-His	- sarcosyl-L-lysyl-L-histidine
Sar-His-His	- sarcosyl-L-histidyl-L-histidine
Sar-Lys-Lys	- sarcosyl-L-lysyl-L-lysine
Sar-Gly-His	- sarcosyl-L-glycyl-L-histidine
Gly-Phe	- glycyl-L-phenylalanine
Gly-Leu	- glycyl-L-leucine
Gly-His	- glycyl-L-histidine
Gly	- glycine
Sar	- sarcosine
Leu	- leucine
Phe	- phenylalanine
His	- histidine
R_f^H	- Hamilton R-factor
R_{lim}^H	- Hamilton R-factor limit
n-bar	- the formation function
Z_H-bar	- the protonation function
Z_M-bar	- the metal formation function
Q_M-bar	- the deprotonation function
Log *K*	- logarithm of equilibrium constants
log β_{pqr}	- logarithm of the overall stability constant
n_T	- the number of titrations
n_P	- the number of titration points
ESTA	- Equilibrium Simulations for Titration Analysis
EDTA	- ethylenediaminetetraacetic acid
KHP	- potassium hydrogen phthalate
UV-Vis	- ultraviolet-visible spectrophotometry
λ_{max}	- maximum wavelength
EPR	- electron paramagnetic resonance spectroscopy
RT	- room temperature
LT	- low temperature

shf	- superhyperfine
$g_{\perp}$	- perpendicular values with respect to an axis of symmetry
$g_{\parallel}$	- parallel values with respect to an axis of symmetry
$A_{\perp}$	- hyperfine coupling constant perpendicular to a unique symmetry axis
$A_{\parallel}$	- hyperfine coupling constant parallel to a unique symmetry axis
^{1}H NMR	- proton nuclear Magnetic resonance spectroscopy
T_2	- transverse relaxation time
TOCSY	- total correlation spectroscopy
MS	- mass spectrometry
ESI-MS	- electrospray ionisation mass spectrometry
IPM	- isopropyl myristate
log $P_{oct/aq}$	- octanol/water partition coefficient
J	- steady state flux
K_p	- the permeability coefficient
ECCLES	- Evaluation of Constituent Concentrations in Large Equilibrium Systems
P.M.I	- Plasma Mobilizing Index
MM	- molecular mechanics
QM	- quantum mechanics
MD	- molecular dynamics
SE	- semi-empirical
HF	- Hartree–Fock
DFT	- density functional theory
SMD	- Solvent Model Density
TD-DFT	- time dependent density functional theory
PXRD	- powder X-ray diffraction

List of Figures

List of Tables

1. Introduction

1.1 Rheumatoid arthritis

Rheumatoid arthritis (RA) is a chronic inflammatory disease that affects the connective tissue of movable joints. Unlike osteoarthritis, which is not an inflammatory disease and is caused by gradual softening and degeneration of the articular hyaline cartilage, RA appears to be an autoimmune disorder.[1,2] The immune system protects the body against foreign elements such as bacteria, fungi, viruses and parasites as well as environmental pollutants, preservatives and additives in food. A healthy immune system achieves this by first identifying the harmful molecules, responding to them by sending immune cells to destroy these molecules and once they have been destroyed, initiate a stop order for the immune cells. When there is an autoimmune disorder, the immune system acts as if it is constantly fighting against foreign elements and in the process damages healthy cells. Inflammation occurs as a natural response to the immune system, by bringing immune cells to the infected areas and increasing blood flow to these areas. This inflammation then becomes chronic when there is an autoimmune disorder.[3,4]

The synovium is the main area of pathology in RA.[5] It is the soft tissue that lines the spaces of diarthrodial joints, tendon sheaths and bursae and is also in contact with the intra-articular cavity. The synovium has two layers called the intimal layer, which is superficial, and a subintimal layer, which consists of the underlying tissue.[6,7] The intimal layer produces the synovial fluid which fills the intra-articular cavity. It is 1-2 cells or 20-40 mm thick in a cross-section and consists of fibroblasts and macrophages. The subintimal layer is up to 5 mm thick and provides nutrients to the cartilage, since it contains scattered blood vessels, fibroblasts, fat cells and macrophages.[5] In RA, the synovium undergoes changes which directly play a role in activating the disease.[8] The intimal layer becomes hypertrophied to 8-10 cells thick and forms a “pannus”, which is mainly due to an increase in macrophage.[9] This “pannus” acts like tumour tissue, which erodes contiguous cartilage and bone.[10] The subintimal layer also undergoes changes during RA since there is mononuclear infiltration, as well as the formation of blood

vessels.[6,11] A schematic representation of a healthy joint compared to a joint with RA can be seen in Figure 1.1.

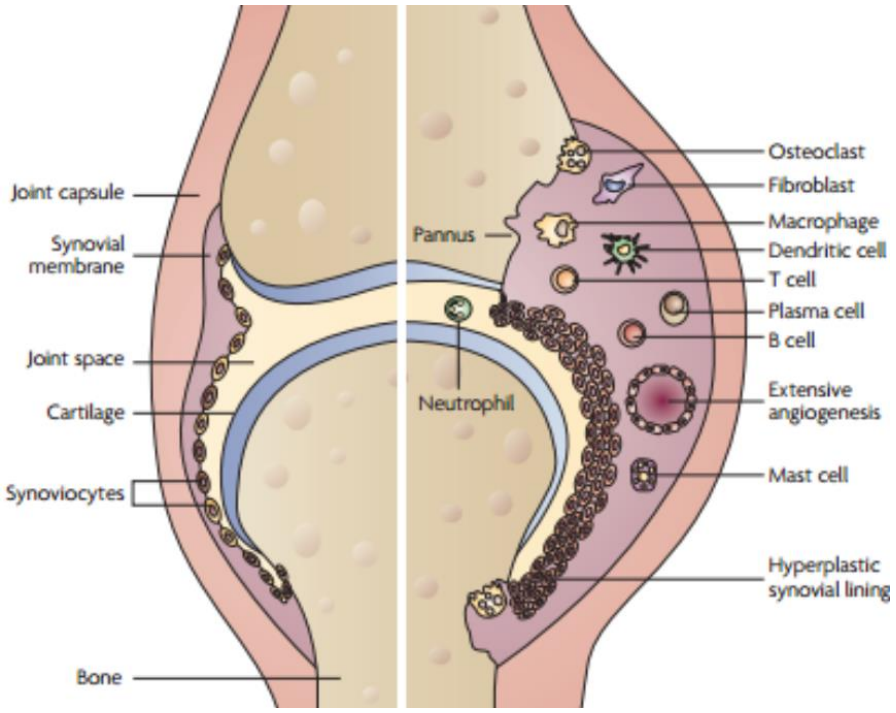

Figure 1.1: A schematic representation comparing the physiological appearance of a healthy joint on the left to a joint that has been affected by RA on the right.[12,13]

The progression of the disease first appears as slight swelling in the knuckle joints, which is accompanied by stiffness and pain. Then the swelling increases and degeneration occurs in the joint. Other articular structures also undergo inflammation and degeneration as the disease progresses, which inevitably leads to immobility and eventually death.[14,15] The progression of RA in the knuckle joints can be seen in Figure 1.2.

Figure 1.2: The progression of RA in the knuckle joints.[16]

The exact cause of RA is unknown, although the search is still on-going. Triggers such as a bacterial or viral infection have been hypothesised, but have not been found to be the single cause of RA. However, together with other factors, they could activate immunological and inflammatory pathways which could then initiate the disease. Research into a periodontal disease, which has bacteria called *Porphyromonas gingivalis* and causes citrullination of proteins, suggests that this type of infection could lead to the development of RA in some patients, although further research is still needed. Another factor that could increase the risk of developing RA is a genetic factor. A specific amino acid residue sequence that is within the hypervariable region of the gene, HLA-DR4, has been associated to have approximately a 30% genetic risk for the disease. Other factors such as hormones and age also contribute to the susceptibility to RA, since RA is more prevalent in women and elderly people, as well as stress.[2,10,17,18]

1.2 Current treatment for rheumatoid arthritis

1-5 % of the world's population is affected with RA and since there is no cure, currently it can only be controlled with immunosuppressive drugs and the symptoms treated with anti-inflammatory drugs.[14] The treatment of RA consists of three general classes of drugs, which are non-steroidal anti-inflammatory drugs (NSAIDs), corticosteroids and disease modifying anti-rheumatic drugs (DMARDs).[19,20]

NSAIDs decrease acute inflammation, which will then decrease pain and improve function. Together with their anti-inflammatory property, all of these drugs have a mild analgesic property which independently treats the pain of the disease. Even though these drugs treat the inflammation, they do not prevent joint destruction or change the course of the disease and therefore cannot prevent the progression of RA. Most of these drugs can be bought over-the-counter and can be taken orally. The advantages of NSAIDs, besides their anti-inflammatory and analgesic properties, are that they do not cause addiction, sedation or respiratory depression.[21] However they do cause problems in the upper gastrointestinal tract, where patients develop subjective discomfort, ulcers and bleeding. NSAIDs block the cyclooxygenase enzymes, COX-1 and COX-2, which then inhibit the production of prostaglandins. This decreases inflammation and pain, since they are mediated by prostaglandins. However, prostaglandins are also responsible for maintaining body functions such as protection from stomach acid, maintaining kidney blood flow and contributing to the stickiness of platelets and vascular functions.[21–23]

While NSAIDs are associated with symptomatic control, DMARDs modify the inflammatory and destructive process of RA, which leads to altering the course of the disease and can improve the outcome of RA in the long term.[24] Unlike NSAIDs, which take hours to have a therapeutic effect, DMARDs take several weeks.[25] Therefore, administering DMARD drugs early in the diagnosis is ideal since it will help to prevent long-term joint damage and disability. However, these drugs are toxic and need to be monitored.[25–30] Some studies have also shown that taking a combination of DMARD drugs early in the diagnosis of RA provides a better clinical response and is well tolerated by patients.[31]

One type of corticosteroid that is used for treating RA is glucocorticoids. Glucocorticoids can be taken orally, intravenously, intramuscularly or directly injected into the articular joints and are fast-acting agents.[19] Like NSAIDs they also provide symptomatic relief and were initially given to RA patients in high doses to reduce flares caused by the disease. However, recent studies show that administering glucocorticoids in low doses for longer periods of time and during the early stages of RA, slow down radiographic progression and therefore have disease-modifying benefits like DMARD drugs.[32–35] Similar to NSAIDs and DMARDs, taking glucocorticoids for long periods of time has adverse side effects like diabetes, infection, hypertension, cataracts and osteoporosis.[36]

All the mentioned treatments for RA are not ideal since they are either toxic or have side effects. Therefore, the search for an effective and easily administrated treatment that has no side effects or toxicity has been ongoing. A cure at this stage is not likely, since more about the disease needs to be known first.

1.3 Copper(II) as a form of treatment

The role of copper in RA became a topic of interest because of the abnormally high serum copper(II) levels in patients who have the disease.[37,38] These high levels were then linked to the antioxidant activity of serum and hence the bodies protective inflammatory response.[39] The higher anti-inflammatory activity found for copper(II) complexes[40] and the traditional use of copper bangles to treat arthritis[41] also helped increase the interest.

The anti-inflammatory activity found in copper has a few possible mechanisms:

- Copper can induce the activity of lysyl oxidase. This is an enzyme (copper dependant) that repairs damaged tissue from inflammation.[42]
- Copper modulates prostaglandin synthesis so that a decrease in prostaglandin prevents inflammation by vasodilation.[43]
- Copper induces the activity of superoxide dismutase, which is an enzyme that initiates inflammation.[44]
- Copper could have a function in stabilizing the lysosomal membrane, so that lysosomal proteolytic enzymes do not get released from abnormal lysosomes and degenerate the surrounding cartilage.[45]
- Copper helps modulate the physiological effects of histamine, since the histamine regulating enzyme, diamine oxidase, is dependent on copper.[46]

Copper is classified as an essential element for all living organisms since it is required in many biological processes such as reproduction, haemoglobin synthesis, bone formation and many other processes. Biologically active copper has three oxidation states; I, II and III, but for biological systems, state I and III are unstable, while state II forms stable copper complexes which get transported around the body to specific sites.[47] In the blood plasma of a normal adult, there is approximately 76 mg of copper(II) with a concentration of about 1.1- 2.0 x 10^{-5} mol/dm^{-3}. In the blood plasma, copper(II) can be classified into four categories: (a) non-

reversibly bound to metaloproteins, (b) reversibly bound to proteins, (c) reversibly bound to low molecular weight (L.M.W) ligands and (d) exists as free hydrated copper(II) ions.[48,49] Most (65-95%) copper(II) ions are bound non-reversibly to ceruloplasmin and the rest are bound reversibly to approximately 15% albumin, 10% transcuprein and smaller portions to peptides and amino acids as well.[50–52] In the blood plasma of adults with RA, the total serum copper(II) can be up to two times higher than normal concentrations.[41] A correlation between the increased serum copper(II) levels and erosion was found and as a result the role of copper(II) was questioned.[39] A main indication that the increased copper(II) levels could have a protective function, was observing the copper(II) levels in patients with Hodgkin's disease, which also showed elevated levels of copper(II) in the blood plasma. When these patients went into remission after being treated with radiotherapy, the levels of serum copper(II) became normal again.[39,53]

After further looking into the role of copper(II) in RA patients, it was also found that there is a correlation between copper(II) and ceruloplasmin, so that an increase in copper(II) also meant an increase in ceruloplasmin (Figure 1.3).[37] There is another correlation between ceruloplasmin and serum antioxidant activity, which suggests that this cuproprotein is the main factor governing antioxidant activity as a protective function against tissue damage.[38] A study[54] found that ceruloplasmin releases copper(II) for cell uptake by interacting with the cell surface. Another study[55] proposed that ceruloplasmin provides a protective shield against the production of oxidative stress, which is caused by myeloperoxidase during inflammation. These factors could be a part of the mechanism for why the body produces high levels of copper(II) complexed to ceruloplasmin in patients with RA.

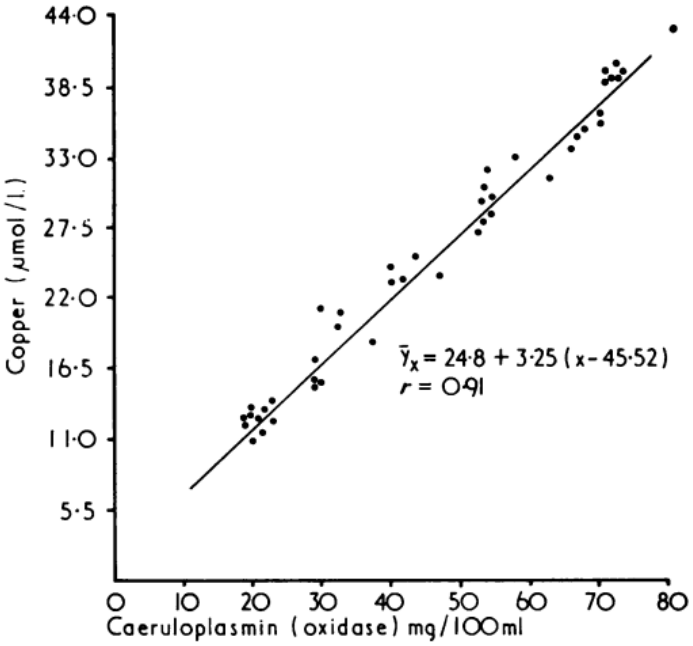

Figure 1.3: Graph showing the correlation between the levels of copper(II) and ceruloplasmin.[37]

As a result of these correlations, a study[40] to decipher whether copper(II) chelates have more anti-inflammatory activity than copper(II), in the form of copper(II) acetate, and their parent chelating compound was carried out. The parent chelating compounds were drugs that are clinically used for treating inflammation. After it was shown through subcutaneous injections that the copper(II) chelates are indeed more active, it was suggested that it is the formation of these metal coordination complexes that is responsible for the anti-inflammatory activity of clinical anti-inflammatory drugs. A depiction of how the activation occurs can be seen in Figure 1.4. However, this statement was difficult to conclude because problems arose with the solubility and stability of the complexes in an acidic medium (oral absorption). But during this process, it was also discovered that many copper(II) complexes also had anti-ulcer activity.

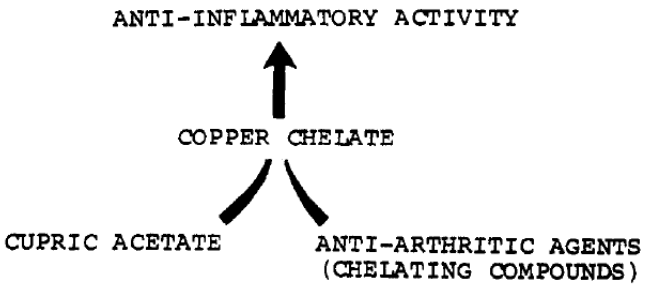

Figure 1.4: Suggested method for activation of anti-arthritic compounds.[40]

Jackson *et al*.[51] took this one step further to decipher whether copper(II) complexes of naturally occurring ligands, like amino-acids, instead of already used anti-inflammatory drugs can induce an anti-inflammatory response. These tests were done via subcutaneous injections and it was found that the decrease in inflammation is proportional to the amount of copper(II) administered. It was also found that once in the blood plasma, the complex acts as a supplement to the metal and ligand components of blood plasma and that the complex as a whole does not undergo cell membrane transmission. Additionally, the mechanism responsible for controlling the anti-inflammatory response can accept copper(II) ions irrespective of whether they are firmly or weakly complexed. This is because injected low molecular weight (L.M.W) complexes dissociate to form an equilibrium with endogenous L.M.W complexes[56] and therefore, the binding ability of copper(II) to endogenous ligands, which enter the tissues, is implied to be powerful.[51] The exact method of how copper(II) complexes exhibit their anti-inflammatory response is not known, but it is thought that copper(II) is needed for both the arrest of the inflammation process, as well as the repair of tissue damage.[56] Nevertheless, this route of administration is therefore increasing the bioavailable pool of copper(II) from exogenous sources by releasing copper(II) into the blood plasma.

Besides the protective function from the copper(II) ceruloplasmin complex against inflammation, evidence has shown that L.M.W copper(II) complexes also have a function in treating the inflammation associated with RA. Walker *et al.*[57] separated plasma according to different molecular weight fractions and showed that species with a molecular weight of below 500 have active chemicals against RA. It was further suggested that these endogenous L.M.W complexes cause the release of copper(II) from serum albumin in response to inflammation. These L.M.W copper(II) complexes are then in a form which can enter tissues, since they are neutral and therefore are soluble in the lipoprotein matrix. Therefore, it was postulated that by increasing the concentration of L.M.W copper(II) complexes, it would increase the bioavailable pool of copper(II) from endogenous sources like serum albumin.

The question about whether intentionally increasing the copper(II) concentration *in vivo* will bring about a toxic response was raised. The body is able to handle a ten-fold increase of copper(II), which means that there are many non-toxic copper(II) complexes present *in vivo*, but not all copper(II) complexes are non-toxic at all dose levels and so the toxicity of the final complexes will need to be evaluated. A known disease that is associated with the accumulation of copper(II) in the body is Wilson's disease. This genetic disease brings about the inability to

excrete copper(II) and results in life-threatening copper(II) levels. However, there are no known chronic degenerative diseases in humans that arise from the exposure of non-industrial copper(II), therefore as long as the copper(II) complex is non-toxic, the body will be able to excrete any unused copper(II).[40,58]

An increase of bioavailable copper(II) *in vivo* can be achieved in three ways. The first is an equilibrium competition between serum albumin and exogenous L.M.W species for albumin bound copper(II). The second is for copper(II) to be administered topically or orally in the form of a neutral, low weight and membrane-penetrable complex. Subcutaneous injections is another route, but it is not favourable because it causes irritation at the site of injection and requires professional help to administer.[59] The third source is from extracting copper(II) from ceruloplasmin by breaking the inert bonds in a chemical process. The third method is not conducive for therapeutic drug designs and so only the first and second methods were considered.[51,60] The objective going forward was to develop a ligand that could incorporate both the first and second method. A diagram depicting these two methods can be seen in Figure 1.5.

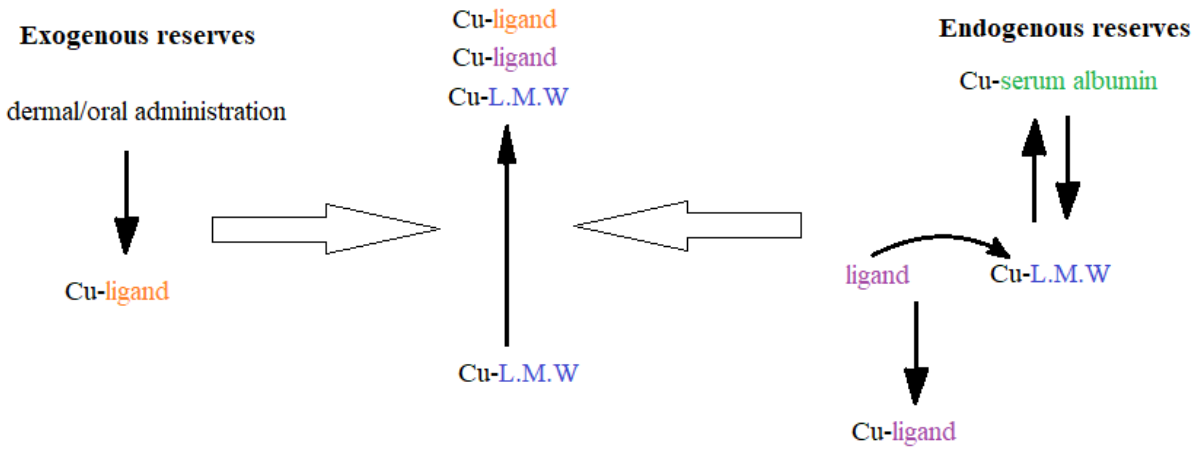

Figure 1.5: Scheme of the endogenous and exogenous methods for increasing the bioavailable pool of copper(II) *in vivo*.

For oral absorption, the normal daily intake of copper(II) is 2.5-5 mg and about 30 % gets absorbed into the small intestine in the form of L.M.W complexes of monomeric and acidic L-configuration amino acids. The absorption percentage is also lowered by the presence of other metals and ligands (Ca^{2+} or PO_4^{3-})[51]. Therefore when orally administering copper(II) salts, there will be a high percentage that is not absorbed and this will cause ulcers and oedema.[40] A

compound thus has to be specifically chosen, so that as a copper(II) complex, it does not irritate the stomach lining and it optimises the degree of intestinal absorption. Neutral complexes can pass through membranes and enter into tissues, as well as have a protective function against ulcer formation at stomach pH levels (pH 2).[56] As a result, neutral complexes were suggested for the drug design.

1.4 Design of first ligands

To design a ligand that would incorporate the first and second method, in terms of the thermodynamics, a strong dianionic chelator that is specific for copper(II) is needed. The donor atoms were the first structural considerations for the design of the ligand, and the atoms of oxygen, sulphur and nitrogen were looked at. It was found that the order of copper(II) mobilization was O < S < N, where nitrogen is 10^6 times more efficient than sulphur. The size was also looked at where three 5-membered rings were 1000 times more efficient at mobilizing copper(II) than a complex with one 5-membered and two 6-membered rings. It was also found that a straight-chain polyamine mobilizes copper(II) best. For a neutral compound, two anionic groups were needed and a comparison between phosphonate, phosphate, carboxylate and phenolate showed that the three latter groups were all better than phosphonate. Overall, it was concluded that in order to mobilize copper(II) directly from serum albumin, as well as pass through tissues, the ligand should be a linear, dicarboxylate or dialkyl phosphate substituted polyamine.[60]

As a result of these structural findings, the ligands 3,6,9,12-tetra-azatetradecanedioate (ttda) and 3,6,9-triazaundecanedioate (dtda) were synthesised (Figure 1.6).[14,61,62] The objective to increase the L.M.W copper(II) complexes by mobilizing copper(II) from endogenous sources was achieved. But as a result of the strong stability and high chelation for copper(II), these ligands were unable to become biologically active since they were rapidly excreted, unchanged in the urine. Additionally, even though they are neutral, they were too hydrophilic to pass through body compartments and so, from these outcomes, were concluded to be ineffective as anti-inflammatory drugs. These results also prompted the realisation that an important physiochemical specification for drug design is the hydrophobicity of the ligand as it governs transport, distribution and the outcome of the complexes in a biological system.[14,61–63] As an

additional outcome, the preferred route of administration became the dermal absorption route for future studies.

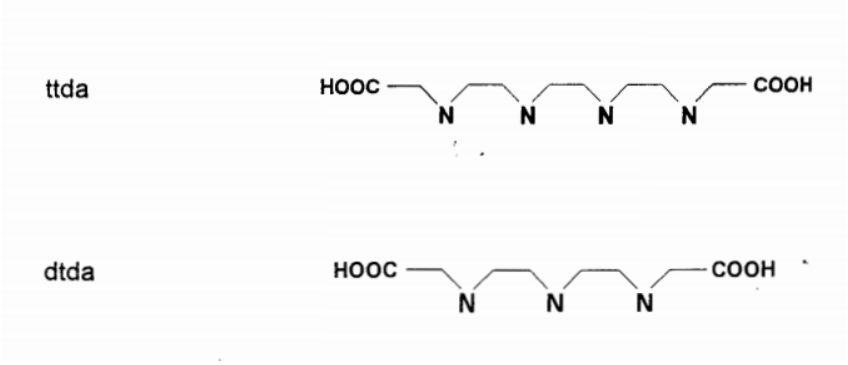

Figure 1.6: Structural representations of ttda and dtda.[61]

To decrease the stability of the complex, it was found that the coordination to amide groups, whereby the amide-N becomes deprotonated upon metal ion coordination, lowers the stability of the complex compared to a coordination to the amine groups.[14] It was also found that using a mixture of amino/amido groups in the ligands, improves the lipophilicity of the complex by 5%.[14,63] Using this information, and building onto it, the ligand, 3,5-diaminodiamido-4-oxahexacyclododecane (cageL) was derived (Figure 1.7).[63] This structure incorporates the alternating amino/amido groups, but also has an attached pentacycloundecane derivative, which forms a cage moiety and increases the lipophilicity further. Due to the low stability of the amide groups, the cage moiety also provided a rigid structure to help copper(II) bind to the ligand by forming an ideal conformation. However, when tested, the complex was still largely hydrophilic, which may have been due to the overall charge of the complex species, hydrogen bonding or the presence of coordinated water molecules.

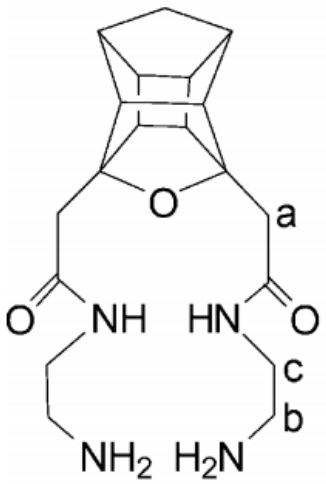

cageL

Figure 1.7: Structural representation of cageL.[63]

An attempt to increase the lipophilicity further was done by designing the ligands, N,N′ -di(aminoethylene)-2,6-pyridinedicarbonylamine[64] (L1), bis-(N,N-dimethylethyl)- 2,6-pyridinedicarboxamide[64] (L2) and N,N′-bis[2(2-pyridyl)-methyl]pyridine-2,6-dicarboxamide[65] (L3) (Figure 1.8). L1 and L2 were still found to be largely hydrophilic and preferentially bound to zinc(II) and calcium(II) instead of copper(II) *in vivo*.[64] L3 was found to be selective for copper(II) and more lipophilic than cageL, but overall still largely hydrophilic.[65] L1, L2, and L3 then underwent a bio-distribution study where the route of administration was percutaneous and dermal absorption.[66] A significant amount of activity was absorbed over 24 h when administered via dermal absorption. The amount absorbed via the transdermal route will always be less than the intravenous route. However, the interesting discovery was that more activity was retained in the body with the dermal absorption route. This indicated that the complex was too lipophilic and became trapped in the dermal layer.

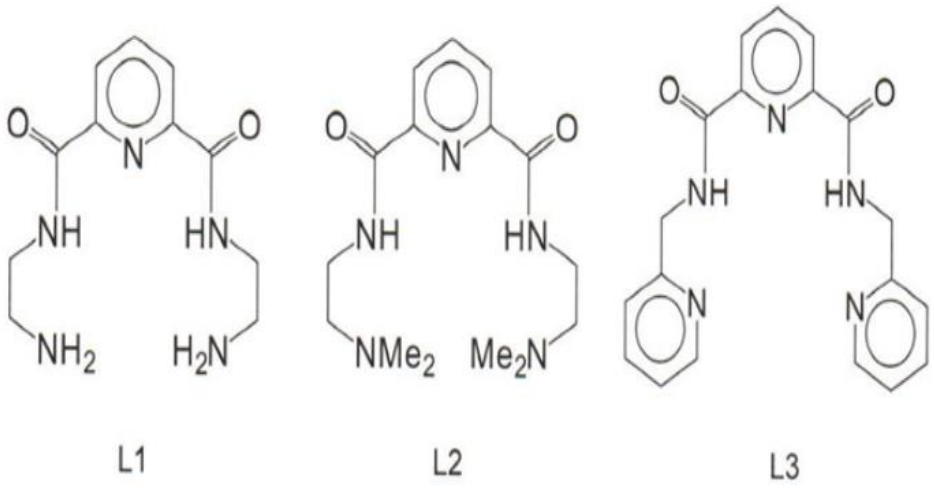

Figure 1.8: Represented structures of L1, L2 and L3 in the conformation that they will most likely adopt when complexed to copper(II).[66]

1.5 Design of peptides as ligands

The design of the ligand changed focus, where it was based on the structure of human serum albumin (Figure 1.9). Serum albumin is a major metal binding protein that transports metals in the body, where 40 μg of copper(II) binds to serum albumin in 1 ml of plasma.[67,68] Serum albumin can be described as a peptide in the form of Asp-Ala-His and copper(II) reversibly binds at the C-terminus to the amine, the amide N-donors and the imidazole-N.[69,70]

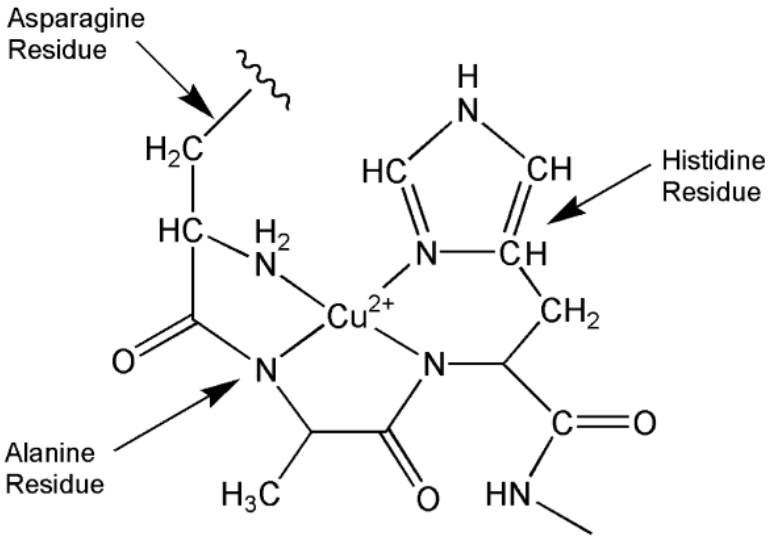

Figure 1.9: Binding sites for copper(II) in human serum albumin.[68]

The first few ligands to base their structure on serum albumin are the series of peptides which enhanced their hydrophobicity by adding bulky groups within the chelating agent. These peptides are, N^1-(2-aminoethyl)-N^2-(pyridin-2-ylmethyl)ethane-1,2-diamine ([555-N])[71], N-(2-(2-aminoethylamino)ethyl)picolinamide ([H(555)-N])[71], 2-amino-N-(2-oxo-2-(2-(pyridin-2-yl)ethyl amino)ethyl)acetamide ([H_2(556)–N])[68] and N,N′-(2,2′-azanediylbis(ethane-2,1-diyl))dipicolinamide ([H_2(5555)-N])[72] and can be seen in Figure 1.10.

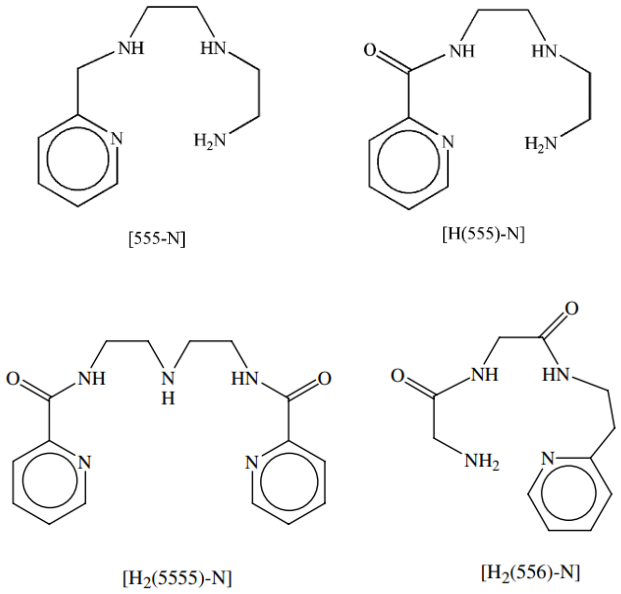

Figure 1.10: Structures of [555-N], [H(555)-N], [H_2(556)-N] and [H_2(5555)-N].[71,72]

In the blood plasma, all the peptides were more selective for copper(II) rather than for zinc(II) and calcium(II) and the order of copper(II) mobility is [555-N] > [H(555)-N] > [H_2(556)–N] > [H_2(5555)-N]. The difference in mobilizing ability between the ligands can be seen in Figure 1.11. The mobilizing ability is measured in terms of the plasma mobilizing index (P.M.I), which is defined as the increase in the total concentration of low molar mass complexes of a specific metal ion, caused by a ligand. There is a difference in the mobilizing ability of three log units between [555-N] and [H(555)-N] and another three log units between [H(555)-N] and [H_2(556)–N]. This difference can be attributed to the presence of one electron withdrawing CONH-group in [H(555)-N] and two in [H_2(556)–N].[71,72]

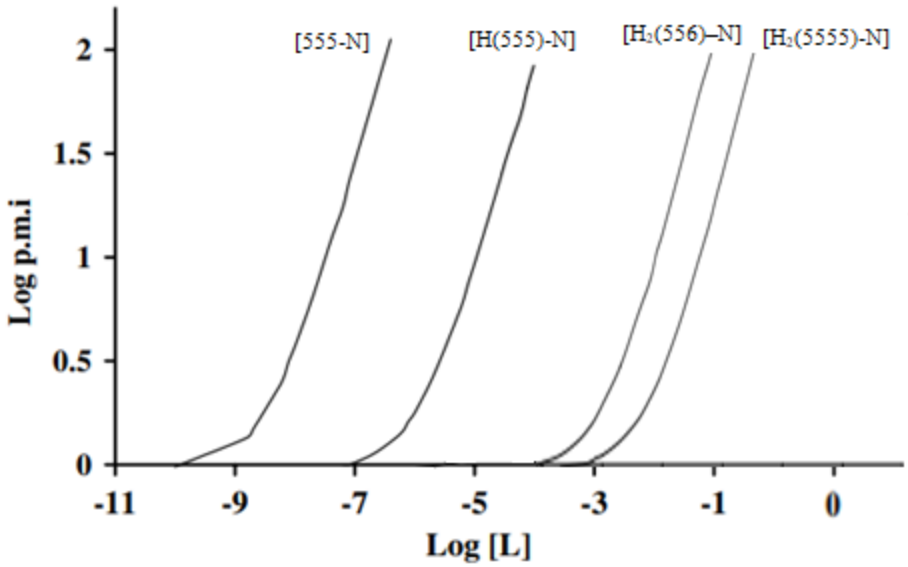

Figure 1.11: A comparison in mobilizing ability for [555-N], [H(555)-N], [H_2(556)-N] and [H_2(5555)-N].[71,72]

For a drug to be lipophilic, its octanol/water partition coefficient should be at least log $P_{oct/aq}$ = 0.6.[68] At the physiological pH, [555-N], [H(555)-N] and [H_2(556)–N] all have negative values of -1.29, -1.39 and -0.30 respectively, but [H_2(5555)-N] has a positive value of 0.08, which is a result of the hydrophobic groups. The high partition coefficient for [H_2(556)–N] and especially [H_2(5555)-N] warranted a bio-distribution and dermal absorption study on rats. But when compared to the activity found from an intravenous administration, a transdermal administration showed a reduced activity in major organs along with a reduction of less than 0.5 % total activity in the blood and less than 7% in the liver after 24 h. However, a high activity was found in the head where twice as much copper(II) was absorbed using [H_2(5555)-N] than [H_2(556)–N].

Using the criteria from literature, a set of aims and objectives were compiled, which will be used to further the research in finding a treatment for rheumatoid arthritis.

1.6 Aims

The focus of this study is to develop a drug that will help treat the inflammation associated with rheumatoid arthritis. To do this, the drug must be able to increase the bioavailable pool of copper(II) *in vivo*. To bring about this increase, the drug which will be in the form of a series of tripeptides, must first form a stable complex with copper(II) and then be able to undergo dermal absorption and consequently release the copper(II) ions into the blood plasma. Additionally, the endogenous metal ions must not be disrupted during this process. A secondary aim is that once in the blood plasma, the tripeptides need to have a sufficient mobilising capacity so that they can release copper(II) from endogenous sources.

1.7 Objectives

In order to achieve the aim of this PhD the following objectives are set:

1. Design a set of four ligands with the potential to act as copper(II) based anti-inflammatory drugs.
2. To measure the stability of these four ligands with H^+, Cu^{2+}, Ni^{2+}, and Zn^{2+}, using glass electrode potentiometry.
3. To measure the lipophilicities of the metal ligand complexes using octanol/water partition coefficients.
4. To measure the dermal absorption using an artificial membrane in a modified Franz cell by obtaining the permeability coefficients.
5. To determine the plasma mobilising capacities using ECCLES (Evaluation of Constituent Concentrations in Large Equilibrium Systems).
6. To determine the structure of the metal ligand complexes using ultraviolet-visible spectrophotometry, proton nuclear magnetic resonance spectroscopy, mass spectrometry and electron paramagnetic resonance spectroscopy.
7. To crystallise different species from solution and determine their structures using single crystal X-ray diffraction methods.
8. To evaluate the structure and coordination mode of the species formed in solution using molecular modelling.

1.8 References

1 J. Carton, R. Daly and P. Raman, *Clinical Pathology*, Oxford University Press, UK, 2007.

2 R. G. Lahita, *Rheumatoid Arthritis: Everything You Need to Know*, Penguin, USA, 2001.

3 R. Redfern, *Improving Rheumatoid Arthritis and Juvenile Arthritis in 30 Days*, Naturally Healthy Publications, UK, 2014.

4 N. R. Rose and I. R. Mackay, Eds., *The Autoimmune Diseases*, Academic Press, Amsterdam, 5th edn., 2013.

5 M. D. Smith, The Normal Synovium, *Open Rheumatol. J.*, 2011, **5**, 100–106.

6 P. Neregård, Solna Karolinska Institutet, 2013.

7 M. S. Taljanovic, D. M. Melville, L. H. Gimber, L. R. Scalcione, M. D. Miller, C. K. Kwoh and A. S. Klauser, High-Resolution US of Rheumatologic Diseases, *RadioGraphics*, 2015, **35**, 2026–2048.

8 C. A. Hitchon, The Synovium in Rheumatoid Arthritis, *Open Rheumatol. J.*, 2011, **5**, 107–114.

9 R. W. Kinne, B. Stuhlmüller and G.-R. Burmester, Cells of the synovium in rheumatoid arthritis. Macrophages, *Arthritis Res. Ther.*, 2007, **9**, 224.

10 Johns Hopkins Arthritis Center, http://www.hopkinsarthritis.org/arthritis-info/rheumatoid-arthritis/ra-pathophysiology-2/, (accessed 22 February 2020).

11 E. M. Paleolog, Angiogenesis in rheumatoid arthritis., *Arthritis Res.*, 2002, **4 Suppl 3**, S81-90.

12 O. S., L. Staunton, O. FitzGerald and S. R., in *Genes and Autoimmunity - Intracellular Signaling and Microbiome Contribution*, InTech, 2013.

13 V. Strand, R. Kimberly and J. D. Isaacs, Biologic therapies in rheumatology: lessons learned, future directions, *Nat. Rev. Drug Discov.*, 2007, **6**, 75–92.

14 G. E. Jackson, L. Mkhonta-Gama, A. Voyé and M. Kelly, Design of copper-based anti-inflammatory drugs, *J. Inorg. Biochem.*, 2000, **79**, 147–152.

15 E. T. Nomkoko, G. E. Jackson and B. S. Nakani, In vitro and in vivo stability investigations of Cu (ii), Zn (ii), Ca (ii) and Gd (iii) complexes with N, N′-bis (2-hydroxyiminopropionyl) propane-1, 3-diamine, *Dalt. Trans.*, 2004, 1432–1440.

16 S. Archer, Queen's Univierity School of Medicine/Department of Medicine,

https://deptmed.queensu.ca/dept-blog/hot-joints-become-hot-topic-new-early-inflammatory-arthritis-clinic-queens-university, (accessed 23 February 2020).

17 W. Bensen, W. Bensen and M. H. Atkinson, *Conquering Rheumatoid Arthritis*, Empowering Press, 1996.

18 P. Batty, *Living with Rheumatoid Arthritis*, eFortune US, 2008.

19 E. U. Tsumbu, Evaluation of tissue permeability of novel copper based anti-arthritic drugs, MSc Thesis, University of Cape Town, 2010.

20 J. N. Zvimba, Copper chelating anti-inflammatory agents of pseudo-mimics of Human Serum Albumin (HSA): copper and rheumatoid arthritis, PhD Thesis, University of Cape Town, 2005.

21 G. A. Green, Understanding NSAIDs: From aspirin to COX-2, *Clin. Cornerstone*, 2001, **3**, 50–59.

22 Johns Hopkins Arthritis Center: Rheumatoid Arthritis Treatment, https://www.hopkinsarthritis.org/arthritis-info/rheumatoid-arthritis/ra-treatment/, (accessed 23 February 2020).

23 P. Emery, H. Zeidler, T. K. Kvien, M. Guslandi, R. Naudin, H. Stead, K. M. Verburg, P. C. Isakson, R. C. Hubbard and G. S. Geis, Celecoxib versus diclofenac in long-term management of rheumatoid arthritis: randomised double-blind comparison, *Lancet*, 1999, **354**, 2106–2111.

24 D. G. Lambert, Disease-modifying antirheumatic drugs, *Anaesth. Intensive Care Med.*, 2012, **13**, 128–130.

25 A. Young, Rheumatoid arthritis: current approaches to drug treatment, *Prescriber*, 2006, **17**, 43–52.

26 K. G. Saag, G. G. Teng, N. M. Patkar, J. Anuntiyo, C. Finney, J. R. Curtis, H. E. Paulus, A. Mudano, M. Pisu, M. Elkins-Melton, R. Outman, J. J. Allison, M. S. Almazor, S. L. Bridges, W. W. Chatham, M. Hochberg, C. Maclean, T. Mikuls, L. W. Moreland, J. O'dell, A. M. Turkiewicz and D. E. Furst, American College of Rheumatology 2008 recommendations for the use of nonbiologic and biologic disease-modifying antirheumatic drugs in rheumatoid arthritis, *Arthritis Rheum.*, 2008, **59**, 762–784.

27 J. A. Singh, D. E. Furst, A. Bharat, J. R. Curtis, A. F. Kavanaugh, J. M. Kremer, L. W. Moreland, J. O'Dell, K. L. Winthrop, T. Beukelman, S. L. Bridges, W. W. Chatham, H. E. Paulus, M. Suarez-almazor, C. Bombardier, M. Dougados, D. Khanna, C. M. King, A. L. Leong, E. L. Matteson, J. T. Schousboe, E. Moynihan, K. S. Kolba, A.

Jain, E. R. Volkmann, H. Agrawal, S. Bae, A. S. Mudano, N. M. Patkar and K. G. Saag, 2012 Update of the 2008 American College of Rheumatology recommendations for the use of disease-modifying antirheumatic drugs and biologic agents in the treatment of rheumatoid arthritis, *Arthritis Care Res. (Hoboken).*, 2012, **64**, 625–639.

28 J. Bondeson, The mechanisms of action of disease-modifying antirheumatic drugs: A review with emphasis on macrophage signal transduction and the induction of proinflammatory cytokines, *Gen. Pharmacol. Vasc. Syst.*, 1997, **29**, 127–150.

29 J. F. Fries, C. A. Williams, D. Ramey and D. A. Bloch, The relative toxicity of disease-modifying antirheumatic drugs, *Arthritis Rheum.*, 1993, **36**, 297–306.

30 M. A. Quinn, The therapeutic approach of early intervention for rheumatoid arthritis: what is the evidence?, *Rheumatology*, 2001, **40**, 1211–1220.

31 M. Korpela, L. Laasonen, P. Hannonen, H. Kautiainen, M. Leirisalo-Repo, M. Hakala, L. Paimela, H. Blåfield, K. Puolakka and T. Möttönen, Retardation of joint damage in patients with early rheumatoid arthritis by initial aggressive treatment with disease-modifying antirheumatic drugs: Five-year experience from the FIN-RACo study, *Arthritis Rheum.*, 2004, **50**, 2072–2081.

32 J. S. Smolen, R. B. M. Landewé, J. W. J. Bijlsma, G. R. Burmester, M. Dougados, A. Kerschbaumer, I. B. McInnes, A. Sepriano, R. F. van Vollenhoven, M. de Wit, D. Aletaha, M. Aringer, J. Askling, A. Balsa, M. Boers, A. A. den Broeder, M. H. Buch, F. Buttgereit, R. Caporali, M. H. Cardiel, D. De Cock, C. Codreanu, M. Cutolo, C. J. Edwards, Y. van Eijk-Hustings, P. Emery, A. Finckh, L. Gossec, J.-E. Gottenberg, M. L. Hetland, T. W. J. Huizinga, M. Koloumas, Z. Li, X. Mariette, U. Müller-Ladner, E. F. Mysler, J. A. P. da Silva, G. Poór, J. E. Pope, A. Rubbert-Roth, A. Ruyssen-Witrand, K. G. Saag, A. Strangfeld, T. Takeuchi, M. Voshaar, R. Westhovens and D. van der Heijde, EULAR recommendations for the management of rheumatoid arthritis with synthetic and biological disease-modifying antirheumatic drugs: 2019 update, *Ann. Rheum. Dis.*, 2020, **6**, 685–699.

33 J. R. Kirwan, The Effect of Glucocorticoids on Joint Destruction in Rheumatoid Arthritis, *N. Engl. J. Med.*, 1995, **333**, 142–147.

34 K. G. Saag, Low-dose corticosteroid therapy in rheumatoid arthritis: Balancing the evidence, *Am. J. Med.*, 1997, **103**, S31–S39.

35 J. W. J. Bijlsma, Disease control with glucocorticoid therapy in rheumatoid arthritis, *Rheumatology*, 2012, **51**, iv9–iv13.

36 H. B. Townsend and K. G. Saag, Glucocorticoid use in rheumatoid arthritis: benefits,

mechanisms, and risks., *Clin. Exp. Rheumatol.*, **22**, S77-82.

37 D. P. Bajpayee, Significance of plasma copper and caeruloplasmin concentrations in rheumatoid arthritis., *Ann. Rheum. Dis.*, 1975, **34**, 162–165.

38 P. R. Scudder, D. Al-Timimi, W. McMurray, A. G. White, B. C. Zoob and T. L. Dormandy, Serum copper and related variables in rheumatoid arthritis., *Ann. Rheum. Dis.*, 1978, **37**, 67–70.

39 A. G. White, P. Scudder, T. L. Dormandy and V. M. Martin, Copper—An Index Of Erosive Activity?, *Rheumatology*, 1978, **17**, 3–5.

40 J. R. J. Sorenson, Copper Chelates as Possible Active Forms of the Antiarthritic Agents, *J. Med. Chem.*, 1976, **19**, 135–148.

41 D. H. Brown, W. W. Buchanan, A. F. El-Ghobarey, W. E. Smith and J. Teape, Serum copper and its relationship to clinical symptoms in rheumatoid arthritis., *Ann. Rheum. Dis.*, 1979, **38**, 174–176.

42 E. D. Harris, Copper-induced activation of aortic lysyl oxidase in vivo., *Proc. Natl. Acad. Sci.*, 1976, **73**, 371–374.

43 M. Chignard and B. B. Vargaftig, Dog platelets fail to aggregate when they form aggregating substances upon stimulation with arachidonic acid, *Eur. J. Pharmacol.*, 1976, **38**, 7–18.

44 J. M. McCord, Free Radicals and Inflammation: Protection of Synovial Fluid by Superoxide Dismutase, *Science (80-.).*, 1974, **185**, 529–531.

45 J. Chayen, L. Bitensky, R. G. Butcher and L. W. Poulter, Redox Control of Lysosomes in Human Synovia, *Nature*, 1969, **222**, 281–282.

46 J. R. J. Sorenson, in *5 Copper Complexes – A Unique Class of Anti-Arthritic Drugs*, 1978, pp. 211–260.

47 H. T. Delves, in *Ciba Foundation Symposium*, 1980, vol. 79, pp. 5–22.

48 P. Djurdjevic, I. Jakovljevic, L. Joksovic, N. Ivanovic and M. Jelikic-Stankov, The Effect of Some Fluoroquinolone Family Members on Biospeciation of Copper(II), Nickel(II) and Zinc(II) Ions in Human Plasma, *Molecules*, 2014, **19**, 12194–12223.

49 P. M. May, P. W. Linder and D. R. Williams, Computer simulation of metal-ion equilibria in biofluids: models for the low-molecular-weight complex distribution of calcium(II), magnesium(II), manganese(II), iron(III), copper(II), zinc(II), and lead(II) ions in human blood plasma, *J. Chem. Soc. Dalt. Trans.*, 1977, 588.

50 G. F. Nordberg, B. A. Fowler and Nordberg, Eds., *Handbook on the Toxicology of Metals*, Elsevier B.V., UK/USA, 4th edn., 2015.

51 G. E. Jackson, P. M. May and D. R. Williams, Metal-ligand complexes involved in rheumatoid arthritis—I, *J. Inorg. Nucl. Chem.*, 1978, **40**, 1189–1194.

52 M. E. Lahey, C. J. Gubler, G. E. Cartwright and M. M. Wintrobe, Studies on copper metabolism. VI. Blood copper in normal human subjects., *J. Clin. Invest.*, 1953, **32**, 322–328.

53 C. F. Tessmer, M. Hrgovcic, F. B. Thomas, L. M. Fuller and J. R. Castro, Serum Copper as an Index of Tumor Response to Radiotherapy, *Radiology*, 1973, **106**, 635–639.

54 D. Ramos, D. Mar, M. Ishida, R. Vargas, M. Gaite, A. Montgomery and M. C. Linder, Mechanism of Copper Uptake from Blood Plasma Ceruloplasmin by Mammalian Cells, *PLoS One*, 2016, **11**, e0149516.

55 A. L. P. Chapman, T. J. Mocatta, S. Shiva, A. Seidel, B. Chen, I. Khalilova, M. E. Paumann-Page, G. N. L. Jameson, C. C. Winterbourn and A. J. Kettle, Ceruloplasmin Is an Endogenous Inhibitor of Myeloperoxidase, *J. Biol. Chem.*, 2013, **288**, 6465–6477.

56 G. E. Jackson, P. M. May and D. R. Williams, Metal-ligand complexes involved in rheumatoid arthritis—VI, *J. Inorg. Nucl. Chem.*, 1978, **40**, 1227–1234.

57 J. R. Walker, M. J. H. Smith, A. W. Ford-Hutchinson and F. J. Billimoria, Mode of action of an anti-inflammatory fraction from normal human plasma, *Nature*, 1975, **254**, 444–446.

58 E. A. Roberts and M. L. Schilsky, Diagnosis and treatment of Wilson disease: An update, *Hepatology*, 2008, **47**, 2089–2111.

59 K. D. Rainsford and M. W. Whitehouse, Concerning the merits of copper aspirin as a potential anti-inflammatory drug, *J. Pharm. Pharmacol.*, 1976, **28**, 83–86.

60 G. E. Jackson and M. J. Kelly, Copper anti-inflammatory drugs in rheumatoid arthritis. Part 1. Computer aided drug design, *Inorganica Chim. Acta*, 1988, **152**, 215–217.

61 M. Kelly, Metal ion equilibria in biofluids-Copper and rheumatoid arthritis, PhD Thesis, University of Cape Town, 1998.

62 G. E. Jackson and M. J. Kelly, Copper anti-inflammatory drugs in rheumatoid arthritis. Part 2. A potentiometric and spectroscopic study of copper(II) polyaminodicarboxylate complexes, *J. Chem. Soc. Dalt. Trans.*, 1989, 2429–2433.

63 S. Odisitse, G. E. Jackson, T. Govender, H. G. Kruger and A. Singh, Chemical speciation of copper(II) diaminediamide derivative of pentacycloundecane - A potential anti-inflammatory agent, *Dalt. Trans.*, 2007, 1140–1149.

64 S. Odisitse and G. E. Jackson, In vitro and in vivo studies of the dermally absorbed Cu(II) complexes of N5O2 donor ligands - Potential anti-inflammatory drugs, *Inorganica Chim. Acta*, 2009, **362**, 125–135.

65 S. Odisitse and G. E. Jackson, In vitro and in vivo studies of N,N′-bis[2(2-pyridyl)-methyl]pyridine-2,6-dicarboxamide-copper(II) and rheumatoid arthritis, *Polyhedron*, 2008, **27**, 453–464.

66 S. Odisitse, In Vivo Bio-Distribution Study of 64Cu (II)-Labelled Copper (II) Complexes of Peptides Mimics in Balb/C Mice-Development of Copper Based Anti-Inflammatory Agents, *MOJ Bioorganic Org. Chem.*, , DOI:10.15406/mojboc.2017.01.00029.

67 M. C. Linder and M. Hazegh-Azam, Copper biochemistry and molecular biology., *Am. J. Clin. Nutr.*, 1996, **63**, 797S-811S.

68 J. N. Zvimba and G. E. Jackson, Thermodynamic and spectroscopic study of the interaction of Cu(II), Ni(II), Zn(II) and Ca(II) ions with 2-amino-N-(2-oxo-2-(2-(pyridin-2-yl)ethyl amino)ethyl)acetamide, a pseudo-mimic of human serum albumin, *Polyhedron*, 2007, **26**, 2395–2404.

69 L. Perrone, E. Mothes, M. Vignes, A. Mockel, C. Figueroa, M.-C. Miquel, M.-L. Maddelein and P. Faller, Copper Transfer from Cu-Aβ to Human Serum Albumin Inhibits Aggregation, Radical Production and Reduces Aβ Toxicity, *ChemBioChem*, 2009, **11**, 110–118.

70 J. E. Weder, C. T. Dillon, T. W. Hambley, B. J. Kennedy, P. A. Lay, J. R. Biffin, H. L. Regtop and N. M. Davies, Copper complexes of non-steroidal anti-inflammatory drugs: an opportunity yet to be realized, *Coord. Chem. Rev.*, 2002, **232**, 95–126.

71 J. N. Zvimba and G. E. Jackson, Copper chelating anti-inflammatory agents; N1-(2-aminoethyl)-N2-(pyridin-2-ylmethyl)-ethane-1,2-diamine and N-(2-(2-aminoethylamino)ethyl)picolinamide: An in vitro and in vivo study, *J. Inorg. Biochem.*, 2007, **101**, 148–158.

72 J. N. Zvimba and G. E. Jackson, Solution equilibria of copper(II) complexation with N,N′-(2,2′-azanediylbis(ethane-2,1-diyl))dipicolinamide: A bio-distribution and dermal absorption study, *J. Inorg. Biochem.*, 2007, **101**, 1120–1128.

2. Design of PhD Ligands

As a result of literature findings, different combinations of amino acids with varying degrees of lipophilic side chains, were used in order to further improve the lipophilicity, as well as have a sufficient endogenous copper(II) mobilizing capacity. Two of these studies, namely Vicatos[1] and Hammouda[2] formed the basis of the ligand design that this PhD is based on.

Vicatos[1] designed two tripeptides, sarcosyl-L-leucyl-phenylalanine (Sar-Leu-Phe) and glycyl-L-leucyl-phenylalanine (Gly-Leu-Phe) which can be seen in Figure 2.1. Compared to serum albumin, where copper(II) only binds with N-donor groups, for these ligands, copper(II) bound to N- and O-donor groups which lowered the stability of the complex compared to serum albumin. The idea behind having a lower stability is that once *in vivo*, the release of copper(II) from serum albumin will come from a shift in the equilibrium of free versus bound endogenous copper(II). This differs from the way ttda and dtda removed copper directly from serum albumin.[3,4] However, it was found that once *in vivo*, the ligands were poor at mobilizing copper(II), as they preferred to bind to zinc(II) and therefore were deemed unable to increase the bioavailable pool of copper(II) from endogenous sources.

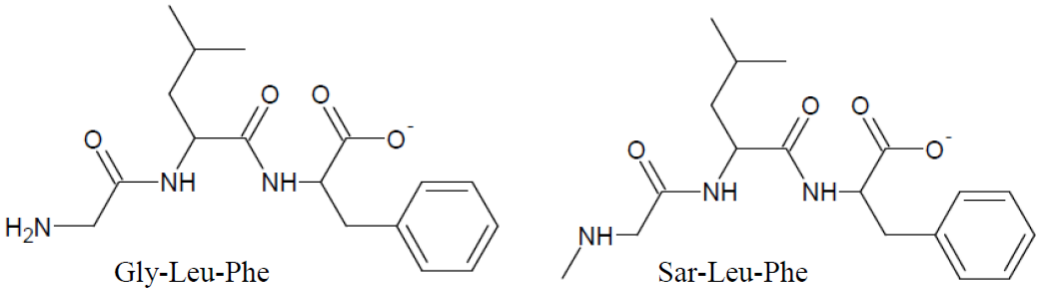

Figure 2.1: Structural representation of Gly-Leu-Phe and Sar-Leu-Phe.[1]

In contrast, the ligands studied by Hammouda[2] had good mobilizing capacities and found that when histidine is in the third position of a tripeptide, the mobilising capacities are higher as opposed to using histidine in the second position, or if histidine is not present in the tripeptide. This conclusion arose from the study of five tripeptides; sarcosyl-L- histidyl-L-lysine (Sar-His-Lys), sarcosyl-L-lysyl-L-histidine (Sar-Lys-His), sarcosyl-L-histidyl-L-histidine (Sar-His-

His), sarcosyl-L-lysyl-L-lysine (Sar-Lys-Lys) and sarcosyl-L-glycyl-L-histidine (Sar-Gly-His), which can be seen in Figure 2.2.

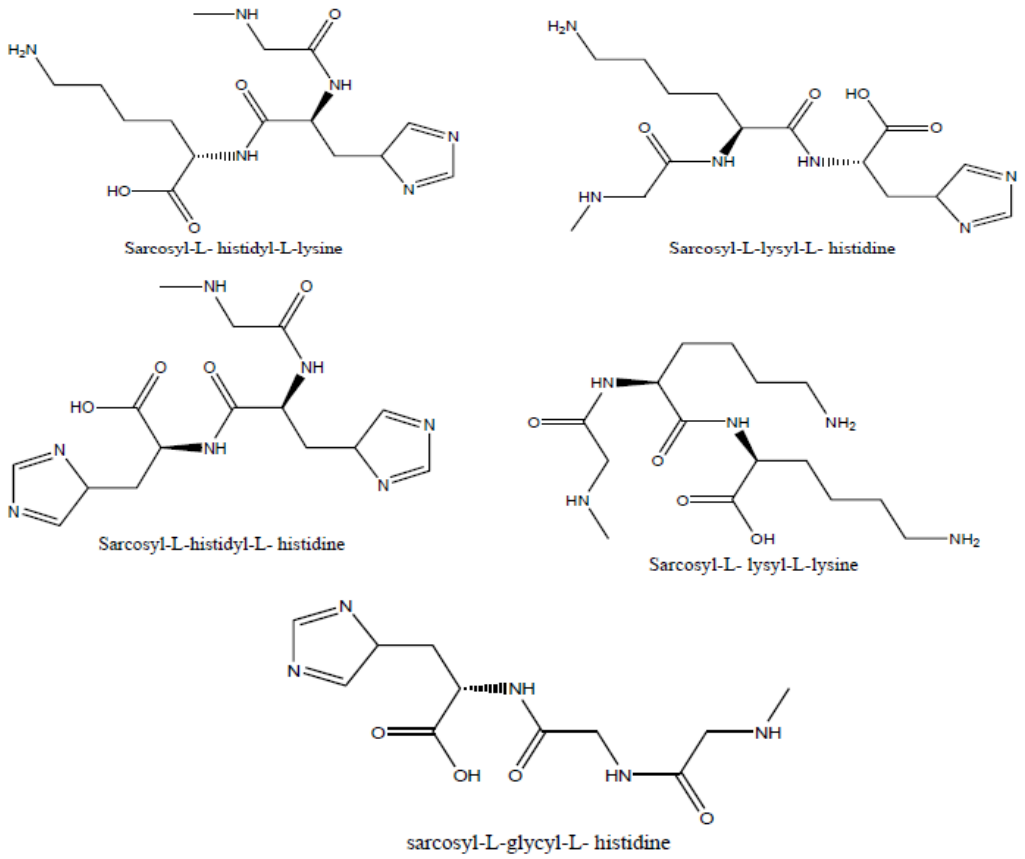

Figure 2.2: Structural representation of Sar-Lys-His, Sar-Gly-His, Sar-His-His, Sar-His-Lys and Sar-Lys-Lys.[2]

The order of the copper(II) mobilising ability was Sar-Lys-His > Sar-Gly-His ≈ Sar-His-His ≈ Sar-His-Lys > Sar-Lys-Lys. Sar-Lys-Lys was the only ligand that was more selective for zinc(II) rather than for copper(II), which was due to the lack of an imidazole group. The mobilizing ability of these ligands can be seen in Figure 2.3.

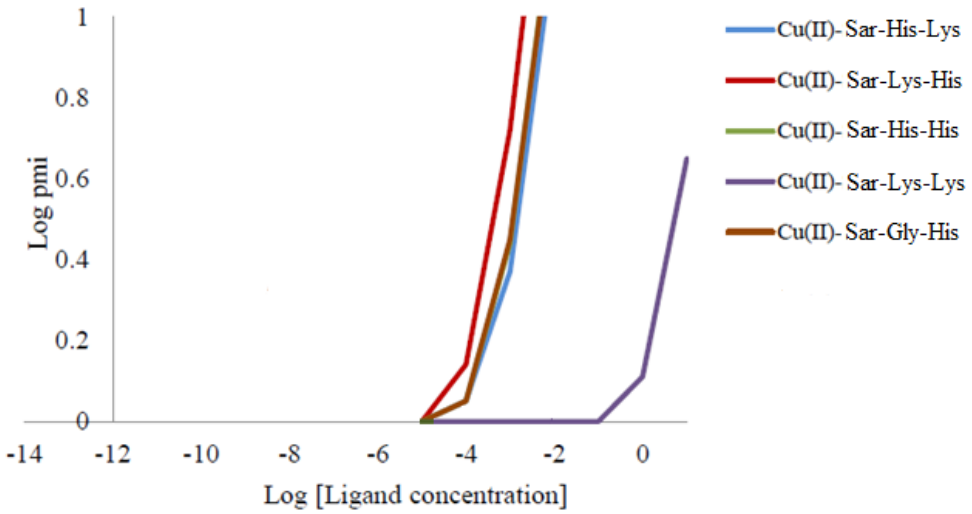

Figure 2.3: A comparison in mobilizing ability for Sar-Lys-His, Sar-Gly-His, Sar-His-His, Sar-His-Lys and Sar-Lys-Lys.[2]

From the two studies of Hammouda[2] and Vicatos[1], it was concluded that an imidazole group in the third position should be included into the ligand design of this PhD to ensure that the ligands would be selective for copper(II).

To study the lipophilicity of the ligands, both Hammouda[2] and Vicatos[1] measured the partition and permeability coefficient values. At the physiological pH, both studies found that all the complexes have negative partition coefficient values (Table 2.1), which indicated that the complexes are relatively hydrophilic. However, the values from the ligands in Vicatos[1] were significantly higher and therefore more lipophilic than the ligands in Hammouda[2].

Table 2.1: Partition coefficient values at pH 7.4 for the copper(II) complexes of Hammouda[2] and Vicatos[1].

Complex	**log $P_{oct\backslash aq}$ at pH 7.4**
Cu-Sar-His-Lys	-3.02 ± 0.01
Cu-Sar-Lys-His	-2.05 ± 0.01
Cu-Sar-His-His	-2.96 ± 0.01
Cu-Sar-Lys-Lys	-2.63 ± 0.01
Cu-Sar-Gly-His	-2.40 ± 0.01
Cu-Gly-Leu-Phe	-1.79 ± 0.05
Cu-Sar-Leu-Phe	-1.72 ± 0.05

The permeability coefficient values, which physically measured the lipophilicity of the ligands using an artificial membrane, found that the ligand complexes from Vicatos[1] were 2.1-8.8 times

more permeable than the ligand complexes from Hammouda[2]. They were also found to have the best transdermal absorption rates for recorded tripeptides in literature.[2,5] The reason behind the higher lipophilicity are the side chains on the amino acids. Leucine has a non-polar, aliphatic isobutyl side chain and phenylalanine has a non-polar benzyl side chain, while histidine has a polar imidazole functional group and lysine has a polar amine side chain. These non-polar groups are what made the overall tripeptides of Vicatos[1] more lipophilic.

Thus, the second position of the ligands in this PhD will either be leucine or phenylalanine. Even though the third position will have a polar imidazole functional group from histidine, the non-polar groups in leucine and phenylalanine should increase the lipophilicity of the complex.

The first position of the ligand will either be glycine or sarcosine and the reason behind this choice is that Vicatos[1] found no difference in lipophilicity between the ligand with glycine or sarcosine. It is predicted that due to the methyl group on sarcosine, the lipophilicity should be higher and so this PhD study will make a comparison to verify the results.

Therefore, based on the results from Hammouda[2] and Vicatos[1], as well as from the results that led up to the use of tripeptides, the new ligand design will consist of the following tripeptides, as seen in Figure 2.4.

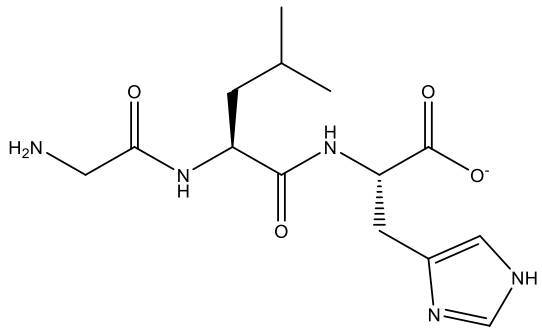

glycyl-L-leucyl-L-histidine (GLH)

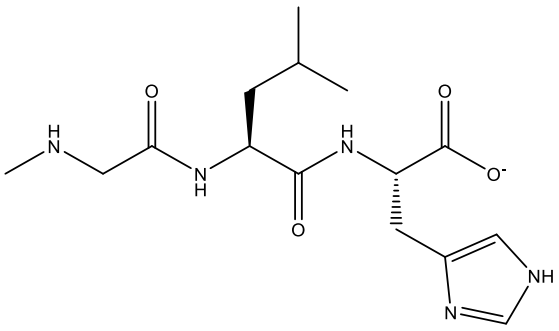

sarcosyl-L-leucyl-L-histidine (Sar-LH)

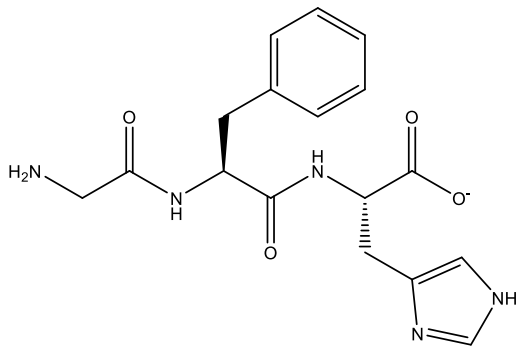

glycyl-L-phenylalanyl-L-histidine (GFH)

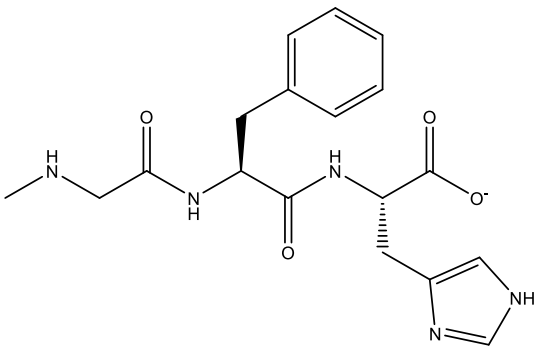

sarcosyl-L-phenylalanyl-L-histidine (Sar-FH)

Figure 2.4: Structural representation of the ligands used in this study, GLH, GFH, Sar-LH and Sar-FH.

2.1 References

1 G. M. Vicatos, In vitro studies of dermally absorbed Cu(II) tripeptide complexes as potential anti-inflammatory drugs, MSc Thesis, University of Cape Town, 2016.

2 A. N. Hammouda, Development of copper peptide complexes as anti-Inflammatory drugs, PhD Thesis, University of Cape Town, 2015.

3 G. E. Jackson and M. J. Kelly, Copper anti-inflammatory drugs in rheumatoid arthritis. Part 2. A potentiometric and spectroscopic study of copper(II) polyaminodicarboxylate complexes, *J. Chem. Soc. Dalt. Trans.*, 1989, 2429–2433.

4 G. E. Jackson, L. Mkhonta-Gama, A. Voyé and M. Kelly, Design of copper-based anti-inflammatory drugs, *J. Inorg. Biochem.*, 2000, **79**, 147–152.

5 L. Mazurowska and M. Mojski, ESI-MS study of the mechanism of glycyl-l-histidyl-l-lysine-Cu(II) complex transport through model membrane of stratum corneum, *Talanta*, 2007, **72**, 650–654.

3. Potentiometric Titrations

3.1 Introduction

Glass electrode potentiometry is a commonly used method to measure the hydrogen ion concentration of acid base solutions.[1,2] However, for accurate readings, it has a restriction which limits measurements of free hydrogen concentrations to be within the pH range of 2-12.[2] In particular, potentiometry can be used as a very successful technique to measure complex stability constants. This application studies how the pH influences a three-component equilibrium system, which includes the metal ion, the ligand and the proton.[3] The process involves the incremental addition of a standard base into an acidic solution that contains the ligand with and without a known concentration of the metal ion.[4]

The stability constant (*K*), which is also known as the equilibrium constant or the formation constant, is a quotient that consists of the multiplication between the activities of the products of a reaction raised to an appropriate power, divided by the multiplication between the activities of the reactants also raised to an appropriate power. A general stability constant for equilibrium 3.1 can be seen in equation 3.2. A and B are reactants, C and D are products, *a*, *b*, c and *d* are the stoichiometric coefficients, and the activity, which describes the effective concentration of a substance in a reaction mixture is depicted as '*a*'.

$$a\mathrm{A} + b\mathrm{B} \rightleftharpoons c\mathrm{C} + d\mathrm{D} \tag{3.1}$$

$$K_a = \frac{a_{\mathrm{C}}{}^{c}\, a_{\mathrm{D}}{}^{d}}{a_{\mathrm{A}}{}^{a}\, a_{\mathrm{B}}{}^{b}} \tag{3.2}$$

The activity can be calculated from the concentration of a substance by using an activity coefficient, as seen in equation 3.3, where the concentration of substance 'C' is depicted as [C], and the activity coefficient is γ.

$$a = \gamma\,[\mathrm{C}] \tag{3.3}$$

Substituting into equation 3.2:

$$K_a = \frac{[\mathrm{C}]^c[\mathrm{D}]^d}{[\mathrm{A}]^a[\mathrm{B}]^b}\frac{\gamma_\mathrm{C}{}^c\,\gamma_\mathrm{D}{}^d}{\gamma_\mathrm{A}{}^a\,\gamma_\mathrm{B}{}^b} \tag{3.4}$$

The activity coefficient measures how much a solution deviates from an ideal solution, and at a constant temperature and constant ionic strength the activity coefficient is constant.[5,6] This means that the stability constant can be represented in terms of the concentrations instead of the activities as seen in equations 3.5-3.7.

$$K_c = \frac{K_a}{\text{constant}} \tag{3.5}$$

If

$$\text{constant} = \frac{\gamma_\mathrm{C}{}^c\,\gamma_\mathrm{D}{}^d}{\gamma_\mathrm{A}{}^a\,\gamma_\mathrm{B}{}^b} \tag{3.6}$$

Then

$$K_c = \frac{[\mathrm{C}]^c[\mathrm{D}]^d}{[\mathrm{A}]^a[\mathrm{B}]^b} \tag{3.7}$$

The advantage of using the concentration of a species instead of the activities, is that it can be substituted directly into the mass balance equations, which are used to solve the stability constants of the metal ion complexes in the reaction. Additionally, the concentration stability constants are very close to the thermodynamic constants of the reaction and therefore the error is minimal. This leads to the determination of $-\Delta G^\circ$, $-\Delta H^\circ$, and ΔS° through the concentration stability constants.[6]

A metal complex can have the general equilibrium equation seen in equation 3.8, where M is the metal, L is the ligand and H is the hydrogen ion and *p*, *q*, *r* are the stoichiometric coefficients.[6]

$$pM + qL + rH \rightleftharpoons M_pL_qH_r \quad (3.8)$$

The accumulative stability constant for this overall reaction (equation 3.9) can be represented by the symbol β_{pqr}, where $[M_pL_qH_r]$ is the complex concentration and $[M]^p$, $[L]^q$ and $[H]^r$ are the free metal, free ligand and free hydrogen ion concentrations respectively.[7]

$$\beta_{pqr} = \frac{[M_pL_qH_r]}{[M]^p[L]^q[H]^r} \quad (3.9)$$

The overall stability constant can be broken down into individual stepwise stability constants, represented by the symbol *K*. The product of the individual stepwise stability constants yields the overall stability constant. An example can be seen in equations 3.10-3.15.[6,8–11]

$$M + L \rightleftharpoons ML \qquad K_{ML} = \frac{[ML]}{[M][L]} \quad (3.10)$$

$$ML + L \rightleftharpoons ML_2 \qquad K_{ML_2} = \frac{[ML_2]}{[ML][L]} \quad (3.11)$$

$$ML_{n-1} + L \rightleftharpoons ML_n \qquad K_{ML_n} = \frac{[ML_n]}{[ML_{n-1}][L]} \quad (3.12)$$

Therefore,

$$\beta_{ML} = K_{ML} = \frac{[ML]}{[M][L]} \quad (3.13)$$

$$\beta_{ML_2} = K_{ML}\,K_{ML_2} = \frac{[ML_2]}{[ML][L]^2} \quad (3.14)$$

$$\beta_{ML_n} = K_{ML}\,K_{ML_2} \ldots\ldots K_{ML_n} = \frac{[ML_n]}{[ML_{n-1}][L]^n} \quad (3.15)$$

In general these stability constants are usually numerically large and so they are expressed in a logarithmic form, as $\log_{10} K$ or $\log_{10} \beta$.[7]

If there are protons being dissociated or added to the complex or ligand, then the pK_a can be used to represent the equilibrium. However, the pK_a can be converted to the logarithm of an individual stepwise stability constant (log K) and vice versa, due to the definition of both entities. The reasoning can be seen in equations 3.16-3.20.

For the deprotonation reaction:

$$L\,H \rightleftharpoons L + H \tag{3.16}$$

The forward reaction gives rise to:

$$K_a = \frac{[L][H]}{[LH]} \tag{3.17}$$

$$pK_a = -\log K_a = -\log \frac{[L][H]}{[LH]} \tag{3.18}$$

But the protonation reaction yields the stability constant K:

$$K = \frac{[LH]}{[L][H]} \tag{3.19}$$

Therefore,

$$\text{Log } K = -\log K_a = pK_a \tag{3.20}$$

To carry out a potentiometric titration analysis, an electrochemical cell is needed. This cell contains the indicator/glass electrode, the reference electrode and a salt bridge. This cell can be represented as;

Reference electrode | salt bridge | analyte solution | indicator electrode

An analyte solution surrounds the glass electrode and connects electrically to the reference electrode through the salt bridge. The reference electrode (E_{ref}) is a half cell. The E_{ref} potential is a set value that remains constant with constant temperature and is not affected by the

concentration of the analyte solution. The potential of the glass electrode (E_g) depends on the hydrogen ion activity of the analyte.[12,13] The salt bridge prevents the contents in the analyte solution from mixing with the contents of the reference electrode. As a result, a potential (E_j) forms across the liquid junctions of the salt bridge at both ends. However, E_j is small enough to be negligible.[13]

The potential of the electrochemical cell can be represented by equation 3.21.

$$E_{cell} = E_{ref} + E_j + E_g \tag{3.21}$$

However, since the glass electrode potential has a dependence on the hydrogen ion activity, the term E_g can be rewritten to equation 3.22 to express this Nernstian response.[13,14]

$$E_{cell} = E_{ref} + E_j + E^0{}_g + \frac{RT\ln\{H^+\}}{F} \tag{3.22}$$

$E^0{}_g$ is the standard glass electrode potential of the hydrogen ions at unit activity, R is the universal gas constant, T is the absolute temperature, F is the Faraday constant and $\{H^+\}$ is the free hydrogen ion activity. The hydrogen ion activity is related to the concentration $[H^+]$ via an activity coefficient Υ_{H^+},[1] so that:

$$\{H^+\} = \Upsilon_{H^+}[H^+] \tag{3.23}$$

Provided the ionic strength of the analyte solution is constant, $\{H^+\}$ can be expressed in terms of concentration.[13] Then by making,

$$S = \frac{2.303\,R\,T}{F} \tag{3.24}$$

and grouping all the constants, including the hydrogen activity coefficient, the term $E_{constant}$,[13,14] is formed, so that:

$$E_{constant} = E_{ref} + E_j + E^0{}_g + S \log \Upsilon_{H^+} \tag{3.25}$$

The electrochemical cell equation becomes:

$$E_{cell} = E_{constant} + S \log [H^+] \quad (3.26)$$

When calibrating the electrodes, a strong acid-strong base titration is the usual method performed to obtain $E_{constant}$ and S at a set ionic strength.[14]

To analyse the potentiometric data, the program, Equilibrium Simulations for Titration Analysis (ESTA) was used. ESTA provides a tool for investigating chemical interactions in solution and for providing the quantitative characterization. Two types of program modules are used to compute the main calculations. The simulation module (ESTA1) sets up and solves the mass balance equations, which allow it to determine a single value for any parameter that characterizes a titration. These results are therefore on a point by point basis. The optimization modules (ESTA2A and ESTA2B) determine the "best" values for one or more parameters, which are based on a least squares process over the whole titration system. Another module, an error-propagation module (ESTA3B), performs a Monte Carlo error-propagation analysis.[15]

The simulation module (ESTA1) has two categories. The one category calculates the speciation distribution calculations and the second calculates the potentiometric titration calculations. The potentiometric calculations include the titration simulation, as well as the analysis of the formation function, deprotonation function, the estimation of the formation constant values, the analytical concentration calculations and the effect of the experimental errors in the data.[15]

The optimization modules (ESTA2A and ESTA2B) refine combinations of the formation constants, vessel and burette concentrations, initial vessel volume, as well as the slope and intercept of the electrode. There is a difference in how ESTA2A and ESTA2B implement the weighting. ESTA2A recalculates the weights during the optimization cycle by taking the new values from the parameters that are being optimized. ESTA2B calculates the weights once from the initial estimated values of the parameters that will be optimized.
For this study, the task function, OBJE, from ESTA2B was used and the task functions, ZBAR, QBAR and SPEC from ESTA1 were used.

The task function, OBJE, optimised the titration parameters, which includes calculating the weight, objective function value, emf's and finding the relative error contribution in weight at

each titration point. The optimization of parameters was achieved by minimizing the objective function, U_{obj}, which is defined as:

$$U_{obj} = (N - n_p)^{-1} \sum_{n=1}^{N} n_e^{-1} \sum_{q=1}^{n_e} w_{nq}(y_{nq}^{obs} - y_{nq}^{calc})^2 \quad (3.27)$$

N is the total number of experimental titration points, n_p is the total number of optimized points, n_e is the total number of electrodes and w_{nq} represents the weights of the q^{th} residual and n^{th} titration point. Y_{nq}^{obs} and y_{nq}^{calc} are the observed/experimental and calculated/theoretical variables of the q^{th} residual at the n^{th} titration point respectively.[16]

The most frequent method for minimizing U_{obj} is to use a Gauss-Newton method, which is the approach that ESTA uses. In the method, there is the assumption that U_{obj} is quadratic. [16]

$$U_{obj} = \bar{a} + \bar{p}^t \bar{b} + \frac{\bar{p}^t H \bar{p}}{2} \quad (3.28)$$

$\bar{a}$ and $\bar{b}$ are the Gauss-Newton quadratic vector parameters, $\bar{p}$ is the optimization vector parameter and H is the Hessian which is defined as:

$$H_{sr} = \frac{\delta^2 U_{obj}}{\delta p_s \delta p_r} \quad (3.29)$$

The standard deviations (σ)[16] of the parameters are the estimated errors that occur during optimization and are calculated by:

$$\sigma = \left(\frac{U_{obj} G_{rr}}{N - n_p} \right)^{\frac{1}{2}} \quad (3.30)$$

where $G = H^{-1}$.

The Hamiltonian *R*-factor, R^{H}, verifies the accuracy of the model by measuring the agreement between the experimental and theoretical/calculated data.[16] It is defined as:

$$R^{H} = \left(\frac{U_{obj}}{\sum_{n=1}^{N} n_e^{-1} \sum_{q=1}^{n_e} w_{nq} (y_{nq}^{obs})2}\right)^{\frac{1}{2}} \tag{3.31}$$

R^{H} also has a significant limit, R_{lim}^{H}, so that if $R^{H} < R_{lim}^{H}$, then the model is accurate and satisfactory. R_{lim}^{H} is centred around the error in the analytical data and the number of variables.[16,17] However, the closer the two expressions are to one another, the more accurate the agreement is between the experimental and theoretical data. The R_{lim}^{H} is defined as:

$$R_{lim}^{H} = \left(\frac{N}{\sum_{n=1}^{N} n_e^{-1} \sum_{q=1}^{n_e} w_{nq} (y_{nq}^{obs})2}\right)^{\frac{1}{2}} \tag{3.32}$$

The task function ZBAR,[15] calculates and plots the experimental and theoretical formation functions. It defines a stepwise complexation and if no metal ion is present, it will plot a Z_H-bar curve for the ligand protonation. The definition for the proton formation function is:

$$Z_{H-bar} = \frac{T_H - H + OH}{T_L} \tag{3.33}$$

where T_H is the total hydrogen ion concentration, T_L is the total ligand concentration and $OH = \frac{Kw}{H}$. If a metal ion is present, then ZBAR will plot the Z_M-bar curve for the complex formation. The definition for the complex formation function is:

$$Z_M\text{-bar} = \frac{T_L - A(1 + \sum_n \beta_{LHn} H^n)}{T_M} \tag{3.34}$$

where T_M is the total concentration of the metal and 'A' can be expressed as:

$$A = \frac{T_H - H + OH}{\sum_n (\beta_{LHn} H^n)} \tag{3.35}$$

To calculate both the experimental and theoretical formation functions, ESTA calculates the residual:

$$\mathrm{Z_{-bar}residual} = \mathrm{Z^{o}_{-bar}} - \mathrm{Z^{c}_{-bar}} \tag{3.36}$$

Where $\mathrm{Z^{o}_{-bar}}$ is the experimental function and $\mathrm{Z^{c}_{-bar}}$ is the theoretical function. There is a good agreement when the experimental and theoretical Z-bar curves can be superimposed.

A representation of a Z_H-bar is shown in Figure 3.1.[18] The Z_H-bar curve shows how many protons are bound to a ligand by levelling off whenever a proton is dissociated. The curve levels at Z_H-bar = 1 and then at Z_H-bar = 2, indicating two protons were dissociated. The pK_a values can also be estimated since they correspond to the pH at the half-bar value. In Figure 3.1, these values are log K_{LH}= 7.8 and log K_{LH_2}= 3.4.

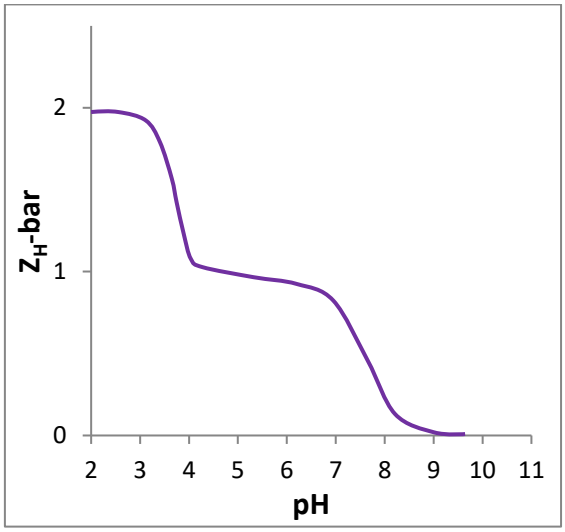

Figure 3.1: Typical Z_H-bar curve.[18]

A representation of a Z_M-bar curve, which is plotted against pL (-log[L]), can be seen in both Figures 3.2a and 3.2b.[18] If a solution has a simple series of ML_n (n=1, 2, 3...n) type species, then the curve will level off at a value equivalent to n. In Figure 3.2a, the curve levels off at 1, which means that the most predominant species type is ML. If the species type is not ML_n, then the Z_M-bar fails and results in the curve curling upwards and backwards. This curling indicates the formation of hydroxyl groups. This can be seen in Figure 3.2b, where the black line indicates that the ML species type is dominant, but then at low pL values, the hydroxyl group MLH_{-1} forms. The pink line curls before levelling off, which either indicates that the ML_n

species is not present or that it is not dominant, since hydroxyl species forms at high pL values, before the ML_n species can be formed. Therefore, depending on the type of curve presented, the complex species types can be predicted.

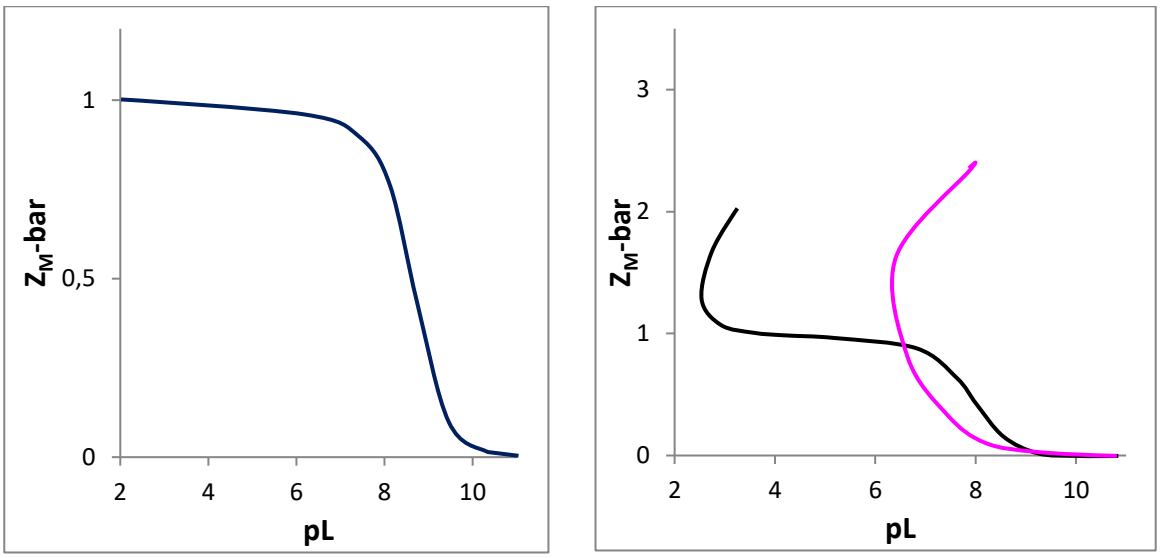

(a) (b)

Figure 3.2: Typical Z_M-bar curves when (a) ML is the only species present and when (b) ML plus hydroxyl species are dominant at different pL values (black), as well as when hydroxyl species are dominant at a high pL (pink).[18]

The deprotonation function, QBAR,[15] calculates and plots the experimental and theoretical deprotonation functions. It is also defined as a stepwise complexation, which determines the average number of protons that are released as a result of complexation. It is defined as:

$$Q_{M-bar} = \frac{T_H^* - T_H}{T_M} \tag{3.37}$$

where T_H^* is the total calculated concentration of protons present in the solution at a particular pH. The mass balance equations 3.38 and 3.39 solve T_H^* and T_L respectively.

$$T_H^* = H - OH + \sum_{J=1}^{NJ} r\left[M_p L_q H_r\right] \tag{3.38}$$

$$T_L = L + \sum_{J=1}^{NJ} q\left[M_p L_q H_r\right] \tag{3.39}$$

where NJ is the total number of titration points, $p = 0$ and $\mathrm{OH} = \frac{Kw}{\mathrm{H}}$.

ESTA plots *n*-bar, which is the total number of protons that would be bound to a ligand in the absence of a metal ion, on the same graph as $\mathrm{Q}_{\mathrm{M-bar}}$. *n*-bar is defined as;

$$n\text{-bar} = \frac{\mathrm{T}_{\mathrm{H}}^{*} - \mathrm{H} + \mathrm{OH}}{\mathrm{T}_{\mathrm{L}}^{\mathrm{r}}} \tag{3.40}$$

A representation of $\mathrm{Q_M}$-bar, which is plotted against pH, can be seen as the blue plot line in Figure 3.3.[18] The pink line represents *n*-bar and since it levels off at 1, it shows that one proton has been dissociated from the ligand. The *n*-bar and $\mathrm{Q_M}$-bar intersect at pH 3.9. The intersection at $\mathrm{Q_M}$-bar = 1, shows that the ligand has lost one proton due to complexation and therefore the species type is ML. At the $\mathrm{Q_M}$-bar peak the difference between $\mathrm{Q_M}$-bar and *n*-bar is 1, which shows that the ligand has lost another proton to form the $\mathrm{MLH_{-1}}$ species. Between pH 6.4-8.9, the $\mathrm{Q_M}$-bar and *n*-bar curves are parallel, which shows that no further protons are being displaced and hence no new species form. At pH 8.9, $\mathrm{Q_M}$-bar curves upwards, indicating the formation of hydroxyl groups.

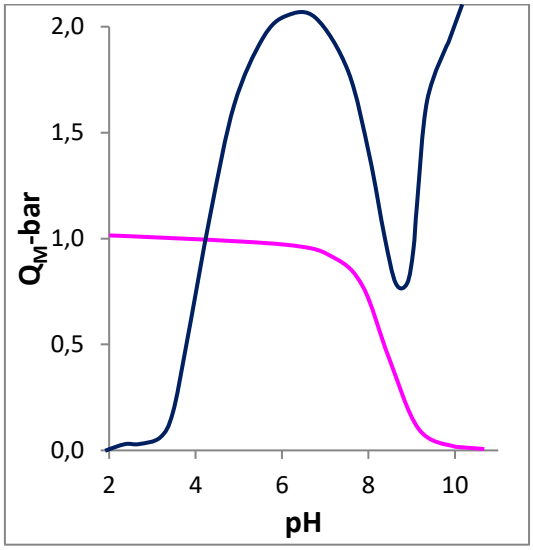

Figure 3.3: Typical $\mathrm{Q_M}$-bar (black) and *n*-bar curves (pink).[18]

The task function, SPEC, is able to plot speciation graphs from initial concentrations once the titration variables have been optimised and have converged. Thus, the task functions, ZBAR, QBAR and SPEC produce useful graphical representations of the data which can help identify many aspects of speciation.

3.2 Experimental

3.2(a) Solution preparations

The ligands, GLH, Sar-LH, GFH and Sar-FH were purchased from GL Biochem (Shanghai) Ltd. The other reagents used were of analytical grade and commercially available.

Boiled Milli-Q water (18.2 MΩ.cm) was used to prepare all the potentiometric titration solutions, so that carbon dioxide was removed. The method is outlined in Vogel.[19] The background electrolyte of the titration solutions was prepared with NaCl to have an ionic strength of 0.15 mol.dm^{-3}, so that it matched the ionic strength found in human blood.[20]

Background electrolyte was used to prepare a solution of HCl (0.01 M), which was then standardised against NaOH according to the method by Gran.[21] A solution of NaOH (0.1 M) was also prepared in background electrolyte, as well as under nitrogen (high purity) to prevent ingress of carbon dioxide. The solution of NaOH was then standardised against potassium hydrogen phthalate (KHP) according to the method by Gran.[21] The standardisation of NaOH was performed as an initial preparative setup.

Ligand solutions (0.005 M) were prepared by dissolving weighed samples of GLH, Sar-LH, GFH and Sar-FH into a standardised hydrochloric acid solution.

Metal solutions (0.01 M) were prepared using $CuCl_2 \cdot 2H_2O$, $NiCl_2 \cdot 6H_2O$ and $ZnCl_2$, according to the method outlined in Vogel. The preparation also involved adding background electrolyte to make the ionic strength 0.15 mol.dm^{-3}. The metal ion concentration was standardised by direct titration with ethylenediaminetetraacetic acid (EDTA) using a Metrohm 765 Dosimat automated burette. Murexide was used as an indicator during the standardisation of all metal ion concentrations.[19]

3.2(b) Potentiometric titrations

The potentiometric titrations were performed under an inert atmosphere of purified nitrogen gas at 25 ^{o}C and at a constant ionic strength of 0.15 mol.dm^{-3} (NaCl) using a Metrohm 888 Titrando (Metrohm, Switzerland). The measurements took place in a double walled titration

vessel in the pH range from 2-11 and kept at 25 ± 0.1 °C by a Haake thermostat bath. The amount of titrant added to the titrated solution was administered by a Metrohm 765 Dosimat automated burette (Metrohm, Switzerland) via a capillary tip, which had a non-return valve. The amount of added titrant was controlled by a software program that is built into Titrando, which also monitored the electromotive force. A magnetic bar stirred the titrated solution throughout the titration analysis. Titrando also has a built-in pH meter. A range of Metrohm ion analysis pH buffers (pH 4, 7 and 9) were used to calibrate the slope of the electrode, and strong acid-strong base titrations (HCl/NaOH) were used to calculate the electrode potential, $E°$, and the dissociation constant of water, pK_w.[12,22] The Nernstian slope was found to be 58.97. The value of E° was 414.77 mV and the value of pK_w was 13.62. These measurements were performed as an initial preparative setup. The metal ligand ratios were 1:1 and both the protonation and metal ligand titrations were titrated against NaOH over a pH range from 2-11. The ESTA suite of programs was then used to analyse the data from the potentiometric titrations.[23]

3.3 Results

Once the potentiometric data had been analysed using ESTA, it automatically gave the log β_{pqr} values for each species. For comparison purposes with literature, the pK_a values were calculated. But in order to calculate the pK_a values, the log K values had to be determined first. An example of how to calculate the log K value can be seen in Figure 3.4, and equations 3.41-3.43 show how to calculate the pK_a value.

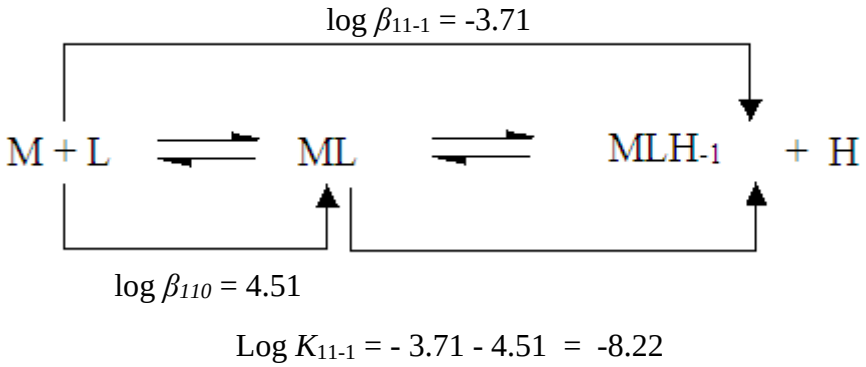

$$\text{Log } K_{11\text{-}1} = -3.71 - 4.51 = -8.22$$

Figure 3.4: Example of a log K calculation using stability constants.

Since the log of the formation constant $K_{11\text{-}1}$ is:

$$\log K_{11\text{-}1} = \log \frac{[MLH_{-1}][\mathrm{H}]}{[\mathrm{ML}]} = -8.22 \tag{3.41}$$

and the dissociation constant,

$$K_a = \frac{[MLH_{-1}][\mathrm{H}]}{[\mathrm{ML}]} \tag{3.42}$$

Therefore,

$$\mathrm{p}K_a = -\log \frac{[MLH_{-1}][\mathrm{H}]}{[\mathrm{ML}]} = 8.22 \tag{3.43}$$

3.3.1 Protonation of GLH, Sar-LH, GFH and Sar-FH

In aqueous solution, GLH, Sar-LH, GFH and Sar-FH are zwitterions, which have three available sites for protonation. The first is an amine group, which is in both the glycine and sarcosine amino acids. The second is the carboxyl group in histidine and the third is the nitrogen in the imidazole group of histidine. The amine group in glycine becomes protonated from a (NH_2) state to a (NH_3^+) state, and in sarcosine from a (NH) state to a (NH_2^+) state. Since these three groups, which undergo reversible proton binding, are all present in each tripeptide, protonation and deprotonation of each tripeptide will occur at similar pH values. With decreasing pH, the amine ($pK_a \approx 9.8$) will become protonated first, then the imidazole ($pK_a \approx 6.0$) and finally, the carboxyl ($pK_a \approx 1.8$).

3.3.1(a) Z_H-bar

The Z_H-bar for GLH, Sar-LH, GFH and Sar-FH can be seen in Figure 3.5. For all the graphs, at a pH of 11 the Z_H-bar curve starts at a value of zero, which indicates that the ligands are completely deprotonated. At approximately a pH of 9.0, the curves rise until a value of 2 is reached, after which they level off. This suggests that the ligands first became protonated from an L to an LH form and then immediately became protonated again to an LH_2 form. Between a pH of approximately 3.7 to 6.2 an equilibrium between LH and LH_2 is established. The high pH of this protonation indicates that the amine is protonated first and then the imidazole. At a

pH of approximately 3.7 all the curves continue to rise, but since the limit of the pH scale is at a value of 2, complete protonation to an LH_3 form cannot occur. The low pH of this protonation indicates that the carboxyl group is protonated. The protonation constants of GLH, Sar-LH, GFH and Sar-FH can be seen in Table 3.1.

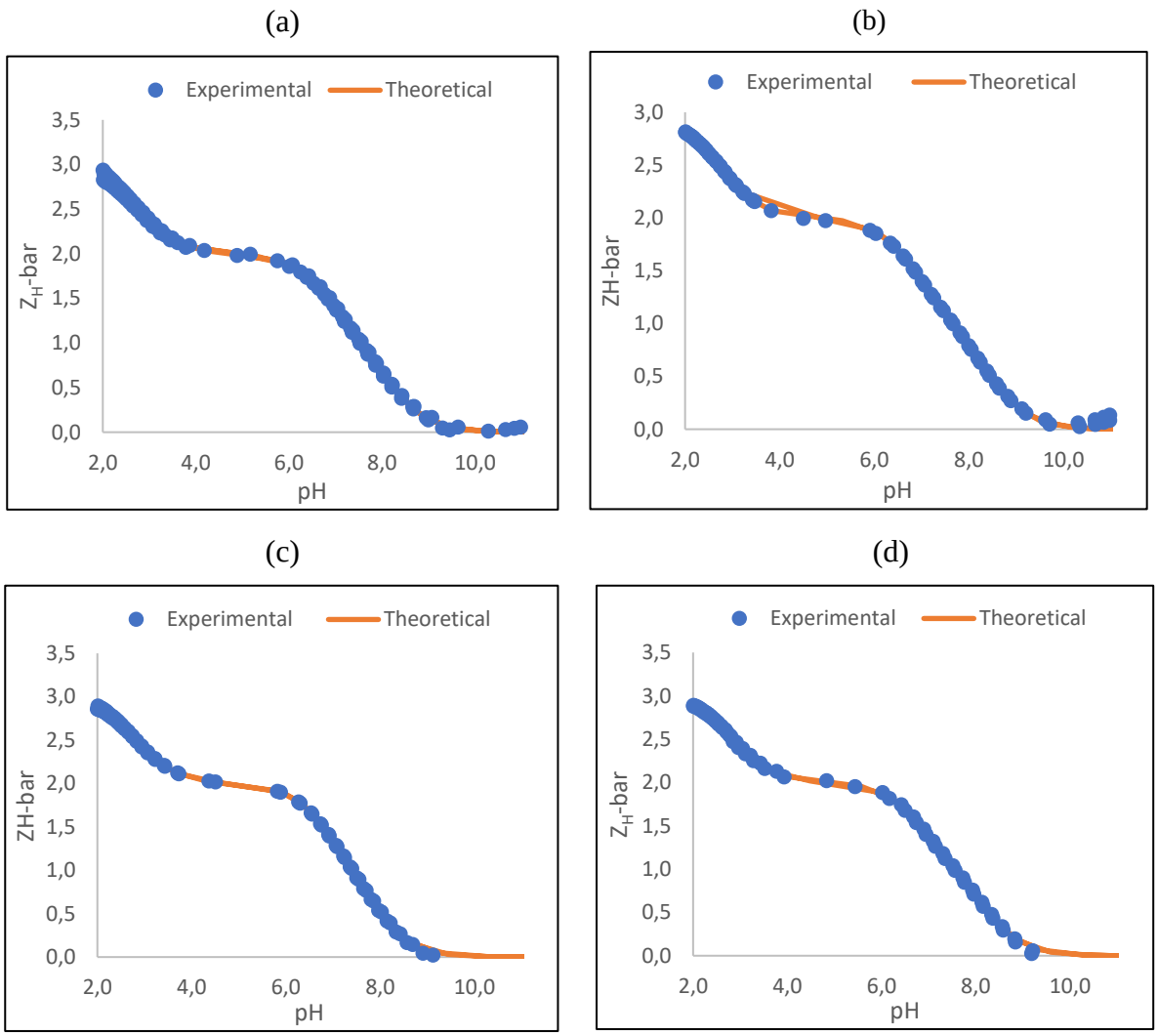

Figure 3.5: Z_H-bar as a function of pH for the protonation of (a) GLH, (b) Sar-LH, (c) GFH and (d) Sar-FH at 25 ^oC in 0.15 $mol.dm^{-3}$ of NaCl.

Table 3.1: Stability constants (log β_{pqr}) for GLH, Sar-LH, GFH and Sar-FH at 25 ^{o}C and 0.15 mol.dm^{-3} NaCl.

Std is the standard deviation; R_f^H is the Hamilton *R*-factor and R_{lim}^H is its limit; n_T is the number of titrations and (n_P) is the number of titration points; *p*, *q*, *r* are the stoichiometric coefficients of a complex with a general formula of $M_pL_qH_r$; M stands for the metal, L stands for the ligand and H stands for a hydrogen atom.

Ligand	**Protonation**	***p***	***q***	***r***	**log β_{pqr}**	**Log *K***	**std**	***R*f^{H}**	***R*$_{lim}^{H}$**	**$n_T(n_p)$**
GLH	LH	0	1	1	8.21	8.21	0.01	0.003	0.001	3(304)
	LH_2	0	1	2	15.10	6.89	0.01			
	LH_3	0	1	3	17.88	2.78	0.01			
Sar-LH	LH	0	1	1	8.45	8.45	0.03	0.007	0.001	2(202)
	LH_2	0	1	2	15.32	6.87	0.04			
	LH_3	0	1	3	18.05	2.73	0.05			
GFH	LH	0	1	1	7.95	7.95	0.02	0.004	0.001	2(202)
	LH_2	0	1	2	14.82	6.87	0.02			
	LH_3	0	1	3	17.65	2.83	0.02			
Sar-FH	LH	0	1	1	8.22	8.22	0.02	0.004	0.001	2(202)
	LH_2	0	1	2	15.09	6.87	0.02			
	LH_3	0	1	3	17.96	2.87	0.03			

3.3.1(b) Species distribution curve

The species distribution curve of GLH, Sar-LH, GFH and Sar-FH can be seen in Figure 3.6. For all graphs, at a pH of approximately 7.7 the LH species is at a maximum concentration and at this point, the LH_2 species has already started forming. From a pH of approximately 3.9 to 5.8, the distributions show that the ligands are protonated with two protons. For all graphs, at a pH of approximately 4.0 the LH_3 species starts forming, but does not reach a maximum concentration in this pH range. This corresponds to the Z_H-bar functions in Figure 3.5.

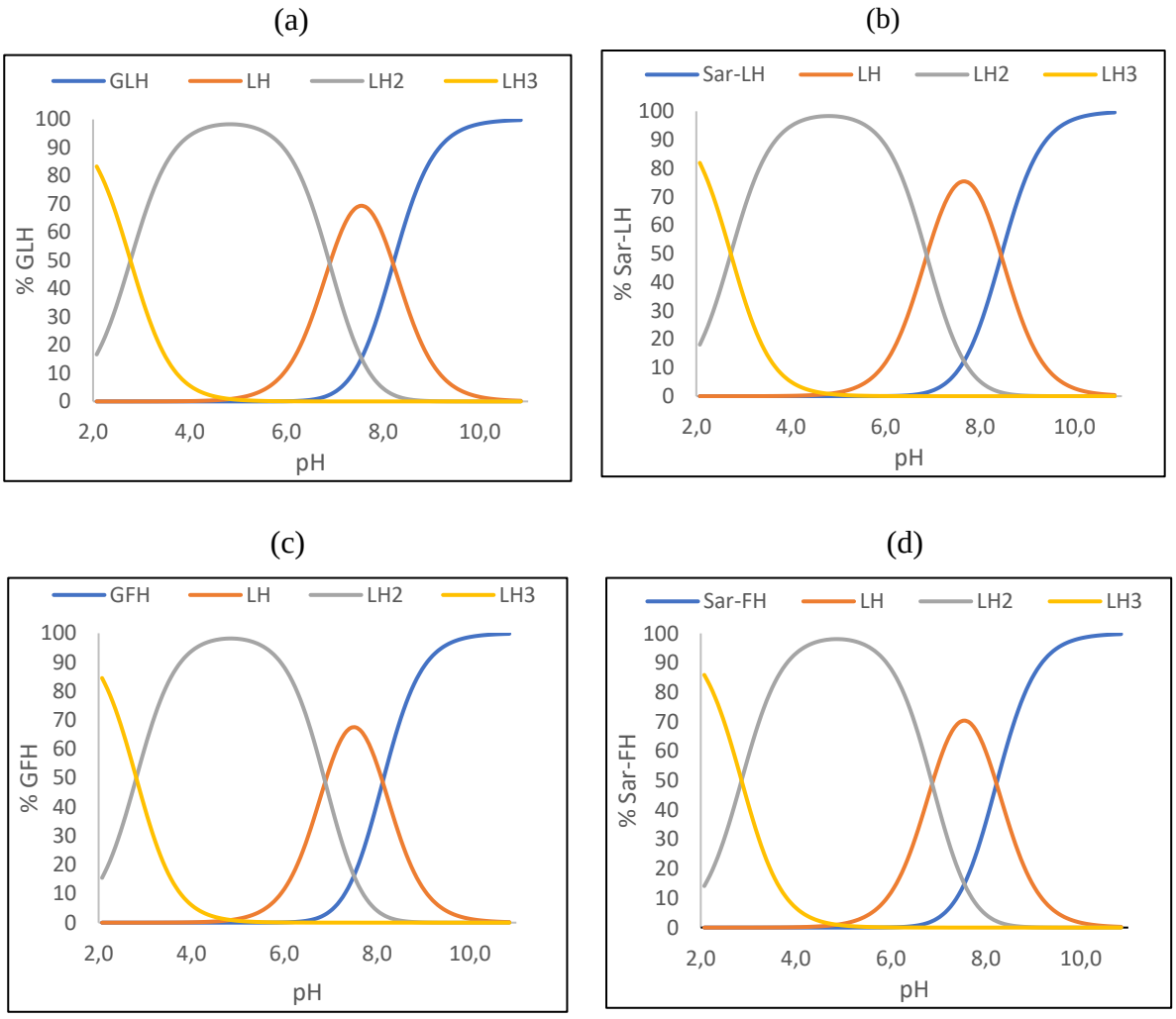

Figure 3.6: Protonation species distribution curve for (a) GLH, (b) Sar-LH, (c) GFH and (d) Sar-FH at 25 ^{o}C in 0.15 mol.dm^{-3} of NaCl.

3.3.2 Copper(II) complexation of GLH, Sar-LH, GFH and Sar-FH

The stability constants (log β_{pqr}) of the Cu-GLH, Cu-Sar-LH, Cu-GFH and Cu-Sar-FH complexations had a 1:1 copper(II) ligand ratio and were determined using ESTA suite of programs. These stability constants were used to calculate Z_M-bar, Q_M-bar and the species distribution functions. In the analysis of the complex titrations, a variety of reasonable models were refined successfully for each system. These models are given in Table 3.2, together with their refined statistics. Since each of these models described the experimental data, the problem was to decide which model best described the data, and at the same time which model makes the most chemical sense. Looking at the different models, the first question that arises, is why there is not an additional model for each ligand where all four of the species co-exist. This was

attempted, but the model would not converge and so does not exist. The models presented are all the possible combinations that converged. Looking at the log β_{pqr} values, there is very little difference between the values for the same species in different models (ligand specific). This shows that when the potentiometric titrations measured the release of protons, the difference between the models could not be distinguished, which is the reason why so many models are available. When comparing the standard deviations of the log β_{pqr} values and Hamilton *R*-factors, the best potentiometric models for Cu-GLH are models 2 and 3, models 3-5 for Cu-Sar-LH, model 1 for Cu-GFH and model 1 and 3 for Cu-Sar-FH.

Table 3.2**:** Stability constants (log β_{pqr}) for the 1:1 complexation between copper(II) and the ligands, GLH, Sar-LH, GFH and Sar-FH at 25 ^{o}C and 0.15 mol.dm^{-3} NaCl.
Std is the standard deviation; R_f^H is the Hamilton *R*-factor and R_{lim}^H is its limit; n_T is the number of titrations and (n_p) is the number of titration points; *p*, *q*, *r* are the stoichiometric coefficients of a complex with a general formula of $M_pL_qH_r$; M stands for the metal, L stands for the ligand and H stands for a hydrogen atom.

Complex	**Model**	**Species**	***p***	***q***	***r***	**log β_{pqr}**	**pK_a**	**std**	***R*f**	**R_{lim}**	**$n_T(n_p)$**
Cu-GLH	1	MLH_{-1} MLH_{-2}	1 1	1 1	-1 -2	2.76 -2.57	5.33	0.02 0.02	0.01	0.002	3(125)
	2	MLH MLH_{-1} MLH_{-2}	1 1 1	1 1 1	1 -1 -2	12.71 2.77 -2.24	5.01	0.03 0.02 0.01	0.007	0.002	3(125)
	3	ML MLH_{-1} MLH_{-2}	1 1 1	1 1 1	0 -1 -2	7.67 2.40 -2.40	5.27 4.80	0.05 0.08 0.02	0.009	0.002	3(125)
	4	MLH ML MLH_{-2}	1 1 1	1 1 1	1 -2	12.14 7.88 -2.27	4.26	0.24 0.03 0.03	0.01	0.002	3(125)
	5	MLH MLH_{-2}	1 1	1 1	1 -2	13.01 -2.11		0.04 0.02	0.02	0.002	3(125)
	6	ML MLH_{-2}	1 1	1 1	0 -2	7.92 -2.31		0.03 0.02	0.01	0.003	3(125)
Cu-Sar-LH	1	MLH_{-1} MLH_{-2}	1 1	1 1	-1 -2	2.23 -2.91	5.14	0.03 0.01	0.01	0.004	2(64)
	2	MLH MLH_{-1} MLH_{-2}	1 1 1	1 1 1	1 -1 -2	12.66 2.06 -2.71	4.77	0.02 0.02 0.01	0.004	0.004	2(64)
	3	MLH ML MLH_{-2}	1 1 1	1 1 1	1 0 -2	12.37 7.38 -2.70	4.99	0.05 0.02 0.008	0.004	0.004	2(64)
	4	MLH MLH_{-2}	1 1	1 1	1 -2	12.89 -2.59		0.03 0.01	0.008	0.004	2(64)
	5	ML MLH_{-2}	1 1	1 1	0 -2	7.47 -2.77		0.01 0.005	0.005	0.004	2(64)

Cu-GFH	1	MLH_{-1} MLH_{-2}	1 1	1 1	-1 -2	3.53 -1.34	4.87	0.02 0.02	0.009	0.002	2(86)
	2	MLH MLH_{-1} MLH_{-2}	1 1 1	1 1 1	1 -1 -2	11.72 3.54 -1.31	4.85	0.38 0.03 0.03	0.009	0.002	2(86)
	3	MLH MLH_{-2}	1 1	1 1	1 -2	12.76 -1.03		0.11 0.05	0.03	0.002	2(86)
	4	ML MLH_{-2}	1 1	1 1	0 -2	8.22 -1.14		0.06 0.03	0.02	0.002	2(86)
Cu-Sar-FH	1	MLH_{-1} MLH_{-2}	1 1	1 1	-1 -2	3.22 -1.75	4.97	0.03 0.01	0.01	0.002	3(134)
	2	MLH MLH_{-2}	1 1	1 1	1 -2	12.66 -1.51		0.14 0.04	0.03	0.002	3(134)
	3	ML MLH_{-2}	1 1	1 1	0 -2	7.86 -1.69		0.04 0.03	0.02	0.002	3(134)

The pK_a for the deprotonation of $Cu(H_2O)$ to CuOH is 8.13 and represents the hydrolysis of the aqua copper(II) complex.[24,25] If the pK_a values of the hydroxyl species are found to be similar to the pK_a of CuOH, then the deprotonation is due to the loss of a proton in water. To determine the pK_a of deprotonation, two species are required: the protonated species and the deprotonated species. Many deprotonated species in various models cannot be analysed, since they do not have the preceding species. For the species that can be analysed; in Model 1, for all complexes, MLH_{-1} to MLH_{-2} has a pK_a value between 4.87-5.33 (log $\beta_{11\text{-}1}$-log $\beta_{11\text{-}2}$). This is much lower than the hydrolysis of copper(II) and so the loss of the second proton is from the ligand and not from water. The same argument can be made for Model 2 of Cu-GLH, Cu-Sar-LH and Cu-GFH where the pK_a of MLH_{-1} to MLH_{-2} is between 4.77-5.11 (log $\beta_{11\text{-}1}$-log $\beta_{11\text{-}2}$). For Model 3 of Cu-GLH, the pK_a from ML to MLH_{-1} (log β_{110}-log $\beta_{11\text{-}1}$) and then to MLH_{-2} (log $\beta_{11\text{-}1}$-log $\beta_{11\text{-}2}$) is 5.27 and 4.80 respectively, which means both deprotonations are from the ligand. For Model 4 of Cu-GLH and Model 3 of Cu-Sar-LH, the pK_a from MLH to ML (log β_{111}-log β_{110}) is 4.26 and 4.99 respectively. Again, the deprotonation is from the ligand. All the other deprotonated species cannot be analysed and so it is uncertain whether their deprotonation is from the ligand or from water.

The first step in the validation of the different models was to compare the experimental and theoretical Z_M-bar, Q_M-bar curves. This is done in 3.3.2(a) and 3.3.2(b) below.

3.3.2(a) Z_M-bar

The complex formation function, Z_M-bar, for Cu-GLH, Cu-Sar-LH, Cu-GFH and Cu-Sar-FH can be seen in Figures 3.7-3.10 respectively. For all graphs, as the pL decreases (pH increases) the Z_M-bar curves increase and then before levelling off, curl backwards. This indicates that hydroxyl species are formed at a high pL (low pH). When comparing the theoretical curves, which are calculated using the refined models, with the experimental curves, all the models have the same theoretical curve at a high pH. This is because the predominant species type at this pH is MLH_{-2}, which is present in all models. In model (a) of Figures 3.7 and 3.8, the two curves do not agree at low Z_M-bar values. This is because this model does not include the MLH or ML species, which cause the Z_M-bar curve to increase at a low pH. For this reason, this model is rejected. For the models that contain an ML species, the Z_M-bar curve still curls backwards before levelling off, which means that the hydroxyl species start forming at around the same pH as the ML species. When comparing the agreement between the theoretical and experimental functions for each model of each ligand, some models have a better overlap than others. For example, Figure 3.7b, Figures 3.8b, c and e, Figures 3.9a and b and Figure 3.10a all have a better overlap compared to the other models for Cu-GLH, Cu-Sar-LH, Cu-GFH and Cu-Sar-FH respectively. The more accurate agreement indicates that those models could be the more correct choice.

3.3.2(a)(i) Cu-GLH

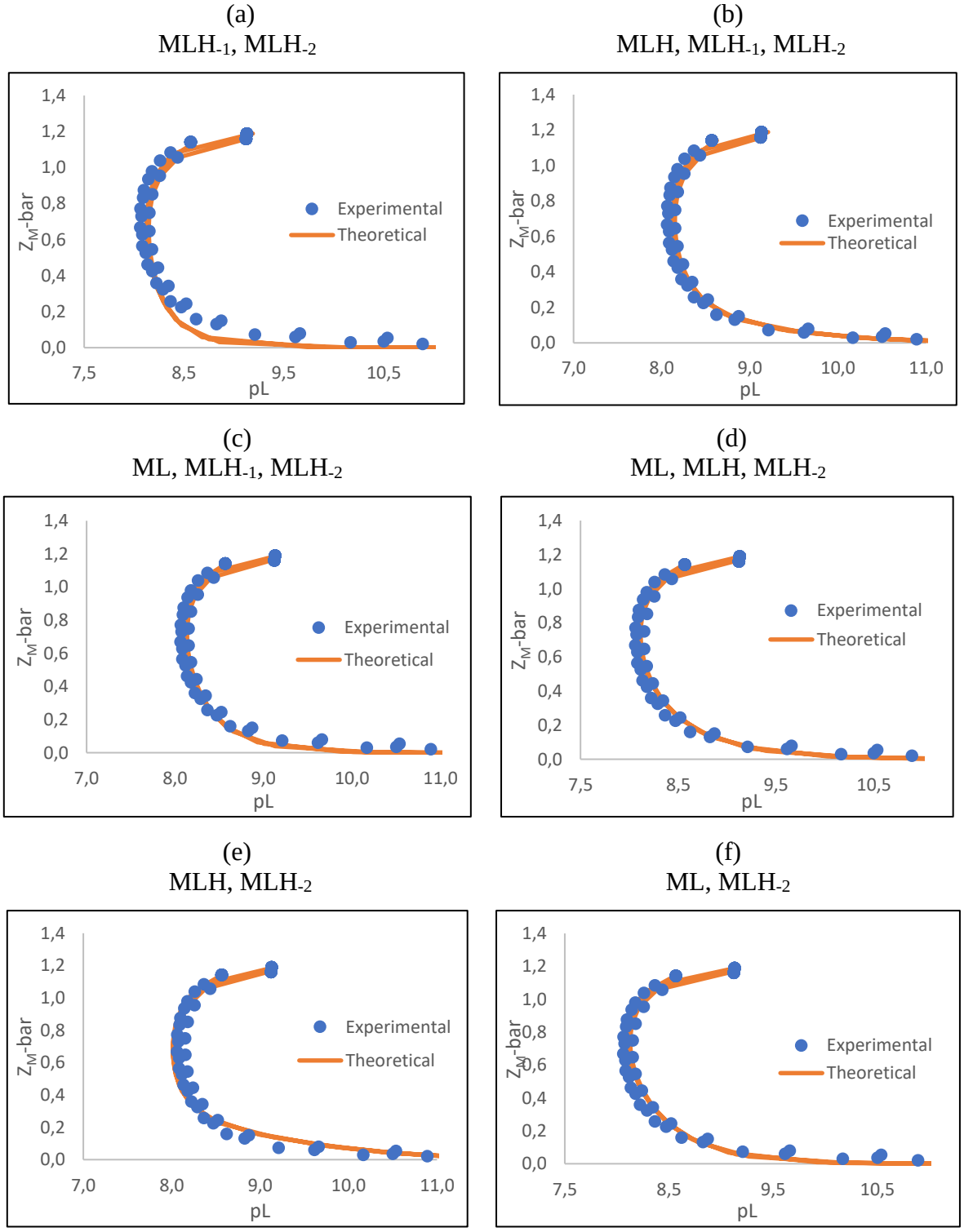

Figure 3.7: Z_M-bar as a function of pH for the 1:1 complexation of copper(II) and GLH (a) Model 1 (MLH_{-1}, MLH_{-2}), (b) Model 2 (MLH, MLH_{-1}, MLH_{-2}), (c) Model 3 (ML, MLH_{-1}, MLH_{-2}), (d) Model 4 (ML, MLH, MLH_{-2}), (e) Model 5 (MLH, MLH_{-2}) and (f) Model 6 (ML, MLH_{-2}) at 25 ^{o}C in 0.15 mol.dm^{-3} NaCl.

3.3.2(a)(ii) Cu-Sar-LH

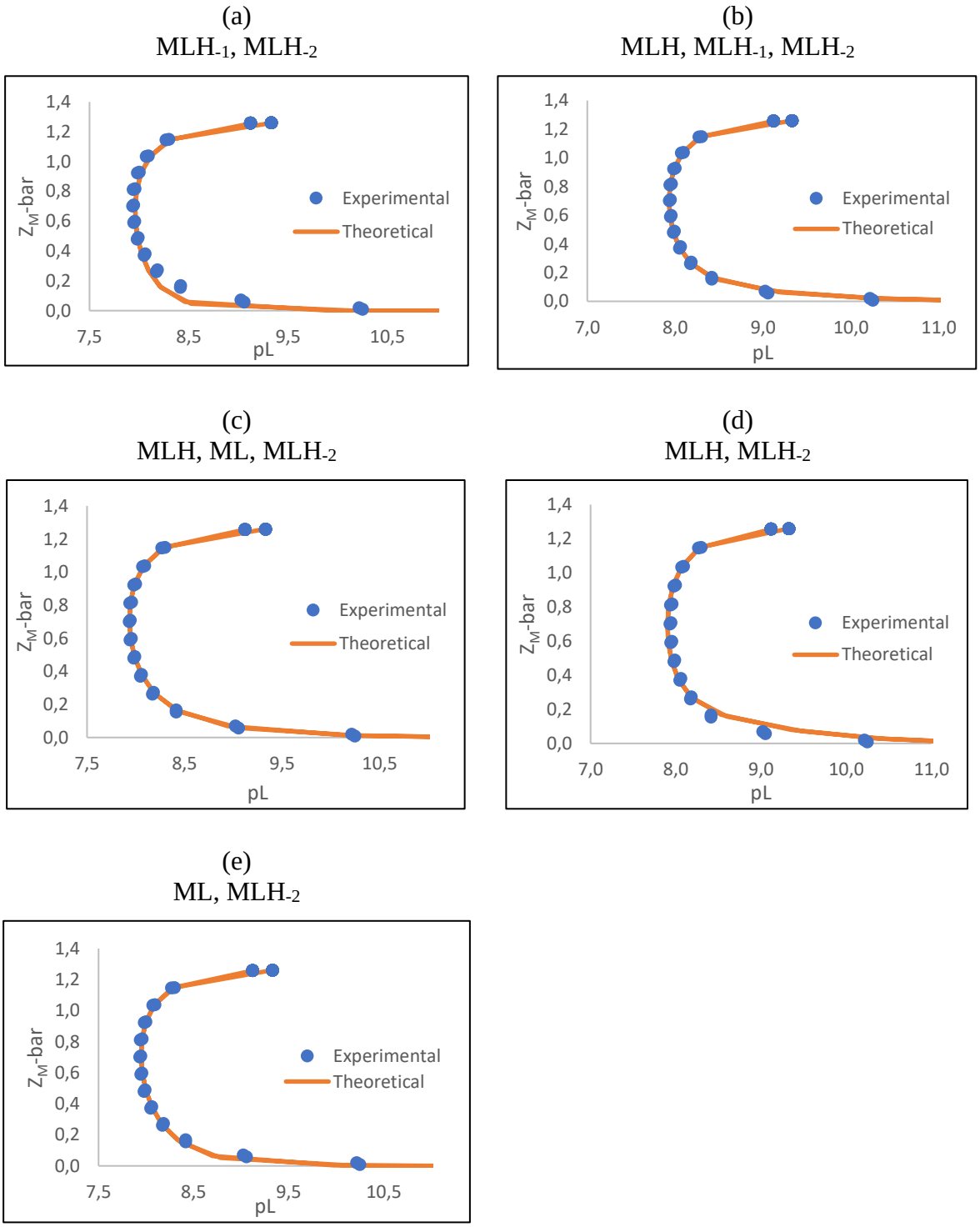

Figure 3.8: Z_M-bar as a function of pH for the 1:1 complexation of copper(II) and Sar-LH (a) Model 1 (MLH_{-1}, MLH_{-2}), (b) Model 2 (MLH, MLH_{-1}, MLH_{-2}), (c) Model 3 (MLH, ML, MLH_{-2}), (d) Model 4 (MLH, MLH_{-2}) and (e) Model 5 (ML, MLH_{-2}) at 25 ^{o}C in 0.15 mol.dm^{-3} NaCl.

3.3.2(a)(iii) Cu-GFH

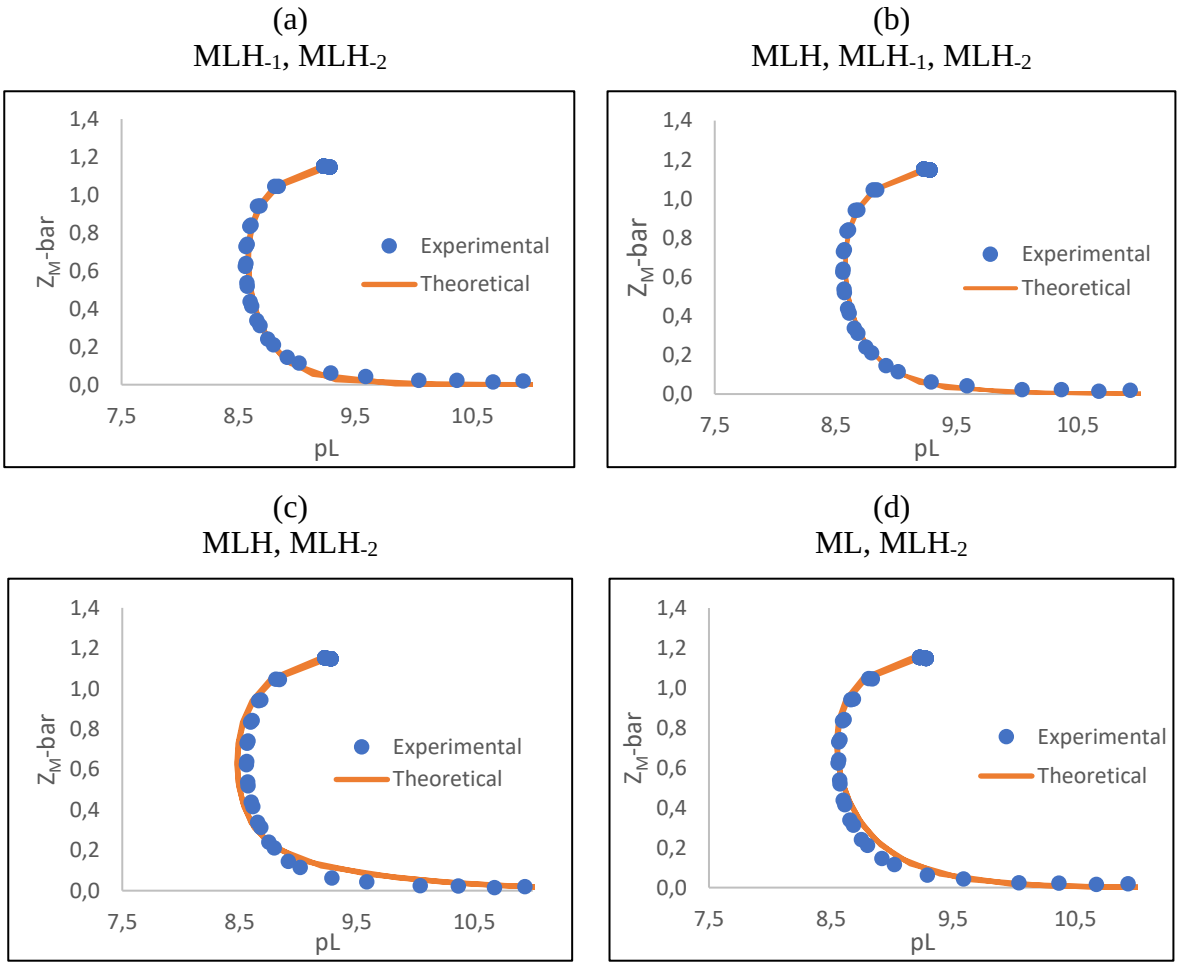

Figure 3.9: Z_M-bar as a function of pH for the 1:1 complexation of copper(II) and GFH (a) Model 1 (MLH_{-1}, MLH_{-2}), (b) Model 2 (MLH, MLH_{-1}, MLH_{-2}), (c) Model 3 (MLH, MLH_{-2}) and (d) Model 4 (ML, MLH_{-2}) at 25 ^{o}C in 0.15 mol.dm^{-3} NaCl.

3.3.2(a)(iv) Cu-Sar-FH

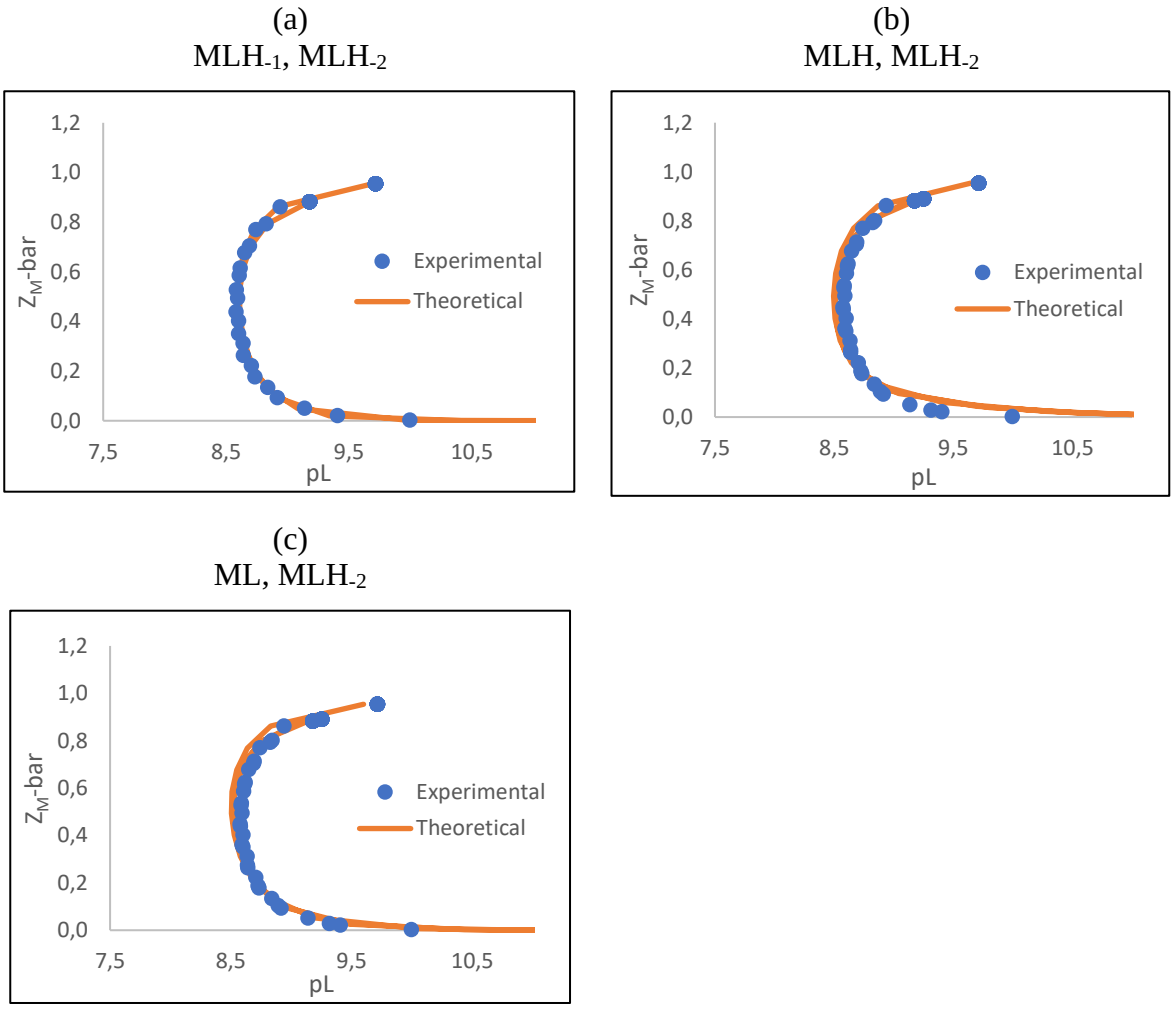

Figure 3.10: Z_M-bar as a function of pH for the 1:1 complexation of copper(II) and Sar-FH (a) Model 1 (MLH_{-1}, MLH_{-2}), (b) Model 2 (MLH, MLH_{-2}) and (c) Model 3 (ML, MLH_{-2}) at 25 ^{o}C in 0.15 mol.dm^{-3} NaCl.

3.3.2(b) Q_M-bar

The deprotonation function, Q_M-bar, for Cu-GLH, Cu-Sar-LH, Cu-GFH and Cu-Sar-FH can be seen in Figures 3.11-3.14. For all complex graphs, the *n*-bar plot line reaches a value of 2 and then levels off between a pH of approximately 3.6 and 5.9. This indicates that the LH_2 species has formed. In each graph, the Q_M-bar curve rises to a value that is between 1.5-1.9 units above the *n*-bar at a pH of approximately 6.0. This indicates that one to two protons are lost due to complexation. At high pH values, the *n*-bar plot line and Q_M-bar plot line in each graph become parallel to one another and the difference between them is 2 units. This means that species still form after a pH of approximately 6.0, but once the *n*-bar plot line and Q_M-bar plot line become parallel, a total of two protons has dissociated and no new species are forming. When comparing the overlap between the experimental and theoretical curves, all the figures besides Figure 3.11a and e, Figure 3.12a and e, Figure 3.13c and d, Figure 3.14b and c, all have an equally 'best fit'.

3.3.2(b)(i) Cu-GLH

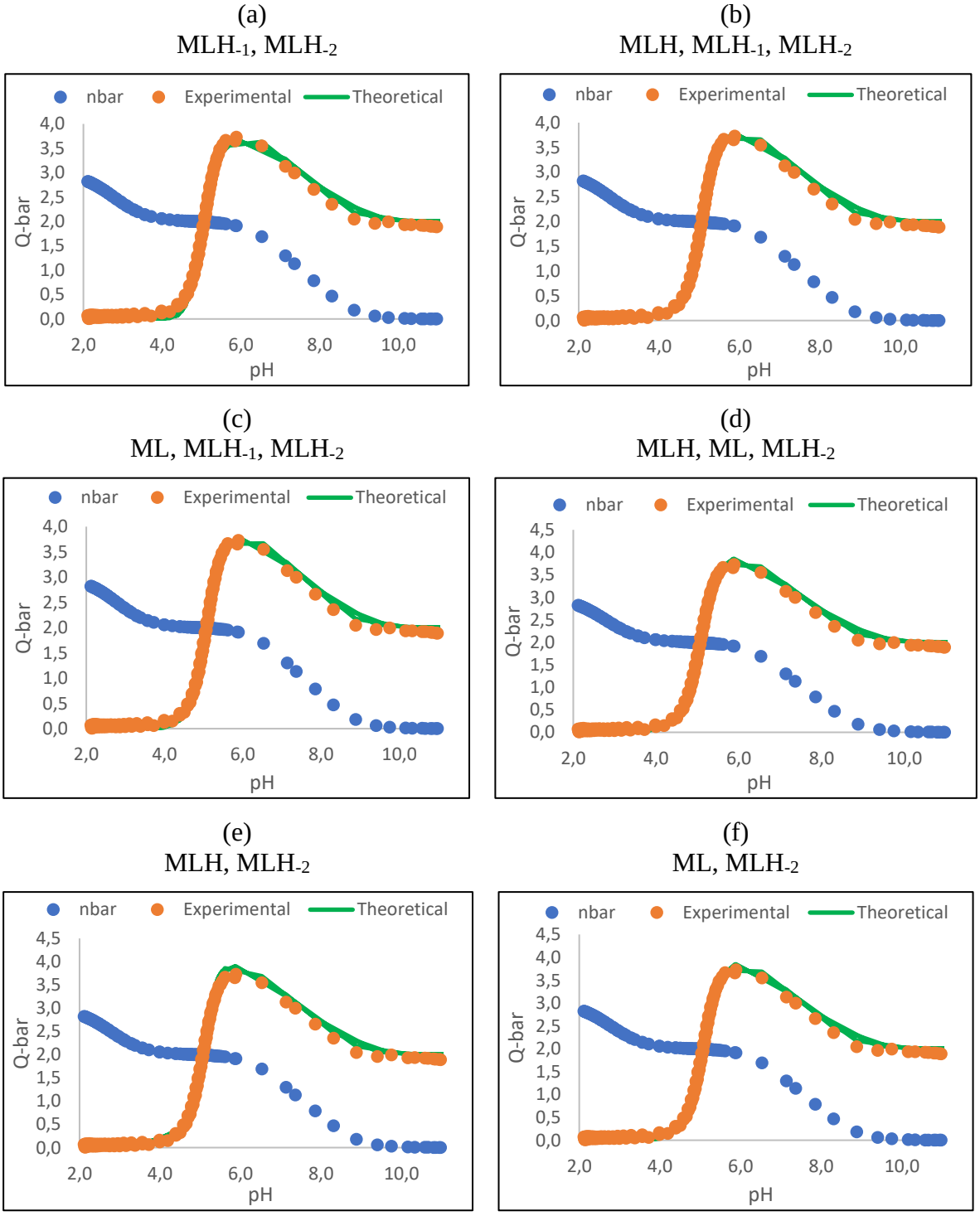

Figure 3.11: Q_M-bar as a function of pH for the 1:1 complexation of copper(II) and GLH (a) Model 1 (MLH_{-1}, MLH_{-2}), (b) Model 2 (MLH, MLH_{-1}, MLH_{-2}), (c) Model 3 (ML, MLH_{-1}, MLH_{-2}), (d) Model 4 (MLH, ML, MLH_{-2}), (e) Model 5 (MLH, MLH_{-2}) and (f) Model 6 (ML, MLH_{-2}) at 25 ^{o}C in 0.15 mol.dm^{-3} NaCl.

3.3.2(b)(ii) Cu-Sar-LH

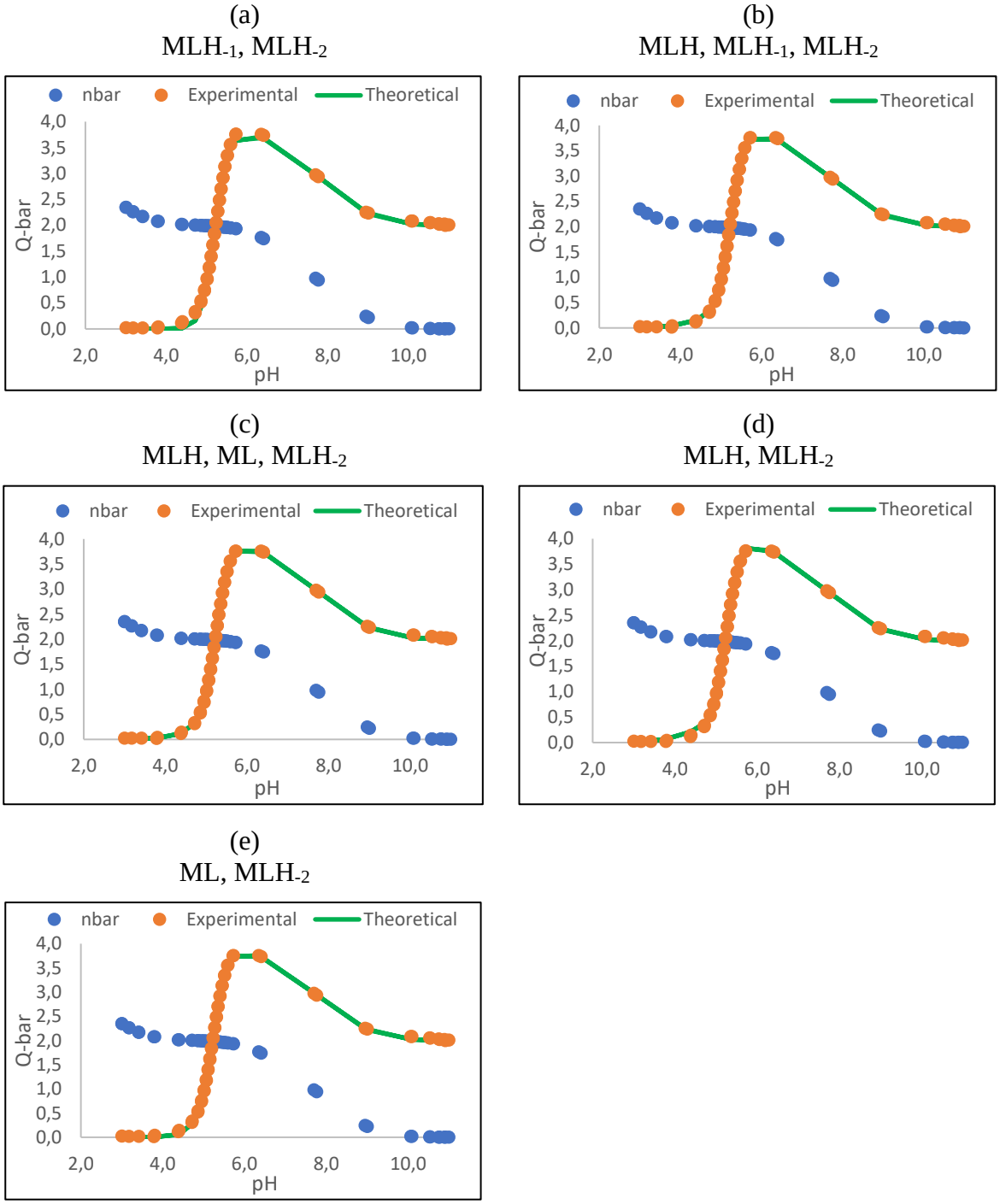

Figure 3.12: Q_M-bar as a function of pH for the 1:1 complexation of copper(II) and Sar-LH (a) Model 1 (MLH_{-1}, MLH_{-2}), (b) Model 2 (MLH, MLH_{-1}, MLH_{-2}), (c) Model 3 (MLH, ML, MLH_{-2}), (d) Model 4 (MLH, MLH_{-2}) and (e) Model 5 (ML, MLH_{-2}) at 25 ^{o}C in 0.15 mol.dm^{-3} NaCl.

3.3.2(b)(iii) Cu-GFH

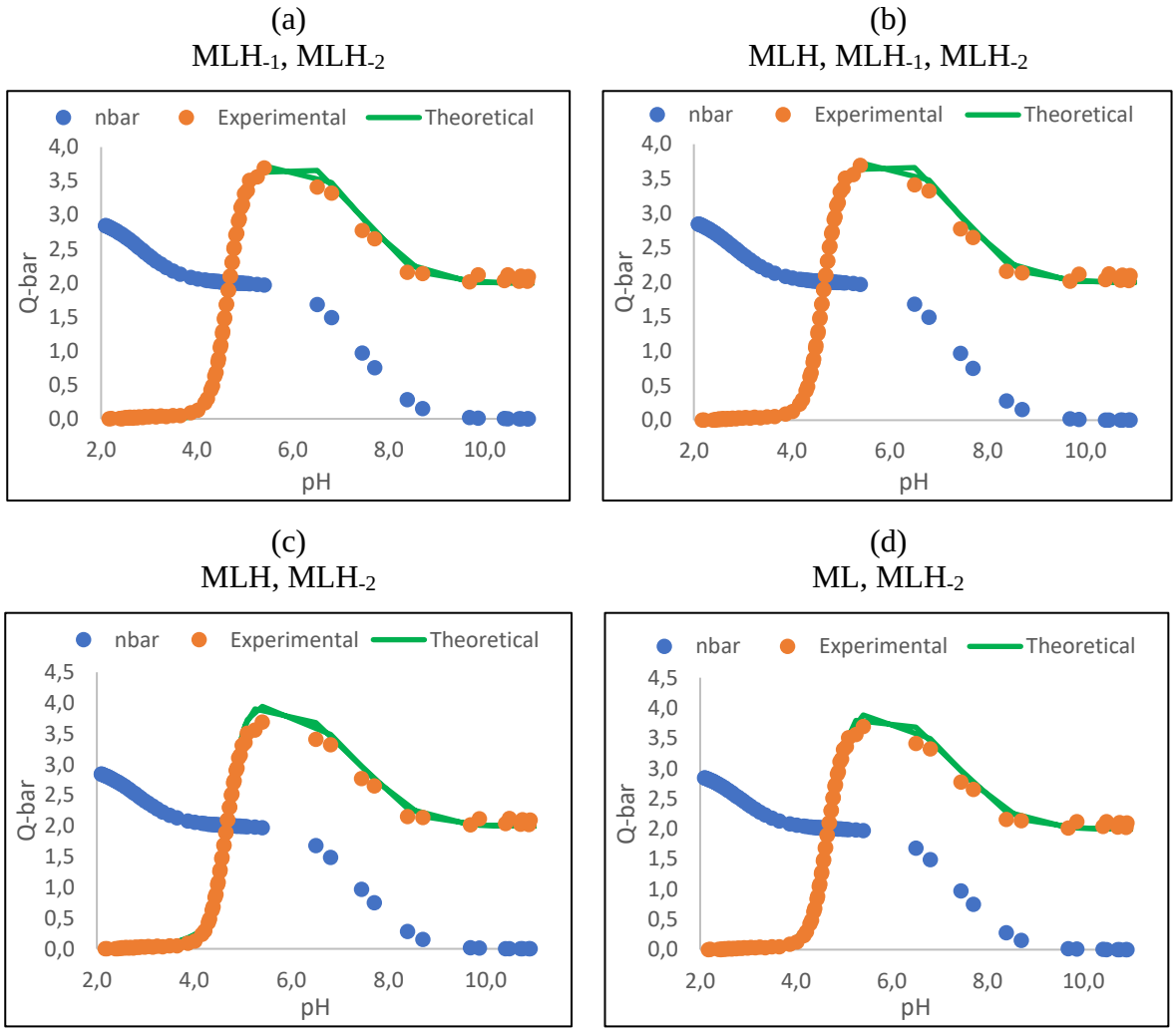

Figure 3.13: Q_M-bar as a function of pH for the 1:1 complexation of copper(II) and GFH (a) Model 1 (MLH_{-1}, MLH_{-2}), (b) Model 2 (MLH, MLH_{-1}, MLH_{-2}), (c) Model 3 (MLH, MLH_{-2}) and (d) Model 4 (ML, MLH_{-2}) at 25 ^oC in 0.15 $mol.dm^{-3}$ NaCl.

3.3.2(b)(iv) Cu-Sar-FH

(a)
MLH_{-1}, MLH_{-2}

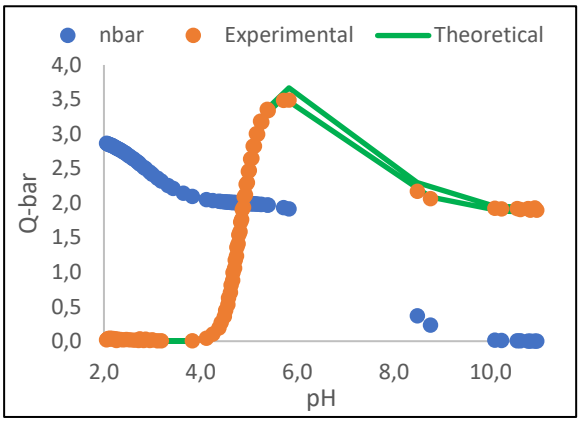

(b)
MLH, MLH_{-2}

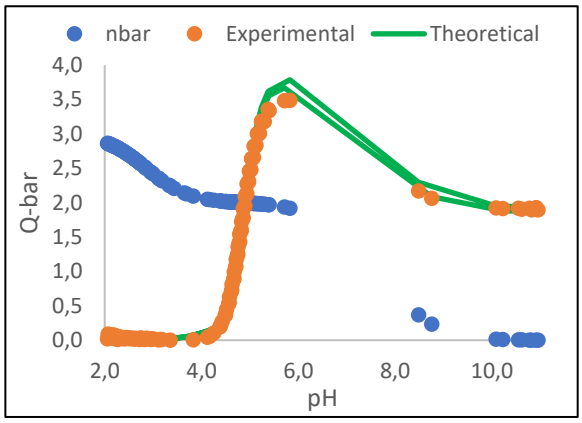

(c)
ML, MLH_{-2}

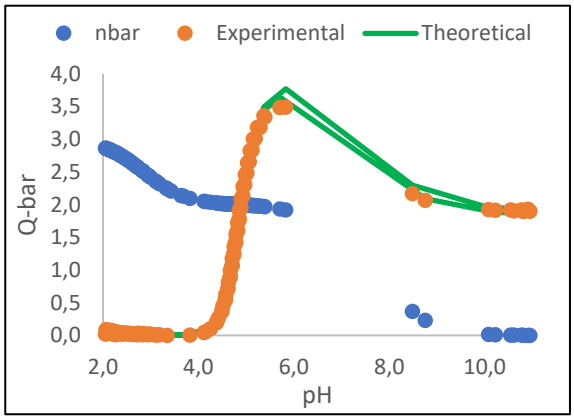

Figure 3.14: Q_M-bar as a function of pH for the 1:1 complexation of copper(II) and Sar-FH (a) Model 1 (MLH_{-1}, MLH_{-2}), (b) Model 2 (MLH, MLH_{-2}) and (c) Model 3 (ML, MLH_{-2}) at 25 ^{o}C in 0.15 mol.dm^{-3} NaCl.

3.3.2(c) Species distribution curve

The species distribution curves for Cu-GLH, Cu-Sar-LH, Cu-GFH and Cu-Sar-FH can be seen in Figures 3.15-3.18. The distribution graphs show that the hydroxyl species start forming at low pH values. The prevalence of the MLH species is roughly between pH 3.0-6.0, while the prevalence of the ML and MLH_{-1} species is roughly between pH 4.0-6.0 and pH 4.0-7.0 respectively. The MLH_{-2} species forms between pH 4.0 to pH 7.0, but after pH 7.0, no new species form and MLH_{-2} reaches a 100 % dominance until pH 11.0. This corresponds to the Z_M-bar and Q_M-bar curves seen in Figures 3.7-3.10 and 3.11-3.14 respectively.

3.3.2(c)(i) Cu-GLH

(a)
MLH$_{-1}$, MLH$_{-2}$

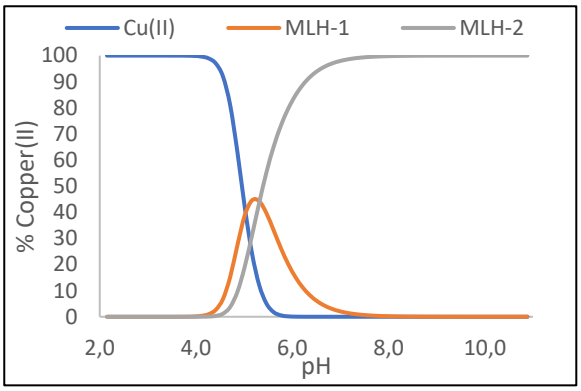

(b)
MLH, MLH$_{-1}$, MLH$_{-2}$

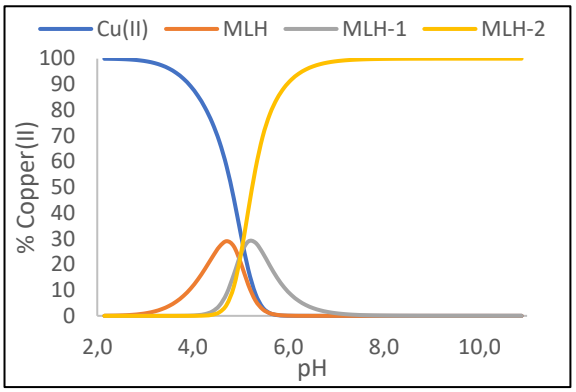

(c)
ML, MLH$_{-1}$, MLH$_{-2}$

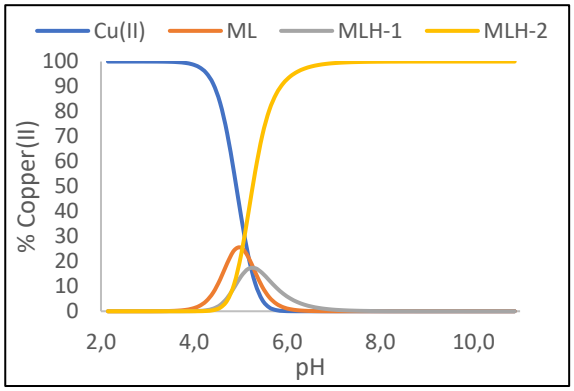

(d)
MLH, ML, MLH$_{-2}$

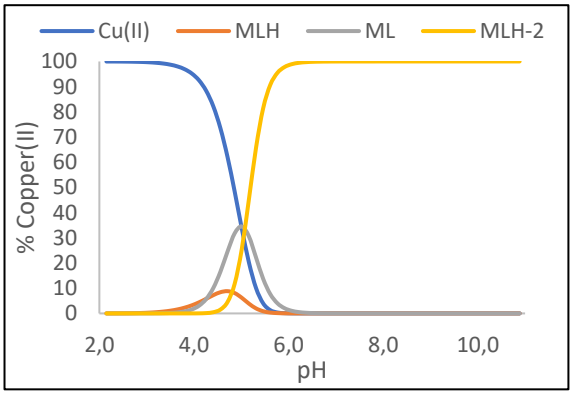

(e)
MLH, MLH$_{-2}$

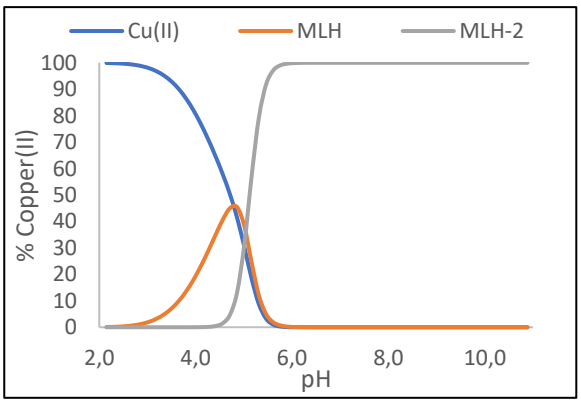

(f)
ML, MLH$_{-2}$

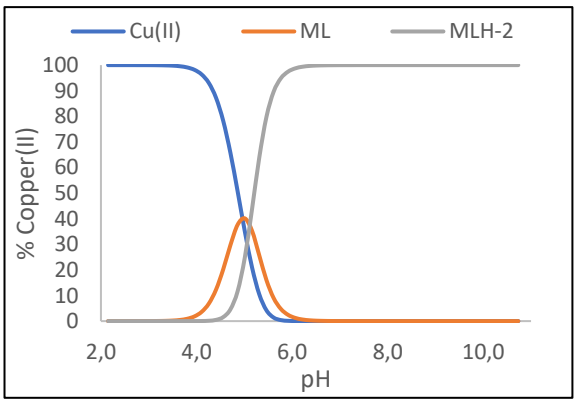

Figure 3.15: Complexation species distribution curve for the 1:1 ratio of copper(II) and GLH (a) Model 1 (MLH$_{-1}$, MLH$_{-2}$), (b) Model 2 (MLH, MLH$_{-1}$, MLH$_{-2}$), (c) Model 3 (ML, MLH$_{-1}$, MLH$_{-2}$), (d) Model 4 (MLH, ML, MLH$_{-2}$), (e) Model 5 (MLH, MLH$_{-2}$) and (f) Model 6 (ML, MLH$_{-2}$) at 25 ^{o}C in 0.15 mol.dm^{-3} of NaCl.

3.3.2(c)(ii) Cu-Sar-LH

(a)
MLH_{-1}, MLH_{-2}

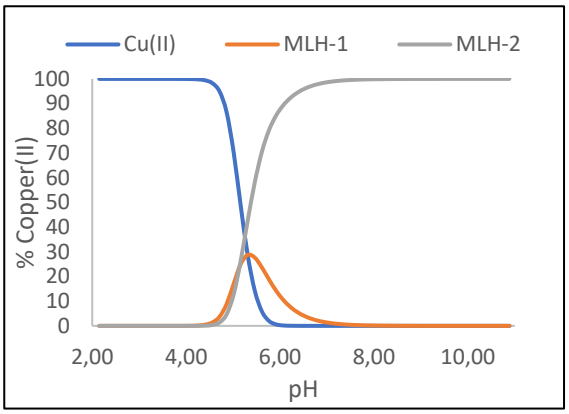

(b)
MLH, MLH_{-1}, MLH_{-2}

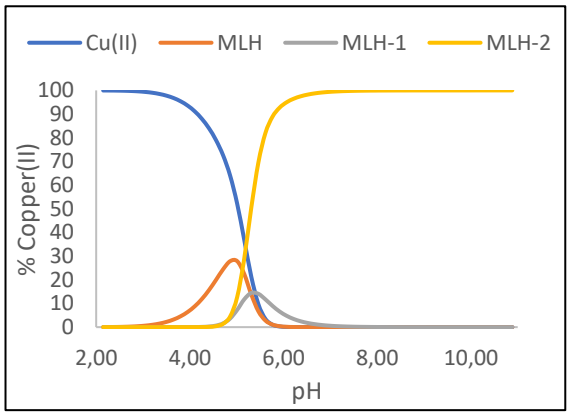

(c)
MLH, ML, MLH_{-2}

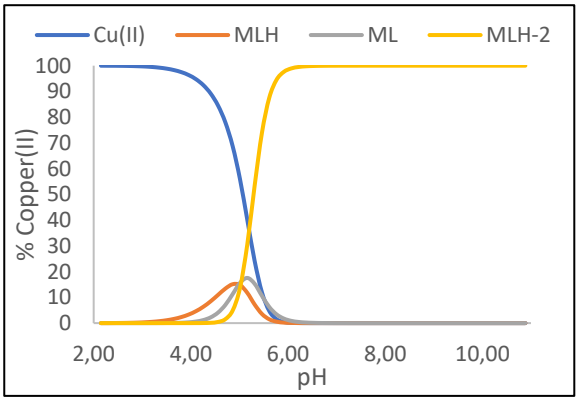

(d)
MLH, MLH_{-2}

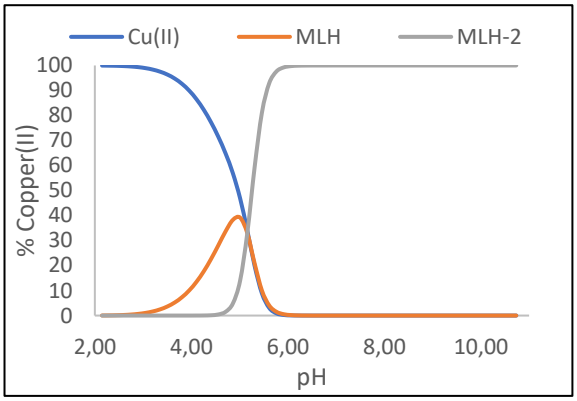

(e)
ML, MLH_{-2}

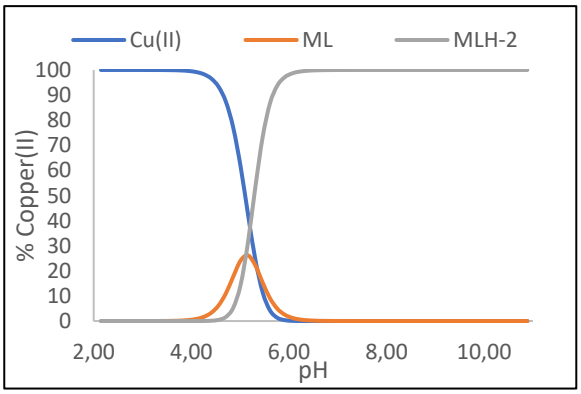

Figure 3.16: Complexation species distribution curve for the 1:1 ratio of copper(II) and Sar-LH (a) Model 1 (MLH_{-1}, MLH_{-2}), (b) Model 2 (MLH, MLH_{-1}, MLH_{-2}), (c) Model 3 (MLH, ML, MLH_{-2}), (d) Model 4 (MLH, MLH_{-2}) and (e) Model 5 (ML, MLH_{-2}) at 25 ^{o}C in 0.15 mol.dm^{-3} of NaCl.

3.3.2(c)(iii) Cu-GFH

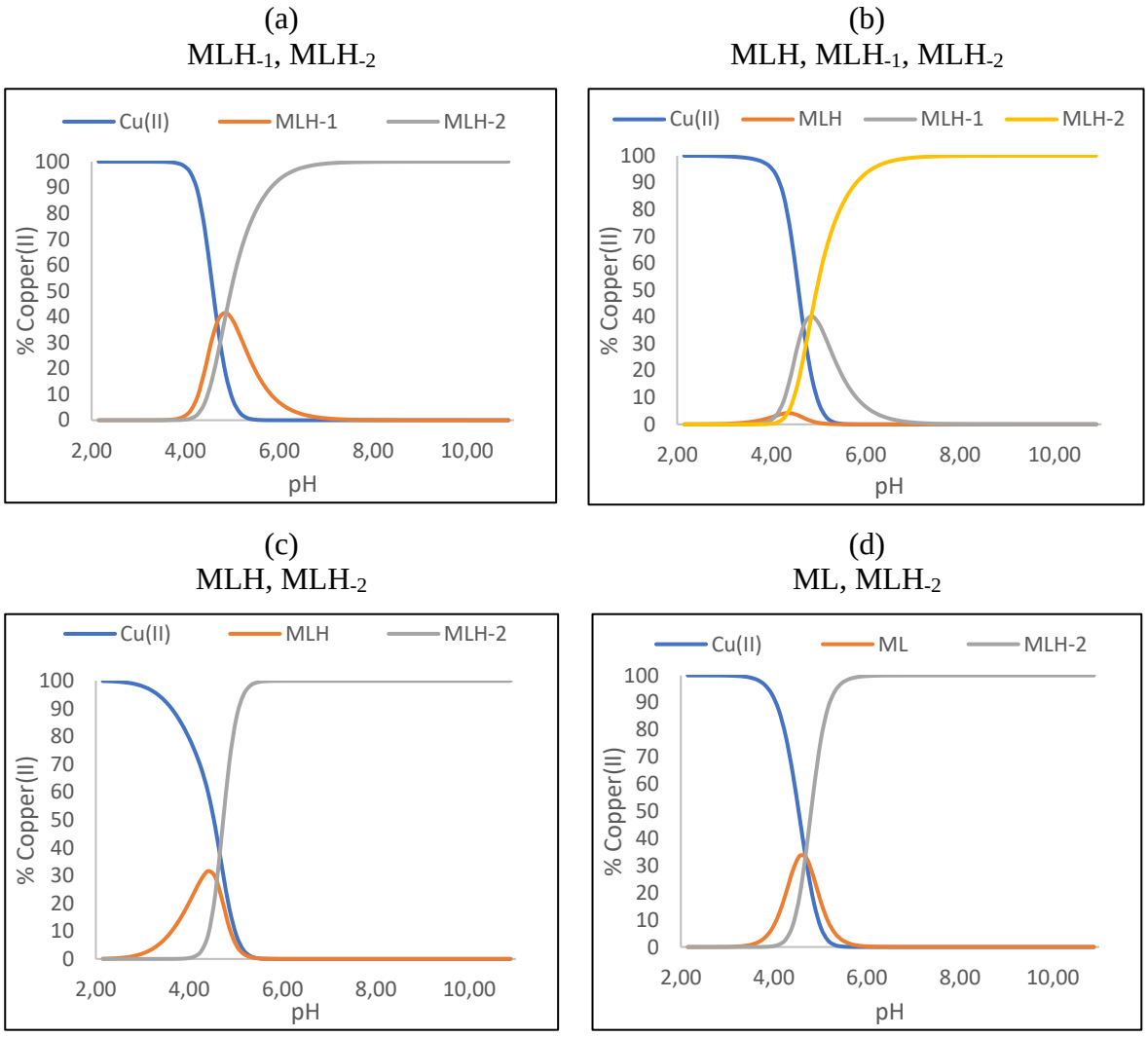

Figure 3.17: Complexation species distribution curve for the 1:1 ratio of copper(II) and GFH (a) Model 1 (MLH_{-1}, MLH_{-2}), (b) Model 2 (MLH, MLH_{-1}, MLH_{-2}), (c) Model 3 (MLH, MLH_{-2}) and (d) Model 4 (ML, MLH_{-2}) at 25 ^{o}C in 0.15 mol.dm^{-3} of NaCl.

3.3.2(c)(iv) Cu-Sar-FH

(a)
MLH_{-1}, MLH_{-2}

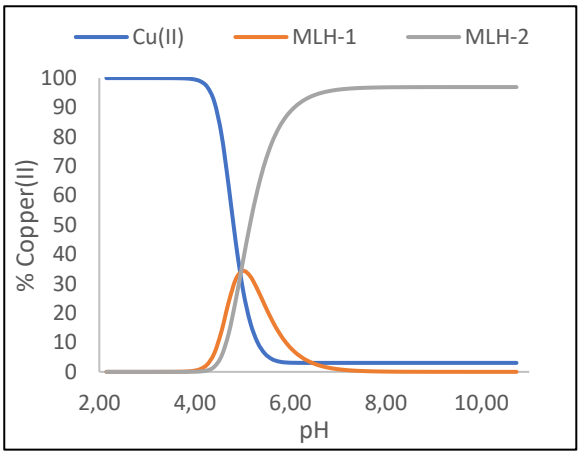

(b)
MLH, MLH_{-2}

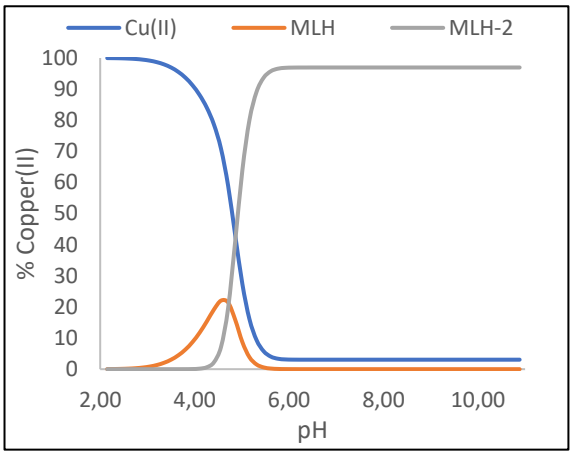

(c)
ML, MLH_{-2}

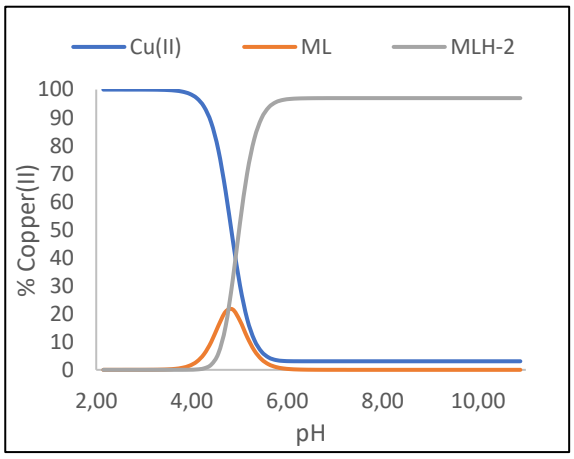

Figure 3.18: Complexation species distribution curve for the 1:1 ratio of copper(II) and Sar-FH (a) Model 1 (MLH_{-1}, MLH_{-2}), (b) Model 2 (MLH, MLH_{-2}) and (c) Model 3 (ML, MLH_{-2}) at 25 ^{o}C in 0.15 $mol.dm^{-3}$ of NaCl.

3.3.3 Nickel(II) complexation of GLH, Sar-LH, GFH and Sar-FH

The stability constants (log β_{pqr}) of the Ni-GLH, Ni-Sar-LH, Ni-GFH and Ni-Sar-FH complexations had a 1:1 nickel(II) ligand ratio and were determined using the ESTA suite of programs. Z_M-bar, Q_M-bar and the species distribution functions were calculated using these stability constants. The standard deviations of the log β_{pqr} values and Hamilton *R*-factors for all the nickel(II) ligand complexes can be seen in Table 3.3. For GLH two models were refined.

Table 3.3**:** Stability constants (log β_{pqr}) for the 1:1 complexation between nickel(II) and GLH, Sar-LH, GFH and Sar-FH at 25 ^{o}C and 0.15 mol.dm^{-3} NaCl.
Std is the standard deviation; R_f^H is the Hamilton *R*-factor and R_{lim}^H is its limit; n_T is the number of titrations and (n_p) is the number of titration points; *p*, *q*, *r* are the stoichiometric coefficients of a complex with a general formula of $M_pL_qH_r$; M stands for the metal, L stands for the ligand and H stands for a hydrogen atom.

Complex	Model	Species	*p*	*q*	*r*	log β_{pqr}	pK_a	std	*R*f	R_{lim}	$n_T(n_p)$
Ni-GLH	1	ML	1	1	0	4.60	6.63	0.08	0.007	0.001	3(303)
		MLH_{-1}	1	1	-1	-2.03	7.18	0.04			
		MLH_{-2}	1	1	-2	-9.21		0.04			
	2	MLH	1	1	1	11.34		0.05	0.007	0.001	3(303)
		MLH_{-1}	1	1	-1	-1.78	7.42	0.02			
		MLH_{-2}	1	1	-2	-9.20		0.03			
Ni-Sar-LH		MLH	1	1	1	11.52		0.07	0.01	0.003	2(90)
		MLH_{-1}	1	1	-1	-2.79	7.07	0.06			
		MLH_{-2}	1	1	-2	-9.86		0.04			
Ni-GFH		MLH	1	1	1	11.32		0.02	0.004	0.003	2(83)
		MLH_{-1}	1	1	-1	-1.84	6.69	0.02			
		MLH_{-2}	1	1	-2	-8.53		0.01			
Ni-Sar-FH		MLH	1	1	1	11.40		0.08	0.01	0.002	2(92)
		MLH_{-1}	1	1	-1	-2.88	6.60	0.09			
		MLH_{-2}	1	1	-2	-9.48		0.04			

The pK_a for the deprotonation of Ni(H_2O) to NiOH is 9.86.[26] Similarly to the copper(II) complexes, the pK_a for some species could not be calculated. For the ones that could be calculated, neither the pK_a of the ML to MLH_{-1} species (log β_{110}-log β_{11-1}) for Model 1 of Ni-GLH, nor the pK_a of the MLH_{-1} to MLH_{-2} species (log β_{11-1}-log β_{11-2}) for all the complexes, are similar to the nickel(II) hydrolysis pK_a. These pK_a values are between 6.60-7.18 and so the loss of these protons is from the ligand and not from water. When comparing the standard deviations of the log β_{pqr} values and Hamilton *R*-factors, both potentiometric models for Ni-

GLH are equally good. The values for the other ligands are satisfactory and verify the validity of the models.

3.3.3(a) Z_M-bar

The complex formation function, Z_M-bar, for Ni-GLH, Ni-Sar-LH, Ni-GFH and Ni-Sar-FH can be seen in Figure 3.19. In all the graphs, the curves begin to rise at a high pL and curl backwards at middling pL values. This shows that the hydroxyl species start forming at low to middling pH values. Since Model 1 for Ni-GLH has an ML species and the Z_M-bar curve for this model curls backwards before levelling off, it means that the hydroxyl species start forming before the formation of the ML species reaches a maximum. When comparing the theoretical and experimental functions, Model 2 for Ni-GLH has a better fit and therefore signifies it is the more correct model. For the other ligands, there is a good agreement which verifies that the proposed models for each ligand are accurate.

(a)(i)
Ni-GLH (ML, MLH_{-1}, MLH_{-2})

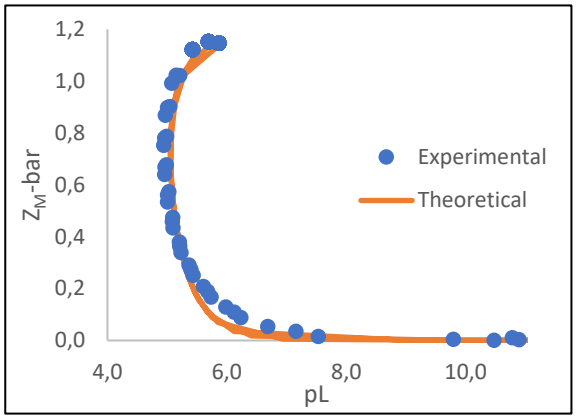

(a)(ii)
Ni-GLH (MLH, MLH_{-1}, MLH_{-2})

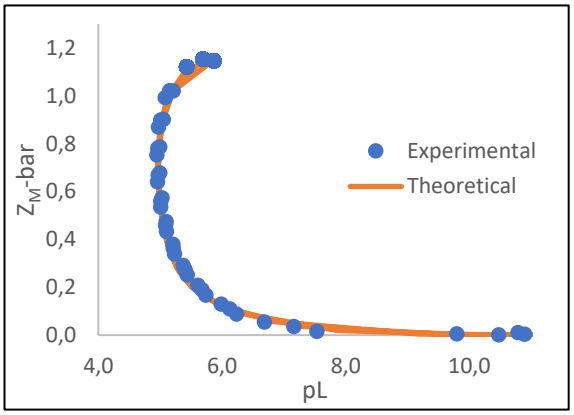

(b)
Ni-Sar-LH (MLH, MLH_{-1}, MLH_{-2})

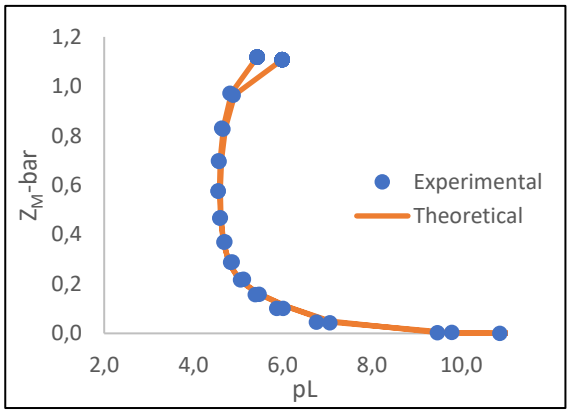

(c)
Ni-GFH (MLH, MLH_{-1}, MLH_{-2})

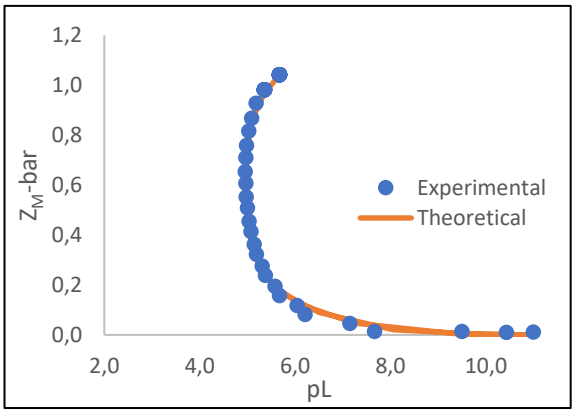

(d)
Ni-Sar-FH (MLH, MLH_{-1}, MLH_{-2})

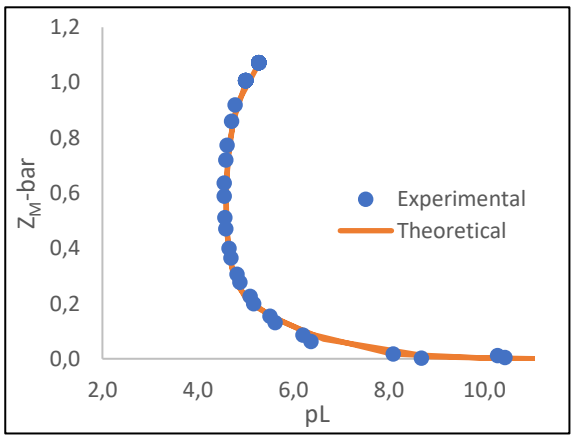

Figure 3.19: Z_M-bar as a function of pH for the 1:1 complexation of nickel(II) and (a)(i) GLH (Model 1 with ML, MLH_{-1}, MLH_{-2}), (a)(ii) GLH (Model 2 with MLH, MLH_{-1}, MLH_{-2}), (b) Sar-LH (MLH, MLH_{-1}, MLH_{-2}), (c) GFH (MLH, MLH_{-1}, MLH_{-2}) and (d) Sar-FH (MLH, MLH_{-1}, MLH_{-2}) at 25 ^{o}C in 0.15 mol.dm^{-3} NaCl.

3.3.3(b) Q_M-bar

The deprotonation function, Q_M-bar, for Ni-GLH, Ni-Sar-LH, Ni-GFH and Ni-Sar-FH can be seen in Figure 3.20. For all the graphs, the *n*-bar curve levels off at a value of 2 between a pH of approximately 3.6 and 6.1, signifying the formation of the LH_2 species. For all graphs, the Q_M-bar curve rises 0.6-0.8 units above the *n*-bar at a pH of approximately 7.4, which shows that up to one proton is dissociated at that pH. As the Q_M-bar curves decrease, the distance between Q_M-bar and *n*-bar increases to almost 2 units and then remains parallel at that value until the end of the titration. This suggests that new species are still forming past the approximate pH of 7.4. It also suggests that by the end of the titration, no new species form and two protons are dissociated from the amide groups. When comparing the theoretical and experimental functions, both models for Ni-GLH, as well as for Ni-Sar-LH, do not overlap too well at high pH values, while the overlap for Ni-GFH and Ni-Sar-FH is good. This suggests that the proposed models for Ni-GLH and Ni-Sar-LH are not as accurate as Ni-GFH and Ni-Sar-FH.

(a)(i)
Ni-GLH (ML, MLH_{-1}, MLH_{-2})

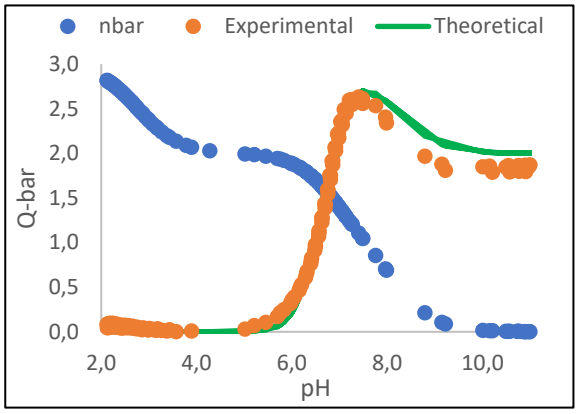

(a)(ii)
Ni-GLH (MLH, MLH_{-1}, MLH_{-2})

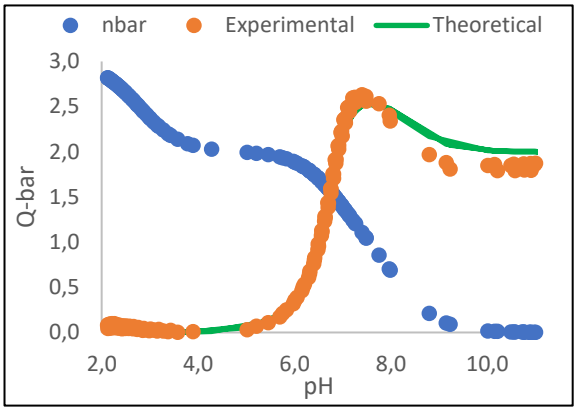

(b)
Ni-Sar-LH (MLH, MLH_{-1}, MLH_{-2})

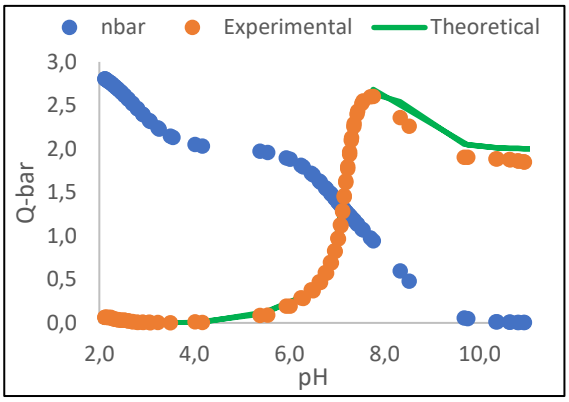

(c)
Ni-GFH (MLH, MLH_{-1}, MLH_{-2})

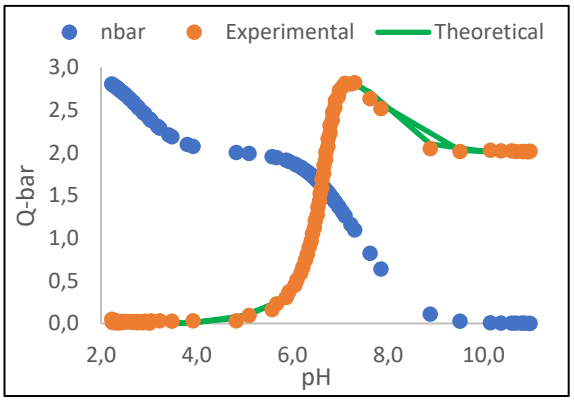

(d)
Ni-Sar-FH (MLH, MLH_{-1}, MLH_{-2})

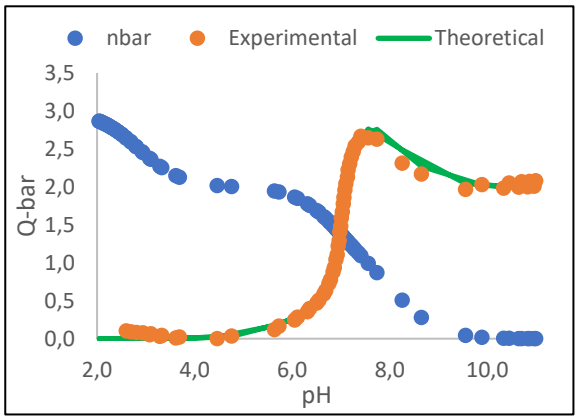

Figure 3.20: Q_M-bar as a function of pH for the 1:1 complexation of nickel(II) and (a)(i) GLH (Model 1 with ML, MLH_{-1}, MLH_{-2}), (a)(ii) GLH (Model 2 with MLH, MLH_{-1}, MLH_{-2}), (b) Sar-LH (MLH, MLH_{-1}, MLH_{-2}), (c) GFH (MLH, MLH_{-1}, MLH_{-2}) and (d) Sar-FH (MLH, MLH_{-1}, MLH_{-2}) at 25 ^{o}C in 0.15 mol.dm^{-3} NaCl.

3.3.3(c) Species distribution curve

The species distribution curve for Ni-GLH, Ni-Sar-LH, Ni-GFH and Ni-Sar-FH can be seen in Figure 3.21. At low pH values the MLH and ML species begin to form and then at middling pH values the other species form. In all graphs, after approximately a pH of 9.0 the formation of new species has ended, and the MLH_{-2} species has reached a 100% dominance. This corresponds to the Z_M-bar and Q_M-bar curves seen in Figures 3.19 and 3.20 respectively.

(a)(i)
Ni-GLH (ML, MLH_{-1}, MLH_{-2})

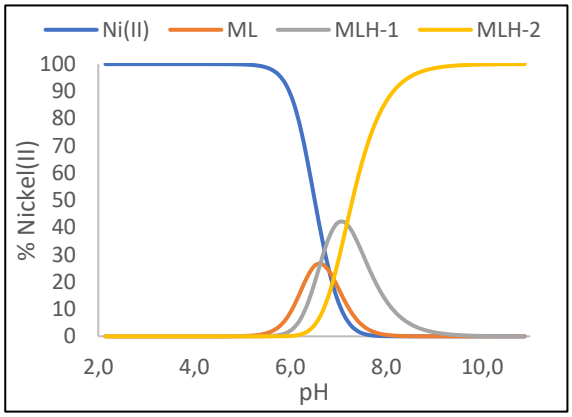

(a)(ii)
Ni-GLH (MLH, MLH_{-1}, MLH_{-2})

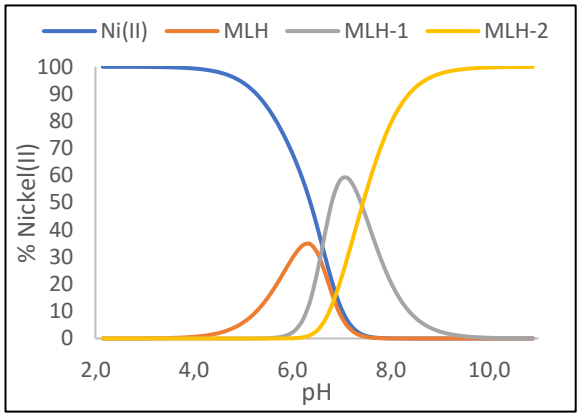

(b)
Ni-Sar-LH (MLH, MLH_{-1}, MLH_{-2})

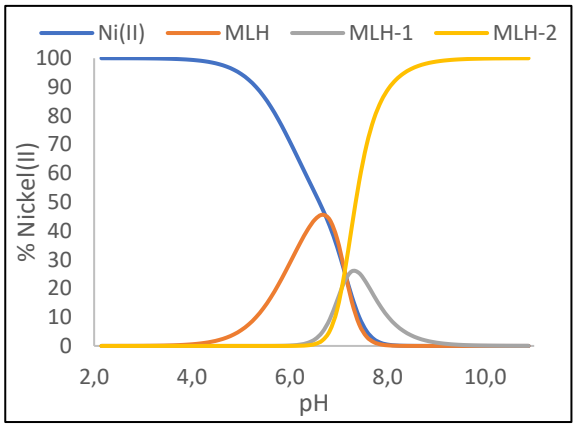

(c)
Ni-GFH (MLH, MLH_{-1}, MLH_{-2})

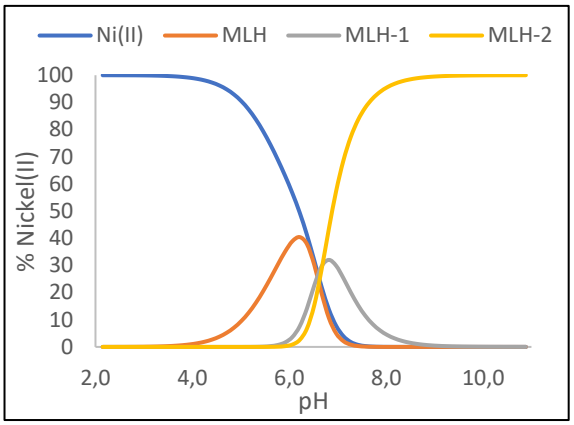

(d)
Ni-Sar-FH (MLH, MLH_{-1}, MLH_{-2})

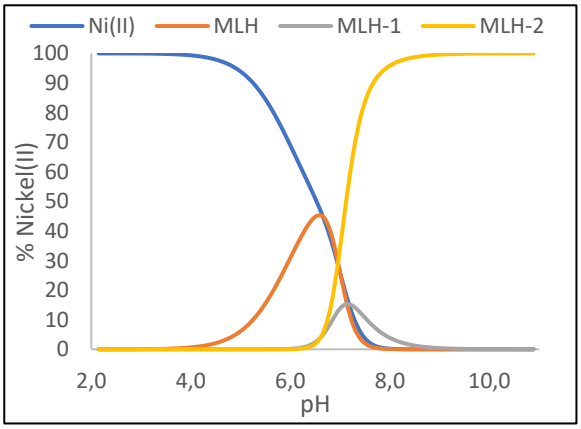

Figure 3.21: Complexation species distribution curve for the 1:1 ratio of nickel(II) and (a)(i) GLH (Model 1 with ML, MLH_{-1}, MLH_{-2}), (a)(ii) GLH (Model 2 with MLH, MLH_{-1}, MLH_{-2}), (b) Sar-LH (MLH, MLH_{-1}, MLH_{-2}), (c) GFH (MLH, MLH_{-1}, MLH_{-2}) and (d) Sar-FH (MLH, MLH_{-1}, MLH_{-2}) at 25 ^{o}C in 0.15 mol.dm^{-3} of NaCl.

3.3.4 Zinc(II) complexation of GLH, Sar-LH, GFH and Sar-FH

The stability constants (log β_{pqr}) of the Zn-GLH, Zn-Sar-LH, Zn-GFH and Zn-Sar-FH complexations had a 1:1 zinc(II) ligand ratio and were determined using ESTA suite of programs. These stability constants were used to calculate Z_M-bar, Q_M-bar and the species distribution functions. The agreement between the theoretical and experimental functions of the Z_M-bar and Q_M-bar curves is good and therefore the potentiometric titrations were performed accurately. The low standard deviations of the log β_{pqr} values and Hamilton *R*-factors for all the zinc(II) ligand complexes also verify the validity of the models and can be seen in Table 3.4.

Table 3.4**:** Stability constants (log β_{pqr}) for the 1:1 complexation between zinc(II) and GLH, Sar-LH, GFH and Sar-FH at 25 ^{o}C and 0.15 mol.dm^{-3} NaCl.
Std is the standard deviation; R_f^H is the Hamilton *R*-factor and R_{lim}^H is its limit; n_T is the number of titrations and (n_p) is the number of titration points; *p*, *q*, *r* are the stoichiometric coefficients of a complex with a general formula of $M_pL_qH_r$; M stands for the metal, L stands for the ligand and H stands for a hydrogen atom.

Complex	Species	*p*	*q*	*r*	log β_{pqr}	pK_a	std	*R*f	R_{lim}	$n_T(n_p)$
Zn-GLH	ML	1	1	0	4.51	8.22	0.05			
	MLH_{-1}	1	1	-1	-3.71	9.91	0.09	0.007	0.001	2(202)
	MLH_{-2}	1	1	-2	-13.62		0.09			
Zn-Sar-LH	MLH	1	1	1	10.66	6.96	0.06			
	ML	1	1	0	3.70	7.83	0.02	0.005	0.003	2(86)
	MLH_{-1}	1	1	-1	-4.13	9.34	0.02			
	MLH_{-2}	1	1	-2	-13.47		0.02			
Zn-GFH	ML	1	1	0	4.23	7.57	0.03			
	MLH_{-1}	1	1	-1	-3.34	10.10	0.03	0.008	0.003	2(89)
	MLH_{-2}	1	1	-2	-13.44		0.04			
Zn-Sar-FH	ML	1	1	0	3.52	7.34	0.07			
	MLH_{-1}	1	1	-1	-3.82	9.53	0.04	0.01	0.002	2(90)
	MLH_{-2}	1	1	-2	-13.35		0.07			

The pK_a for the deprotonation of $Zn(H_2O)$ to ZnOH is 8.96.[26] Similarly to the copper(II) complexes, the pK_a for some species could not be calculated. The only pK_a values that can be compared to the hydrolysis of zinc(II) is the pK_a from ML to MLH_{-1} (log β_{110}-log β_{11-1}) for Zn-GLH, and the pK_a from MLH_{-1} to MLH_{-2} (log β_{11-1}-log β_{11-2}) for Zn-Sar-LH. Thus, the first and second deprotonation for all the other species are due to the loss of a proton from the ligand. When forming both the MLH_{-1} species of Zn-GLH and the MLH_{-2} species of Zn-Sar-LH, the

deprotonation could have been from either an amide group or from water. When looking at the standard deviations of the log β_{pqr} values and Hamilton *R*-factors, all models for each ligand have low values, which are therefore satisfactory and verify the validity of the models.

3.3.4(a) Z_M-bar

The complex formation function, Z_M-bar, for Zn-GLH, Zn-Sar-LH, Zn-GFH and Zn-Sar-FH can be seen in Figure 3.22. The curves rise and curl backwards at middling pL values, which shows that hydroxyl species are present at middling pH values and before the ML species reaches a maximum. An added observation is that the curve of Zn-Sar-LH begins to rise more noticeably at high pL values compared to the curves of the other complexes which do not have the MLH species. This is an indication that the MLH species is present and dominant. When comparing the theoretical and experimental functions, only the curve belonging to Sar-FH has a section in it where the overlap is not too good but is still satisfactory. All the other ligands have a good overlap.

(a)
Zn-GLH (ML, MLH_{-1}, MLH_{-2})

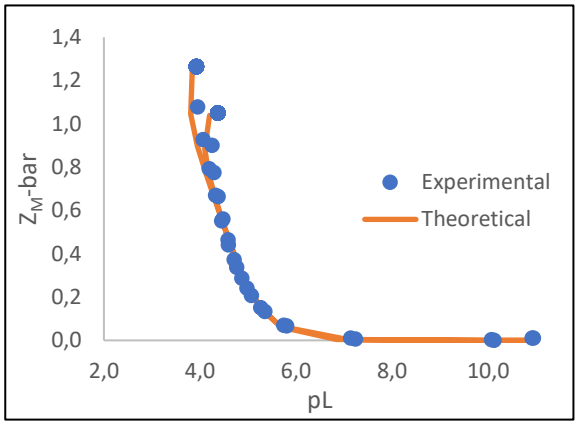

(b)
Zn-Sar-LH (MLH, ML, MLH_{-1}, MLH_{-2})

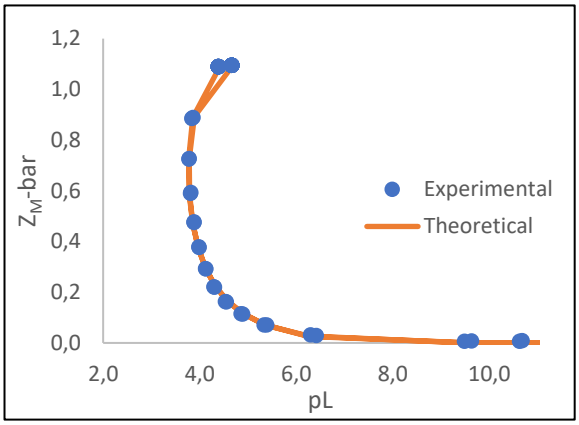

(c)
Zn-GFH (ML, MLH_{-1}, MLH_{-2})

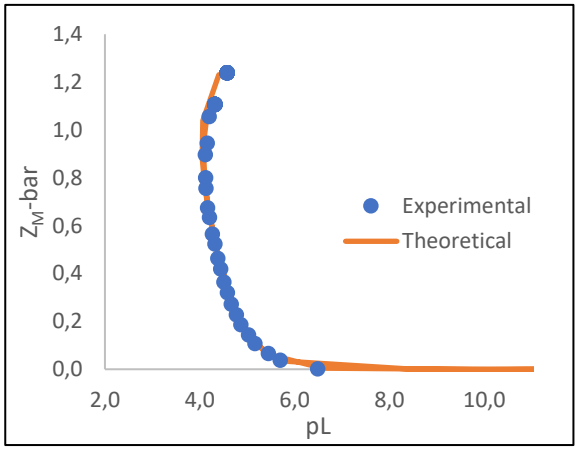

(d)
Zn-Sar-FH (ML, MLH_{-1}, MLH_{-2})

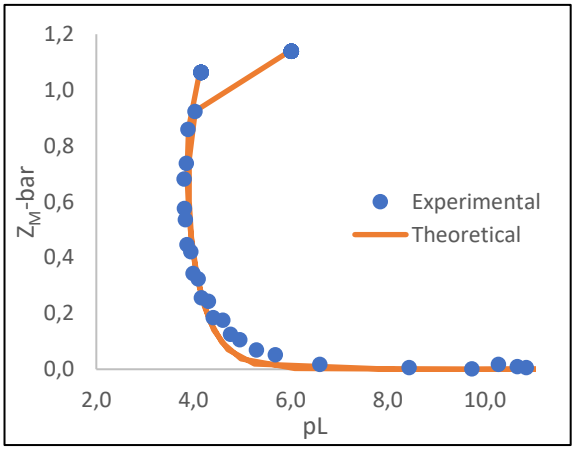

Figure 3.22: Z_M-bar as a function of pH for the 1:1 complexation of zinc(II) and (a) GLH (ML, MLH_{-1}, MLH_{-2}), (b) Sar-LH (MLH, ML, MLH_{-1}, MLH_{-2}), (c) GFH (ML, MLH_{-1}, MLH_{-2}) and (d) Sar-FH (ML, MLH_{-1}, MLH_{-2}) at 25 ^{o}C in 0.15 mol.dm^{-3} NaCl.

3.3.4(b) Q_M-bar

The deprotonation function, Q_M-bar, of Zn-GLH, Zn-Sar-LH, Zn-GFH and Zn-Sar-FH can be seen in Figure 3.23. For all graphs, *n*-bar levels off at 2 between a pH of approximately 3.8 and 5.9, which shows the formation of the LH_2 species. For all graphs, the Q_M-bar curve intersects the *n*-bar curve between a pH of 7.1-7.8, which shows that the ML or MLH species have formed. From this pH onwards, the difference between the Q_M-bar curves and the *n*-bar curves continually increases and at pH 11 the difference between them is 2 units. Unlike both the copper(II) and nickel(II) complexes, where the two curves become parallel to one another at the end of the titration and show that no new species form, these curves are not yet parallel to

each other. This shows that even though two protons have been lost from an amide, species are still forming. When comparing the theoretical and experimental functions, only Zn-Sar-LH has a good overlap, while the other ligands have sections in the curves where the overlap is not as good but still satisfactory.

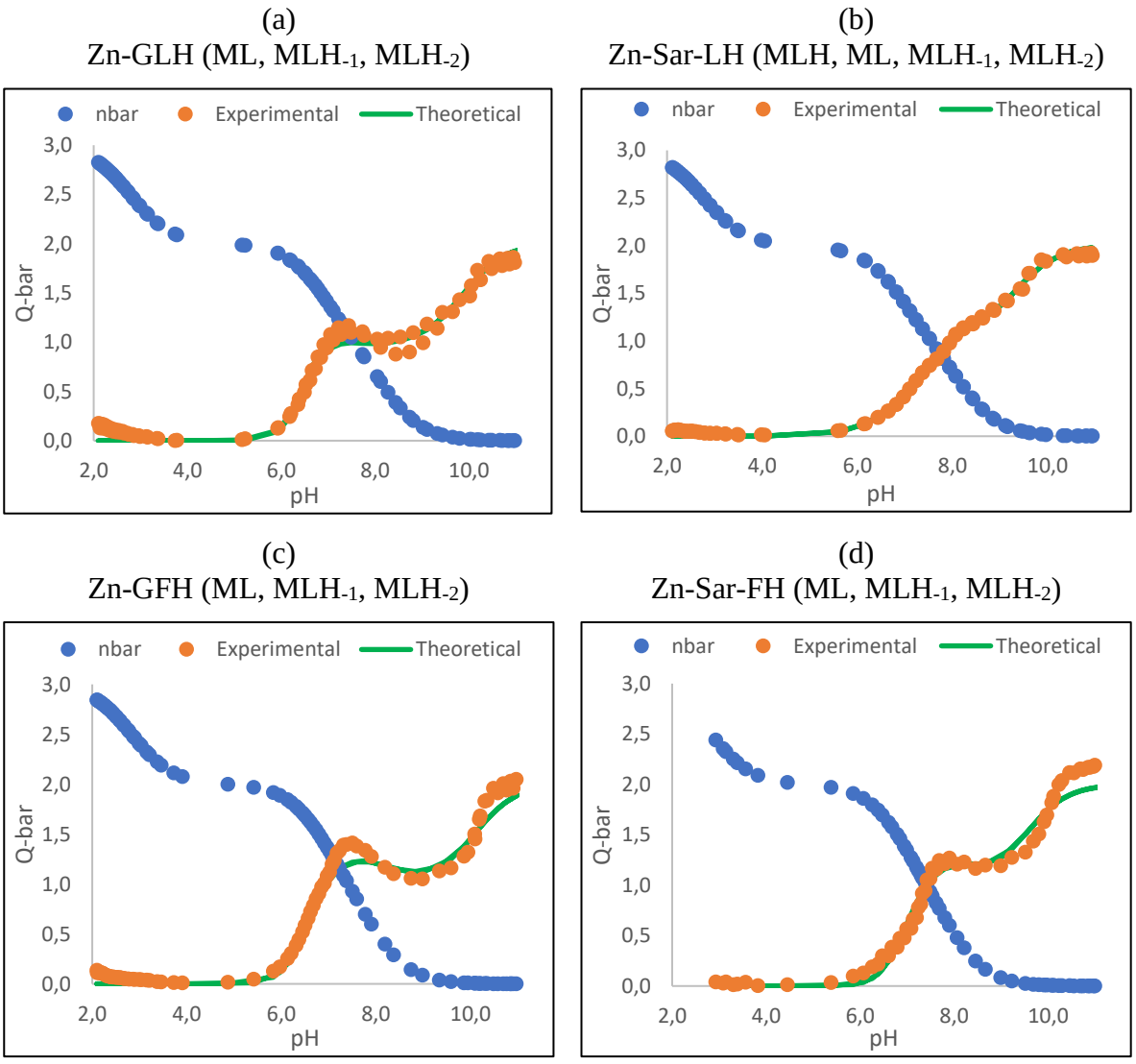

Figure 3.23: Q_M-bar as a function of pH for the 1:1 complexation of zinc(II) and (a) GLH (ML, MLH_{-1}, MLH_{-2}), (b) Sar-LH (MLH, ML, MLH_{-1}, MLH_{-2}), (c) GFH (ML, MLH_{-1}, MLH_{-2}) and (d) Sar-FH (ML, MLH_{-1}, MLH_{-2}) at 25 ^{o}C in 0.15 mol.dm^{-3} NaCl.

3.3.4(c) Species distribution curve

The species distribution curve for Zn-GLH, Zn-Sar-LH, Zn-GFH and Zn-Sar-FH can be seen in Figure 3.24. In all graphs, the hydroxyl species begin to form before the ML species has reached a maximum. The MLH species in the Zn-Sar-LH complex is dominant between the pH values of 5.0-7.0. In all graphs, at pH 11 the MLH_{-2} species has reached approximately a 90% dominance, which shows these species are still forming at the end of the titration. This corresponds to the Z_M-bar and Q_M-bar curves seen in Figures 3.22 and 3.23 respectively.

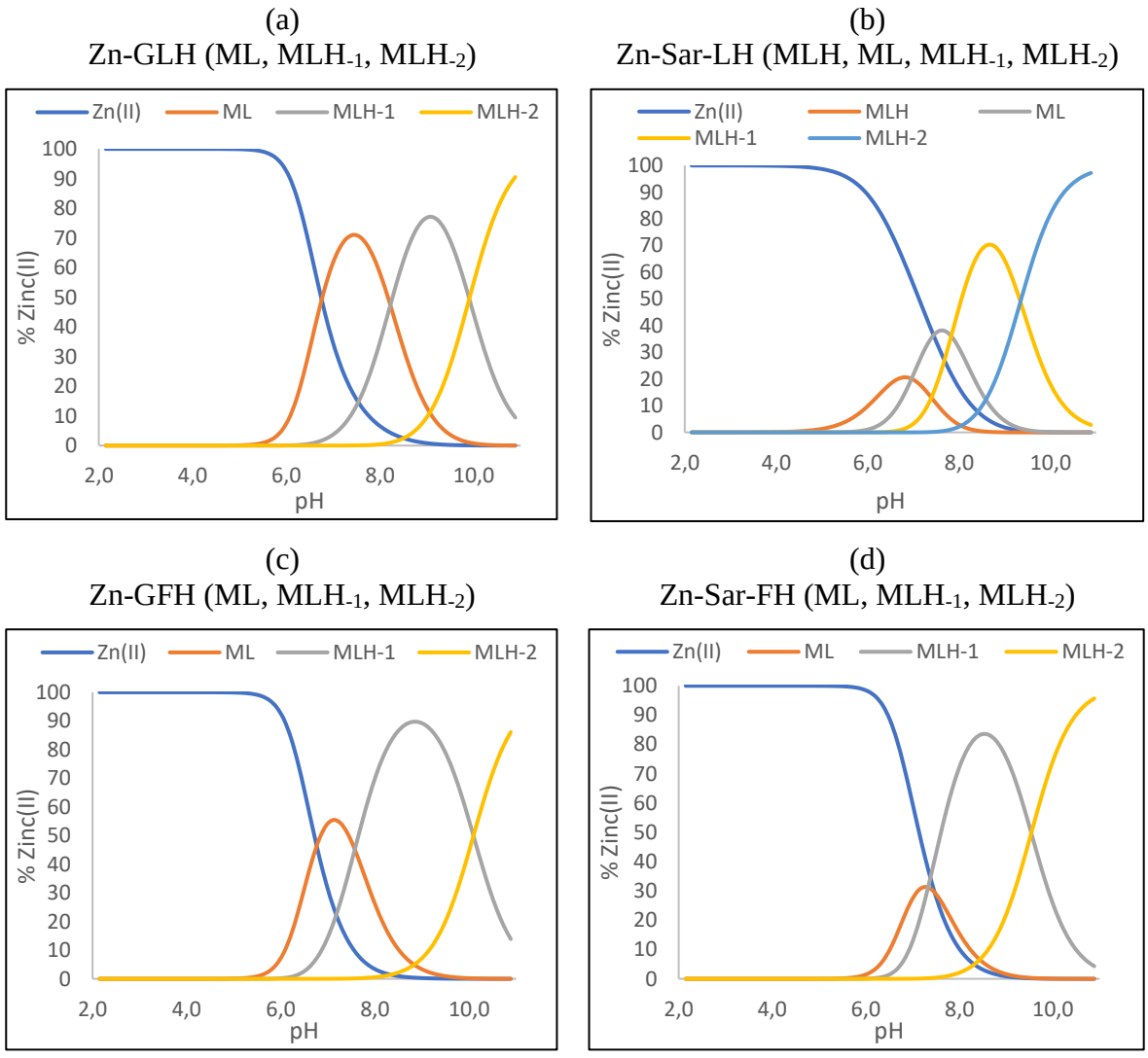

Figure 3.24: Complexation species distribution curve for the 1:1 ratio of zinc(II) and (a) GLH (ML, MLH_{-1}, MLH_{-2}), (b) Sar-LH (MLH, ML, MLH_{-1}, MLH_{-2}), (c) GFH (ML, MLH_{-1}, MLH_{-2}) and (d) Sar-FH (ML, MLH_{-1}, MLH_{-2}) at 25 ^{o}C in 0.15 mol.dm^{-3} of NaCl.

3.4 Discussion

To form a copper(II) complex that satisfies the aim of undergoing transdermal absorption and releasing copper(II) ions into the blood plasma, means that it is essential to establish whether copper(II) can form a stable complex with the four tripeptides. Hence a study on determining the stability constants was carried out. However, the complex must not be so stable that copper(II) cannot be released once it is in the blood plasma. The stability constants of nickel(II) and zinc(II) with the four tripeptides were also measured, since the copper(II) complexes will encounter nickel(II) and zinc(II) ions in the blood plasma. The protonation and complexation stability constants for the four tripeptides with copper(II), nickel(II) and zinc(II) can be seen in Tables 3.5-3.8. Literature values have also been added into each table, because the four tripeptides have never been studied before, and so they need to be compared to relatable ligands. The dipeptides and tripeptides chosen from literature all have their first amino acid as either glycine or sarcosine and their last amino acid as histidine. This was done so that their structures and therefore protonation/complexation stability constants are similar to the four tripeptides of this study. As can be seen, all the protonation and complexation stability constants are indeed similar to literature and therefore verify their validity.

Table 3.5: Protonation constants for GLH, Sar-LH, GFH and Sar-FH, as well as literature values.

Ligand	***p q r***	**log β_{pqr}**
GLH	0 1 1 0 1 2 0 1 3	8.21 15.10 17.88
Sar-LH	0 1 1 0 1 2 0 1 3	8.45 15.32 18.05
GFH	0 1 1 0 1 2 0 1 3	7.95 14.82 17.65
Sar-FH	0 1 1 0 1 2 0 1 3	8.22 15.09 17.96
Sar-His-His[27,28] (lit)	0 1 1 0 1 2 0 1 3	8.57 15.74 21.64
Sar-Gly-His[27] (lit)	0 1 1 0 1 2 0 1 3	8.72 15.44 17.79
Gly-Gly-His[29] (lit)	0 1 1 0 1 2 0 1 3	7.96 14.60 17.52

Table 3.6: Stability constants for the complexes Cu-GLH, Cu-Sar-LH, Cu-GFH and Cu-Sar-FH, as well as literature values for Cu-dipeptides and Cu-tripeptides.

Ligand	**p q r**	**log β_{pqr}**
GLH	1 1 -1	2.76
	1 1 -2	-2.57
	1 1 1	12.71
	1 1 -1	2.77
	1 1 -2	-2.24
	1 1 0	7.67
	1 1 -1	2.40
	1 1 -2	-2.40
	1 1 1	12.14
	1 1 0	7.88
	1 1 -2	-2.27
	1 1 1	13.01
	1 1 -2	-2.11
	1 1 0	7.92
	1 1 -2	-2.31
Sar-LH	1 1 -1	2.23
	1 1 -2	-2.91
	1 1 1	12.66
	1 1 -1	2.06
	1 1 -2	-2.71
	1 1 1	12.37
	1 1 0	7.38
	1 1 -2	-2.70
	1 1 1	12.89
	1 1 -2	-2.59
	1 1 0	7.47
	1 1 -2	-2.77
GFH	1 1 -1	3.53
	1 1 -2	-1.34
	1 1 1	11.72
	1 1 -1	3.54
	1 1 -2	-1.31
	1 1 1	12.76
	1 1 -2	-1.03
	1 1 0	8.22
	1 1 -2	-1.14

Sar-FH	1 1 -1 1 1 -2 1 1 1 1 1 -2 1 1 0 1 1 -2	3.22 -1.75 12.66 -1.51 7.86 -1.69
Gly-His[30] (lit)	1 1 -1	4.91
Gly-Gly-His[31] (lit)	1 1 -2	-0.74
Gly-Gly-His[29,30] (lit)	1 1 -2	-1.73
Gly-His-His[31] (lit)	1 1 -2	0.86
Sar-His-His[27,28] (lit)	1 1 -1 1 1 -2	5.27 -3.78
Sar-Gly-His[27] (lit)	1 1 -1 1 1 -2	3.11 -2.72

Table 3.7: Stability constants for the complexes Ni-GLH, Ni-Sar-LH, Ni-GFH and Ni-Sar-FH, as well as literature values for Ni-dipeptides and Ni-tripeptides.

Ligand	**p q r**	**log β_{pqr}**
GLH	1 1 0 1 1 -1 1 1 -2 1 1 1 1 1 -1 1 1 -2	4.60 -2.03 -9.21 11.34 -1.78 -9.20
Sar-LH	1 1 1 1 1 -1 1 1 -2	11.52 -2.79 -9.86
GFH	1 1 1 1 1 -1 1 1 -2	11.32 -1.84 -8.53
Sar-FH	1 1 1 1 1 -1 1 1 -2	11.40 -2.88 -9.48
Gly-His[30]	1 1 0 1 1 -1	4.68 -1.35
Sar-His-His[9]	1 1 0 1 1 -1 1 1 -2	6.22 0.02 -8.37
Gly-Gly-His[30]	1 1 1 1 1 0 1 1 -1	11.34 4.68 -1.35

Table 3.8: Stability constants for the complexes Zn-GLH, Zn-Sar-LH, Zn-GFH and Zn-Sar-FH, as well as literature values for Zn-dipeptides and Zn-tripeptides.

Ligand	**p q r**	**log β_{pqr}**
GLH	1 1 0	4.51
	1 1 -1	-3.71
	1 1 -2	-13.62
Sar-LH	1 1 1	10.66
	1 1 0	3.70
	1 1 -1	-4.13
	1 1 -2	-13.47
GFH	1 1 0	4.23
	1 1 -1	-3.34
	1 1 -2	-13.44
Sar-FH	1 1 0	3.52
	1 1 -1	-3.82
	1 1 -2	-13.35
Gly-His[30]	1 1 1	10.87
	1 1 0	3.98
	1 1 -1	-2.75
	1 1 -2	-12.66
Sar-His-His[28]	1 1 0	5.20
	1 1 -1	-1.89
	1 1 -2	-11.69
Gly-Gly-His[30]	1 1 1	11.30
	1 1 0	4.10
	1 1 -1	-3.81

The four tripeptides can be grouped so that the effect of the N-methylated group on sarcosine can be analysed. To do this, constants from GLH will be compared with constants from Sar-LH and constants from GFH will be compared with constants from Sar-FH. For the protonation constants, the species from Sar-LH or Sar-FH, i.e. with the methyl group, are 0.17-0.31 log units bigger and more stable than their glycine counterparts. For the copper(II) complexation stability constants, the species, ML, MLH_{-1} and MLH_{-2} without the methyl group (GLH and GFH) are all 0.02-0.80 log units bigger and therefore more stable than the methylated species (Sar-LH and Sar-FH). The only exception is the MLH species, where some MLH species with the methyl group (Sar-LH and Sar-FH) were up to 0.94 log units bigger than the non-methylated species (GLH and GFH), and other MLH species without the methyl group (GLH and GFH) were up to 0.64 log units bigger than the methylated species (Sar-LH and Sar-FH). For the nickel(II) complexes, the MLH species can be considered as equally stable, since the difference is only 0.18 log units between the methylated and non-methylated groups. The MLH_{-1} and MLH_{-2} species without the methyl group (GLH and GFH) are 0.65-1.04 log units bigger and more stable than the methylated species (Sar-LH and Sar-FH). The ML species could not be compared. For the zinc(II) complexes, the ML and MLH_{-1} species without the

methyl group (GLH and GFH) are 0.42-0.81 log units bigger and more stable than the methylated species (Sar-LH and Sar-FH). The MLH_{-2} species can be considered as equally stable since there is only a difference of 0.09-0.15 log units between the methylated and non-methylated groups. The MLH species could not be compared.

The methyl group has an electron donating inductive effect and so it was expected that the ligands/complexes with sarcosine would have larger stability coefficients and thus be more stable than the complexes with glycine. This was seen for the protonation constants and therefore it is confirmed that the methyl group does affect the stability. However, it was mostly found that the complexes without the methyl group were slightly more stable, which leads to the suggestion that the methyl group also has steric effects. This finding was also seen in literature between the tripeptides of Gly-Leu-Phe and Sar-Leu-Phe.[32,33] A steric effect makes the inductive effect less prominent. Another reason could be due to the ammonium ions or charged amine groups preferentially forming hydrogen bonds with water and thereby decreasing available charge. This phenomenon was also reported for solvated alkylamines, where the order of base strength was rearranged. The true base strength, in a vacuum, should have been $NH_3 < RNH_2 < R_2NH < R_3N$, since the methyl groups increase, which subsequently increases the electron density on the nitrogen atom. However, the order for aqueous solutions was found to be $NH_3 < RNH_2$, $R_2NH > R_3N$, which was explained by the preference of the amine to form hydrogen bonds with water.[34]

The four tripeptides can be split again, so that an analysis of the leucine and phenylalanine amino acids can be done to determine how they affect the stability constants. Thus, GLH and GFH will be compared, and Sar-LH and Sar-FH will be compared. Starting with the protonation constants, the species with leucine (GLH and Sar-LH) are 0.09-0.28 log units bigger and more stable than the species with phenylalanine (GFH and Sar-FH). For the copper(II) complexes, the ML, MLH_{-1} and MLH_{-2} species with phenylalanine (GFH and Sar-FH) have constants that are between 0.30-1.54 log units bigger than the species with leucine (GLH and Sar-LH) and are thus more stable. However, some MLH species with leucine (GLH and Sar-LH) were up to 1.29 log units bigger than those with phenylalanine (GFH and Sar-FH) and other MLH species with phenylalanine (GFH and Sar-FH) were up to 0.62 log units bigger than those with leucine (GLH and Sar-LH). For the nickel(II) complexes, the comparison between the MLH species, as well as the comparison between the MLH_{-1} species, differs so slightly that the effect between the compounds with leucine and phenylalanine can be described

as negligible. The MLH_{-2} species with phenylalanine (GFH and Sar-FH) are 0.38-0.68 log units bigger and more stable than the species with leucine (GLH and Sar-LH). The ML species could not be compared. For the zinc(II) complexes, the ML species with leucine (GLH and Sar-LH) are 0.18-0.28 log units bigger and more stable than the species with phenylalanine (GFH and Sar-FH), while the MLH_{-1} and MLH_{-2} species with phenylalanine (GFH and Sar-FH) are 0.12-0.37 log units bigger and more stable than the species with leucine (GLH and Sar-LH). The MLH species could not be compared.

The difference between leucine and phenylalanine is that leucine contains an isobutyl group, while phenylalanine contains a benzyl group. Both groups should contribute to an inductive effect; but the benzyl group will be electron withdrawing, while the isobutyl group will be electron donating. Therefore, since the metal ions are positively charged, the isobutyl group is expected to stabilize the complex and hence increase the stability constants, while the benzyl group is expected to destabilize the complex and lower the stability constants. This was seen for the protonation constants. However, when analysing the complexation stability constants, a similar scenario is seen as with the comparison between the metal complexes of glycine versus sarcosine; where steric effects or charged amine groups preferentially forming hydrogen bonds must also be affecting the stability of these complexes.

When comparing the stability constants of the same species from copper(II), nickel(II) and zinc(II), the ordering corresponds to the Irving Williams series.[35,36] The copper(II) species are more stable than the nickel(II) species, which in turn are more stable than the zinc(II) species. It is also interesting to note, that the complexation itself seems to influence how well the inductive effect of the methyl and isobutyl group can exert a stabilizing result. This can be seen when comparing the protonation stability constants to the complexation stability constants. The appearance of the stabilizing inductive effect was present in all the protonation constants, whereas with the complexation stability constants, the inductive effect was less effective or appeared to have minimal impact. When examining the impact of the inductive effect between metal ions, the zinc(II) complex species were affected the most, while the copper(II) complex species were affected the least. This appears to be in the reverse order of the Irving Williams series[35,36] and therefore the actual bond between the metal ion and the ligand could influence the extent of the inductive effect.

The thermodynamics of potentiometry cannot directly give information about how copper(II) coordinates to each ligand, but it can give indirect clues. Since there are many models associated with each ligand for the copper(II) complexes, only the model which has been signalled out as the best model will be discussed. The process of choosing the best model was done by combining structural information from a series of structure determining techniques, each of which will be discussed in the following chapters. The correct model for Cu-Sar-LH is Model 3, which has the MLH, ML and MLH_{-2} species and the correct model for Cu-GLH is Model 2, which has the MLH, MLH_{-1} and MLH_{-2} species. The correct models for Cu-GFH and Cu-Sar-FH are Model 3 and Model 2 respectively, which both have the MLH and MLH_{-2} species. The potentiometric titrations agreed with the choice for Cu-GLH and Cu-Sar-LH, since the overlap between the theoretical and experimental Z_M-bar and Q_M-bar curves for Model 2 and Model 3 respectively were signalled out as the 'best fit'. Additionally, these models for Cu-GLH and Cu-Sar-LH were signalled out as having the lowest standard deviations and Hamilton *R*-factors.

The first step in identifying the coordination mode was comparing the pK_a value for the hydrolysis of the complex with the hydrolysis of copper(II). This determined if the loss of the proton is from the ligand or from water. Going from MLH_{-1} to MLH_{-2} for Cu-GLH, the pK_a value of MLH_{-1} ($\log \beta_{11\text{-}1} - \log \beta_{11\text{-}2}$) is 5.01 and going from MLH to ML for Cu-Sar-LH, the pK_a value of MLH ($\log \beta_{111} - \log \beta_{110}$) is 4.99 (Table 3.2). These values showed that the deprotonation is a result of the ligand, and the location where the proton came from will be discussed further on. The transitions from MLH to MLH_{-1} for Cu-GLH; ML to MLH_{-2} for Cu-Sar-LH; and MLH to MLH_{-2} for Cu-GFH and Cu-Sar-FH, are not stepwise processes and therefore these pK_a values are not known.

An indication of how the MLH species coordinates, was found by comparing the stability constants of this species with the stability constants of other ligands found in literature. The MLH species most likely has the copper(II) either coordinated to the amine and neighbouring carbonyl-O, or to the imidazole-N and the carboxyl-O. For the former comparison, literature compounds glycylglycine (GGOMe) and glycylsarcosine (GSOMe) were selected. They coordinate to copper(II) through the amine-N and carbonyl-O.[37] Their log *K* values are 4.11 and 5.18 respectively. To compare these values with the MLH species of Cu-GLH, Cu-Sar-LH, Cu-GFH and Cu-Sar-FH, the corresponding protonation of the imidazole group had to be subtracted from the complex stability constant. This gives log *K* values of 5.82, 5.5, 5.89 and

5.71 respectively. These values correspond to the literature values above, suggesting that this is the mode of coordination of these ligands. Unfortunately, the comparison could not be made for the imidazole-N and carboxyl-O, since literature for this comparison could not be found. There is reason to believe that copper(II) also coordinates to the imidazole-N and to the carboxyl-O. This will be discussed in the NMR chapter. This 'double-sided' coordination was also proposed for the MLH species of copper(II) complexes containing peptides with a histidyl residue.[38]

As a result of the MLH species forming at low pH values, the coordination to the imidazole-N and to the carboxyl-O is viable, since the charge of the carboxylic acid needs to be neutralised at low pH values. As the pH increases, the need for the charge to be neutralised diminishes and the charged carboxylic acid can remain uncoordinated. This means that because the ML species of Cu-Sar-LH occurs at a higher pH, it is most likely that copper(II) only coordinates via the amine route and not via the imidazole. This is due to the higher basicity of the amine than the imidazole. Therefore, a possible coordination for the ML species is to the amine and neighbouring amide-N with a protonated imidazole-N. The most likely mechanism in going from an MLH to ML species is for the sarcosine amide to switch from a carbonyl-O to an amide-N coordination, while the imidazole-N remains protonated. The transition from MLH to ML gives a pK_a value of 4.99, which is a value typical of a metal assisted amide deprotonation. The proposed switch has been seen in literature for the species of Cu-di, tri and tetraglycine when they go from an ML to MLH_{-1} species.[39,40] These ligands have pK_a values of 4.23, 5.41 and 5.56 respectively and represent the first amide deprotonation. The only difference between the transition from ML to MLH_{-1} for the species of Cu-di, tri and tetraglycine and the proposed transition from MLH to ML for Cu-Sar-LH, is that the histidine in the Cu-Sar-LH species is still protonated. Therefore, since these pK_a values from literature and Cu-Sar-LH are comparable, it supports the suggestion that the first metal assisted amide coordination in the ML species of Cu-Sar-LH is a result of copper(II) switching from a carbonyl-O to an amide-N coordination. Additionally, literature for a Cu-GGG complex suggests that the binding site is not a simple bidentate coordination between the amine and amide-N, since the oxygen donor from the carbonyl-O is also involved in the coordination.[40] Therefore the coordination mode for the ML species could also be a tridentate coordination consisting of the amine, neighbouring amide-N and the carbonyl-O belonging to leucine, with a protonated imidazole-N.

The pK_a value of the ML to MLH_{-2} species of Cu-Sar-LH is not attainable, but it can be speculated that the transition happens in one step. This means that another coordination switch occurs between the carbonyl-O of leucine and its neighbouring amide-N, as well as the coordination to the imidazole-N. Likewise, the pK_a value from the MLH to MLH_{-2} species for Cu-GFH and Cu-Sar-FH is also not attainable, but it is reasonable to suggest that for this transition to occur, the coordination to two amide-Ns and to the imidazole-N all happen in one step. Therefore, the proposed coordination mode of the MLH_{-2} species for all ligands, is to the amine, both amide-Ns and to the imidazole-N. This coordination is favourable because it forms three fused, very stable, chelate rings, which comprise of two 5-membered and one 6-membered chelate rings. This 4N-complex has been seen in other copper(II) peptide complexes.[28,29,38,39,41] In tripeptides without the imidazole, the carboxylic acid becomes the fourth coordination site, as seen in Cu-GGG.[39,40] The reason why the coordination of the charged carboxylic acid is not favoured over the coordination to the imidazole, is because the imidazole has a very efficient nitrogen donor, which makes it more basic and therefore the coordination is more stable. A flow diagram visually explaining the transition in coordination from MLH → ML → MLH_{-2} of Cu-Sar-LH can be seen in Figure 3.25. This coordination mechanism can be transferred to Cu-GFH and Cu-Sar-FH by removing the ML species.

Similar to the ML species of Cu-Sar-LH, for the MLH_{-1} species of Cu-GLH, copper(II) is also thought to only coordinate via the amine route, because the MLH_{-1} species also occurs at a higher pH than the MLH species. Unfortunately, the transition from the MLH to the MLH_{-1} species is not stepwise, so the pK_a value for the amide deprotonation cannot be compared with literature. However, the pK_a value for the MLH_{-1} to MLH_{-2} transition is known and because the value is 5.01, it was originally thought to suggest a second amide deprotonation. This would produce an MLH_{-1} coordination mode where copper(II) is coordinated to the amine, neighbouring amide-N and imidazole-N. Transitioning to the MLH_{-2} species would then just include the coordination to the second amide-N. But since the value of 5.01 represents the second amide deprotonation, when comparing this value with literature (Cu-GGG: pK_a = 6.86)[39,40], it was found that it is not close enough to literature values to confirm a second amide deprotonation. Another thought was that the MLH_{-1} species is coordinated to the amine and two amide-Ns with a protonated imidazole-N, or to the amine, two amide-Ns and the carboxyl-O with a protonated imidazole-N. The only difference between these two coordination modes is the coordination to the carboxyl-O. Transitioning to the MLH_{-2} species would then include a coordination to the imidazole-N. However, the protonation of the

imidazole-N has a log *K* of 6.89, which also is not close enough to the 5.01 pK_a value to confirm a coordination mode. Since these three coordination modes are the most likely possible modes for MLH_{-1} to transition to MLH_{-2}, one of them should be correct. Várnagy *et al.*[38] also could not identify the site of coordination for Cu-Gly_nHis complexes (n=3,4,5) through the pK_a values, and so they used other techniques to validate the coordination mode. Therefore, further structural analyses are required to distinguish between the three proposed coordination modes.

However, the coordination to the amine, two amide-Ns and the carboxyl-O, yields three stable 5-membered chelate rings; while the coordination mode to only the amine and two amide-Ns, yields two stable 5-membered chelate rings; and the coordination to the amine, neighbouring amide-N and imidazole-N, yields one 5-membered chelate ring and one macro chelate ring. Therefore, the three 5-membered ring system could be favoured. This coordination mode is seen in the MLH_{-2} species of Cu-GGG where the geometry is square planar, but the protonated imidazole-N of Cu-GLH makes it an MLH_{-1} species.[39,40] The other two coordination modes were also seen for the MLH_{-1} species of a Cu-glycylglycylhistamine system.[42] A flow diagram visually explaining the transitions for Cu-GLH, can be seen in Figure 3.26.

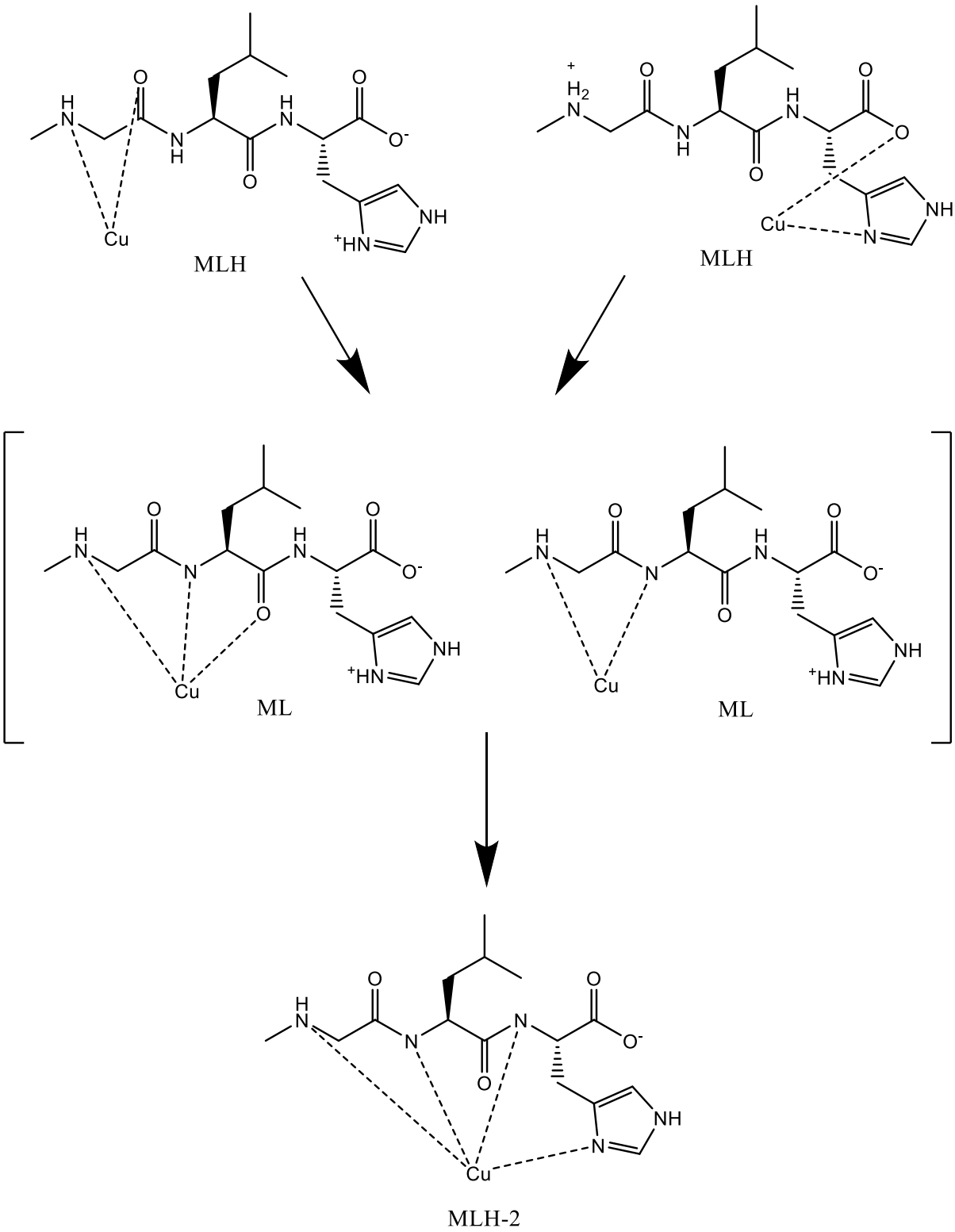

Figure 3.25: Visual representation explaining the transition mechanism of the species, MLH, ML and MLH_{-2} from Cu-Sar-LH.

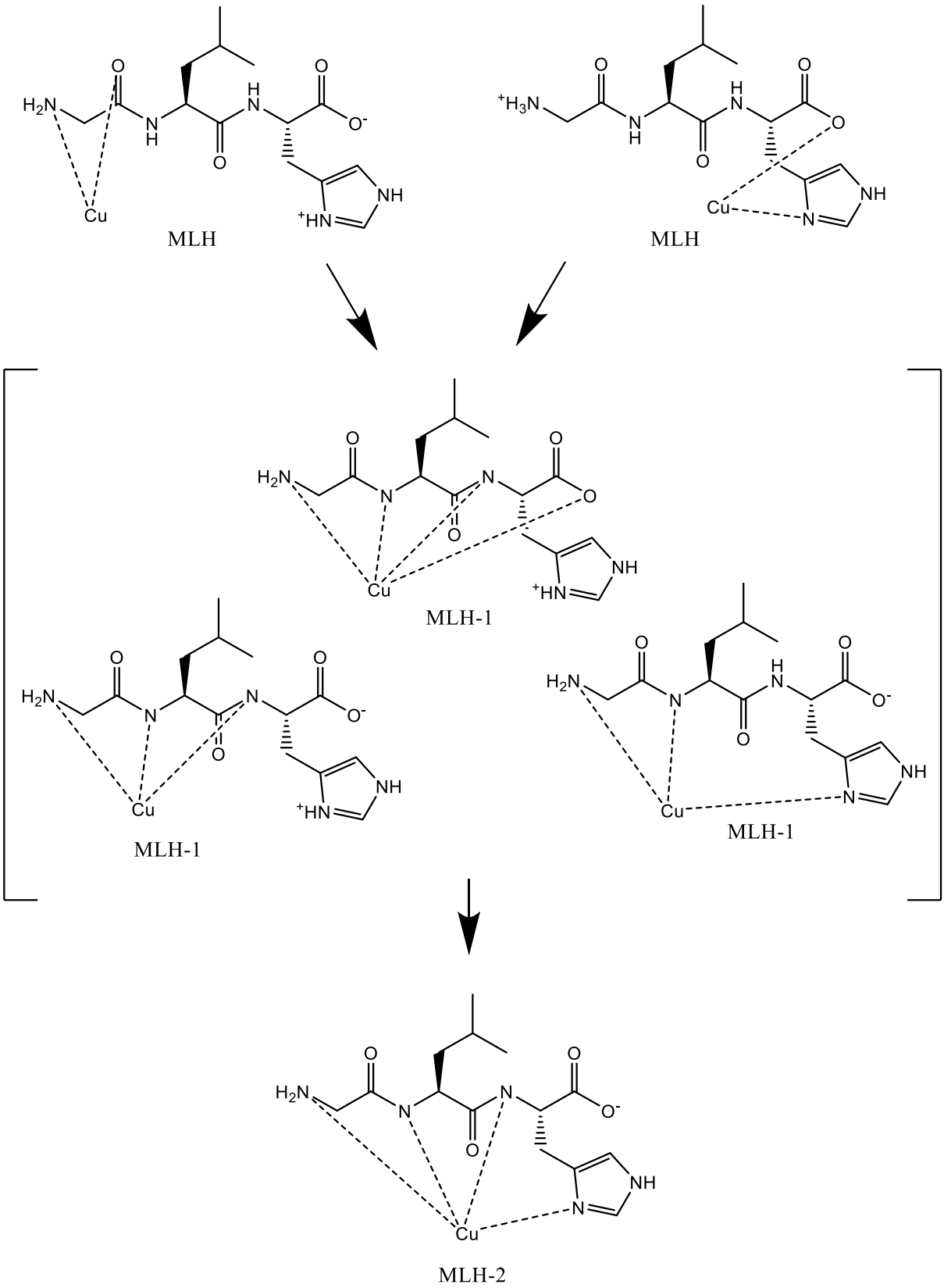

Figure 3.26: Visual representation explaining the transition mechanism of the species, MLH, MLH_{-1} and MLH_{-2} from Cu-GLH.

The complexation between nickel(II) and GLH yields two models with either the MLH, MLH_{-1} and MLH_{-2} species or the ML, MLH_{-1} and MLH_{-2} species. The standard deviations and Hamilton *R*-factors for these models are similar, and so further investigations are required to determine which model is more likely to be present in solution. An Ultraviolet-Visible spectrophotometric analysis was used to try and distinguish between the models. However, the absorption bands for the MLH, ML and MLH_{-1} species were not visible and therefore could not determine the more likely model. Due to the focus of this thesis, further structural investigations for the nickel(II) and zinc(II) complexes were not carried out. But since the complexation of copper(II) to GLH yielded an MLH, MLH_{-1} and MLH_{-2} species, it is reasonable to suggest that the model to represent the complexation between nickel(II) and GLH is Model 2 with the species MLH, MLH_{-1} and MLH_{-2}.

3.5 Conclusion

The first objective to measure the stability of the complex between copper(II) and the ligands, GLH, Sar-LH, GFH and Sar-FH was achieved. The stability of complexes between nickel(II) and the ligands, as well as with zinc(II), was also measured. The comparison between the thermodynamic stability of complexes with a N-methylated group and a non-N-methylated group, was carried out. The expected increase in stability for the complexes with the N-methylated group was not seen, and it was rationalised that the methyl group either has steric effects, or that the charged amine group has a preference to bind to water (entropic effect). The comparison between the thermodynamic stability of complexes with the leucine group and the phenylalanine group was also carried out. The expected increase in stability for the complexes with leucine was also not seen, and again the rationalisation was the same as with the N-methylated and non-N-methylated groups. This could mean that copper(II) complexes with glycine and phenylalanine might be able to release copper(II) *in vivo* more effectively than copper(II) complexes with sarcosine and leucine.

In terms of structure determination, the species types associated with each complex were identified and proposed coordination modes for each species were made. The MLH species, for all ligands, are coordinated to an amine and neighbouring carbonyl-O with a protonated imidazole-N. A second coordination mode for the MLH species was suspected to be to the imidazole-N and carboxyl-O with a protonated amine, but this is only discussed in the NMR

chapter. The ML species of Cu-Sar-LH is coordinated through an amine, the neighbouring amide-N and the carbonyl-O of leucine, with a protonated imidazole-N, or to only the amine and neighbouring amide-N with a protonated imidazole-N. The MLH_{-1} species of Cu-GLH has three possible coordination modes: the first has a coordination to the amine and two amide-Ns with a protonated imidazole-N; the second is to the amine, two amide-Ns and the carboxyl-O with a protonated imidazole-N; and the third is to the amine, neighbouring amide-N and imidazole-N. The MLH_{-2} species, for all ligands, is coordinated to the amine, two amide-Ns and the imidazole-N.

3.6 References

1 C. Billing and I. Cukrowski, Glass Electrode Calibration for Use in the Voltammetric Determination of Stability Constants under Extreme Acidic Conditions, *South African J. Chem.*, 2009, **62**, 168–178.

2 X. Subirats, E. Fuguet, M. Rosés, E. Bosch and C. Ràfols, in *Reference Module in Chemistry, Molecular Sciences and Chemical Engineering*, ed. J. Reedijk, Elsevier Inc., 2015.

3 J. Mohammad and S. Masoud, Potentiometric Study of Complex Formation Between Some Transition Metal Ions and 2 - Aminopyridine. Part 1. A Model for Therapeutic Agent for Wilson's Disease, *Iran. J. Chem. Chem. Eng.*, 2003, **22**, 17–21.

4 A. E. Martell and R. J. Motekaitis, *Determination and Use of Stability Constants*, VCH Publishers, Inc., USA, 1988.

5 R. G. Bates, *Determination of pH, Theory and Practice*, John Wiley & Sons, Inc., New York, 2nd edn., 1973.

6 A. E. Martell and R. D. Hancock, *Metal Complexes in Aqueous Solution*, Springer Science & Business Media, 1996.

7 A. Braibanti, G. Ostacoli, P. Paoletti, L. D. Pettit and S. Sammartano, Recommended procedure for testing the potentiometric apparatus and technique for the pH-metric measurement of metal-complex equilibrium constants, *Pure Appl. Chem.*, 1987, **59**, 1721–1728.

8 H. M. Irving and H. S. Rossotti, The calculation of formation curves of metal complexes from pH titration curves in mixed solvents, *J. Chem. Soc.*, 1954, 2904–2910.

9 H. Irving, H. Rossotti, K. Taugbøl, H. Theorell and B. Thorell, Some Relationships Among the Stabilities of Metal Complexes., *Acta Chem. Scand.*, 1956, **10**, 72–93.

10 W. J. O'Sullivan and D. D. Perrin, The Stability Constants of Metal-Adenine Nucleotide Complexes, *Biochemistry*, 1964, **3**, 18–26.

11 S. C. Wallis, L. R. Gahan, B. G. Charles, T. W. Hambley and P. A. Duckworth, Copper(II) complexes of the fluoroquinolone antimicrobial ciprofloxacin. Synthesis, X-ray structural characterization, and potentiometric study, *J. Inorg. Biochem.*, 1996, **62**, 1–16.

12 G. G. Guilbault, D. N. Kramer and P. Goldberg, The application of modified Nernstian equations to the electrochemical determination of enzyme kinetics, *J. Phys. Chem.*,

1963, **67**, 1747–1749.

13 P. May, The use of glass electrodes for the determination of formation constants—I A definitive method for calibration, *Talanta*, 1982, **29**, 249–256.

14 S. Fiol, F. Arce, X. L. Armesto, F. Penedo and M. Sastre de Vicente, Analysis of systematic errors in calibrating glass electrodes with H+ as a concentration probe, *Fresenius. J. Anal. Chem.*, 1992, **343**, 469–472.

15 K. Murray and P. M. May, *Equilibrium Simulation for Titration Analysis*, 1989.

16 P. M. May, K. Murray and D. R. Williams, The use of glass electrodes for the determination of formation constants—III Optimization of titration data: The esta library of computer programs, *Talanta*, 1988, **35**, 825–830.

17 A. Vacca, A. Sabatini and M. A. Gristina, Two problems involved in solving complex formation equilibria: the selection of species and the calculation of stability constants, *Coord. Chem. Rev.*, 1972, **8**, 45–53.

18 M. Mohajane, Dipeptides as potential anti-flammatory drugs for rheumatoid arthritis, PhD Thesis, University of Cape Town, 2013.

19 A. I. Vogel, *Vogel's Qualitative Inorganic Analysis*, Longman, London, 3rd edn., 1961.

20 A. K. Covington and R. A. Robinson, References standards for the electrometric determination, with ion-selective electrodes, of potassium and calcium in blood serum, *Anal. Chim. Acta*, 1975, **78**, 219–223.

21 G. Gran, Determination of the equivalence point in potentiometric titrations. Part II, *Analyst*, 1952, **77**, 661.

22 Y. H. Lee and C. Brosset, The slope of Gran's plot: A useful function in the examination of precipitation, the water-soluble part of airborne particles, and lake water, *Water. Air. Soil Pollut.*, 1978, **10**, 457–469.

23 K. Murray and P. M. May, *ESTA: Equilibrium Simulation for Titration Analysis*, 1984.

24 A. J. Paulson and D. R. Kester, Copper(II) ion hydrolysis in aqueous solution, *J. Solution Chem.*, 1980, **9**, 269–277.

25 F. J. Millero and D. J. Hawke, Ionic interactions of divalent metals in natural waters, *Mar. Chem.*, 1992, **40**, 19–48.

26 K. J. Powell, *Academic software and database: Structure and displays V. Solov'ev*, 2001.

27 G. E. Jackson, A. N. Hammouda, F. M. Elmagbari and R. P. Bonomo, In vitro studies of dermally absorbed Cu(II) tripeptide complexes as potential anti-inflammatory drugs,

Polyhedron, 2017, **123**, 23–32.

28 A. N. Hammouda, Development of copper peptide complexes as anti-Inflammatory drugs, PhD Thesis, University of Cape Town, 2015.

29 E. Farkas, I. Sóvágó, T. Kiss and A. Gergely, Studies on transition-metal–peptide complexes. Part 9. Copper(II) complexes of tripeptides containing histidine, *J. Chem. Soc., Dalt. Trans.*, 1984, 611–614.

30 E. Farkas, E. Csapó, P. Buglyó, C. A. Damante and G. Di Natale, Metal-binding ability of histidine-containing peptidehydroxamic acids: Imidazole versus hydroxamate coordination, *Inorganica Chim. Acta*, 2009, **362**, 753–762.

31 R. R. Khoury, G. J. Sutton, D. Ebrahimi and D. B. Hibbert, Formation Constants of Copper(II) Complexes with Tripeptides Containing Glu, Gly, and His: Potentiometric Measurements and Modeling by Generalized Multiplicative Analysis of Variance, *Inorg. Chem.*, 2014, **53**, 1278–1287.

32 G. M. Vicatos, G. E. Jackson, A. N. Hammouda, R. P. Bonomo and G. Valora, Potentiometric and spectroscopic studies of the complex formation between copper(II) and Gly-Leu-Phe or Sar-Leu-Phe tripeptides, *Polyhedron*, 2019, **170**, 553–563.

33 G. M. Vicatos, In vitro studies of dermally absorbed Cu(II) tripeptide complexes as potential anti-inflammatory drugs, MSc Thesis, University of Cape Town, 2016.

34 H. K. Hall, Potentiometric Determination of the Base Strength of Amines in Non-protolytic Solvents, *J. Phys. Chem.*, 1956, **60**, 63–70.

35 H. Irving and R. J. P. Williams, 637. The stability of transition-metal complexes, *J. Chem. Soc.*, 1953, 3192.

36 Y. Altun, F. Köseoglu, H. Demirelli, İ. Yılmaz, A. Çukurovalı and N. Kavak, Potentiometric studies on nickel(II), copper(II) and zinc(II) metal complexes with new schiff bases containing cyclobutane and thiazole groups in 60% dioxane-water mixture, *J. Braz. Chem. Soc*, 2009, **20**, 299–308.

37 R. Nakon and R. J. Angelici, Copper(II) complexes of glycylglycine and glycylsarcosine and their methyl esters, *Inorg. Chem.*, 1973, **12**, 1269–1274.

38 K. Várnagy, J. Szabó, I. Sóvágó, G. Malandrinos, N. Hadjiliadis, D. Sanna and G. Micera, Equilibrium and structural studies on copper(II) complexes of tetra-, penta- and hexa-peptides containing histidyl residues at the C-termini, *J. Chem. Soc. Dalt. Trans.*, 2000, 467–472.

39 M. Turek and X. L. Senar, Potentiometric and Spectroscopic Studies on Di-, Tri- and Tetraglycine with Copper (II) Ions Systems, *Food Chem. Biotechnol.*, 2008, **72**, 15–33.

40 D. Sanna, C. G. Ágoston, G. Micera and I. Sóvágó, The effect of the ring size of fused chelates on the thermodynamic and spectroscopic properties of peptide complexes of copper(II), *Polyhedron*, 2001, **20**, 3079–3090.

41 H. Kozłowski, W. Bal, M. Dyba and T. Kowalik-Jankowska, Specific structure–stability relations in metallopeptides, *Coord. Chem. Rev.*, 1999, **184**, 319–346.

42 T. Gajda, B. Henry, A. Aubry and J.-J. Delpuech, Proton and Metal Ion Interactions with Glycylglycylhistamine, a Serum Albumin Mimicking Pseudopeptide, *Inorg. Chem.*, 1996, **35**, 586–593.

4. Ultraviolet-Visible Spectrophotometry

4.1 Introduction

The results from potentiometry found which species formed for each complex over a pH range from 2-11. But it gave multiple combinations or models for each ligand, where each model had a different set of species. The first challenge is to identify which is the correct model for each ligand and the second challenge is to find the correct coordination modes of each species. Ultraviolet-visible spectrophotometry (UV-Vis) is useful because it can identify the different species and provide information about their geometry. In addition, the coordination modes for each species can also be verified. This technique can be used for both the copper(II) and nickel(II) species because they both absorb light in the visible region, unlike zinc(II). These absorptions arise because electron transitions take place between the electronic energy levels. The two types of transitions that can occur and produce absorption bands are *d-d* transitions and charge transfer transitions.[1]

d-d transitions are specific for transition metal complexes, since electrons can become excited and move from the highest occupied molecular *d* orbital to the lowest unoccupied molecular *d* orbital. The separation between these sets of *d* orbitals corresponds to the wavelengths of visible light. As an electron becomes excited, it produces an absorption band which appears in the ultraviolet and visible regions of the electromagnetic spectrum.[2–5] The separation between *d* orbitals depends on the geometry of the complex, the type of ligand and the oxidation of the metal ion. Thus, by analysing the absorption bands, it is possible to gain information on the structural aspects of the complex.[4,6] The intensity of the absorption bands are governed by selection rules which include the Laporte rule. This states that for a transition to occur there must be a change of parity in molecules. This means that only *gerade* to *ungerade* ($g \rightarrow u$) or *ungerade* to *gerade* ($u \rightarrow g$) transitions are allowed and $g \rightarrow g$ or $u \rightarrow u$ transitions are forbidden. Another rule states that the multiplicity has to be maintained during a transition, so that if an electron changes spin, the transition is labelled as multiplicity forbidden.[1] Therefore, because of the selection rules, the colouring that is seen as a result of these absorption bands can appear as a pale colour. However, the more allowed a *d-d* transition is, the stronger the colouring will become.[1,6–8]

Unlike *d-d* transitions, charge transfer bands are a result of a change in the electron distribution between the metal and the ligand, which means that they are not Laporte forbidden and the probability of this transition occurring is high. This results in an intense absorption band and thus very intense colouring, such as dyes.[1,8] In metal complexes these charge transfer bands can either be caused by ligand-centred *n* - π^* or π^*- π^* transitions, or from the transfer of an electron between the metal and the ligand, which can be a ligand-to-metal or metal-to-ligand charge transfer.[1]

Depending on what type of transition is present, the molar absorption extinction coefficient values will vary. For spin-forbidden *d-d* transitions, values below 1 $dm^3mol^{-1}cm^{-1}$ are seen. Laporte forbidden, spin-allowed *d-d* transitions can either originate from a centrosymmetric complex, which will produce values between 0-10 $dm^3mol^{-1}cm^{-1}$, or the transitions can originate from a non-centrosymmetric complex and produce values between 10-1000 $dm^3mol^{-1}cm^{-1}$. Charge transfer transitions are fully allowed and so have values between 1000-50000 $dm^3mol^{-1}cm^{-1}$.

Copper(II) and nickel(II) can both accommodate six donor atoms and form an octahedral complex. The *d* orbitals in octahedral complexes are split into a higher doubly degenerate e_g set (d_{z^2}, $d_{x^2-y^2}$) and a lower triply degenerate t_{2g} set (d_{xy}, d_{xz}, d_{yz}). An electronic transition between these orbitals is spin-allowed but Laporte forbidden, because octahedral complexes have a centre of symmetry and therefore should appear as colourless.[1,4,9] Each complex experiences vibrations, which leads to a breakdown in Laporte selection rules and causes even octahedral complexes to have some degree of colour. To add to this, if a complex undergoes distortions, then this also adds to the colour.

For example, copper(II) ions have a d^9 configuration which gives rise to Jahn Teller distortion. The distortions can result in either an axial or equatorial elongation. This causes a lack of symmetry in an octahedrally coordinated copper(II) complex, which allows electron *d-d* transitions to occur and form an absorption band.[1] For tetragonally distorted octahedral copper(II) complexes, only a single absorption band in the visible region is produced. However, there are three spin-allowed transitions, which are $^2A_{1g} \leftarrow {}^2B_{1g}$, $^2B_{2g} \leftarrow {}^2B_{1g}$ and $^2E_g \leftarrow {}^2B_{1g}$.[10,11] But because these bands are broad and cannot be distinguished, they appear as a single absorption band at around 625 nm.

In contrast, nickel(II) ions have a d^8 configuration and the most common geometry for nickel(II), with a d^8 configuration, is a square planar diamagnetic derivative. The square planar coordination produces three spin-allowed *d-d* absorption bands with the transitions, $^1A_{1g} \rightarrow {}^1A_{2g}$, $^1A_{1g} \rightarrow {}^1B_{1g}$ and $^1A_{1g} \rightarrow {}^1Eg$.[12] However, when analysing a spectrum in the visible region, only a single *d-d* transition absorption band is usually seen in the 400-555 nm range with an intensity of 50-500 $dm^3mol^{-1}cm^{-1}$. This often gives the complex either a yellow, orange or red colour. A second more intense charge transfer absorption band may be seen between 333-434 nm.[11]

The theory[7,8] behind UV-Vis is that a beam of light with varying wavelength is shone onto a solution containing the analyte. The intensity of the different wavelengths emitted by the spectrophotometer is modulated by the amount the analyte absorbs, which can be quantified as the ratio:

$$T = \frac{I}{I_0} \tag{4.1}$$

where T is the transmittance, I is the light intensity with the analyte present and I_0 is the light intensity without the analyte. The ratio is measured as a function of wavelength, and at the wavelength where the analyte absorbs the most, the transmittance is the smallest. The transmittance can get converted to absorbance A, so that:

$$A = - \log \frac{I}{I_0}. \tag{4.2}$$

The absorbance is proportional to the concentration of the analyte and can be quantified by the Beer-Lambert law:

$$A = \varepsilon c b \tag{4.3}$$

Where ε is the molar extinction coefficient or molar absorption coefficient, c is the concentration of the analyte and b is the length of the absorbing layer.

More than one species can be present in the solution, which also absorbs light at a specific wavelength. The Beer-Lambert law can then be written as:

$$A^{\lambda} = b(\varepsilon_1^{\lambda} c_1 + \varepsilon_2^{\lambda} c_2 + \varepsilon_3^{\lambda} c_3 + \ldots\ldots \varepsilon_i^{\lambda} c_i)$$
$$= b\sum \varepsilon_i^{\lambda} ci$$

(4.4)

The superscript λ, is the particular wavelength that each species absorbs and the subscripts *1,2,3…i* are the species which absorb light.[13]

Since the structure of a species determines the energy at which it absorbs radiation, a correlation can be made between the structure and the λ_{max}. Therefore, if the λ_{max} of a particular species is known, the structure can be predicted. Billo[14] proposed an empirical equation to estimate the λ_{max} of copper(II) complexes in solution:

$$\lambda_{max} = \frac{10^3}{\sum_{i=1}^{4} n_i \bar{\nu}_i}$$

(4.5)

where n_i is the number of equatorial donor groups ($1 \leq n \leq 4$) and $\bar{\nu}_i$ represents the individual contribution from each donor group to the ligand field of the complex. This equation has reasonable accuracy, but can only include the equatorial coordinating groups. This means that any structures with axial coordinating groups cannot be calculated.[15,16]

The four investigated ligands each have five possible coordination groups, which will donate electrons to a coordinated copper(II) ion. These groups are the amine-N, the carbonyl-O, the amide-N, the carboxyl-O and the imidazole-N. Another group which can also donate electrons through an oxygen, is water.[15] The contribution that these groups give to the ligand field of the complex is given in Table 4.1. Sigel and Martin[17] then updated Billo's correlation[14] with a set of parameters that are within 2% of Billo's parameters, which can also be seen in Table 4.1.

Table 4.1: Individual contribution from each donor group to the ligand field of a copper(II) complex ($\bar{\nu}_i$).[15]

Electron donor group	**Contribution to ligand field ($\bar{\nu}_i$) (μm^{-1})**	
	Billo[14]	**Sigel and Martin**[17]
N_{amino}	0.453	0.460
$N_{peptide}$	0.485	0.494
$N_{imidazole}$	0.430	0.434
$O_{carboxylate}$	0.342	0.346
$O_{carbonyl/water}$	0.301	0.294

4.2 Experimental

The ligand solutions were prepared in the same manner as for the potentiometric titrations, where each solution contained a 1:1 copper(II)/nickel(II) to ligand ratio in HCl (0.01 M) and background electrolyte (0.15 M). A series of 1.5 ml extracts from each metal ligand solution was placed into multiple vials. The pH was then adjusted in increments of pH 0.5 with NaOH or HCl, so that a pH ranged from 2-11. All volumes added into each vial were noted. The pH of the solution in each vial was measured using a Crison micropH 2000 pH meter (Crison, Spain), with an attached Ω Metrohm glass electrode. pH readings were recorded with an accuracy of 0.1 and each solution was kept at a constant temperature of 25 °C. Spectrophotometric absorbance measurements were performed on a Shimadzu UV-1800 (Shimadzu, Japan) recording spectrophotometer in the range from 200-800 nm. A blank cell containing HCl (0.01 M) and background electrolyte (0.15 M), was used to zero the spectrophotometer and a baseline correction was done before the measurements were taken. The spectrometer measured the total spectrum of all the species present in solution at the different pH values.

4.3 Results and Discussion

Colour changes occurred during the potentiometric titrations for the copper(II) and nickel(II) complexes. As the pH of the copper(II) solution increased, its colour changed from a clear to a violet-pink colour, while the nickel(II) solution changed from a clear to a yellow colour. This colour change showed that different species formed at different pH values.[18] As a result of the colour change, a UV-Vis analysis could be carried out, which aided in the identification of the coordination modes for each species. As zinc(II) is d^{10}, its complexes remained colourless throughout the titration and so a UV-Vis analysis could not be done. The colour changes for the copper(II) and nickel(II) complexes can be seen in Figure 4.1.

(a)(i)

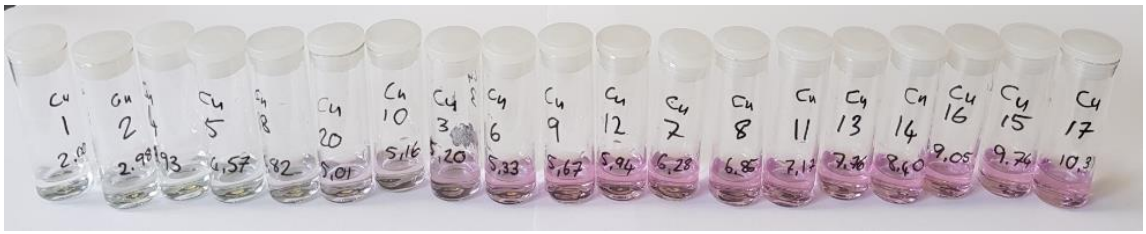

(a)(ii)

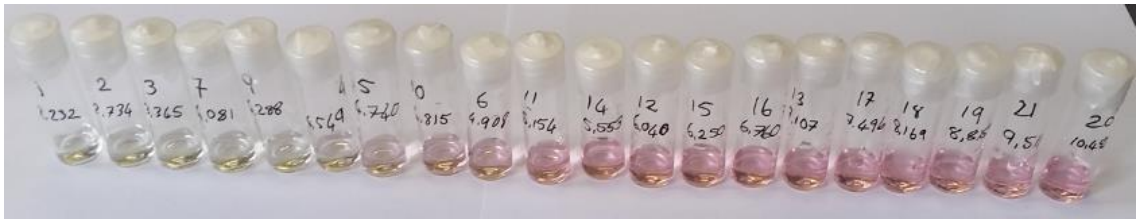

(a)(iii)

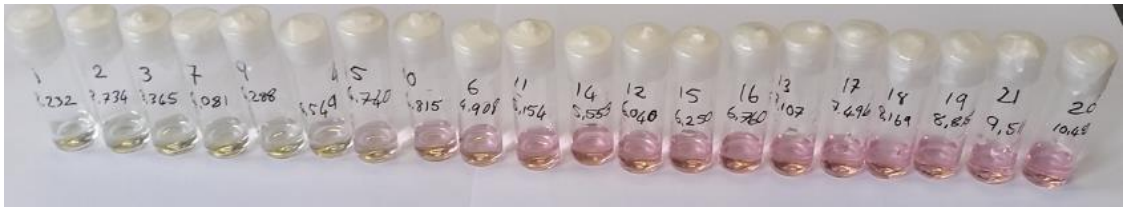

(a)(iv)

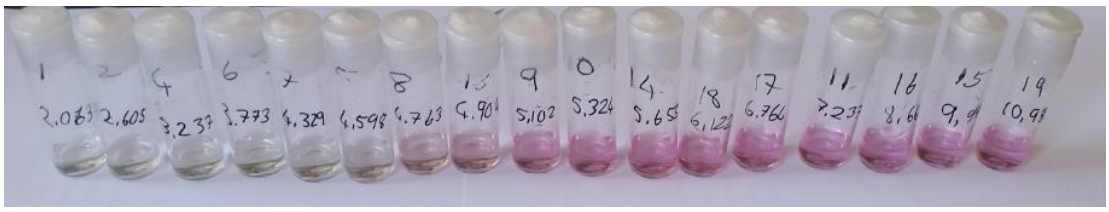

(b)(i)

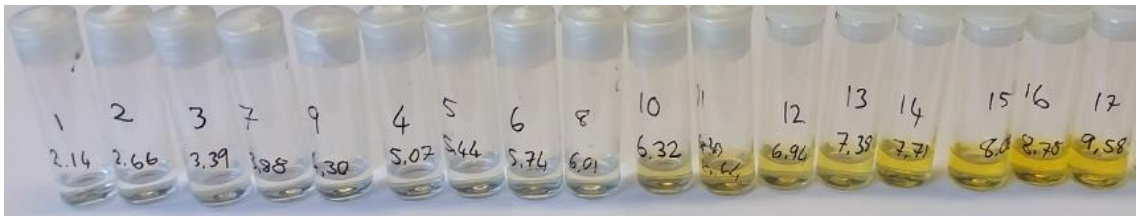

(b)(ii)

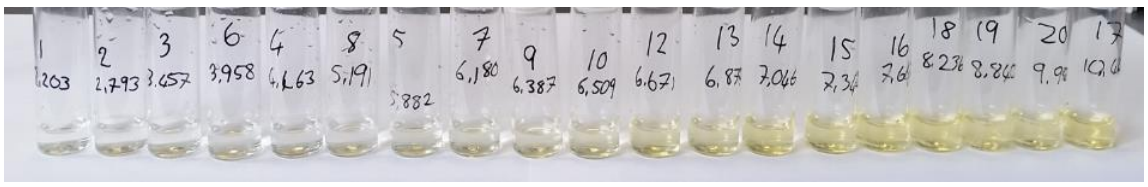

(b)(iii)

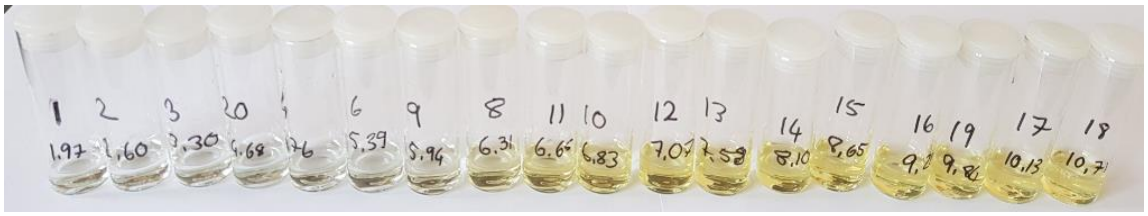

(b)(iv)

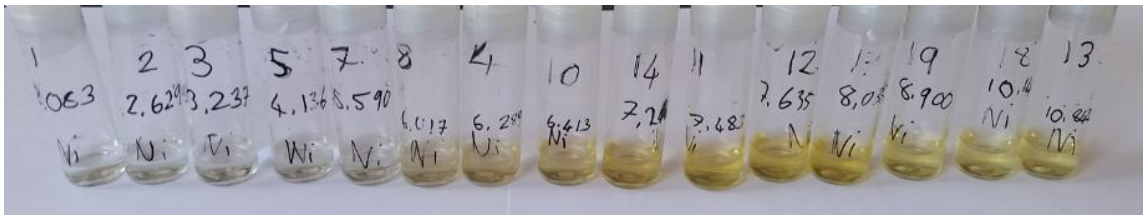

Figure 4.1: Visual observation of the colour change during a pH increase from 2-10, in increments of 0.5 from left to right for the copper(II) complexes, (a)(i) Cu-GLH, (a)(ii) Cu-Sar-LH, (a)(iii) Cu-GFH and (a)(iv) Cu-Sar-FH, as well as for the nickel(II) complexes (b)(i) Ni-GLH, (b)(ii) Ni-Sar-LH, (b)(iii) Ni-GFH and (b)(iv) Ni-Sar-FH.

4.3(a) Copper(II) complexes

The absorption spectra for the copper(II) ligand complexes, Cu-GLH, Cu-Sar-LH, Cu-GFH and Cu-Sar-FH can be seen in Figure 4.2 as a function of pH. For all the complexes, at low pH values there are absorbance bands that show a wavelength maximum at approximately 800 nm. This corresponds to $Cu(H_2O)_6$, which has a recorded absorbance band of 600-1000 nm, with a maximum at approximately 800 nm.[19] The most noticeable peak occurs at a λ_{max} between 517-523 nm and appears as the solution reaches pH 4-5. As the pH continues to increase, the intensity of these peaks increases. These absorbance bands result from the complexation of copper(II), and the increase in intensity, which is brought about by the colour of the solution becoming more prominent, could be due to two factors. From the Beer-Lambert Law, the intensity increase could either mean that there is a change in the coordination sphere of the complex, which increases the extinction coefficients, or that there is an increase in the concentration of a particular species.[13] From potentiometry, the MLH_{-2} species predominates at a high pH, and thus it is reasonable to assign the peak at ~520 nm to this species. Table 4.2 tabulates λ_{max}, as well as the corresponding molar extinction coefficient for MLH_{-2} and $Cu(H_2O)_6$ of all four ligands.

(a)

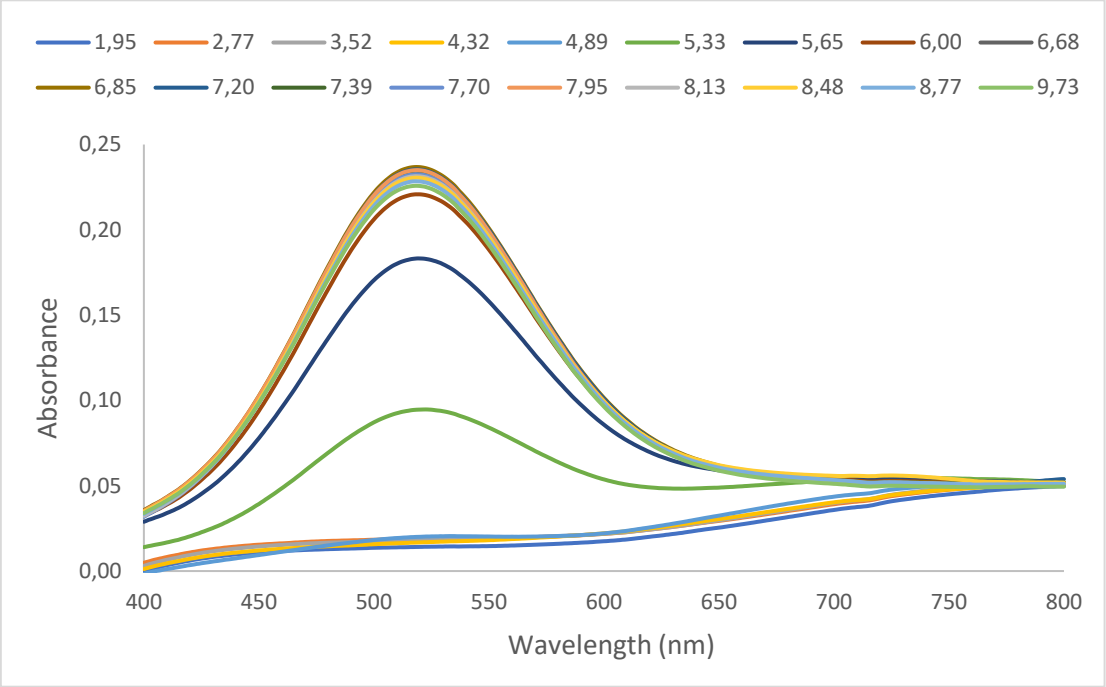
1,95
2,77
3,52
4,32
4,89
5,33
5,65
6,00
6,68
6,85
7,20
7,39
7,70
7,95
8,13
8,48
8,77
9,73
0,25
0,20
0,15
0,10
0,05
0,00
Absorbance
400
450
500
550
600
650
700
750
800
Wavelength (nm)

(b)

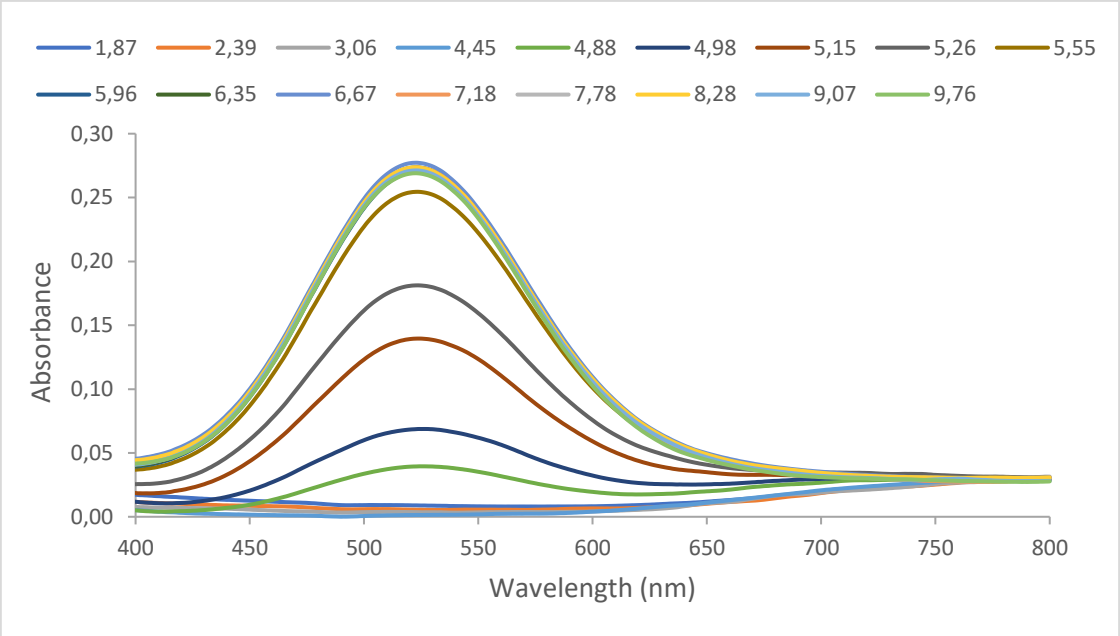
1,87
2,39
3,06
4,45
4,88
4,98
5,15
5,26
5,55
5,96
6,35
6,67
7,18
7,78
8,28
9,07
9,76
0,30
0,25
0,20
0,15
0,10
0,05
0,00
Absorbance
400
450
500
550
600
650
700
750
800
Wavelength (nm)

(c)

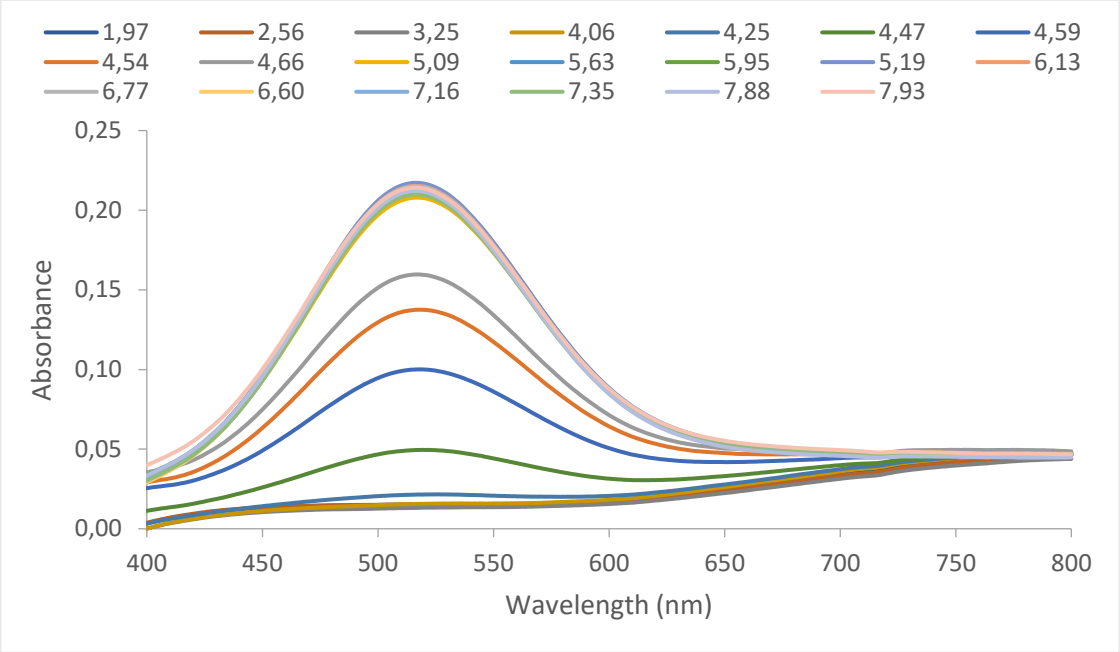

(d)

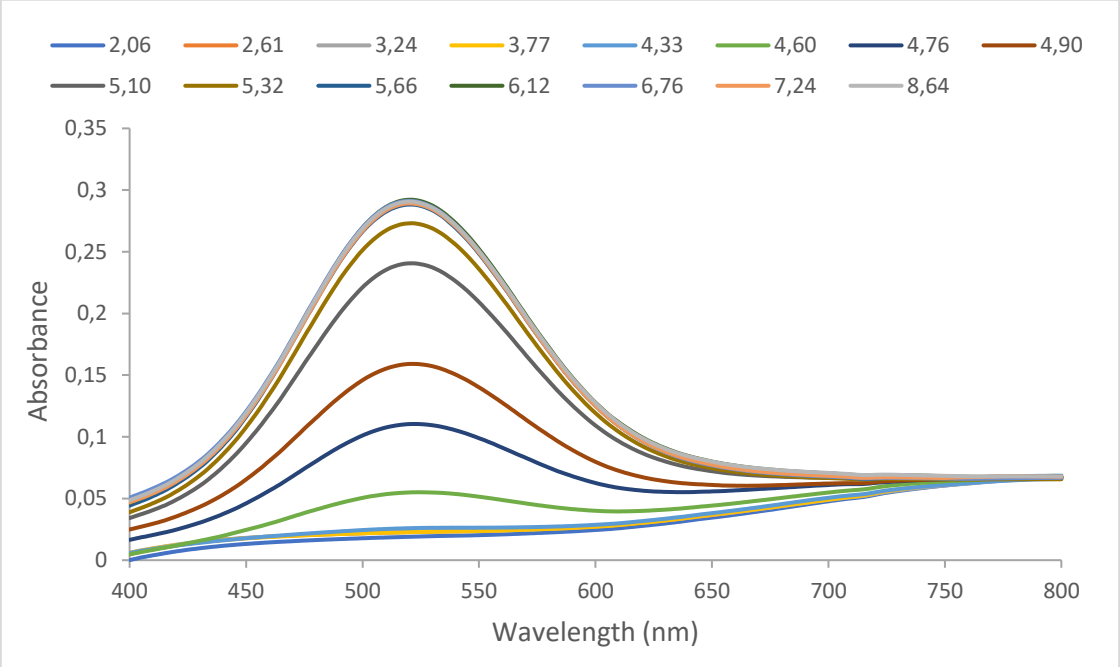

Figure 4.2: Electronic spectra of solutions containing (a) Cu-GLH (3.04×10^{-3} M of GLH and 2.69×10^{-3} M of copper(II)), (b) Cu-Sar-LH (2.93×10^{-3} M of Sar-LH and 2.58×10^{-3} M of copper(II)), (c) Cu-GFH (3.09×10^{-3} M of GFH and 2.55×10^{-3} M of copper(II)) and (d) Cu-Sar-FH (3.66×10^{-3} M of Sar-FH and 2.97×10^{-3} M of copper(II)).

Table 4.2: The maximum wavelengths and their corresponding molar extinction coefficients of the MLH_{-2} species and $Cu(H_2O)_6$, formed from Cu-GLH, Cu-Sar-LH, Cu-GFH and Cu-Sar-FH.

Complex	Species	λ_{max} (nm)	ε ($dm^3mol^{-1}cm^{-1}$)
Cu-GLH	$M(H_2O)_6$	800	18
	MLH_{-2}	518	88
Cu-Sar-LH	$M(H_2O)_6$	800	11
	MLH_{-2}	523	105
Cu-GFH	$M(H_2O)_6$	796	18
	MLH_{-2}	517	85
Cu-Sar-FH	$M(H_2O)_6$	800	23
	MLH_{-2}	521	98

Looking at Table 4.2, the molar extinction coefficients for MLH_{-2} were calculated by taking the absorbance band produced at the highest pH and dividing it by the copper(II) concentration. For the $Cu(H_2O)_6$ molar extinction coefficients, the absorbance band produced at the lowest pH was divided by the copper(II) concentration. Octahedral environments typically have extinction coefficients of about 10 $dm^3mol^{-1}cm^{-1}$.[1,9] Therefore the low molar extinction coefficients for the octahedral $Cu(H_2O)_6$ complexes are expected. The higher molar extinction coefficients for the MLH_{-2} species verify that the coordination of the complex is unsymmetrical. This is because the larger the coefficient is, the more unsymmetrical the coordination of a complex is.[20]

Each model from the potentiometric section has more than one complex species and so it is plausible to reason that when the pH changes and each species forms, there will be a change in the absorption maxima wavelengths. This is because each species will have a different coordination with copper(II), which will result in a change in the Ligand Field Splitting Energy between the e_g and t_{2g} orbitals. The energy change will then cause a shift in the wavelengths and result in different absorption maxima.[9,18] However, when looking at the absorption spectra in Figure 4.2, only one complex species can be seen (λ_{max} = 517-523 nm). For all the ligands, this complex species is the MLH_{-2} species, since the λ_{max} peaks follow the MLH_{-2} formation trend. None of the other supposed species can be identified. However, in Figure 4.2a and b at approximately 700 nm there seems to be a small wavelength maximum, which could correspond to a species, but it is too small to confirm its presence.

Based on previous research, the expected geometry for these complexes is a tetragonally distorted octahedral geometry.[10,21] As mentioned before, the three spin-allowed transitions are broad and cannot be distinguished and so appear as a single absorption at around 625 nm.[22]

Unlike Odisitse *et al.*,[18,21,23] who found copper(II) complexes exhibiting a blue-violet[21] colour, with a single absorption band in the range of 540-620 nm for the MLH_{-2} species, all four copper(II) ligand complexes displayed a violet-pink colour, with a single absorption band between the wavelengths of 517-523 nm. At high pH values, the MLH_{-2} species is the only species present, which confirms that the MLH_{-2} species forms the violet-pink colour. A square planar coordination has a wavelength of 526 nm[22] and so the MLH_{-2} species from all the copper(II) complexes most likely have undergone such extensive axial elongation that they have lost their axial bonds and become square planar in coordination.[1,20]

Even though the MLH_{-1} and MLH_{-2} species form at similar pH values, which therefore suggests the possibility that the MLH_{-1} species also contributes to the colour change, the presence of only one complex absorption band indicates that the colour change is only due to the MLH_{-2} species. In the potentiometric section, three possible coordination modes for the MLH_{-1} species were proposed and all could potentially form a square planar coordination. This will make distinguishing between the two wavelengths difficult and could be the reason why the MLH_{-1} species is not visible in the spectrum. This means that, if this is true, the MLH_{-1} species also contributes to the colour formation. However, other reasons could also be that the concentration of the MLH_{-1} species is too low and therefore cannot be read by the spectrophotometer or that another type of geometry forms, such as square pyramidal or octahedral, and since these geometries can potentially form wavelengths of a magnitude similar to the absorption band belonging to $Cu(H_2O)_6$, they could be hidden.[11] Possible reasons why the MLH and ML species could not be identified could also be due to their low concentration, or that they formed an octahedral geometry or another type of geometry, such as square pyramidal which would overlap and thus be hidden by the broad absorption band belonging to $Cu(H_2O)_6$. An attempt to deconvolute the spectra for each ligand complex was tried, but neither the UVSPEC in-house program or SOLVER[24] succeeded in solving spectra that potentially contained species other than the MLH_{-2} species. This is presumably because the spectral parameters are so similar and/or the concentration is too low.

Tripeptides from literature, which also formed the MLH_{-2} species, reported λ_{max} values in the range of 520-553 nm.[25–29] These values are close to the MLH_{-2} species (517-523 nm) found in this study, which firstly verifies the validity of this study's results and secondly, suggests that there is a high probability of finding similar geometries. These literature species coordinated in a square planar geometry which corresponds to the proposal that the MLH_{-2} species of this study also forms a square planar geometry.

When using Billo's equation to help identify the coordination mode and structure of the species, the coordination mode that gives a calculated λ_{max} value that is close to the observed MLH_{-2} λ_{max} values, is a coordination to the amine-N, two amide-Ns and an imidazole-N. This gives a calculated λ_{max} of 540 nm, which is close to the observed λ_{max} range of 517-523 nm.[15,30] Using Sigel and Martin's[17] updated parameters, the calculated λ_{max} value is 531 nm, which is closer to the observed range.[16,17] Since both calculated λ_{max} values correspond so closely to the observed λ_{max} values, it is reasonable to suggest that the geometry is square planar, with copper(II) coordinated equatorially to the amine-N, two amide-Ns and an imidazole-N for the MLH_{-2} species.

If the MLH_{-1} species forms a complex which has planar equatorial coordinating bonds, the one possible coordination mode is when copper(II) coordinates to the amine, two amide-Ns and the carboxyl-O with the imidazole-N protonated. Using Sigel and Martin's[17] parameters, this gives a λ_{max} of 557 nm. Another possible coordination mode is when copper(II) coordinates to the amine, two amide-Ns and a water molecule with the imidazole-N protonated, and the third possible coordination mode is when copper(II) coordinates to the amine, neighbouring amide-N, the imidazole-N and to a water molecule. Using Sigel and Martin's[17] parameters, this gives a λ_{max} of 574 nm and 595 nm respectively. The 557 nm value is close to the calculated λ_{max} (531 nm) of the MLH_{-2} species and thus the resultant absorption bands could be too close to distinguish the one from the other. The 574 nm and 595 nm values are slightly further away, but since the absorption band of the MLH_{-2} species is large, these coordination modes, should they exist, could still be hidden by the MLH_{-2} absorption band.

If the MLH and ML species did form a colourless octahedral complex or another geometry, such as square pyramidal, and these geometries overlap with the absorption bands of $Cu(H_2O)_6$, then their λ_{max} values would be around 800 nm. For the MLH species, which has the speculated

'double-sided' coordination, the coordination to the amine-N, carbonyl-O and two water molecules with the protonated imidazole-N gives a λ_{max} of 745 nm, when using Sigel and Martin's updated parameters.[17] A coordination to the imidazole-N, carboxyl-O and two water molecules with the amine-N protonated gives a calculated λ_{max} of 731 nm. Similarly, for the ML species, a coordination to the amine, neighbouring amide-N and two water molecules with a protonated imidazole-N; or a coordination to the amine, neighbouring amide-N, the leucine carbonyl-O and one water molecule with a protonated imidazole-N, both give a calculated λ_{max} of 649 nm.[17] Since these calculated values are relatively close to 800 nm, it gives credibility to the suggestion that the absorption bands of the MLH and ML species are hidden by the broad absorption bands of $Cu(H_2O)_6$.

4.3(b) Nickel(II) complexes

The absorption spectra for the nickel(II) ligand complexes, Ni-GLH, Ni-Sar-LH, Ni-GFH and Ni-Sar-FH can be seen in Figure 4.3 as a function of pH. For all the spectra, at low pH values and at a wavelength of approximately 400 nm, there is a small absorbance band. This corresponds to $Ni(H_2O)_6$, which has a recorded maximum at 410 nm.[31] Similarly to the copper(II) complexes, as the pH increases, absorption bands appear between the wavelengths of 424-428 nm, signalling the complexation of nickel(II). As the pH increases, the intensity of the peaks increase, signalling either an increase in extinction coefficients or an increase of a particular species concentration.[13]

As mentioned before, when d^8 nickel(II) forms a square planar coordination, it produces three spin-allowed *d-d* absorption bands. But only a single *d-d* transition absorption band is usually seen in the visible region with a 400-555 nm range and a molar extinction coefficient of 50-500 $dm^3mol^{-1}cm^{-1}$.[11] In Figure 4.3 a single absorption band between 424-428 nm can be seen for all the nickel(II) complexes, with the exception of Ni-GLH, which has what appears to be a second absorption band at 390 nm between pH 7.5-9.3. A possible explanation for this appearance could be due to spin-orbit coupling, since it causes transition band peaks to split.[32,33] The single absorption bands in Figure 4.3, as well as the appearance of a yellow colour, verifies a square planar coordination. The λ_{max} values, as well as the corresponding molar extinction coefficient for the MLH_{-2} species and $Ni(H_2O)_6$ of all four ligands, can be seen in Table 4.3. The molar extinction coefficients in Table 4.3 for MLH_{-2} and $Ni(H_2O)_6$ were

calculated in a similar way to the copper(II) complexes. Similarly, the $Ni(H_2O)_6$ complexes produced typically low molar extinction coefficients, indicating an octahedral geometry. The high coefficients associated with the MLH_{-2} species suggest unsymmetrical complexes, which is expected for a d^8 square planar nickel(II) coordination.

(a)

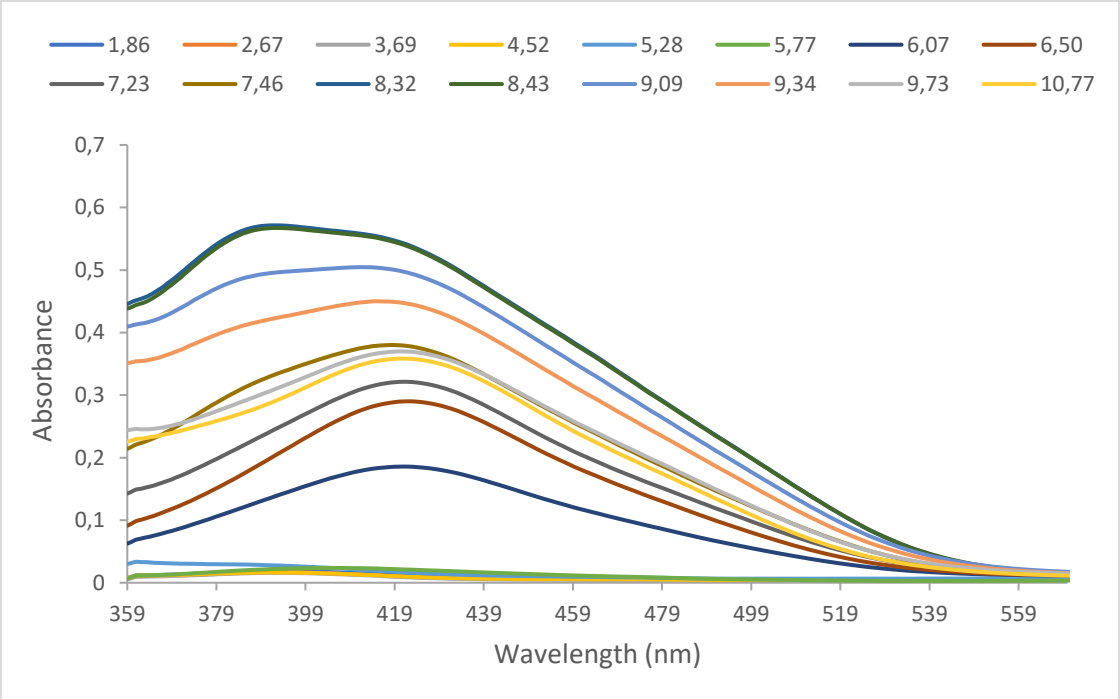

(b)

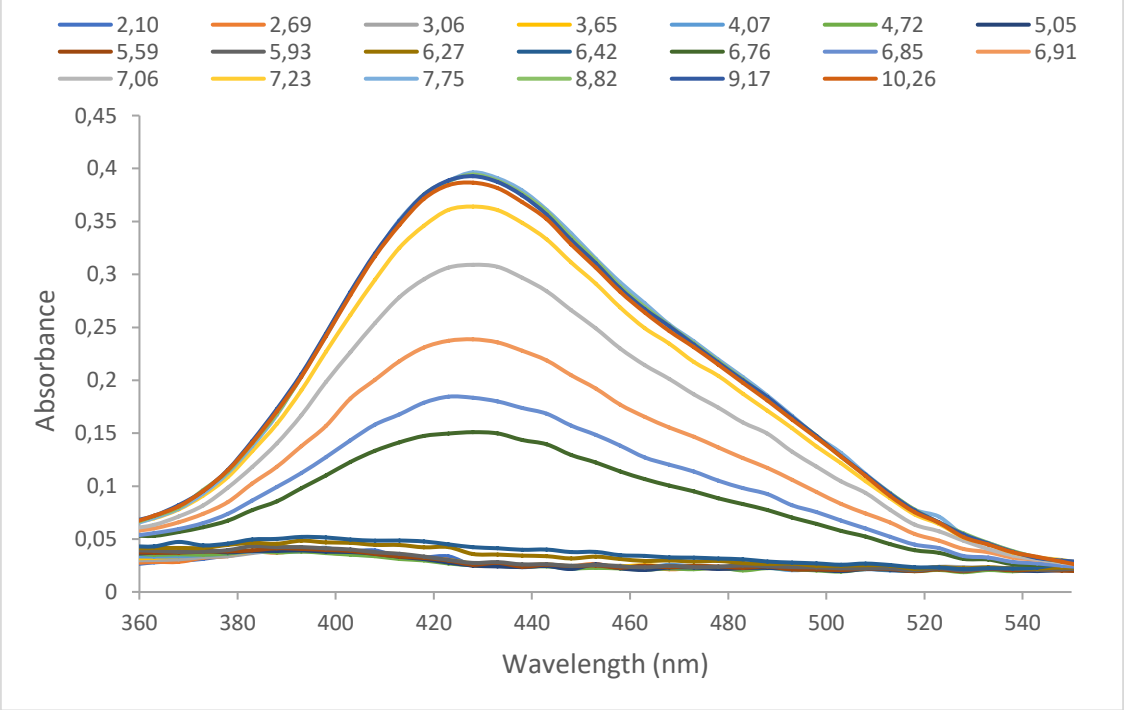

(c)

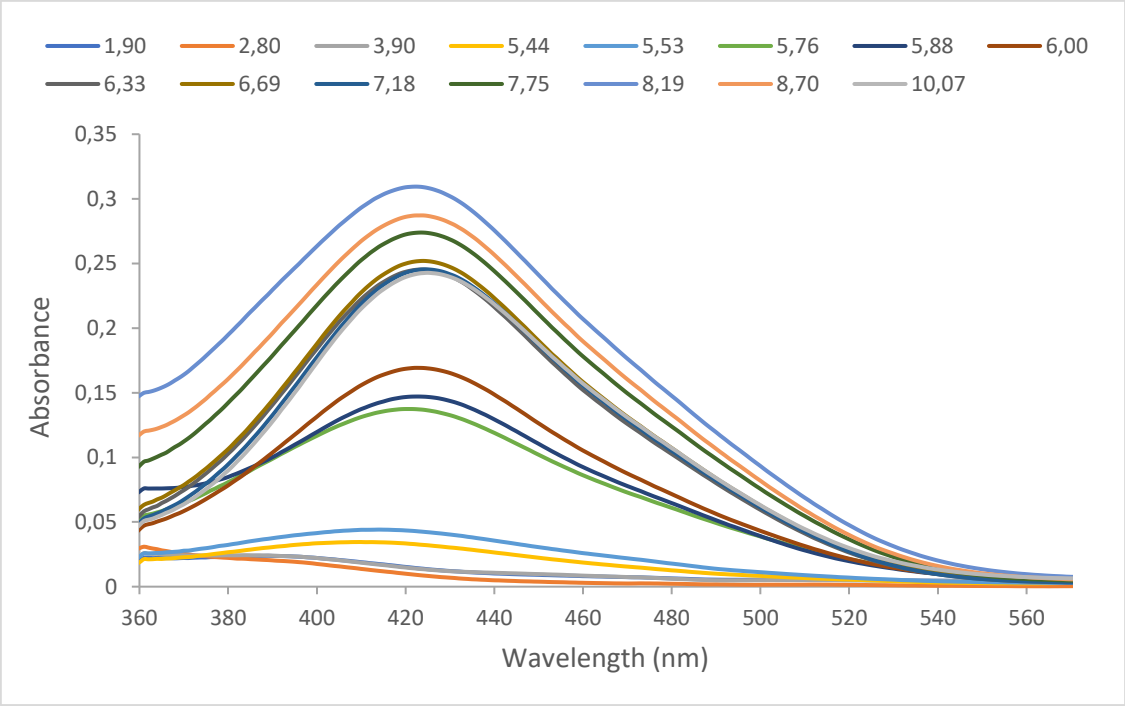

(d)

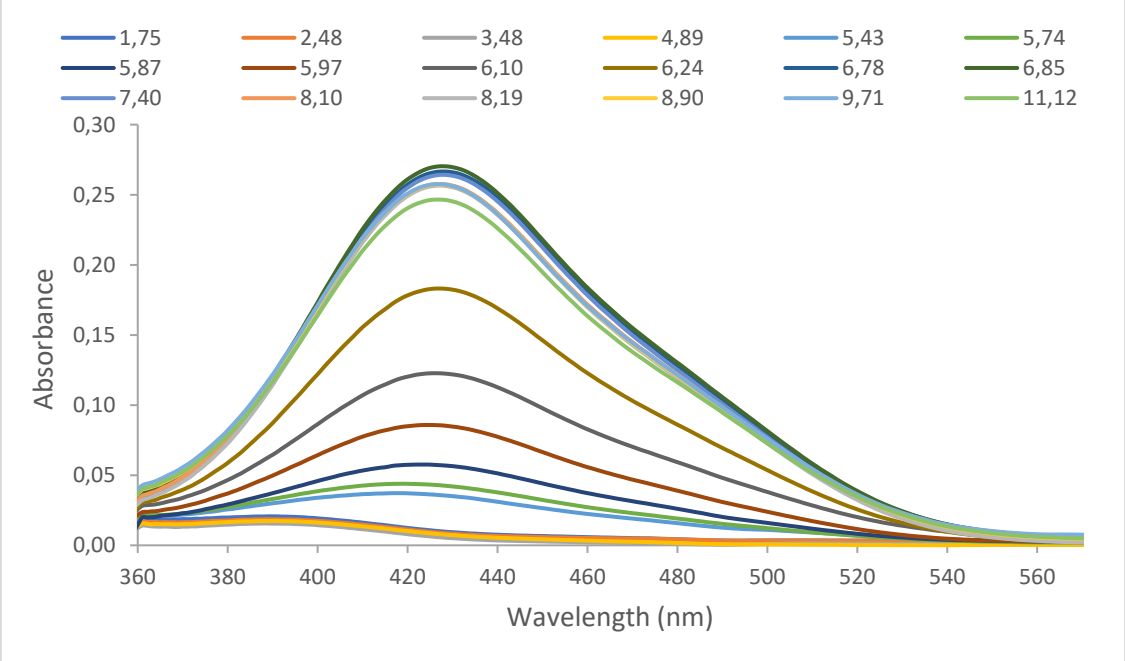

Figure 4.3: Electronic spectra of (a) Ni-GLH (2.95×10^{-3} M of GLH and 2.29×10^{-3} M of nickel(II)), (b) Ni-Sar-LH (3.79×10^{-3} M of Sar-LH and 3.41×10^{-3} M of nickel(II)), (c) Ni-GFH (2.88×10^{-3} M of GFH and 2.27×10^{-3} M of nickel(II)) and (d) Ni-Sar-FH (2.67×10^{-3} M of Sar-FH and 2.42×10^{-3} M of nickel(II)).

Table 4.3: The maximum wavelengths and their corresponding molar extinction coefficients of the MLH_{-2} species and $Ni(H_2O)_6$, formed from Ni-GLH, Ni-Sar-LH, Ni-GFH and Ni-Sar-FH.

Complex	Species	λ_{max} (nm)	ε ($dm^3mol^{-1}cm^{-1}$)
Ni-GLH	$M(H_2O)_6$	400	10
	MLH_{-2}	424	239
Ni-Sar-LH	$M(H_2O)_6$	400	15
	MLH_{-2}	427	115
Ni-GFH	$M(H_2O)_6$	400	10
	MLH_{-2}	425	136
Ni-Sar-FH	$M(H_2O)_6$	400	8
	MLH_{-2}	428	109

Similar to the copper(II) complexes, the absorption spectra in Figure 4.3 only indicates that one species can be seen. From the potentiometric results it was found that all the nickel(II) complexes formed the MLH, MLH_{-1} and MLH_{-2} species, with the exception of the Ni-GLH complex, which formed another model consisting of the ML, MLH_{-1} and MLH_{-2} species. Nevertheless, both of these models have the MLH_{-1} and MLH_{-2} species and since these species form at similar pH values, it suggests that the colour change could be attributed to both species. However, similar to the copper(II) complexes, the absorption spectra in Figure 4.3 only indicates that one species can be seen. This means that only the MLH_{-2} species can be confirmed to contribute to the colour change, since the absorption bands follow the formation of the MLH_{-2} species. From this, it can be deduced that the MLH_{-2} species is square planar. Since the absorption bands of the MLH, ML and MLH_{-1} species are all not visible, as with the copper(II) species, they can be speculated to overlap with either the MLH_{-2} or $Ni(H_2O)_6$ absorption band. More than likely, the MLH and ML species will have a λ_{max} value that overlaps with the $Ni(H_2O)_6$ absorption band and thus could be octahedral or even square pyramidal. Furthermore, for Ni-GLH, the transition band splitting appears to start at pH 8.3 and ends at pH 9.7. Since the splitting occurs at high pH values where only the MLH_{-2} species is present, it is viable to suggest that the spin-orbit coupling only occurs in this particular complex species.

Another observation in the absorption spectra of Ni-GLH and Ni-GFH, is that at high pH values, where the MLH_{-1} and MLH_{-2} species are present, the spectra curves upwards at low wavelengths. This could be due to a charge transfer band forming below the measured wavelength spectrum.[11] The band can be assigned as a ligand to metal charge transfer, since nickel(II) would have coordinated to the amide groups to form MLH_{-1} and MLH_{-2}. Amide

groups are negatively charged and thus can donate charge to a positively charged nickel(II) ion.

The speciation for the nickel(II) complexes is similar to the speciation for the copper(II) complexes and so it is reasonable to suggest that the coordination modes for the nickel(II) species are the same as the coordination modes for the copper(II) species. Therefore, following the coordination for copper(II), which is discussed in the potentiometric section, for the MLH species, nickel(II) is suggested to coordinate to the amine-N and neighbouring carbonyl-O, with the imidazole-N still protonated. This proposal was supported by literature which studied Ni-glycylhistamine[34] and Ni-glycylglycylhistamine[35]. There is also the possibility that nickel(II) coordinates to the imidazole-N and the carboxyl-O, with the amine protonated. For the ML species, nickel(II) is suggested to coordinate to the amine, neighbouring amide-N and the carbonyl-O from leucine/phenylalanine with the imidazole-N protonated. This proposal was also supported by literature.[34,35] Another possibility is for nickel(II) to coordinate only to the amine and neighbouring amide-N with the imidazole-N protonated. For the MLH_{-1} species, the three possible coordination modes for nickel(II) are either a coordination to the amine and two amide-Ns with the imidazole-N protonated; or to the amine, neighbouring amide-N and imidazole-N. Both of these coordination modes were suggested for the MLH_{-1} species of Ni-glycylglycylhistamine.[35] Another possibility could be similar to the MLH_{-2} species of Ni-GGG, where nickel(II) is coordinated to the amine, two amide-Ns and the carboxyl-O, but in the case of the four ligands in this study, the imidazole-N is protonated to make it MLH_{-1}.[36] Further structure determining techniques are needed to distinguish between which one is more probable. Due to the appearance of the yellow colour at high pH values, the MLH_{-2} species is thought to be square planar. This is in agreement with literature, where nickel(II) has coordinated to the amine-N, two amide-Ns and the imidazole-N.[29,35] The speculation that the ML and MLH species for the nickel(II) complexes form an octahedral arrangement, was also suggested by literature.[16,34,35,37]

4.4 Conclusion

The UV-Vis analysis found that the MLH_{-2} species of the copper(II) complexes formed a violet-pink colour with a single absorption band that had λ_{max} values ranging between 517-523 nm. Due to this, these species are square planar. Sigel and Martin's[17] empirical equation and set of parameters verified this geometry, as well as proposed that the MLH_{-2} species has an equatorial CuN_4 coordination. Due to the lack of colour and lack of an absorption band for the MLH and ML species, these species were speculated to have a λ_{max} value that overlaps and is thus hidden by the broad absorption band belonging to $Cu(H_2O)_6$. This was supported by calculating the anticipated λ_{max} values using Sigel and Martin's[17] set of parameters. This suggests that possible geometries could be octahedral or square pyramidal. For the MLH_{-1} species, Sigel and Martin's[17] set of parameters showed that the calculated λ_{max} values of the three possible coordination modes were close to the absorption band for the MLH_{-2} species. Therefore, the lack of an absorption band for the MLH_{-1} species could be due to an overlap with the absorption band for the MLH_{-2} species.

For the UV-Vis analysis of the nickel(II) complexes, the yellow colour and the appearance of a single absorption band, which has λ_{max} values ranging between 424-428 nm for the MLH_{-2} species, is an indication that the species is square planar.

4.5 References

1 C. E. Housecroft and A. G. Sharpe, *Inorganic Chemistry*, Pearson, London, 3rd edn., 2008.

2 P. W. Atkins, *Physical Chemistry*, Oxford University Press, Oxford, U. K., 2nd edn., 1982.

3 J. E. Huheey, *Inorganic Chemistry: Principles of Structure and Reactivity*, Harper and Row, New York, 3rd edn., 1983.

4 M. S. Silberberg, *Chemistry: The Molecular Nature of Matter and Change*, McGraw-Hill, New York, 5th edn., 2009.

5 E. F. H. Brittain, W. O. George and C. H. J. Wells, *Introduction to Molecular Spectroscopy: Theory and Experiment*, Academic Press, London, 1970.

6 P. W. Atkins, *Physical Chemistry*, Oxford University Press, Oxford, U. K., 4th edn., 1990.

7 P. W. Atkins and J. De Paula, *Physical Chemistry*, Oxford University Press, Oxford, U. K., 9th edn., 2010.

8 H. Kuhn, H.-D. Försterling and D. H. Waldeck, *Principles of Physical Chemistry*, John Wiley & Sons, Inc., Hoboken, Jew Jersey, 2nd edn., 2009.

9 R. J. Deeth and L. J. A. Hearnshaw, Molecular modelling of Jahn–Teller distortions in Cu(II)N6 complexes: elongations, compressions and the pathways in between, *Dalt. Trans.*, 2006, 1092–1100.

10 J. N. Zvimba and G. E. Jackson, Copper chelating anti-inflammatory agents; N1-(2-aminoethyl)-N2-(pyridin-2-ylmethyl)-ethane-1,2-diamine and N-(2-(2-aminoethylamino)ethyl)picolinamide: An in vitro and in vivo study, *J. Inorg. Biochem.*, 2007, **101**, 148–158.

11 A. B. P. Lever, *Inorganic Electronic Spectroscopy*, Elsevier, Amsterdam, 2nd edn., 1984.

12 H. B. Gray and C. J. Ballhausen, A Molecular Orbital Theory for Square Planar Metal Complexes, *J. Am. Chem. Soc.*, 1963, **85**, 260–265.

13 F. R. Hartley, C. Burgess and R. M. Alcock, *Solution Equilibria*, Ellis Horwood Ltd, Chichester, U.K, 1980.

14 E. J. Billo, Copper(II) chromosomes and the rule of average environment, *Inorg. Nucl. Chem. Lett.*, 1974, **10**, 613–617.

15 E. Prenesti, P. G. Daniele, M. Prencipe and G. Ostacoli, Spectrum–structure correlation for visible absorption spectra of copper(II) complexes in aqueous solution, *Polyhedron*, 1999, **18**, 3233–3241.

16 E. Farkas, E. Csapó, P. Buglyó, C. A. Damante and G. Di Natale, Metal-binding ability of histidine-containing peptidehydroxamic acids: Imidazole versus hydroxamate coordination, *Inorganica Chim. Acta*, 2009, **362**, 753–762.

17 H. Sigel and R. B. Martin, Coordinating properties of the amide bond. Stability and structure of metal ion complexes of peptides and related ligands, *Chem. Rev.*, 1982, **82**, 385–426.

18 S. Odisitse and G. E. Jackson, In vitro and in vivo studies of N,N′-bis[2(2-pyridyl)-methyl]pyridine-2,6-dicarboxamide-copper(II) and rheumatoid arthritis, *Polyhedron*, 2008, **27**, 453–464.

19 G. L. Miessler and D. A. Tarr, *Inorganic Chemistry*, Pearson Education, Inc., Philippines, 3rd edn., 2004.

20 R. C. Rosenberg, C. A. Root, P. K. Bernstein and H. B. Gray, Spectral studies of copper(II) carboxypeptidase A and related model complexes, *J. Am. Chem. Soc.*, 1975, **97**, 2092–2096.

21 S. Odisitse, G. E. Jackson, T. Govender, H. G. Kruger and A. Singh, Chemical speciation of copper(II) diaminediamide derivative of pentacycloundecane - A potential anti-inflammatory agent, *Dalt. Trans.*, 2007, 1140–1149.

22 S. Nigam and H. Mohabey, Electronic Spectra of Mixed Ligand Complexes of Copper(II) with Different Amino Acids., *Aisan J. Chem.*, 2001, **13**, 107–110.

23 S. Odisitse and G. E. Jackson, In vitro and in vivo studies of the dermally absorbed Cu(II) complexes of N5O2 donor ligands - Potential anti-inflammatory drugs, *Inorganica Chim. Acta*, 2009, **362**, 125–135.

24 Microsoft Corporation, *Microsoft Excel*, Office 365.

25 G. E. Jackson, A. N. Hammouda, F. M. Elmagbari and R. P. Bonomo, In vitro studies of dermally absorbed Cu(II) tripeptide complexes as potential anti-inflammatory drugs, *Polyhedron*, 2017, **123**, 23–32.

26 G. M. Vicatos, G. E. Jackson, A. N. Hammouda, R. P. Bonomo and G. Valora, Potentiometric and spectroscopic studies of the complex formation between copper(II) and Gly-Leu-Phe or Sar-Leu-Phe tripeptides, *Polyhedron*, 2019, **170**, 553–563.

27 D. Sanna, C. G. Ágoston, G. Micera and I. Sóvágó, The effect of the ring size of fused chelates on the thermodynamic and spectroscopic properties of peptide complexes of

copper(II), *Polyhedron*, 2001, **20**, 3079–3090.

28 M. Turek and X. L. Senar, Potentiometric and Spectroscopic Studies on Di-, Tri- and Tetraglycine with Copper (II) Ions Systems, *Food Chem. Biotechnol.*, 2008, **72**, 15–33.

29 T. Sakurai and A. Nakahara, Interaction of copper(II) and nickel(II) with L-histidine and glycylglycyl-L-histidine as an albumin model, *Inorg. Chem.*, 1980, **19**, 847–853.

30 E. J. Billo, Copper(II) chromosomes and the rule of average environment, *Inorg. Nucl. Chem. Lett.*, 1974, **10**, 613–617.

31 A. Mittal, *Chemistry*, APH Publishing, New Delhi, 2007.

32 D. Maganas, A. Grigoropoulos, S. S. Staniland, S. D. Chatziefthimiou, A. Harrison, N. Robertson, P. Kyritsis and F. Neese, Tetrahedral and Square Planar Ni[(SPR2)2N]2 complexes, R = Ph & iPr Revisited: Experimental and Theoretical Analysis of Interconversion Pathways, Structural Preferences, and Spin Delocalization, *Inorg. Chem.*, 2010, **49**, 5079–5093.

33 E. González, A. Rodrigue-Witchel and C. Reber, Absorption spectroscopy of octahedral nickel(II) complexes: A case study of interactions between multiple electronic excited states, *Coord. Chem. Rev.*, 2007, **251**, 351–363.

34 T. Gajda, B. Henry and J.-J. Delpuech, Potentiometric and Spectroscopic Study of Nickel(II) and Cobalt(II) Complexes of Histamine-Containing Dipeptides, *Inorg. Chem.*, 1995, **34**, 2455–2460.

35 T. Gajda, B. Henry, A. Aubry and J.-J. Delpuech, Proton and Metal Ion Interactions with Glycylglycylhistamine, a Serum Albumin Mimicking Pseudopeptide, *Inorg. Chem.*, 1996, **35**, 586–593.

36 K. Várnagy, B. Bóka, I. Sóvágó, D. Sanna, P. Marras and G. Micera, Potentiometric and spectroscopic studies on the copper(II) and nickel(II) complexes of tripeptides of methionine, *Inorganica Chim. Acta*, 1998, **275**–**276**, 440–446.

37 C. Gábor Ágoston, Z. Miskolczy, Z. Nagy and I. Sóvágó, The effect of ring size of fused chelates on the stability constants and spectroscopic properties of nickel(II) and palladium(II) complexes of peptides, *Polyhedron*, 2003, **22**, 2607–2615.

5. Electron Paramagnetic Resonance Spectroscopy

5.1 Introduction

The concept of electron paramagnetic resonance (EPR) spectroscopy is very similar to the technique of nuclear magnetic resonance, since they both involve the interaction between the electromagnetic radiation and magnetic moments. However, with EPR, the magnetic moments come from the electrons instead of the nuclei.[1–3] As a result EPR works with paramagnetic compounds and therefore makes it useful for studying transition metal complexes such as copper(II) complexes.[4–7]

Currently, it is unknown which model from the potentiometric section is correct for each of the four copper(II) complexes. Each model, for a particular ligand, has a different set of species that are produced over a pH range from 2-11. The species that were produced are MLH, ML, MLH_{-1} and $MLH_{-2,}$ but no model contains all four species. The possible coordination sites on the ligands are the amine, two amide-Ns, two carbonyl-Os, a carboxyl-O and an imidazole-N. Due to the nitrogen having a nuclear spin, when using the EPR spectroscopic techniques, it should be possible to identify the coordination of copper(II) to the nitrogen and oxygen atoms, as well as obtain their geometry at different pH values. This will then confirm which model is correct, as well as verify the coordination mode of each species.

5.2 Experimental

A Bruker Elexsys E500 CW-EPR spectrometer (Bruker, United States) driven by a PC running XEpr program under Linux and equipped with a Super-X microwave bridge operating at 9.3-9.9 GHz and a SHQE cavity was used throughout this work. All the frozen solution EPR spectra of copper(II) complexes were recorded in quartz tubes at 150 K by means of an ER4131VT variable temperature apparatus. The measurements at room temperature (RT) were recorded by means of a WG-812-H flat quartz cell and occasionally a glass capillary was inserted into a quartz tube. In the case of RT EPR spectra, the isotropic magnetic parameters were evaluated from the average distances among the peaks of the experimental spectra recorded in the 2nd

derivative mode. Copper(II) complexes with these ligands (charges are often omitted for simplicity) were prepared by adding the appropriate amount of isotopically pure $^{63}Cu(NO_3)_2$ (50 mM) to an aqueous solution containing the pertinent ligand in slight excess. The absolute copper(II) concentrations ranged from 1 to 4 mM. The final aqueous solution pH was adjusted by means of an Orion 9103SC combined glass microelectrode, which was connected to an Orion Star A 211 pH meter. The pH was adjusted by using concentrated NaOH or HNO_3 as required.

Up to 10 % methanol or glycerin was added to the aqueous solution containing the copper(II) complex species in order to increase resolution of the low temperature (LT) frozen solution spectra. EPR anisotropic magnetic parameters were obtained directly from the experimental EPR spectra, calculating them from the 2nd and the 3rd line to get rid of second order effects.[8] Perpendicular parameters were obtained by exploiting the appearance of the extra peak due to the angular anomaly, whose field can be used in connection with the parallel parameters to calculate with a certain accuracy $g_\perp$ and $A_\perp$ as explained in the literature.[9,10]

Instrumental settings of the frozen solution EPR spectra recording were as follows: number of scans 1-5 (In the case of RT spectra, occasionally more than 10 scans were required to collect an acceptable signal to noise ratio); microwave frequency 9.46-9.48 GHz; modulation frequency 100 kHz; modulation amplitude 0.2-0.6 mT; time constant 164-327 ms; sweep time 3-6 min; microwave power 10-20 mW; linear receiver gain 1×10^4 - 1×10^5. The instrumental settings of RT solution EPR spectra were substantially the same, except for the value of the microwave frequency. This was in the range of 9.70-9.80 GHz, when using the flat quartz cell and the microwave was powered up to 40 mW.

5.3 Results and Discussion

The four copper (II) complexes, Cu-GLH, Cu-Sar-LH, Cu-GFH and Cu-Sar-FH were examined at pH 7, and following the species distribution diagrams, only one copper(II) species should be found at this pH. RT spectra were first run in a more acidic pH to check the presence of prominent complex species in the system, which took into account that all the EPR spectra were run in the absence of added ionic strength.

An isotropic EPR spectrum is obtained at RT conditions, which is characterised by four lines (copper nuclear spin equal to 3/2, and then 2I + 1 lines). In contrast, an anisotropic EPR spectrum is obtained at LT conditions, which generally has an axial symmetry, characterized by two sets of four transitions occurring at different values of the magnetic field. These two sets are either parallel or perpendicular transitions. The parallel transitions of the LT EPR spectrum are well separated by the hyperfine coupling constant, whose values together with the g parallel values give information on the geometry of the copper(II) complex. By contrast, the perpendicular hyperfine coupling constant has a much lower numeric value than the parallel one, which is not resolved and presented as a single transition at higher magnetic fields. The two sets of transitions can overlap, and because the parallel lines are easily recognizable due to their low intensity, two or three of the parallel lines are generally visible.

The RT spectra of the four copper(II) complexes at pH 7 are reported in Figure 5.1. Looking at these spectra, it is evident that they all look very similar to each other. This can be a result of the MLH_{-2} complex species since, according to the species distribution diagram, it is present in the pH range from approximately 4.5-11. Due to the presence of donor nitrogen atoms on the ligand, at a higher magnetic field, it is possible to see that all the RT spectra contain the fourth line. This shows a superhyperfine (shf) structure that is coming from the delocalization of the spin density of the copper(II) free electron on the nitrogen atoms. Since the nitrogen nuclear spin is 1, from the multiplicity of the $2\Sigma I + 1$ lines, it is possible to count the number of nitrogen atoms bound to copper(II) in the complex equatorial plane. Nine shf lines indicate that copper(II) is bound to four quasi-equivalent nitrogen atoms and so the chromophore of this species can be considered as CuN_4.

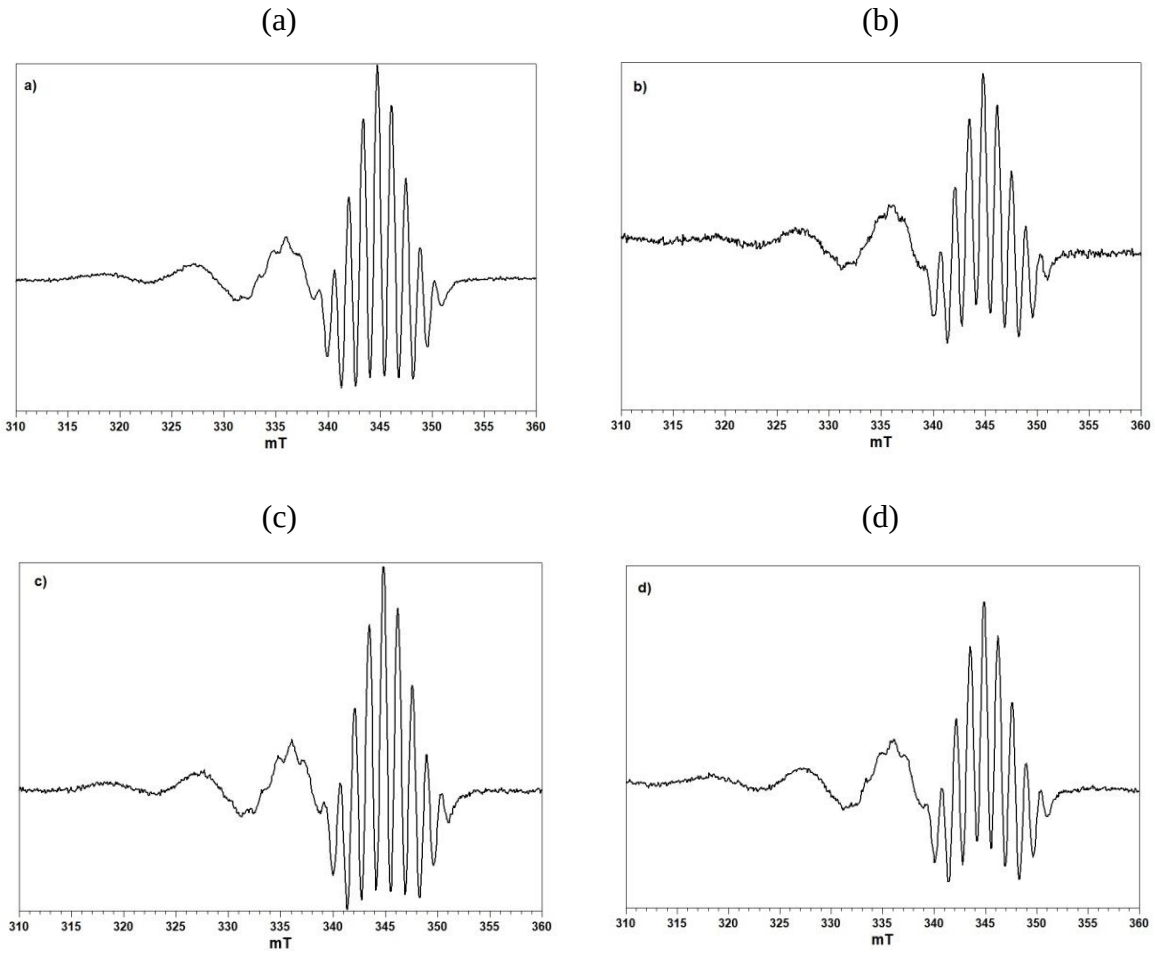

Figure 5.1: RT EPR 2nd derivative spectra recorded in aqueous solution for the copper(II) complexes, (a) Cu-GLH, (b) Cu-Sar-LH, (c) Cu-GFH and (d) Cu-Sar-FH.

The magnetic parameters from the LT EPR spectrum can be seen in Table 5.1. All the LT frozen EPR spectra show $g_{\|} > g_{\perp} \geq 2.04$.[11] This suggests that the copper(II) ground state could be reasonably assigned to the $d_{x^2-y^2}$ orbital in an octahedral, square planar or square based pyramidal geometry. The low value of the $g_{\|}$ and the relatively high absolute value of the parallel hyperfine constant suggest that these copper(II) complex species have a square planar geometry in a probable macrochelate complex. Since only subtle and negligible differences are observed among the copper(II) complexes with these ligands, they can be considered to have the same stereochemistry.

Table 5.1: Spin Hamiltonian parameters of copper(II) complexes with Cu-GLH, Cu-Sar-LH, Cu-GFH and Cu-Sar-FH at pH 7.0, which have been drawn out from RT EPR spectra and LT frozen aqueous solution EPR spectra. All the hyperfine coupling constants are expressed in 10^4 cm^{-1} units. Presumed errors in the last decimal figure are reported between brackets.

Complex	g_{iso} **(3)**	a_{iso} **(3)**	$g_{\|}$ **(4)**	$A_{\|}$ **(4)**	$g_{\perp}$ **(7)**	$A_{\perp}$ **(7)**	a_{iso}^{N} **(1)**	$A_{\perp}^{N}$ **(1)**	$A_{\|}^{N}$ **(1)**
Cu-GLH	2.092	86	2.174	210	2.046	23	14	-	15
Cu-Sar-LH	2.094	88	2.171	211	2.046	24	14	-	15
Cu-GFH	2.091	84	2.175	208	2.040	27	14	11	16
Cu-Sar-FH	2.091	86	2.172	208	2.040	28	14	-	15

When lowering the pH of the aqueous solutions to pH 5, only Cu-Sar-LH displays signals from other species that are present in the system. The RT spectrum showing three different complex species of Cu-Sar-LH at pH 5.1 can be seen in Figure 5.2.

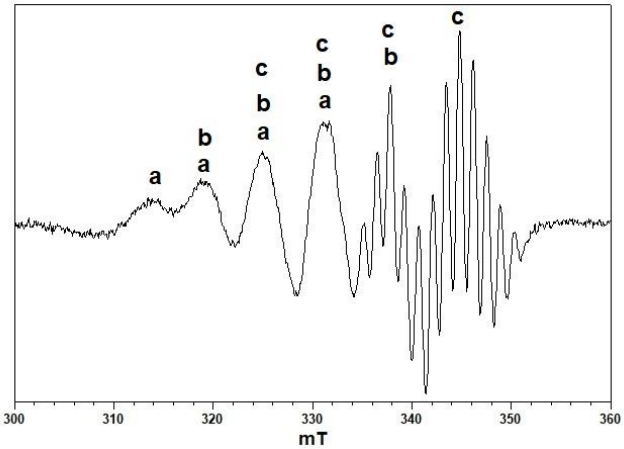

Figure 5.2: RT EPR 2nd derivative spectrum in an aqueous solution of Cu-Sar-LH at pH 5.1. Three copper(II) species are found and are designated as **a**, **b** and **c**.

Species **c** is the same species that was found at higher pH values and is thus the MLH_{-2} species. It can also be noted that it is evident that the MLH_{-2} species has already formed at pH 5.1. Species **a** and **b** both occur simultaneously with species **c** at this pH and give the following isotropic magnetic values: where **a** gives $g_{iso} = 2.151 \pm 0.007$ and $a_{iso} = 59 \pm 0.005 \times 10^{-4}$ cm^{-1} and **b** gives $g_{iso} = 2.111 \pm 0.007$, $a_{iso} = 62 \pm 0.005 \times 10^{-4}$ cm^{-1} and $a_{iso}^{N} = 13 \pm 0.002 \times 10^{-4}$ cm^{-1}. Species **b** shows a shf interaction with a pattern of five lines and an approximate intensity distribution of 1:2:3:2:1 and thus this indicates a CuN_2O_2 chromophore. The last two lines of species **b** overlap with the shf lines of species **c**. Looking at the isotropic magnetic parameters, which show a low value of g_{iso} and a high value of a_{iso}, it is probable that the pattern (species

b) is due to the nitrogen atoms coming from the amine and neighbouring amide-N. At pH 5.1, the imidazole-N is still protonated, and therefore the species would be the ML species. Species **a** shows isotropic magnetic parameters, which are compatible with the formation of MLH.

Unfortunately, the RT EPR spectra of Cu-GLH, Cu-GFH and Cu-Sar-FH were not well resolved in the pH range of 4.8-5.2. This meant that the detection of other complex species, that could be present in the system, could not be found and consequently the determination of their isotropic magnetic parameters also could not be found. The low resolution is due to the predominant MLH_{-2} species at low pH values.

For all four complexes, the shf structure at LT is present in all the EPR spectra of the frozen solutions (pH 7-8), which can be seen in Figure 5.3. But unfortunately, it is only resolved in the parallel part of the spectrum for Cu-GFH (Figure 5.4). This LT spectrum reveals the nine-line shf structure that was already seen in the RT EPR spectra in Figure 5.1.

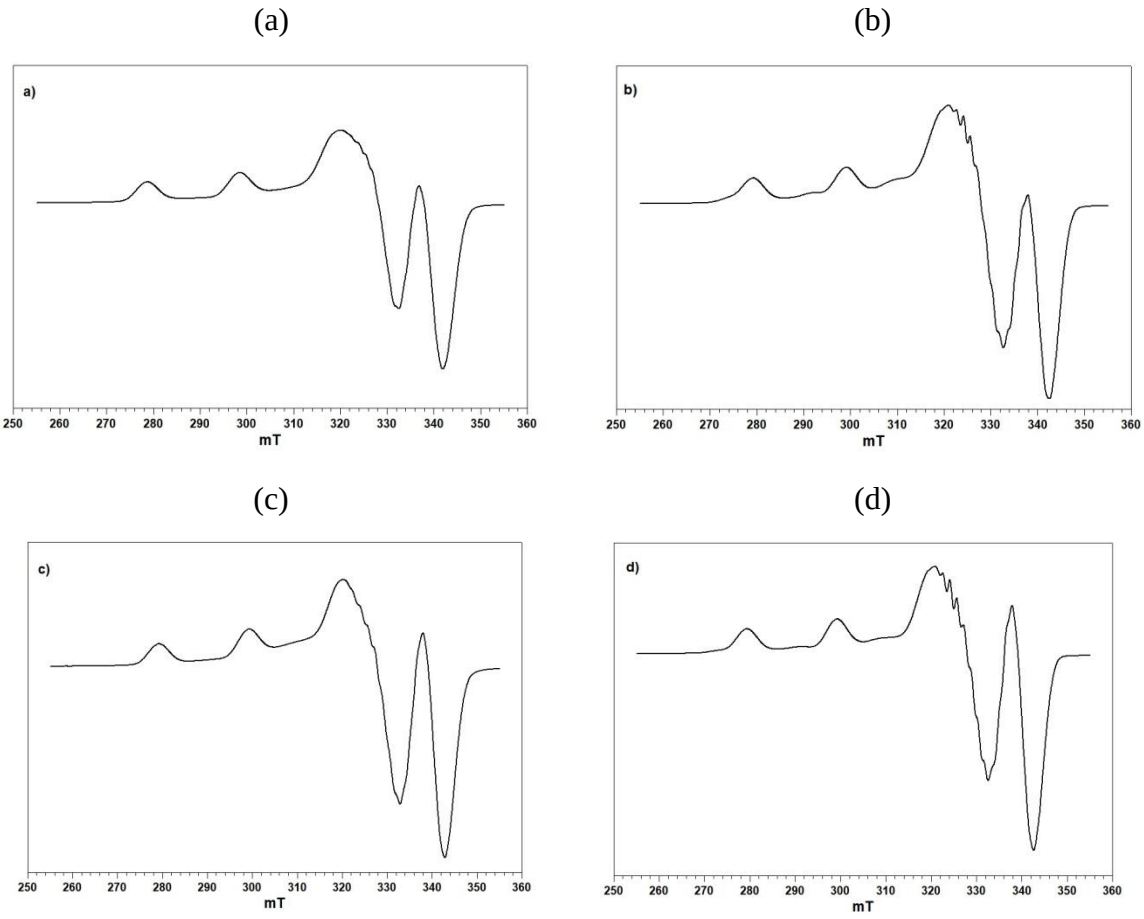

Figure 5.3: LT EPR spectra of (a) Cu-GLH, (b) Cu-Sar-LH, (c) Cu-GFH and (d) Cu-Sar-FH in frozen aqueous solution at pH 7-8.

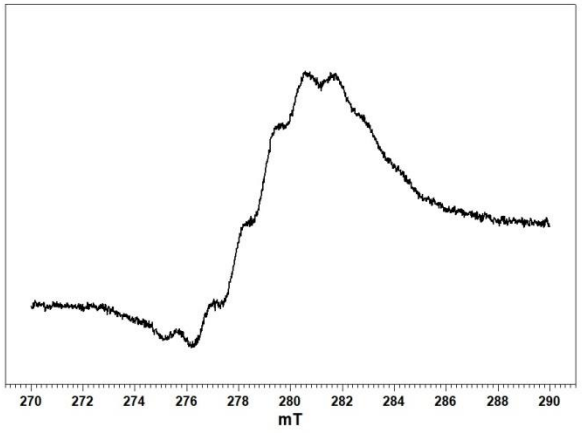

Figure 5.4: LT EPR 2nd derivative spectrum of the lowest magnetic field feature of Cu-GFH in frozen aqueous solution at pH 7-8.

The results from the EPR spectra suggest that for Cu-Sar-LH, Model 3 from the potentiometric section is the correct model, since this model contains the MLH, ML and MLH_{-2} species. The

results also confirmed the findings of both the potentiometric and UV-Vis sections that the MLH_{-2} species is present in all four of the copper(II) complexes, with a square planar CuN_4 chromophore.

5.4 Conclusion

At pH 7 all four ligands form a macrochelate with copper(II) by using their nitrogen atoms as donor atoms to form an MLH_{-2} species with a CuN_4 chromophore. All the isotropic and anisotropic parameters (obtained at pH 7) between the complexes are similar and any differences fall within the experimental error. This suggests that all four ligands behave in the same manner when forming the MLH_{-2} species with the copper(II) ions (starting at approximately pH 5). Their magnetic parameters suggest the formation of a square planar stereochemistry for the MLH_{-2} species.

At pH 5 only the EPR spectrum of the Cu-Sar-LH system was resolved into a total of three species, with the one being the MLH_{-2} species. Using the isotropic magnetic parameters, the other two were suggested to be an ML species with a CuN_2O_2 chromophore and an MLH species. This suggested that Model 3 for Cu-Sar-LH of the potentiometric section is the correct model.

5.5 References

1 J. A. Weil and J. R. Bolton, *Electron Paramagnetic Resonance: Elementary Theory and Practical Applications*, John Wiley & Sons, Inc., Hoboken, Jew Jersey, 2nd edn., 2007.

2 G. R. Eaton and S. S. Eaton, in *Comprehensive Coordination Chemistry II*, Elsevier, 2003, pp. 37–48.

3 M. S. Jahan, in *UHMWPE Biomaterials Handbook*, Elsevier, 2016, pp. 668–692.

4 J. G. Speight, in *Environmental Inorganic Chemistry for Engineers*, Elsevier, 2017, pp. 231–282.

5 L. J. Berliner, Ed., *In Vivo EPR (ESR)*, Springer US, Boston, MA, 2003, vol. 18.

6 D. T. Petasis and M. P. Hendrich, in *Quantitative Interpretation of Multifrequency Multimode EPR Spectra of Metal Containing Proteins, Enzymes, and Biomimetic Complexes*, 2015, pp. 171–208.

7 R. Cammack, in *Encyclopedia of Spectroscopy and Spectrometry*, Elsevier, 1999, pp. 457–469.

8 A. Lund and T. Vänngård, Note on the Determination of the Principal Fine and Hyperfine Coupling Constants in ESR, *J. Chem. Phys.*, 1965, **42**, 2979–2980.

9 R. P. Bonomo and F. Riggi, Study of angular anomalies in the X-band powder EPR spectra of copper (II) complexes with axial symmetry, *Lett. al Nuovo Cim.*, 1981, **30**, 304–310.

10 R. P. Bonomo and F. Riggi, Determination of the perpendicular magnetic parameters for Cu(II) EPR spectra from angular anomalies, *Chem. Phys. Lett.*, 1982, **93**, 99–102.

11 B. J. Hathaway and D. E. Billing, The electronic properties and stereochemistry of mono-nuclear complexes of the copper(II) ion, *Coord. Chem. Rev.*, 1970, **5**, 143–207.

6. Nuclear Magnetic Resonance Spectroscopy

6.1 Introduction

In the present study, there are two issues which proton nuclear magnetic resonance spectroscopy (^{1}H NMR) can help to solve. Firstly, the correct model for each Cu-GLH, Cu-Sar-LH, Cu-GFH and Cu-Sar-FH complex has not been confirmed and secondly, once the correct model has been identified, the coordination mode for each species needs to be determined.

Copper(II) is a paramagnetic metal ion and can thus affect both the chemical shifts and relaxation rates of the ligand nuclei. This is because it will have strong interactions between the unpaired electron of copper(II) and the magnetic dipoles of the nuclei of the ligand.[1,2] These interactions can be described as a through-bond effect and a through-space effect. The through-bond effect is a Fermi contact interaction, while a through-space effect is a dipolar interaction. As copper(II) coordinates to the ligand, the dipolar interaction causes the relaxation rates to increase and hence causes the ^{1}H NMR signals to broaden. The increase in the relaxation rates are dependent on the distance between the nuclei of the ligand and the copper(II) ion, and so the closer the signals are to the binding sites, the more they broaden.[3–8]
To be exact, the transverse relaxation time (T_2) determines the line width of the peaks, which is defined as:

$$T_2 = \frac{1}{\pi W_{\frac{1}{2}}} \tag{6.1}$$

where $W_{1/2}$ is the line width at half height.[9]

The technique to view the broadening of the ^{1}H NMR signals is to titrate the ligands with copper(II) at a predetermined pH. This will cause the ^{1}H NMR signals to broaden at a slow rate, which will make it visually convenient for a structural analysis. This is possible because NMR is a relatively slow spectroscopic technique, where the relaxation rates are in minutes, while the reactions for copper(II) exchange are fast. This means that the average is seen

between the free and bound ligand spectrum, which consequently causes the signals to only broaden gradually.[5]

6.2 Experimental

For the ^{1}H NMR spectra, a 0.005 M solution for all ligands was prepared using 90 % Milli-Q water (18.2 MΩ.cm) and 10 % D_2O (99.9 % isotopic purity, Sigma-Aldrich). Tertiary butyl alcohol was added as an internal reference and the pH was adjusted using NaOH/HCl. The pH of each solution was recorded with an accuracy of 0.1 using a Crison micropH 2000 pH meter, which is equipped with a Ω metrohm glass electrode.

For the complexes, pH values were chosen in accordance with the species distribution diagrams, firstly to verify the existence of an MLH species for each copper(II) complex and secondly to correspond to the maximum concentration of each single species. A copper(II) solution of 0.05 M was prepared using 90 % Milli-Q water and 10 % D_2O. The 0.05 M copper(II) solution was titrated in increments of 10 µl into each of the different pH solutions for all four ligands. After each titration, the pH of the solution was checked and kept constant. The ^{1}H NMR spectra were recorded on a Bruker 300 MHz spectrometer and processed using Bruker Topspin software, version 4.0.7. The residual water peak was suppressed using excitation sculpting.

For the 1d Total Correlation Spectroscopy (TOCSY) NMR spectra, 0.001 g of GLH was weighed out and added to 0.9 ml of Milli-Q water and 0.1 ml of D_2O. A phosphate buffer was also added, and the pH was adjusted to 4.5 using NaOH/HCl. The TOCSEY spectra were recorded on a Bruker 600 MHz spectrometer (Bruker, United States) and processed using Bruker Topspin software, version 4.0.7.

6.3 Results and Discussion

6.3.1 Protonation of ligands

Before the ligands are titrated with copper(II), an analysis on the chemical shifts is needed. As the pH changes and protonation occurs, the chemical shifts will be affected. Potentiometric titrations verified that the available sites for protonation of the four ligands are the amine, the imidazole and the carboxyl groups. These chemical shifts are necessary, so that the effect copper(II) has on the spectrum can be analysed.

The ^{1}H NMR spectrum for each ligand and its proton assignment can be seen in Figures 6.1-6.4. The chemical shifts for the protonation of the amine and imidazole groups can be seen, but the pH range does not go low enough to detect the protonation of the carboxyl groups. For the protonation of the amine, peak **j** in GLH, peaks **j** and **k** in Sar-LH, peaks **h** and **h′** in GFH, as well as peaks **h**, **h′** and **i** in Sar-FH, shifted towards a lower ppm as the pH increased. This chemical shift signalled that there is an increase in shielding, which verifies that the amine group has been protonated. For the imidazole protonation, peaks **a** and **a′** in all four ligands also shift towards a lower ppm as the pH increases, which verifies the imidazole protonation.

(a)

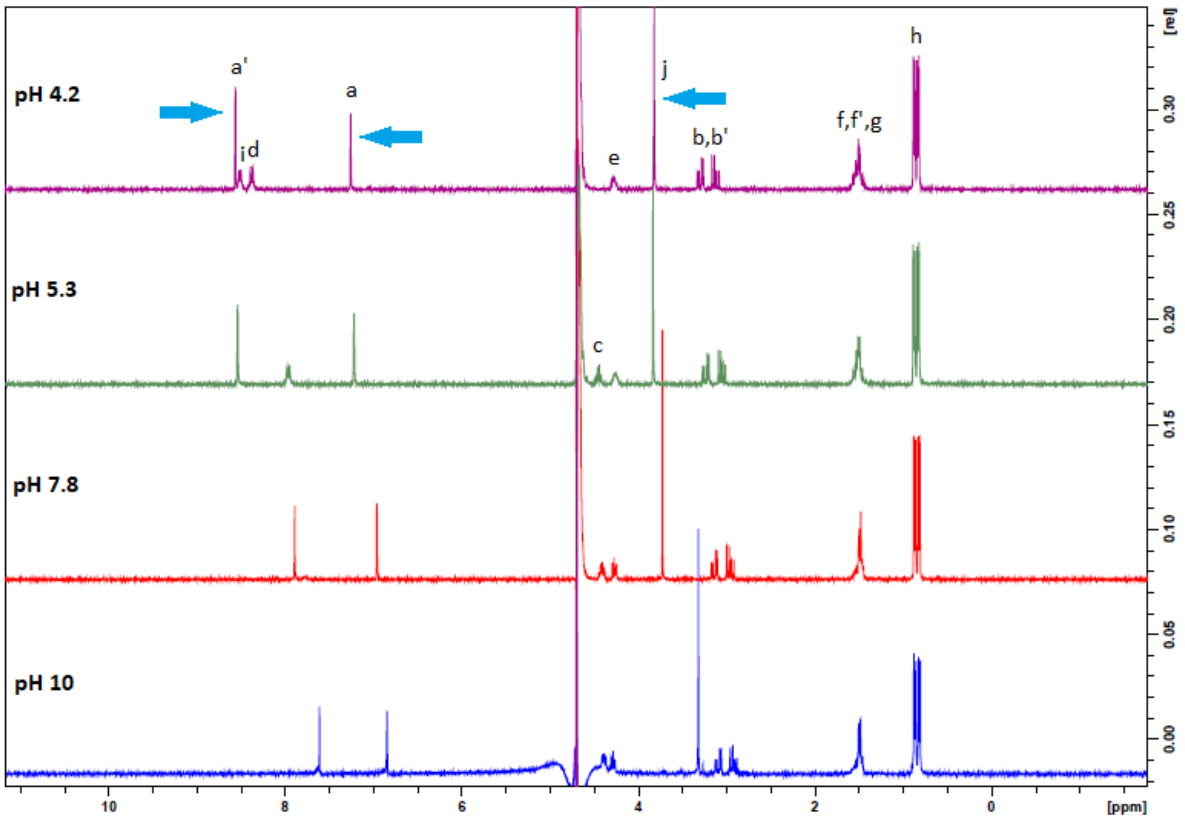

(b)

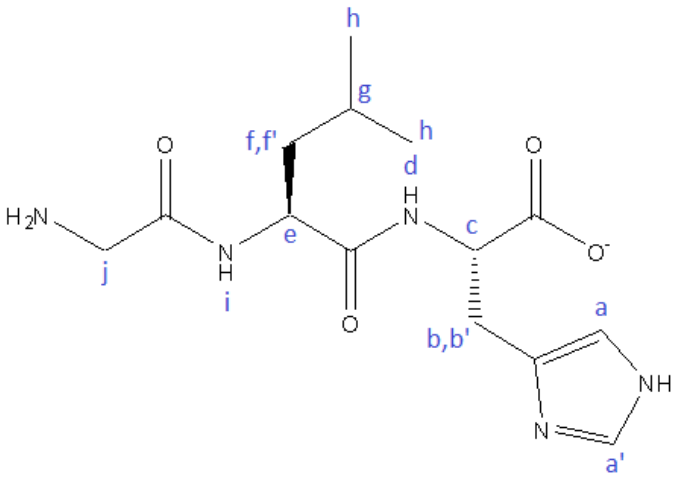

Figure 6.1: (a) ^{1}H NMR spectra of GLH at increasing pH values from 2-11. An arrow has been added to indicate the shifting of peaks **a**, **a′** and **j** over increasing pH values. (b) The proton assignments.

(a)

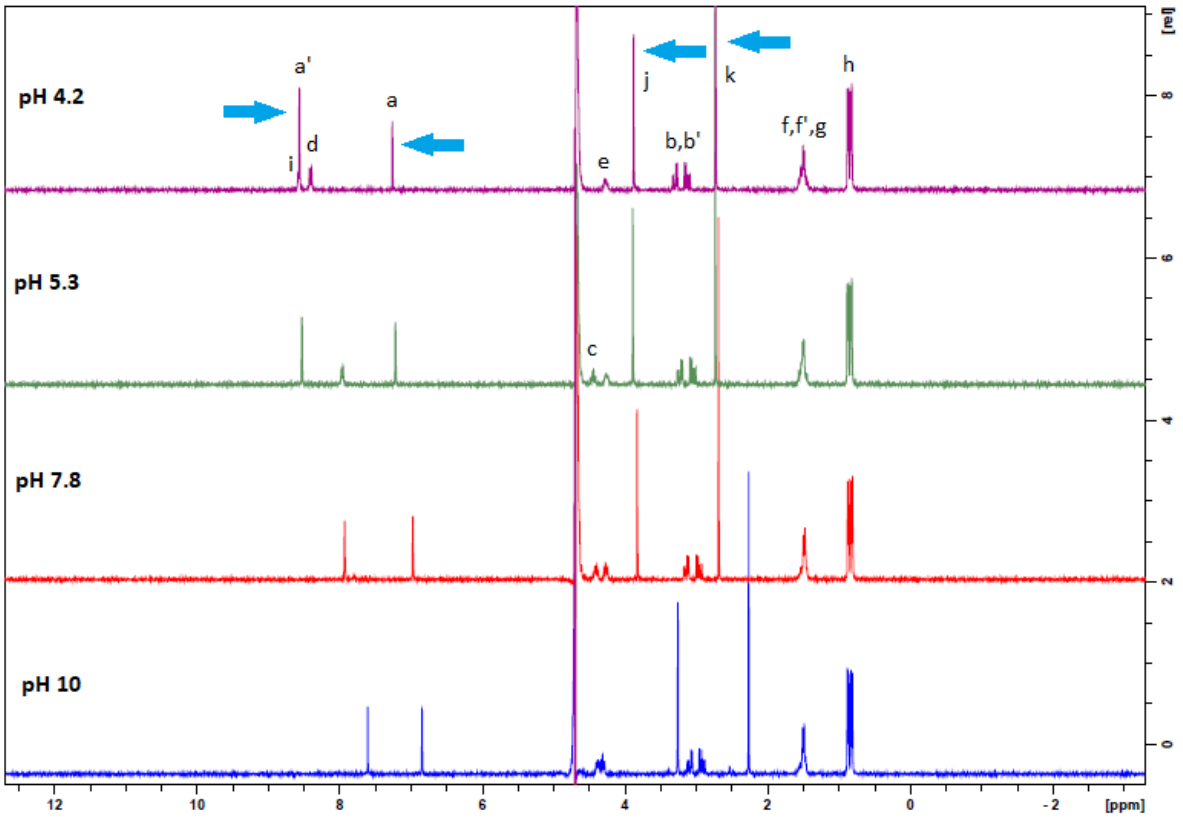

(b)

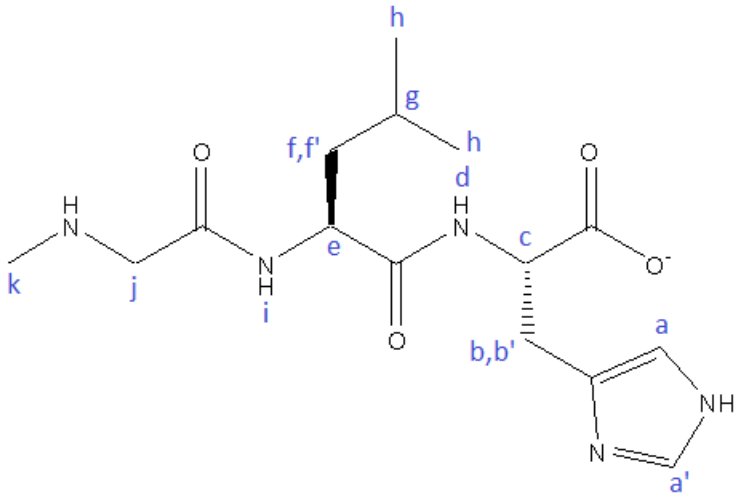

Figure 6.2: (a) ^{1}H NMR spectra of Sar-LH at increasing pH values from 2-11. An arrow has been added to indicate the shifting of peaks, **a**, **a′**, **j** and **k** over increasing pH values. (b) The proton assignments.

(a)

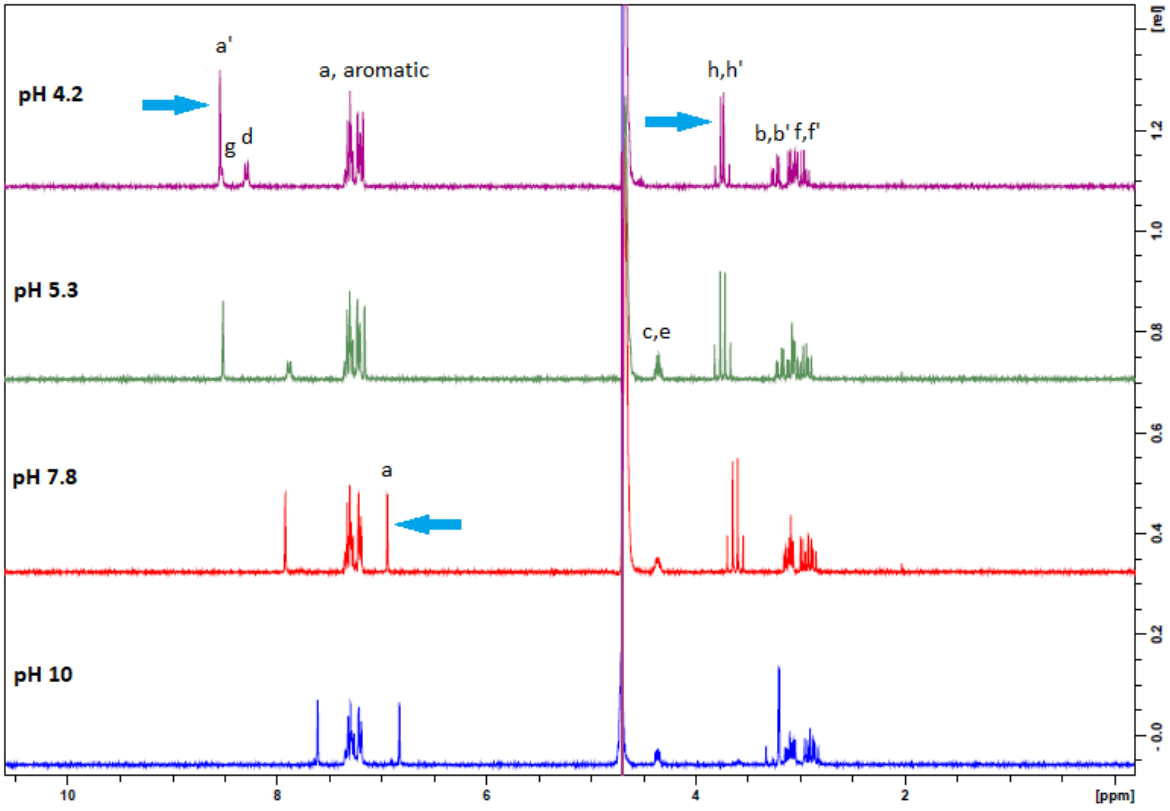

(b)

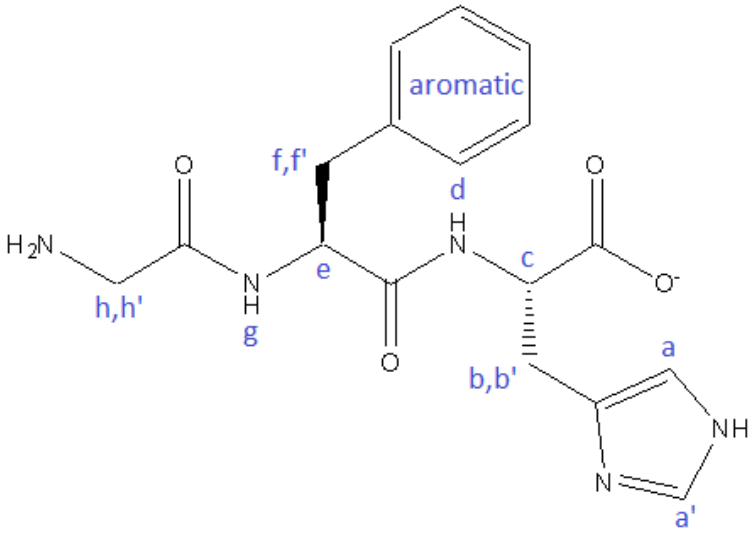

Figure 6.3: (a) ^{1}H NMR spectra of GFH at increasing pH values from 2-11. An arrow has been added to indicate the shifting of peaks **a**, **a′**, **h** and **h′** over increasing pH values. (b) The proton assignments.

(a)

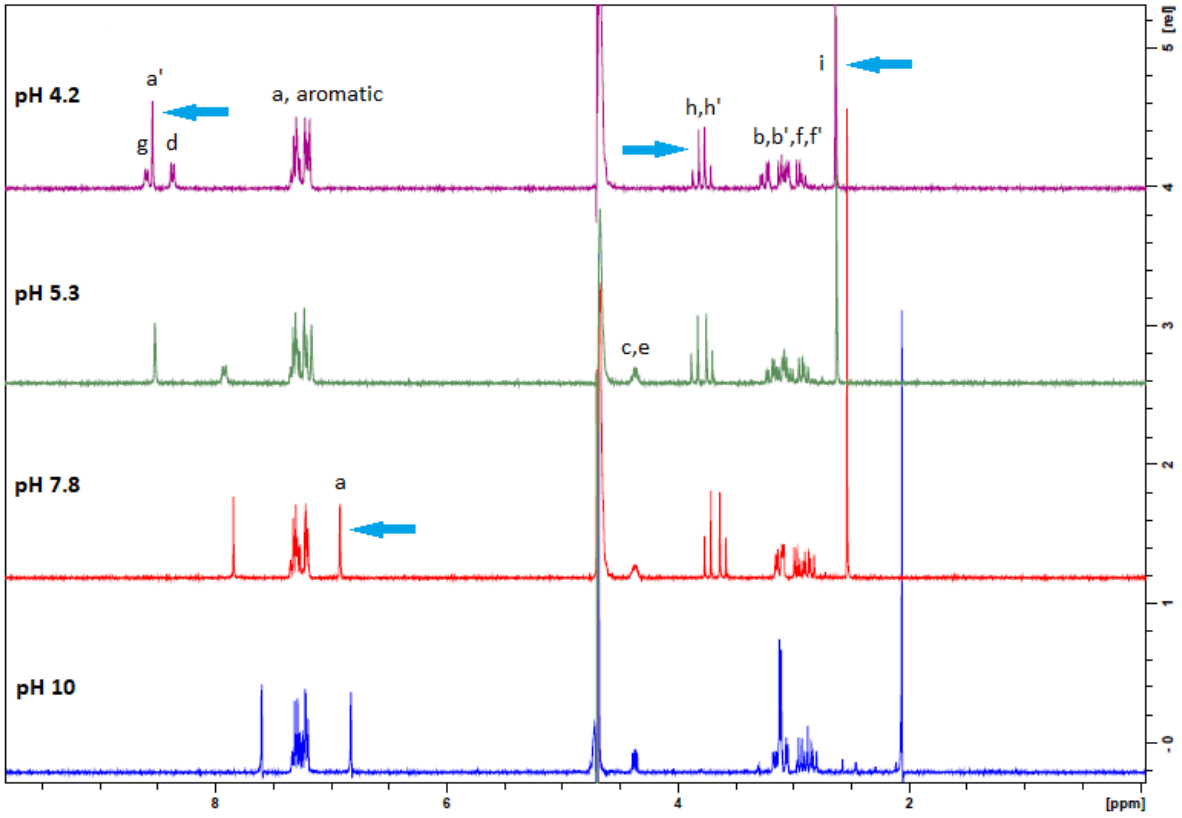

(b)

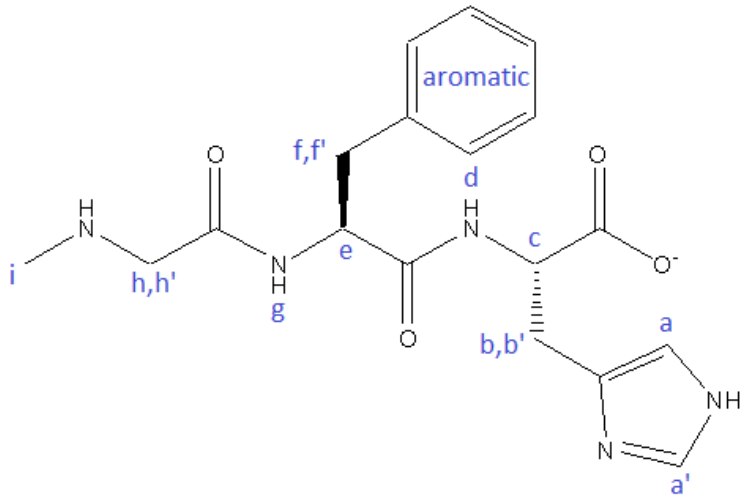

Figure 6.4: (a) ^{1}H NMR spectra of Sar-FH at increasing pH values from 2-11. An arrow has been added to indicate the shifting of peaks **a**, **a′**, **h**, **h′** and **i** over increasing pH values. (b) The proton assignments.

Figures 6.5a-d show the change in chemical shifts for selected protons in GLH, Sar-LH, GFH and Sar-FH respectively as a function of pH. As expected, the peaks marked with arrows in Figures 6.1-6.4 undergo the biggest shift and display inflection points. From the inflection points of these curves, the protonation stepwise formation constants can be estimated. These estimated stepwise formation constants agree with the potentiometric results and a summary can be seen in Table 6.1.

(a)

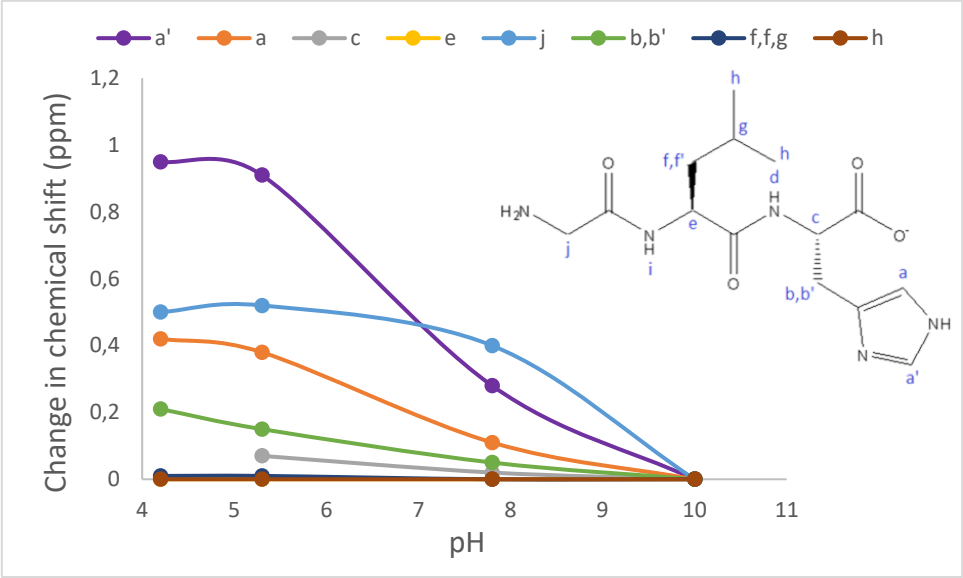

(b)

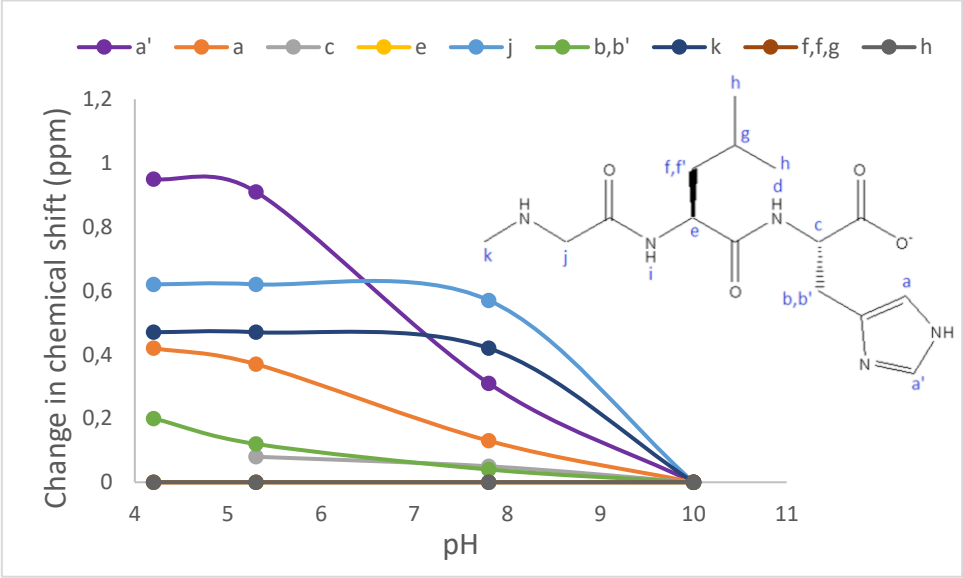

(c)

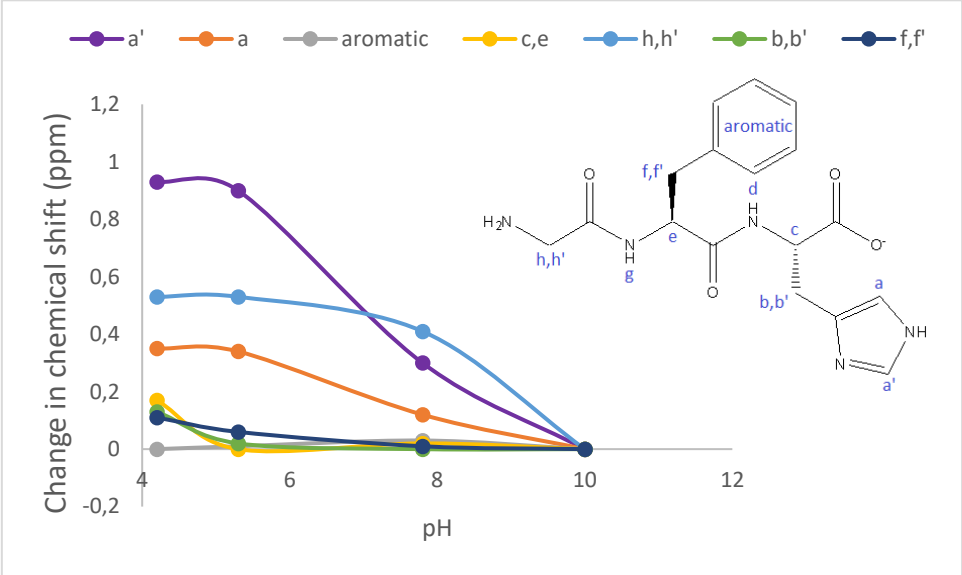

(d)

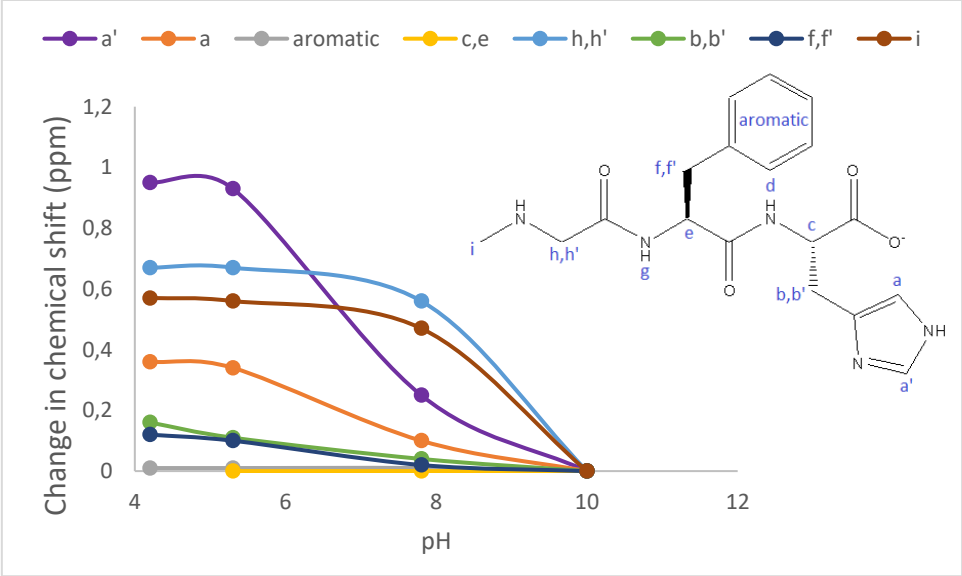

Figure 6.5: The change in ^{1}H chemical shift as a function of pH for (a) GLH, (b) Sar-LH, (c) GFH and (d) Sar-FH.

Table 6.1: Estimated stepwise formation constants found from the inflection points of the ^{1}H chemical shifts in Figure 6.5a-d.

Ligand	**Protonation**	**Estimated stepwise formation constants for each peak**					**Potentiometric stepwise formation constants**
		a,a′	**j**	**k**	**h,h′**	**i**	
GLH	LH LH_2	 6.8	8.8				8.21 6.89
Sar-LH	LH LH_2	 6.8	8.8	8.8			8.45 6.87
GFH	LH LH_2	 6.9			8.6		7.95 6.87
Sar-FH	LH LH_2	 6.9			8.8	8.8	8.22 6.87

Looking at Figures 6.1-6.4, the exchange rates of the amine protons are fast and therefore these protons cannot be seen. In contrast the exchange of amide protons for GLH and Sar-LH (peaks **d** and **i)** and for Sar-FH and GFH (peaks **d** and **g**) are slower and thus can be seen at low pH values. However, as the pH increases the amide protons are lost as the exchange rate increases. As an observation, the proton from peak **g/i** exchanges more quickly with the solvent than the proton from peak **d**, and therefore disappears before peak **d**.

For all the ligands, the amide proton peaks **d** and **g/i** were indistinguishable from each other and so a TOCSY NMR was carried out to differentiate between the signals. The proton signals with the assignments of **c** and **e** were also indistinguishable from each other. Conveniently the signal labelled **c** is next to the histidine amide group and the signal labelled **e** is next to the leucine/phenylalanine amide group. This means that the same 1D TOCSY NMR spectra that are used to assign peaks **d** and **g/i**, will be able to differentiate between peaks **c** and **e.** This analysis can be seen in Figure 6.6 and since all the ligands contain both amide groups, as well as peaks **c** and **e**, the random selection of GLH was chosen for the analysis.

(a)

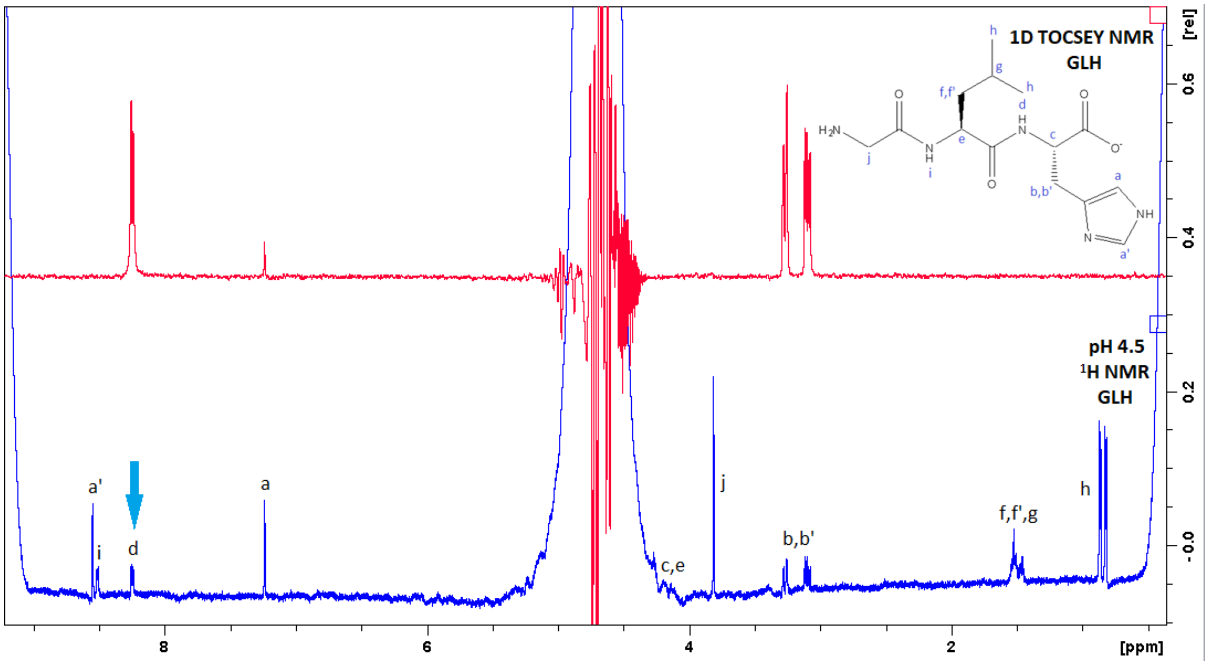
1D TOCSEY NMR
GLH
pH 4.5
¹H NMR
GLH
a'
i
d
a
c,e
j
b,b'
f,f',g
h
[ppm]
[rel]

(b)

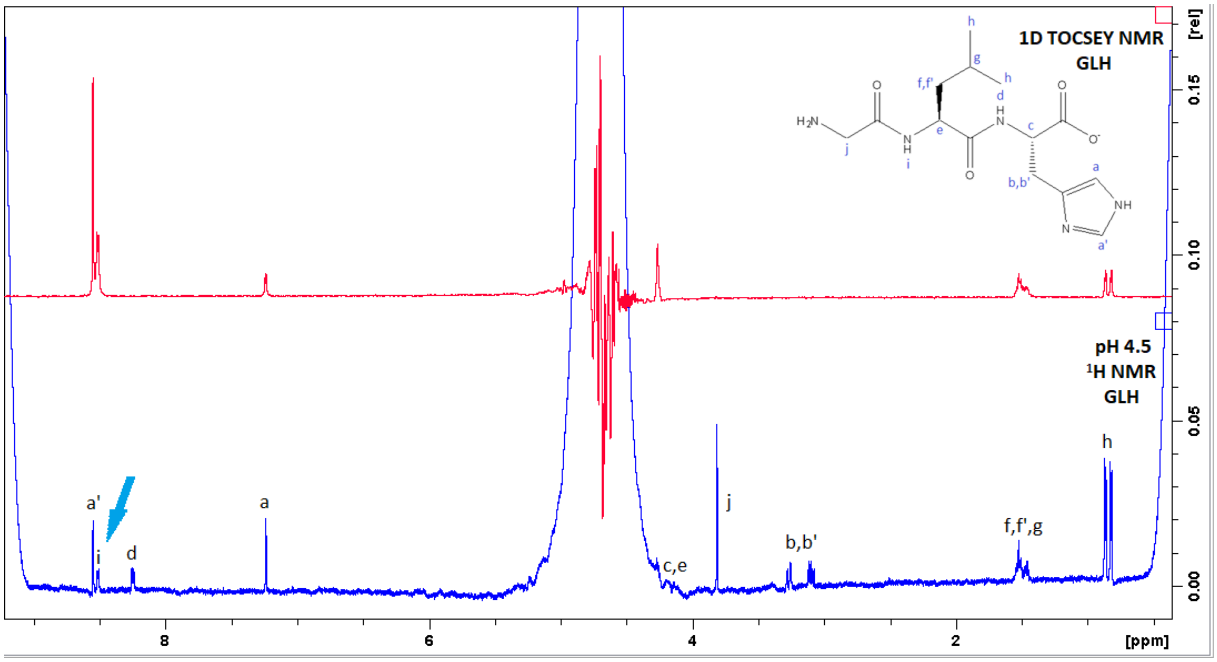
1D TOCSEY NMR
GLH
pH 4.5
¹H NMR
GLH
a'
i
d
a
c,e
j
b,b'
f,f',g
h
[ppm]
[rel]

(c)

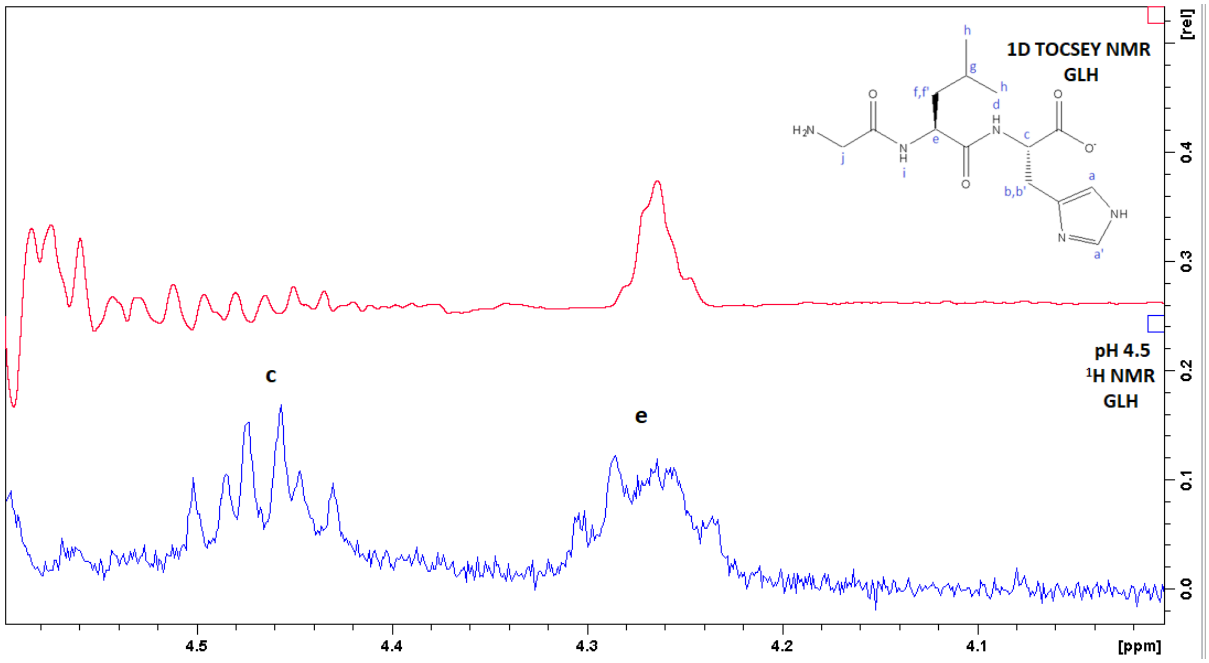

Figure 6.6: 1D selective gradient TOCSY NMR spectra (red) and ^{1}H NMR spectra (blue) of GLH at pH 4.5. (a) full spectrum of the irradiated amide-NH peak **d** at 8.246 ppm, (b) full spectrum of the irradiated amide-NH peak **i** at 8.511 ppm and (c) section of the spectrum of the irradiated amide-NH peak **i** at 8.511 ppm. An arrow has been added to indicate the irradiated amide-N.

The 1D spectrum of the TOCSY NMR, which has a mixing time of 120 ms, produces through bond correlations via spin-spin coupling and these correlations are seen over the whole coupling network. Distant protons, up to 5 or 6 bonds away, can be seen as long as there is coupling between each intervening proton and the transfer is not disrupted by zero proton-proton couplings or hetero-atoms.[10] If there is coupling, magnetization will be transferred and the intensity of the peaks corresponding to the affected protons will increase. The intensity is proportional to the distance travelled, so further protons will produce less intense peaks. If there is a disruption in the transfer, then the unaffected protons will produce close to zero intensity peaks.

In Figure 6.6a, amide-NH peak **d** is irradiated which affects peaks **b** and **b′**, while peaks **j**, **h**, **f, f′** and **g** are not affected. Since the magnetic transfer is disrupted by the carbonyl groups, the amide that is affected in Figure 6.6a belongs to the histidine amino acid and therefore peak **d** is assigned to this amide. In Figure 6.6b, the amide-NH peak **i** is irradiated, which should

belong to the leucine amino acid. As expected, peaks **b, b′** and **j** disappear and peaks **h, f, f′** and **g** are slightly affected, since these protons are further away but still connected to the coupling network. In both spectra peaks **a** and **a′** are also slightly affected; this is because they overlap the amide peaks and therefore have the same frequency as the amide groups. In Figure 6.6a, peaks **c** and **e** are hidden by the water peak in the TOCSY NMR spectrum, but in Figure 6.6b they are visible, so an expansion that focuses on this region of the spectrum can be seen in Figure 6.6c. Looking at Figure 6.6c, in the TOCSY NMR spectrum the second peak is affected, which means that this is peak **e**.

6.3.2 Titration with copper(II)

All the species distribution diagrams for each model of Cu-Sar-LH, Cu-GLH, Cu-Sar-FH and Cu-GFH have been added in Figures 6.7, 6.11, 6.15 and 6.18 respectively for convenience. At this point, it has been confirmed by the potentiometric titrations, UV-Vis and EPR that the MLH_{-2} species is present at high pH values for all four copper(II) complexes. EPR has also suggested that for Cu-Sar-LH, there is an MLH and ML species. An ^{1}H NMR analysis will try to verify and build on this information.

The species involved in the process of identifying the correct model for each complex are the MLH, ML and MLH_{-1} species. The MLH_{-2} species is not considered for now because it is in every model. Looking at the speciation diagrams for each model, the MLH, ML and MLH_{-1} species start forming at different pH values. Going from a low to high pH, the MLH species is the first to start forming at approximately pH 3.5, then the ML species start forming usually just before pH 4, while the MLH_{-1} species start forming usually just after pH 4. Therefore, the method used to try and identify which species are present and hence find the correct model, is to lower the pH to a point were only the MLH species is meant to occur. At this pH the ligands will be titrated with copper(II) and if signals in the ^{1}H NMR diagram broaden in comparison to the respective ligand ^{1}H NMR spectrum, it means that an MLH species is present. The coordination mode of the MLH species can also be found from the spectrum.

It is also possible to find the coordination mode of the MLH_{-2} species since it is the only species present at high pH values, but finding the coordination modes of the ML and MLH_{-1} species, should they be present, is not as easy because they overlap with the other species.

Since titrating the ligands with copper(II) does not give a 1:1 copper(II) ligand ratio, it is a concern that at different ratios other species types besides MLH, ML, MLH_{-1} and MLH_{-2} might be present or that their distribution will be different. Therefore, for all the ^{1}H NMR data, copper(II) was added until it reached a 1:1 copper(II) ligand ratio, so that any change in the spectrum could be observed. For all spectra below, besides the expected further broadening of peaks, no change was observed and so this analysis can be used to verify the species present in this study and their coordination modes.

6.3.2(a) Cu-Sar-LH

Looking at Figure 6.7, only Models 2, 3 and 4 have an MLH species, and at a pH of 3.5 the MLH species is the only species present. As a result, the pH of the Sar-LH solution was lowered to 3.5 and titrated with copper(II), and the resulting ^{1}H NMR spectrum can be seen in Figure 6.8. If the ^{1}H NMR spectrum showed signs of broadened peaks, then it would signify that the MLH complex species has formed and either Model 2, 3 or 4 is correct. If the ^{1}H NMR spectrum had no broadened peaks and simply resembled only the ligand, then it would signify that the MLH species is not present and that Model 1 or 5 is correct. Looking at Figure 6.8, peaks have broadened, which signifies that the MLH species is present. This agrees with the EPR results. More specifically, peaks **a**, **a′**, **b**, **b′** and **c** broaden, which suggests that copper(II) is coordinating to the imidazole-N and to the carboxyl-O, while the amine-N is protonated. Peaks **j** and **k** also broaden more than the reference peak, which suggests that copper(II) is also coordinating to the amine-N and carbonyl-O of leucine, while the imidazole-N is protonated. This suggests that in MLH, copper(II) coordinates at two different locations of the ligand. As was discussed in the potentiometric titrations section, this ‘double-sided’ coordination has been suggested in literature.[11]

The analysis of the MLH_{-2} ^{1}H NMR spectrum was carried out at the physiological pH of 7.4 and can be seen in Figure 6.9. All the peaks, besides peak **a** and **a′**, do not appear to broaden more than the others or do not broaden at all. This observation can be explained by a decrease in the exchange rate. At high pH values, the rate of exchange decreases to an extent where the individual spectra of the free ligand and the complex are seen. Since the line widths of the complex are so broad (457 Hz)[12], the spectrum will appear in the baseline. This then results in the peaks appearing to sharpen instead of broaden, since only the spectrum of the free ligand

is seen.[13–15] This means that ^{1}H NMR cannot be used to identify the coordination mode of the MLH_{-2} species. This was also observed in literature.[16–19]

At pH 5 (Figure 6.10), there is more than one species present in solution and therefore the broadening of the peaks is due to all the species present. As expected, in Figure 6.10 all the peaks broaden except for **f**, **f′**, **g** and **h**, which means that copper(II) is potentially coordinating to each coordination site. From the information that is already known, this most likely represents the 'double-sided' coordination of the MLH species, as well as the MLH_{-2} species.

Analysing and confirming the presence of the ML or MLH_{-1} species is not possible, because ML and MLH_{-1} overlap with the other species and therefore cannot be analysed as a single species. ^{1}H NMR thus cannot further distinguish between Models 2, 3 and 4, but as mentioned previously, the EPR data have identified the presence of the MLH, ML and MLH_{-2} species, and so since the ^{1}H NMR data agree with the MLH species, Model 3 can remain as the proposed model for Cu-Sar-LH. This also agrees with the potentiometric titrations, since Model 3 was signalled out as having the 'best fit' between the theoretical and experimental functions, as well as having one of the lowest standard deviations and Hamilton R factors.

(a)
MLH_{-1}, MLH_{-2}

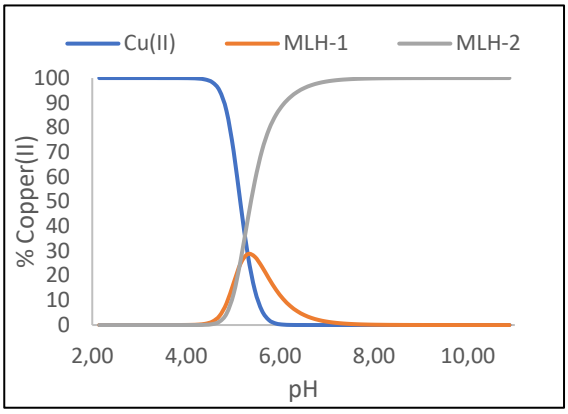

(b)
MLH, MLH_{-1}, MLH_{-2}

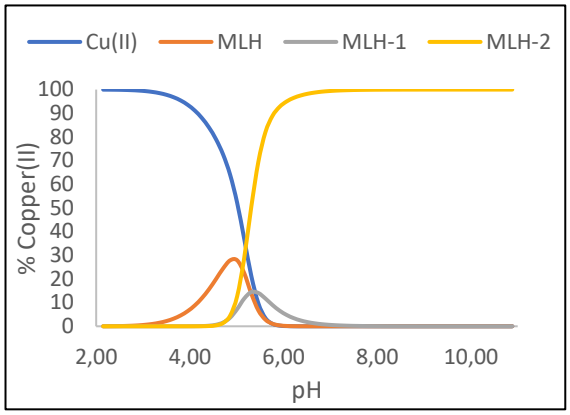

(c)
MLH, ML, MLH_{-2}

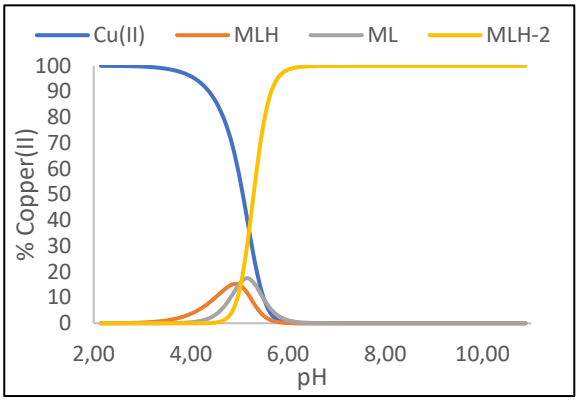

(d)
MLH, MLH_{-2}

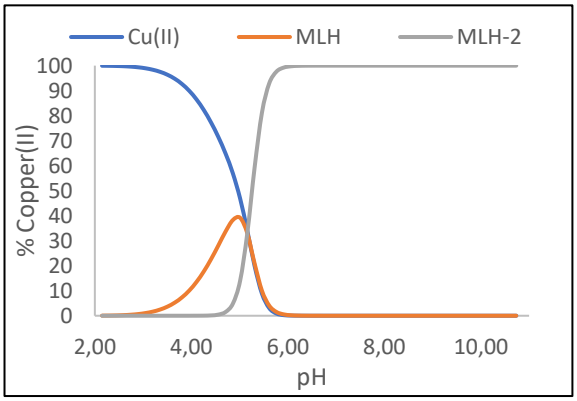

(e)
ML, MLH_{-2}

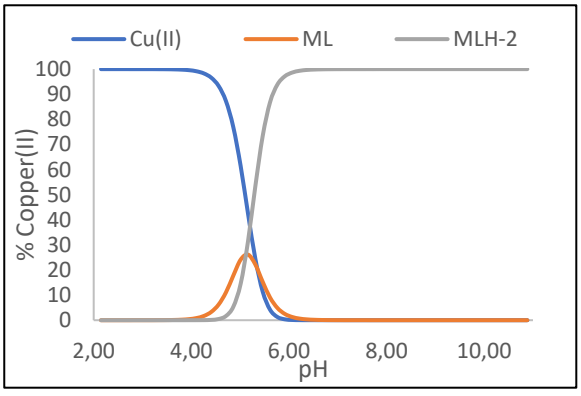

Figure 6.7: Complexation species distribution curve for the 1:1 ratio of copper(II) and Sar-LH (a) Model 1 (MLH_{-1}, MLH_{-2}), (b) Model 2 (MLH, MLH_{-1}, MLH_{-2}), (c) Model 3 (MLH, ML, MLH_{-2}), (d) Model 4 (MLH, MLH_{-2}) and (e) Model 5 (ML, MLH_{-2}) at 25 ^{o}C in 0.15 mol.dm^{-3} of NaCl.

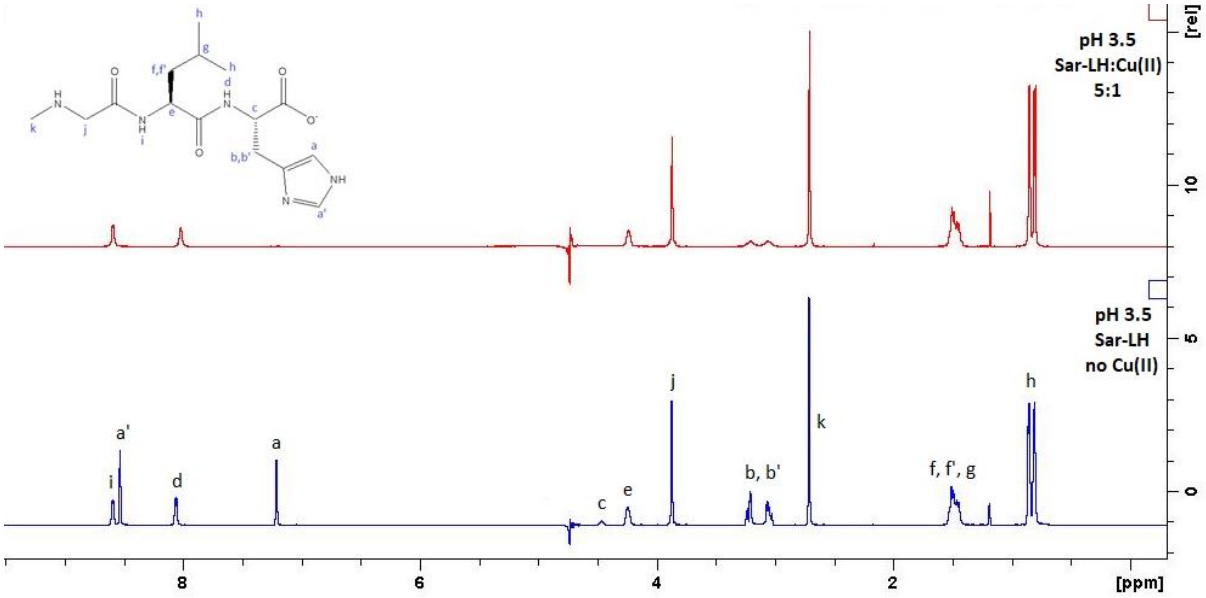

Figure 6.8: The ^{1}H NMR spectra (blue) of the ligand Sar-LH and the ^{1}H NMR spectra (red) after Sar-LH has been titrated with copper(II) to reach a 5:1 ligand copper(II) ratio at a pH of 3.5 in 90 % water and 10 % D_2O.

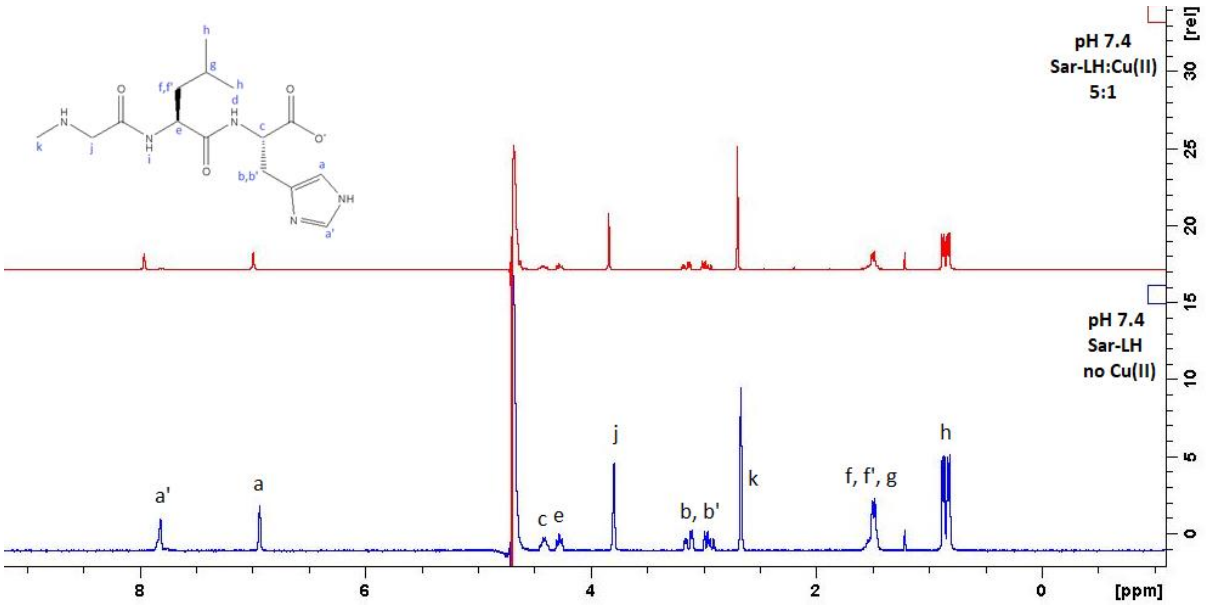

Figure 6.9: The ^{1}H NMR spectra (blue) of the ligand Sar-LH and the ^{1}H NMR spectra (red) after Sar-LH has been titrated with copper(II) to reach a 5:1 ligand copper(II) ratio at a pH of 7.4 in 90 % water and 10 % D_2O.

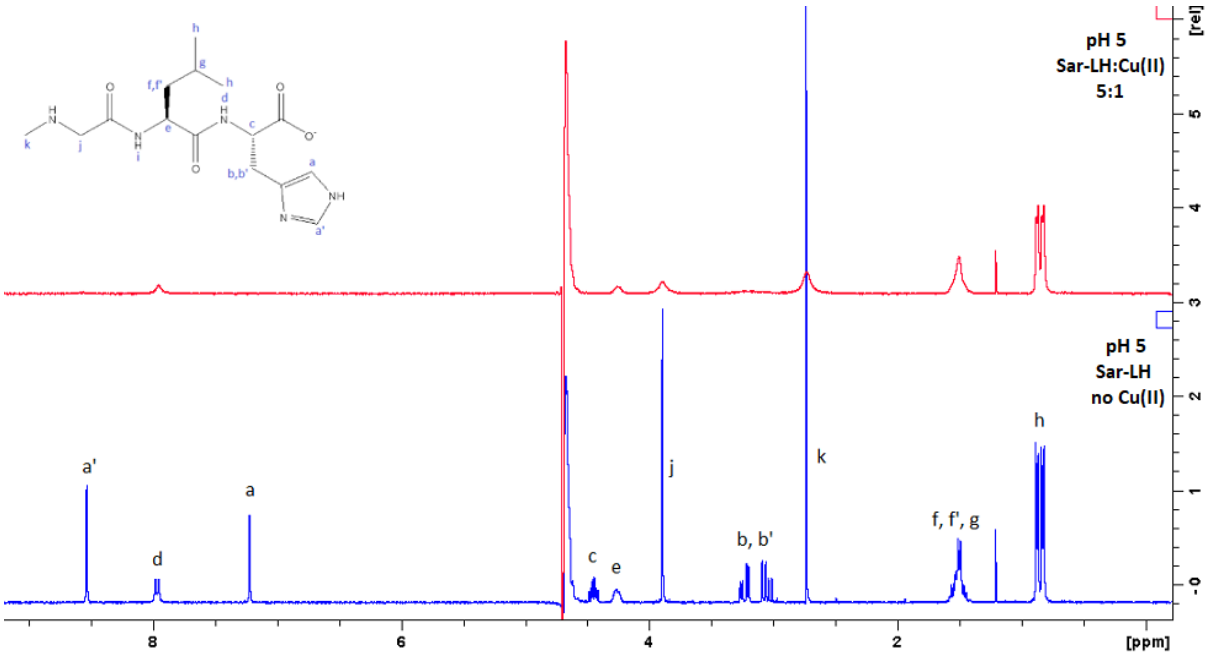

Figure 6.10: The ^{1}H NMR spectra (blue) of the ligand Sar-LH and the ^{1}H NMR spectra (red) after Sar-LH has been titrated with copper(II) to reach a 5:1 ligand copper(II) ratio at a pH of 5 in 90 % water and 10 % D_2O.

6.3.2(b) Cu-GLH

Looking at Figure 6.11, if the pH for the ^{1}H NMR spectrum is set to 3.5, then the broadening of peaks will indicate that the MLH species is present and thus select between Models 1, 3 and 6 vs Models 2, 4 and 5. The ^{1}H NMR spectrum in Figure 6.12 shows that at pH 3.5 there is a clear broadening of peaks **a**, **a′**, **b**, **b′**, **c**, and **j**, which means that either Model 2, 4 or 5 is correct and that there is an MLH species present. As with Cu-Sar-LH, the broadened peaks indicate that copper(II) is coordinating to two sites on the ligand. Peaks **a**, **a′**, **b**, **b′** and **c** suggest a coordination to the imidazole-N and carboxyl-O, with the amine-N protonated. Broadening of peak **j** suggests coordination to the amine-N and neighbouring carbonyl-O, with the imidazole-N protonated.

For the analysis of the MLH_{-2} species, increasing the pH to isolate MLH_{-2} will cause a decrease in the exchange rate, and peak sharpening would occur instead of peak broadening. So, the pH was only adjusted to 5 (Figure 6.13) where, according to the species distribution diagrams, an overlap of species occurs. All peaks except for **f**, **f′**, **g** and **h** broaden, which like Cu-Sar-LH, could represent both the MLH species and the MLH_{-2} species.

^{1}H NMR cannot further distinguish between Models 2, 4 and 5, since the presence of a possible MLH_{-1} species overlaps with MLH_{-2} and thus cannot be analysed as a single species. Additionally, the EPR data could only confirm the presence of the MLH_{-2} species, since the species were not well resolved, and the MLH_{-2} species was predominant at low pH values. Therefore, from the potentiometric results, Model 2 has been signalled out as having the 'best fit' between the theoretical and experimental functions, as well as having the lowest standard deviations and Hamilton R factors out of Models 2, 4 and 5, and therefore is the proposed model for Cu-GLH.

(a)
MLH$_{-1}$, MLH$_{-2}$

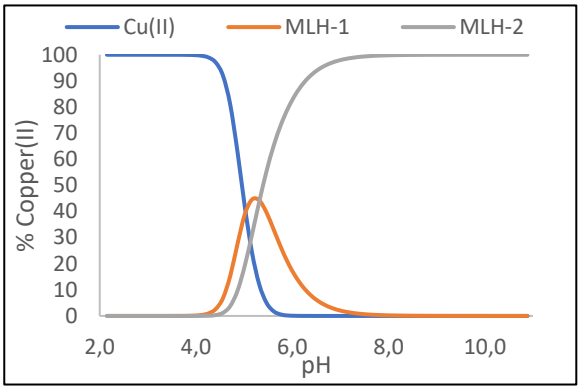

(b)
MLH, MLH$_{-1}$, MLH$_{-2}$

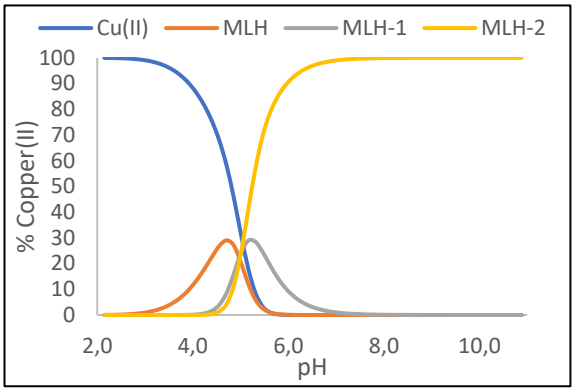

(c)
ML, MLH$_{-1}$, MLH$_{-2}$

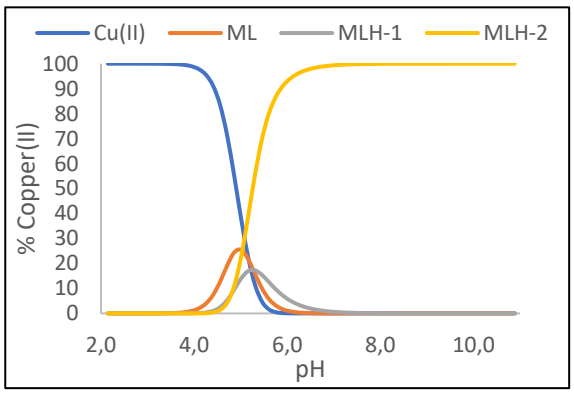

(d)
MLH, ML, MLH$_{-2}$

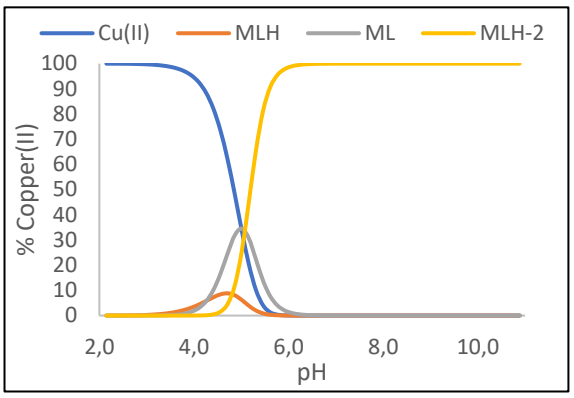

(e)
MLH, MLH$_{-2}$

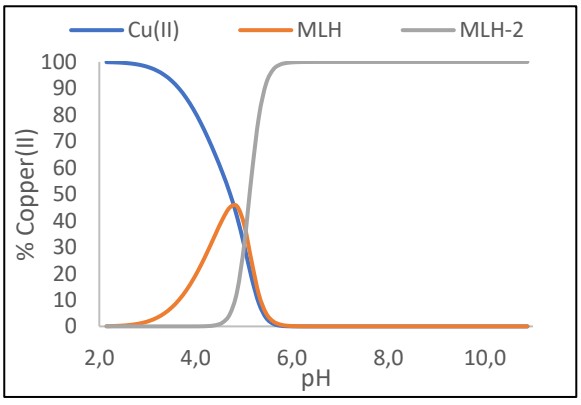

(f)
ML, MLH$_{-2}$

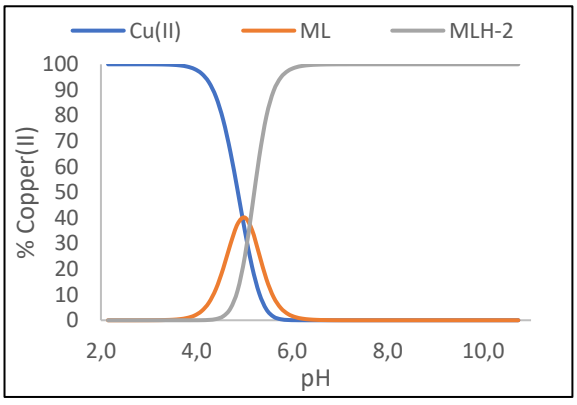

Figure 6.11: Complexation species distribution curve for the 1:1 ratio of copper(II) and GLH (a) Model 1 (MLH$_{-1}$, MLH$_{-2}$), (b) Model 2 (MLH, MLH$_{-1}$, MLH$_{-2}$), (c) Model 3 (ML, MLH$_{-1}$, MLH$_{-2}$), (d) Model 4 (MLH, ML, MLH$_{-2}$), (e) Model 5 (MLH, MLH$_{-2}$) and (f) Model 6 (ML, MLH$_{-2}$) at 25 ^{o}C in 0.15 mol.dm^{-3} of NaCl.

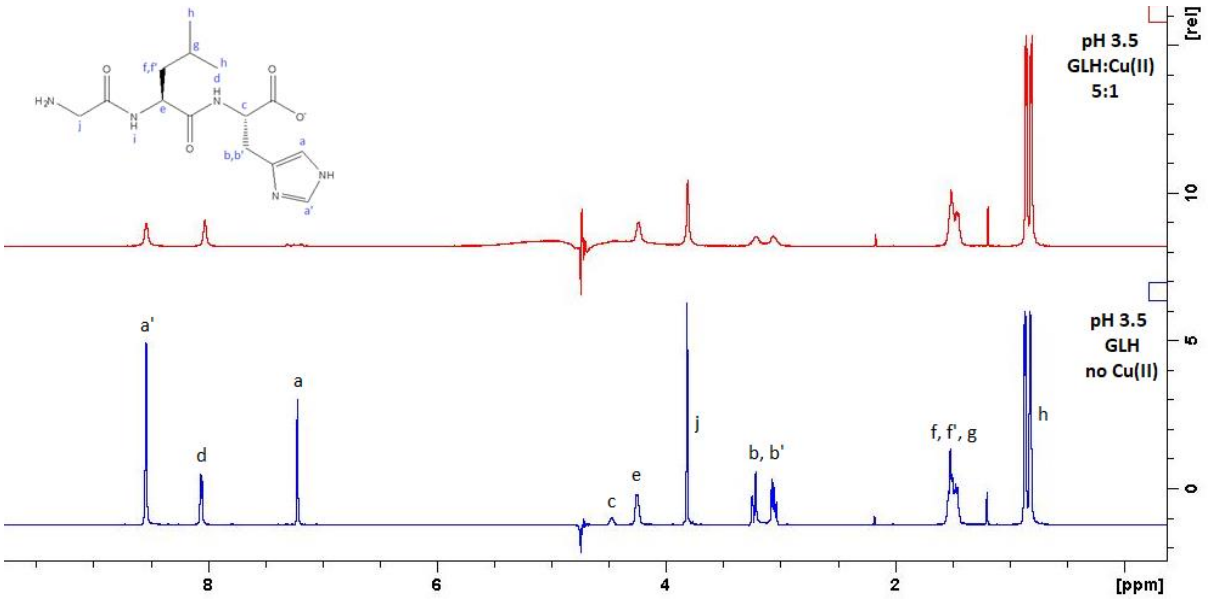

Figure 6.12: The ^{1}H NMR spectra (blue) of the ligand GLH and the ^{1}H NMR spectra (red) after GLH has been titrated with copper(II) to reach a 5:1 ligand copper(II) ratio at a pH of 3.5 in 90 % water and 10 % D_2O.

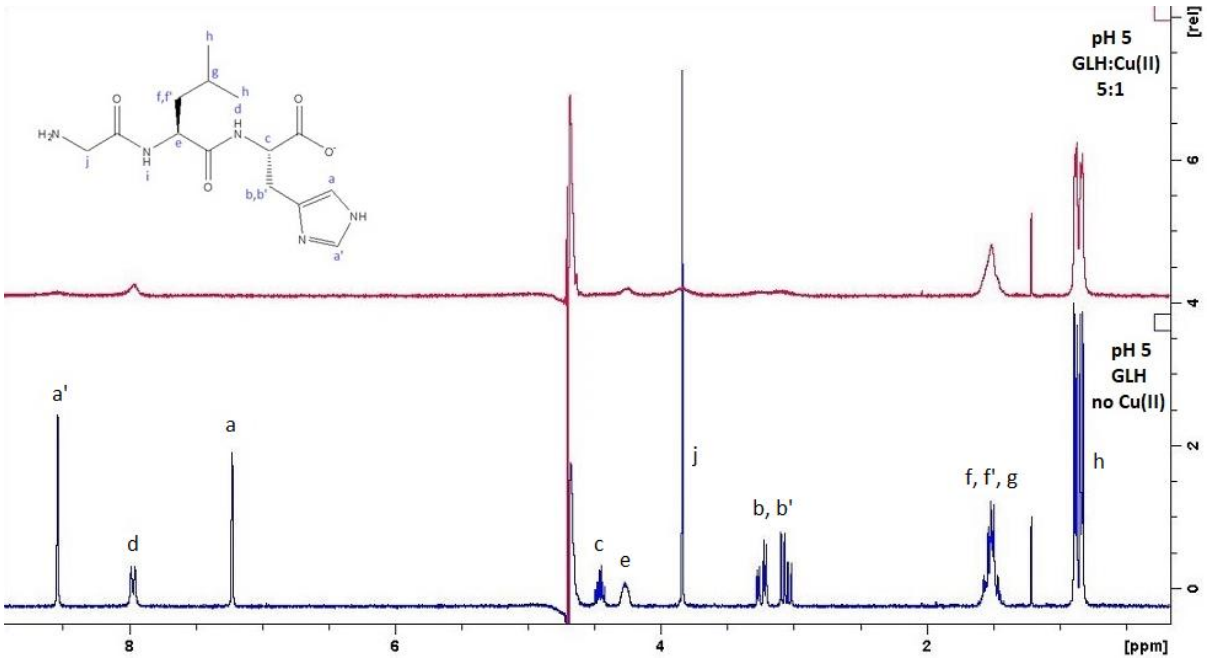

Figure 6.13: The ^{1}H NMR spectra (blue) of the ligand GLH and the ^{1}H NMR spectra (red) after GLH has been titrated with copper(II) to reach a 5:1 ligand copper(II) ratio at a pH of 5 in 90 % water and 10 % D_2O.

6.3.2(c) Cu-Sar-FH

The ligand Sar-FH has overlapping **b**, **b′**, **f** and **f′** peaks and so before an analysis is done to determine the correct model, distinguishing between these peaks is necessary. Setting the pH to 4.8 means that the species present will cause peaks **b** and **b′** to broaden, while peaks **f** and **f′** will not broaden. This can be seen in Figure 6.14a, where the ^{1}H NMR spectrum shows that peaks **a**, **a′**, **c**, **e**, **h**, **h′** and **i** all broaden significantly, as well as either the peaks representing **b** and **b′** or **f** and **f′**. Thus, to distinguish between **b**, **b′**, **f** and **f′**, a comparison between Sar-FH, Cu-Sar-FH and Sar-LH was made and can be seen in Figure 6.14b. Both Sar-LH and Sar-FH have peaks **b** and **b′** positioned at approximately 3 ppm, but only Sar-FH has peaks **f** and **f′** also positioned at approximately 3 ppm. Thus, as Sar-FH is titrated with copper(II), the comparison in Figure 6.14b shows that only peaks **b** and **b′** broaden significantly. The broadening of **a**, **a′**, **c**, **e**, **h**, **h′**, **b**, **b′** and **i** suggests that copper(II) has potentially coordinated to all the binding sites. The speciation diagrams in Figure 6.15 show that at pH 4.8, there is an overlap of species and therefore the broadened peaks are a representation of two or more species, where the one is the MLH_{-2} species. Isolating the MLH_{-2} species at higher pH values is not possible because of slow exchange.

(a)

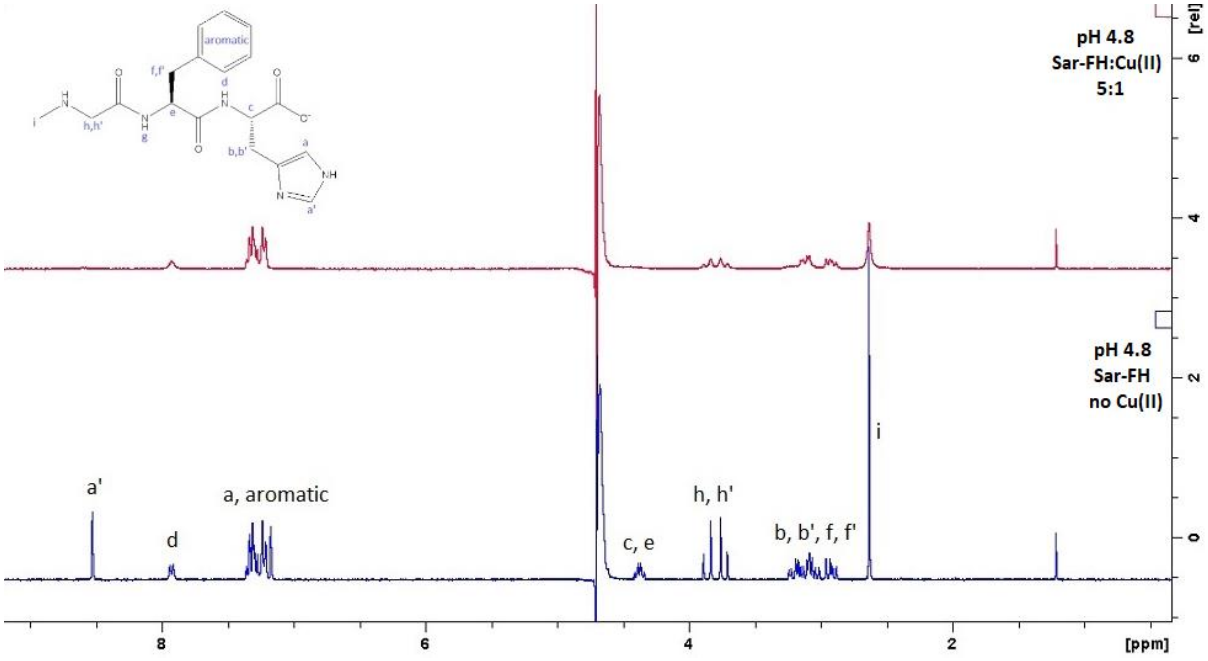

(b)

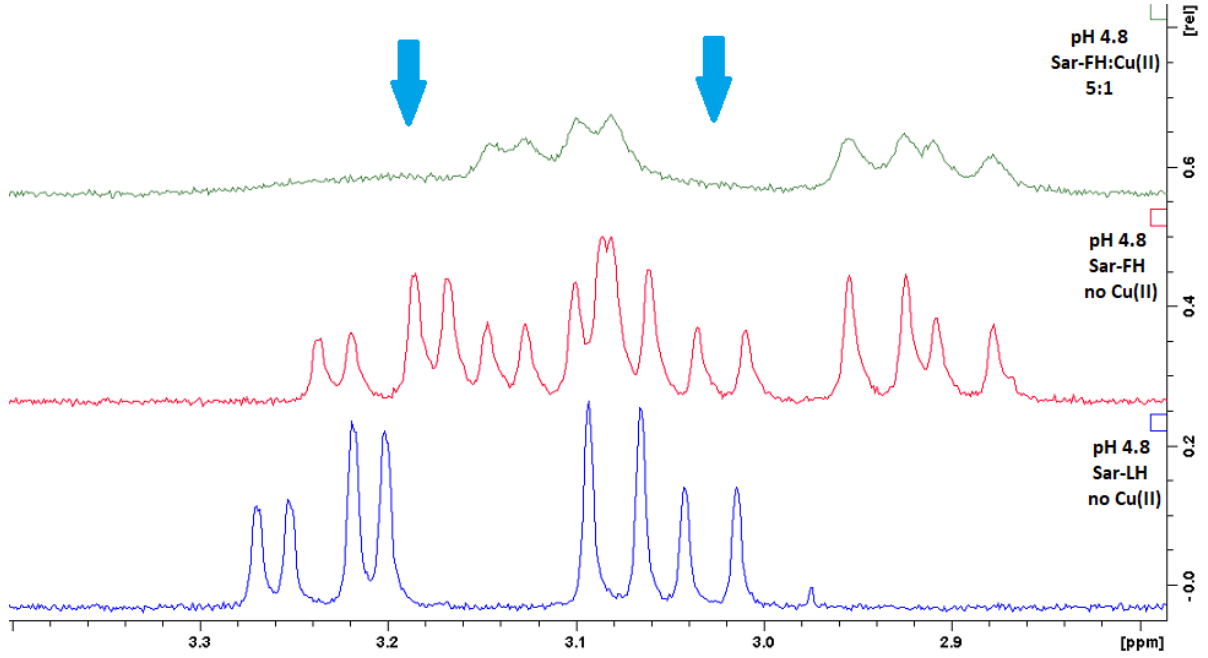

Figure 6.14: (a) The ^{1}H NMR spectra (blue) of the ligand Sar-FH and the ^{1}H NMR spectra (red) after Sar-FH has been titrated with copper(II) to reach a 5:1 ligand copper(II) ratio at a pH of 4.8 in 90 % water and 10 % D_2O. (b) ^{1}H NMR spectra with arrows pointing to the significant broadening of peaks **b** and **b′**, after Sar-FH has been titrated with copper(II) (green).

Proceeding on to determine the correct model, if the pH for the ^{1}H NMR spectrum is set to 3.5 and peak broadening occurs, then the presence of the MLH species will help to decide between Models 1 and 3 vs Model 2. These models can be seen in Figure 6.15. At pH 3.5 peak broadening can be seen (Figure 6.16), which means that Model 2 is the correct model. Similarly, the broadened peaks indicate that copper(II) is coordinating at different locations of the ligand for the MLH species. The broadening of peaks **a**, **a′**, **b**, **b′** and **c**, suggest a coordination to the imidazole-N and carboxyl-O, with a protonated amine-N, while the broadening of peaks **e**, **h**, **h′** and **i**, suggest a coordination to the amine-N and neighbouring carbonyl-O, with a protonated imidazole-N. Note, at this pH, the amide proton signals are still present, which means that the amide-N cannot be coordinated.

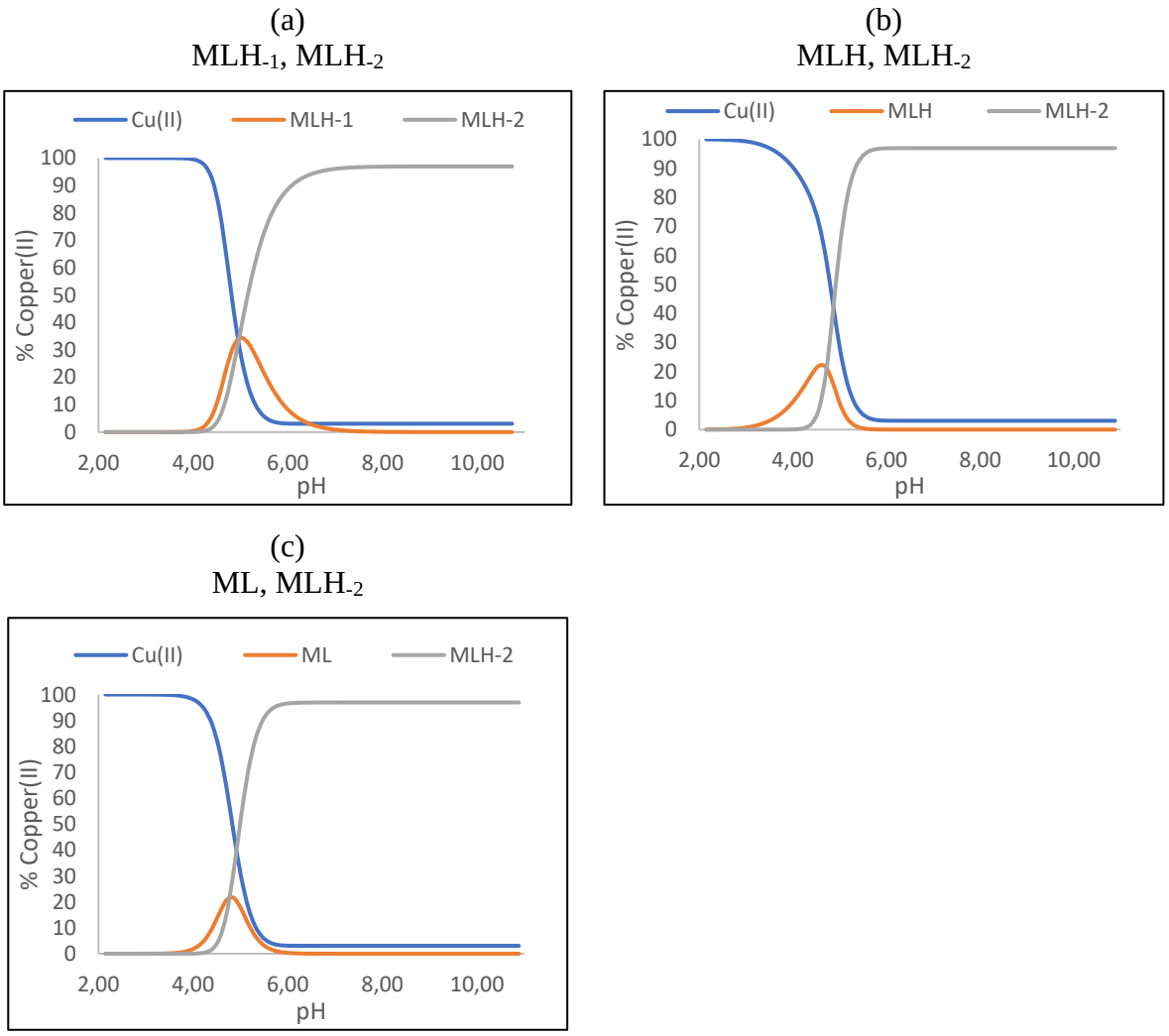

Figure 6.15: Complexation species distribution curve for the 1:1 ratio of copper(II) and Sar-FH (a) Model 1 (MLH_{-1}, MLH_{-2}), (b) Model 2 (MLH, MLH_{-2}) and (c) Model 3 (ML, MLH_{-2}) at 25 ^{o}C in 0.15 mol.dm^{-3} of NaCl.

(a)

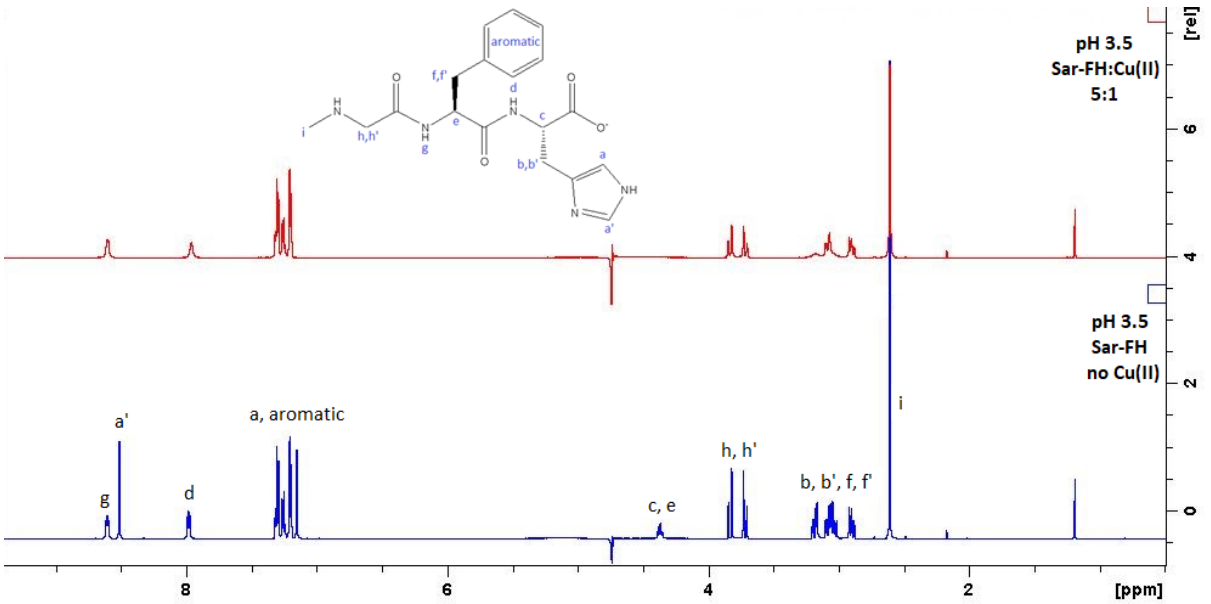

Figure 6.16: The ^{1}H NMR spectra (blue) of the ligand Sar-FH and the ^{1}H NMR spectra (red) after Sar-FH has been titrated with copper(II) to reach a 5:1 ligand copper(II) ratio at a pH of 3.5 in 90 % water and 10 % D_2O.

6.3.2(d) Cu-GFH

Similar to Sar-FH, GFH has overlapping **b**, **b′**, **f** and **f′** peaks, and so again before an analysis is done to determine the correct model, these peaks need to be assigned. The pH was also set to 4.8 which caused peaks **a**, **a′**, **c**, **e**, **h** and **h′**, as well as either peaks **b** and **b′** or **f** and **f′**, to broaden (Figure 6.17a). Thus, to distinguish between **b**, **b′**, **f** and **f′**, a comparison between the spectra of GFH, Cu-GFH and GLH was made (Figure 6.17b). The comparison shows that only peaks **b** and **b′** broaden significantly. This, as well as the other broadened peaks, indicates that copper(II) has potentially coordinated to all the available binding sites. Likewise, this represents the combination of two species, where the one is the MLH_{-2} species, but increasing the pH to isolate the MLH_{-2} species will cause peak sharpening.

(a)

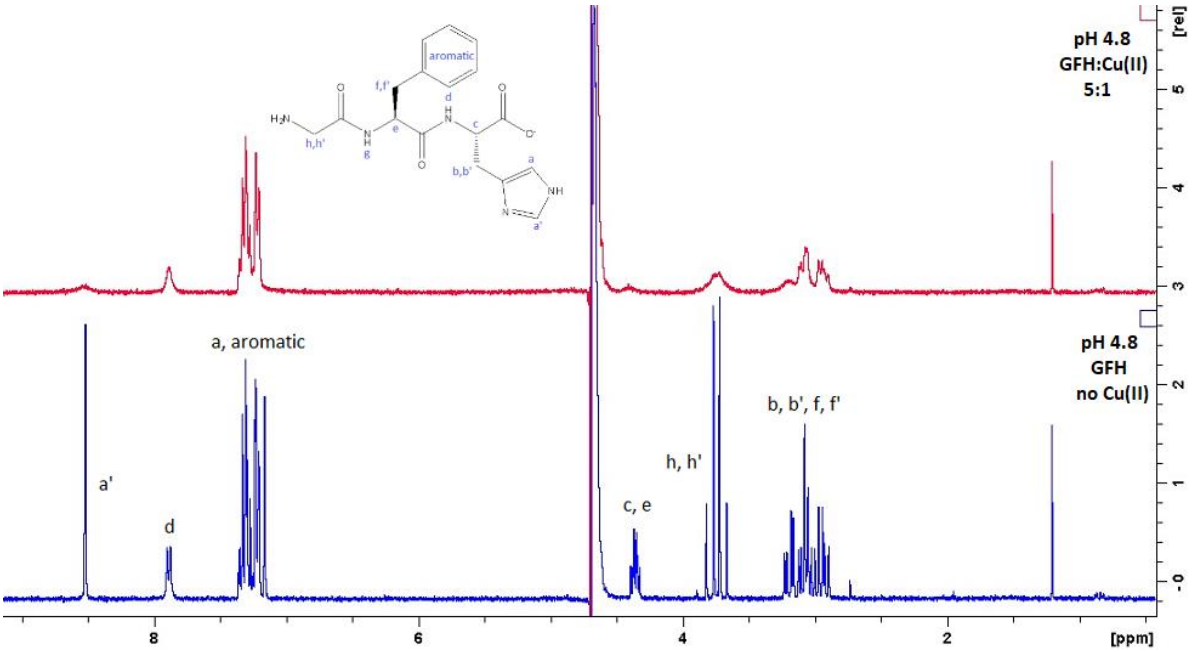

(b)

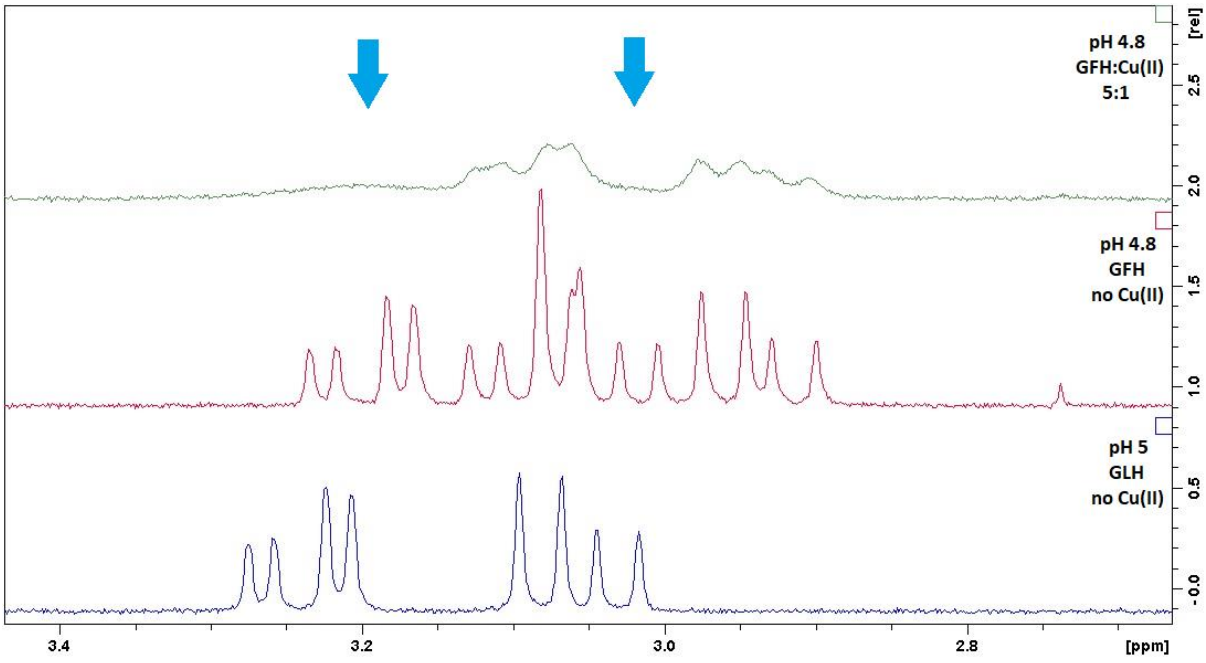

Figure 6.17: (a) The ^{1}H NMR spectra (blue) of the ligand GFH and the ^{1}H NMR spectra (red) after GFH has been titrated with copper(II) to reach a 5:1 ligand copper(II) ratio at a pH of 4.8 in 90 % water and 10 % D_2O. (b) ^{1}H NMR spectra with arrows pointing to the significant broadening of peaks **b** and **b′**, after GFH has been titrated with copper(II) (green).

Proceeding on to determine the correct model, the species distribution diagram in Figure 6.18, shows that if the pH for the ^{1}H NMR spectrum is set to 3.5, then the possible presence of an MLH species will cause peak broadening, which will help to decide between Models 1 and 4 vs Models 2 and 3. After setting the pH to 3.5, peak broadening can be seen (Figure 6.19), which means that an MLH species is present and either Model 2 or 3 is correct. Similarly, the broadening of peaks **a**, **a′**, **b**, **b′** and **c**, suggests a coordination to the imidazole-N and carboxyl-O, with a protonated amine-N, while the broadening of peaks **e**, **h** and **h′** suggests a coordination to the amine-N and neighbouring carbonyl-O, with a protonated imidazole-N. Similar to the Cu-Sar-FH spectrum, the amide proton signals are still present, which means that the amide-N cannot be coordinated.

Since ^{1}H NMR cannot further identify between Models 2 or 3 and the EPR data could only confirm the presence of the MLH_{-2} species, the potentiometric results were looked at. Comparing Models 2 and 3, Model 3 has lower standard deviations and Hamilton R factors. Therefore Model 3 is proposed as the correct model for Cu-GFH.

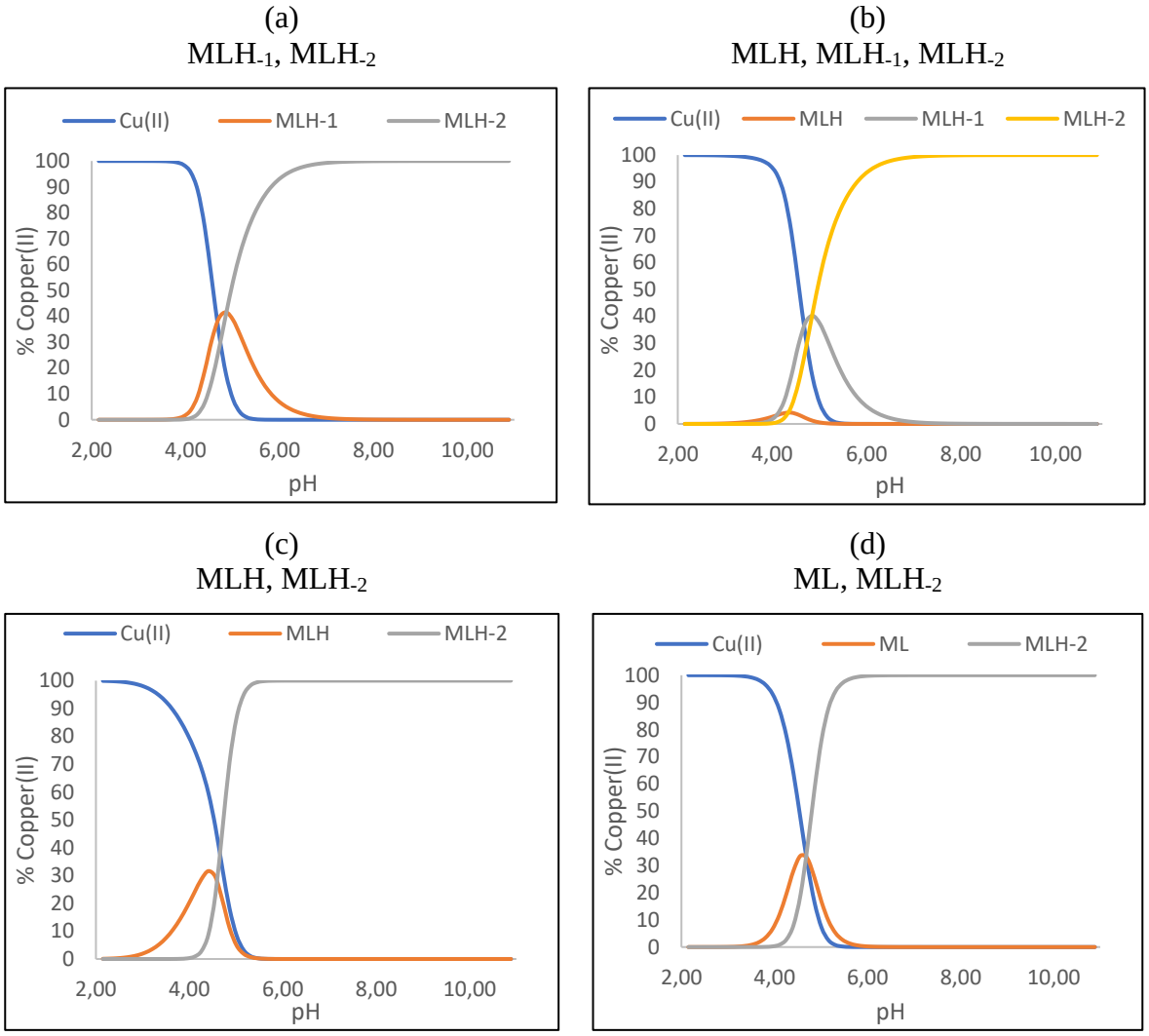

Figure 6.18: Complexation species distribution curve for the 1:1 ratio of copper(II) and GFH (a) Model 1 (MLH_{-1}, MLH_{-2}), (b) Model 2 (MLH, MLH_{-1}, MLH_{-2}), (c) Model 3 (MLH, MLH_{-2}) and (d) Model 4 (ML, MLH_{-2}) at 25 ^{o}C in 0.15 mol.dm^{-3} of NaCl.

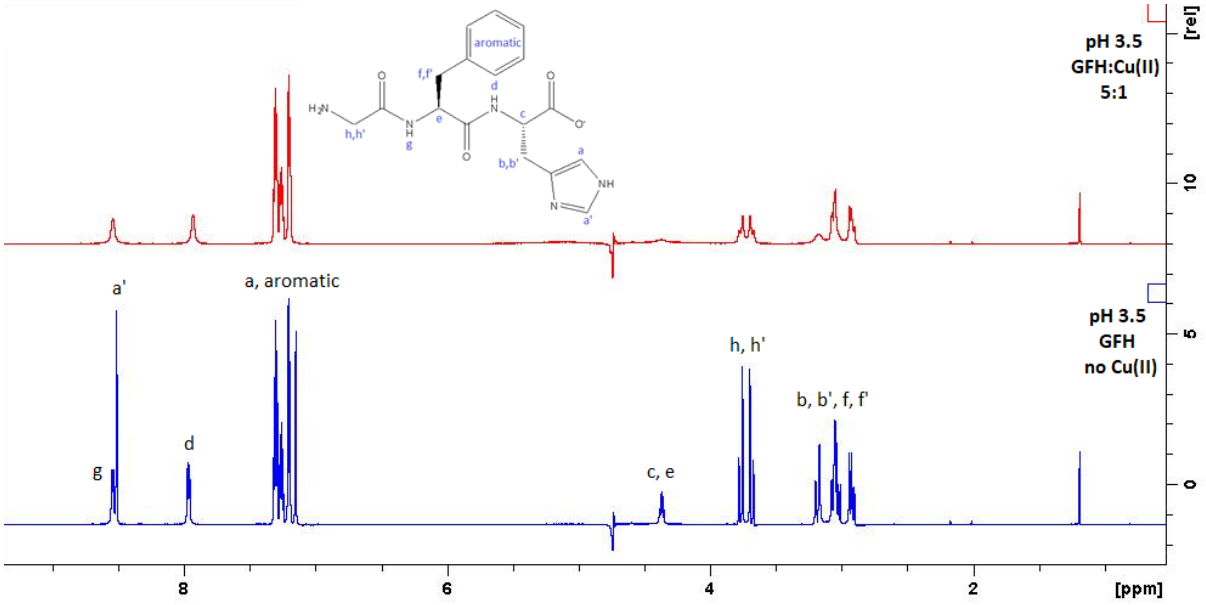

Figure 6.19: The ^{1}H NMR spectra (blue) of the ligand GFH and the ^{1}H NMR spectra (red) after GFH has been titrated with copper(II) to reach a 5:1 ligand copper(II) ratio at a pH of 3.5 in 90 % water and 10 % D_2O.

6.4 Conclusion

The proton assignments for each ligand were successfully achieved using a combination of ^{1}H NMR and TOCSY spectra. All the models from potentiometry that were found for each copper(II) complex were taken into consideration when searching for the correct model using ^{1}H NMR. As a result of using ^{1}H NMR to narrow the selection of models down, a model for each copper(II) complex has been proposed. Cu-Sar-LH has the MLH, ML and MLH_{-2} species, Cu-GLH has the MLH, MLH_{-1} and MLH_{-2} species, while Cu-GFH and Cu-Sar-FH only have the MLH and MLH_{-2} species. These models where proposed using a 1:5 copper(II) ligand ratio. However, the ratio was increased to 1:1 to verify that the species distribution and species type are the same at different ratios.

As copper(II) coordinated to the ligands, signal broadening was expected. This was true for low pH values, but at high pH values, peak sharpening instead of peak broadening occurred. This meant that only the coordination mode for MLH species was identified and found to coordinate at two different locations of the ligand. The one coordination is to the amine-N and neighbouring carbonyl-O with a protonated imidazole-N, and the other is to the imidazole-N and carboxyl-O with a protonated amine-N.

6.5 References

1 R. T. Morrison and R. N. Boyd, in *Organic Chemistry*, Allyn and Bacon, Boston, 5th edn., 1987, pp. 578–580.

2 I. R. Kleckner and M. P. Foster, An introduction to NMR-based approaches for measuring protein dynamics, *Biochim. Biophys. Acta - Proteins Proteomics*, 2011, **1814**, 942–968.

3 B. Liang, J. H. Bushweller and L. K. Tamm, Site-directed parallel spin-labeling and paramagnetic relaxation enhancement in structure determination of membrane proteins by solution NMR spectroscopy, *J. Am. Chem. Soc.*, 2006, **128**, 4389–4397.

4 A. M. Ure and C. M. Davidson, Eds., in *Chemical Speciation in the Environment*, Blackwell Science Ltd, Oxford, UK, 2nd edn., 2002, p. 46.

5 M. A. Wells, C. Jelinska, L. L. P. Hosszu, C. J. Craven, A. R. Clarke, J. Collinge, J. P. Waltho and G. S. Jackson, Multiple forms of copper (II) co-ordination occur throughout the disordered N-terminal region of the prion protein at pH 7.4., *Biochem. J.*, 2006, **400**, 501–510.

6 X. Z. Zhao, T. Jiang, L. Wang, H. Yang, S. Zhang and P. Zhou, Interaction of curcumin with Zn(II) and Cu(II) ions based on experiment and theoretical calculation, *J. Mol. Struct.*, 2010, **984**, 316–325.

7 L. Hou and M. G. Zagorski, NMR reveals anomalous copper(II) binding to the amyloid Aβ peptide of Alzheimer's disease, *J. Am. Chem. Soc.*, 2006, **128**, 9260–9261.

8 Nuclear Magnetic Resonance: An Introduction, http://instructor.physics.lsa.umich.edu/adv-labs/NMR/Ch12_NMRTEC.pdf, (accessed 3 November 2019).

9 R. A. Marusak, K. Doan and S. D. Cummings, *Integrated Approach to Coordination Chemistry: An Inorganic Laboratory Guide*, John Wiley & Sons, Inc., New Jersey, 2007.

10 J. H. Simpson, in *Organic Structure Determination Using 2-D NMR Spectroscopy: A Problem-Based Approach*, Elsevier Inc., London UK, 2008, pp. 120–123.

11 K. Várnagy, J. Szabó, I. Sóvágó, G. Malandrinos, N. Hadjiliadis, D. Sanna and G. Micera, Equilibrium and structural studies on copper(II) complexes of tetra-, penta- and hexa-peptides containing histidyl residues at the C-termini, *J. Chem. Soc. Dalt. Trans.*, 2000, 467–472.

12 F. M. Elmagbari, A. N. Hammouda, G. E. Jackson and R. P. Bonomo, Stability, solution structure and X-ray crystallography of a copper (II) diamide complex, *Inorganica Chim. Acta*, 2019, **498**, 119132.

13 S. J. Lau, J. P. Laussac and B. Sarkar, Synthesis and copper(II)-binding properties of the N -terminal peptide of human α -fetoprotein, *Biochem. J.*, 1989, **257**, 745–750.

14 J. P. Laussac, R. Haran and B. Sarkar, N.m.r. and e.p.r. investigation of the interaction of copper(II) and glycyl-l-histidyl-l-lysine, a growth-modulating tripeptide from plasma, *Biochem. J.*, 1983, **209**, 533–539.

15 Z. Szabó, Multinuclear NMR studies of the interaction of metal ions with adenine-nucleotides, *Coord. Chem. Rev.*, 2008, **252**, 2362–2380.

16 F. M. A. Elmagbari, Synthesis and design of ligand copper complexes as anti-inflammatory drugs, PhD Thesis, University of Cape Town, 2015.

17 G. M. Vicatos, In vitro studies of dermally absorbed Cu(II) tripeptide complexes as potential anti-inflammatory drugs, MSc Thesis, University of Cape Town, 2016.

18 G. M. Vicatos, G. E. Jackson, A. N. Hammouda, R. P. Bonomo and G. Valora, Potentiometric and spectroscopic studies of the complex formation between copper(II) and Gly-Leu-Phe or Sar-Leu-Phe tripeptides, *Polyhedron*, 2019, **170**, 553–563.

19 T. Gajda, B. Henry, A. Aubry and J.-J. Delpuech, Proton and Metal Ion Interactions with Glycylglycylhistamine, a Serum Albumin Mimicking Pseudopeptide, *Inorg. Chem.*, 1996, **35**, 586–593.

7. Electrospray Ionisation Mass Spectrometry

7.1 Introduction

Mass spectrometry (MS) is an analytical technique that gives an analysis on both the qualitative and quantitative aspects of a molecule. The general procedure is to introduce the molecules into the ionisation source of the mass spectrometer, where they become ionised as either positive or negative charges. The ions then travel through the mass analyser, where they are separated according to their mass/charge ratio (m/z) and end at different parts of the detector. The detector then generates the mass spectrum that shows the relative abundance of signals with respect to their m/z ratio.[1,2]

Mass spectrometry has several ionization methods such as electron ionization and chemical ionization, but these methods cannot overcome the tendency for the molecules to fragment. In contrast, electrospray ionisation mass spectrometry (ESI-MS) is a soft ionization technique that ionizes intact chemical species by multiple charging.[3] The ionization is described as "soft" because only a small amount of residual energy is retained by the molecule and generally no fragmentation occurs when ionized.[4] Additionally noncovalent interactions are also preserved in the gas phase.[5]

When detecting the presence of the different species, MLH, ML, MLH_{-1} and MLH_{-2}, there is only a difference of a few mass units, so using a method that does not cause fragmentation is ideal. This is the reason why ESI-MS was chosen to analyse the copper(II) complex species, as well as the reported successful analyses of literature using ESI-MS to analyse copper(II) peptides.[6–8] However, exceptions in ESI-MS have been reported where the loss of an electron results in radical ions and causes fragmentation.[9] Therefore, when analysing the complexes, it is probable that a combination of intact and fragmented complexes will be detected.

When analysing the ESI-MS data, the analysis can be done in either a positive ion mode or a negative ion mode, depending on the compound's affinity for protons. Only analytes that have at least one positive elementary charge can be analysed in the positive ion mode, whereas the

negative ion mode needs at least one negative elementary charge. In general, molecules with basic characteristics can be analysed in the positive ion mode, since they can make adducts with protons, while molecules that lack basic functional groups but have acidic ones, are generally analysed in the negative ion mode spectrum.[10] Basically, the optimal selection of an ionization mode is based on the Brønsted-Lowry acid-base theory.[11]

The most common type of ions that are generated in the positive ion mode spectrum usually are singly or multiply protonated and are represented as: $[molecule + zH]^{z+}$. If the compounds have multiple sites for protonation, then they are usually multiply-protonated, but also have more of a tendency to fragment due to charge repulsion. Depending on the Lewis basicity of the compound, the formation of adducts with NH_4^+, Na^+, K^+, Li^+ or Ag^+ can also occur.[12,13] The ions that are generated in the negative ion mode spectrum usually have lost a proton and are in the form of $[molecule - H]^{1-}$. Adduct formation is also possible in the negative mode spectrum with ions such as Cl^-.[10]

When analysing the species from Cu-GLH, Cu-Sar-LH, Cu-GFH and Cu-Sar-FH, it is likely to find both the uncomplexed and complexed ligands existing simultaneously in solution. Thus, as a reference, a typical isotopic pattern for copper, the uncomplexed ligand and the complexed ligand, can be seen in Figure 7.1a, 7.1b and 7.1c respectively. The random selection of GLH and the MLH_{-2} species of Cu-GLH was chosen, but similar patterns are seen for the other ligands and complexes. In particular, the isotopic pattern from the complexed ligand (Figure 7.1c) is the combination of the peaks from the uncomplexed ligand (Figure 7.1b) and copper (Figure 7.1a). Therefore, when assigning complex species which display patterns such as Figure 7.1c, it will be certain that the species is a copper species. This is because copper has two isotopes, Cu^{63} (70% abundant) and Cu^{65} (30% abundant), so any copper containing species should have at least two lines of relative intensity 70:30, which reflects these two isotopic masses. During the analysis, the first three peaks of the isotopic pattern belonging to an uncomplexed ligand will be labelled and the first four peaks belonging to a complex species will be labelled.

(a)

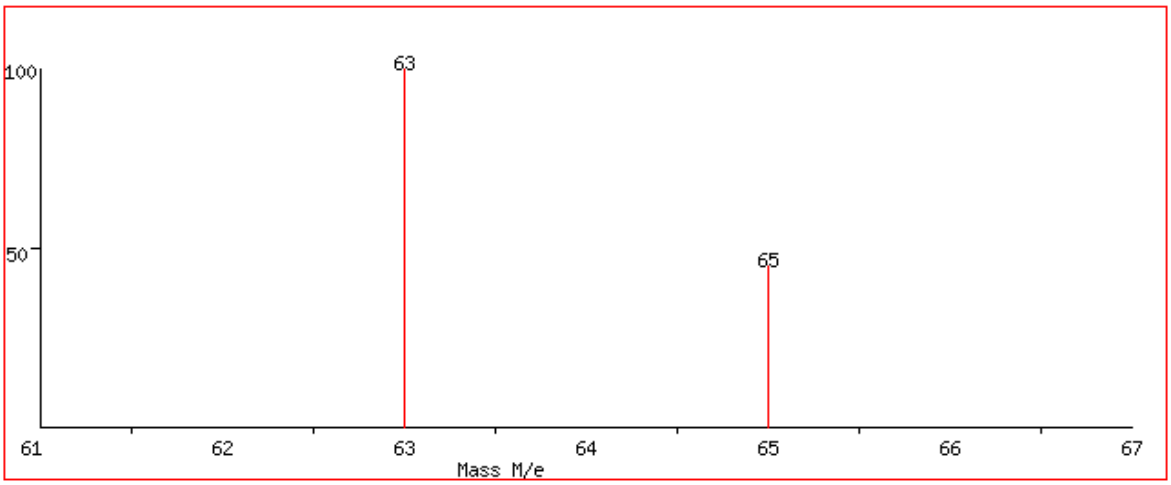

(b)

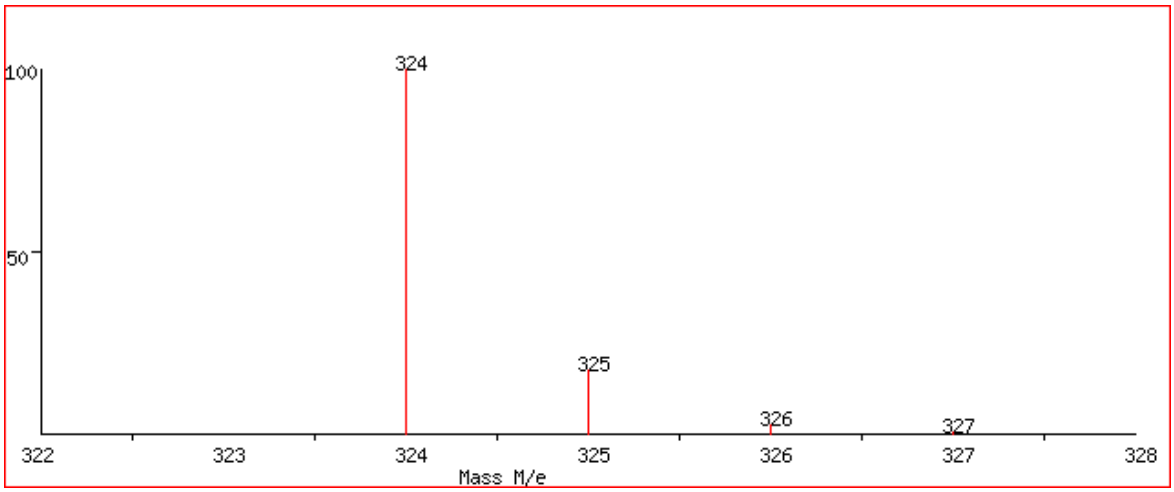

(c)

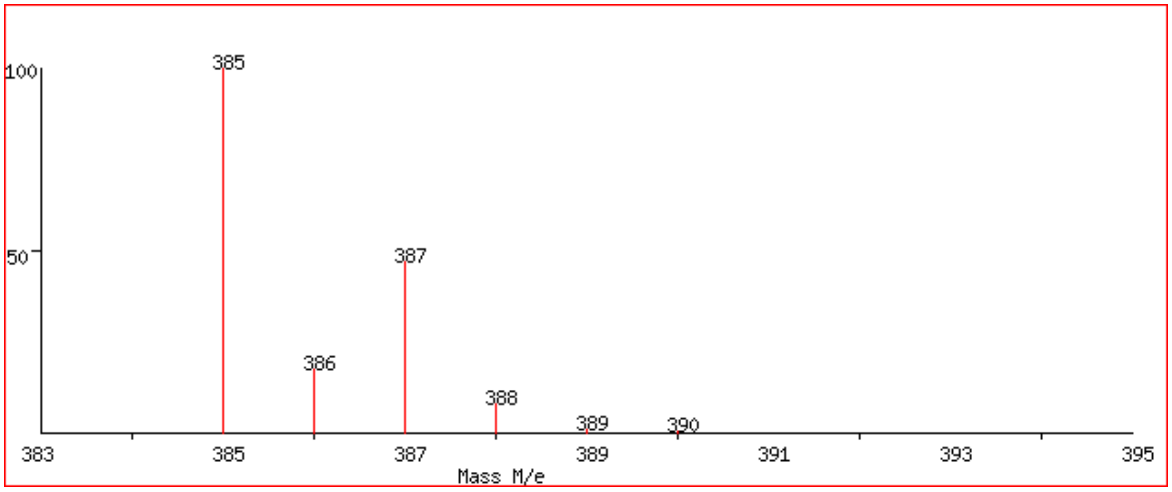

Figure 7.1: Examples of (a) copper isotopic pattern, (b) uncomplexed isotopic pattern and (c) complex species isotopic pattern (MLH_{-2} species). The random selection of GLH was chosen.

Key characteristics to remember when assigning a signal, is the mass-to-charge ratio (m/z), which is defined as the molecular weight of the molecule divided by the charge. Therefore, if the uncomplexed or complexed ligand has a +1 charge either by gaining protons/+ions, or in the case of the ML species, already has a +1 charge, then the signal for that ion will appear at the molecular weight of the ion. If the ion has a +2 charge, then it will appear at half the mass, and so on. Another point about the signals is that if the ion has a +1 charge, then the distance between the peaks of the isotopic pattern is 1 m/z, but if the ion has a charge of +2, then the distance decreases by 0.5 m/z, and so forth.[14]

The purpose of this section is to identify and confirm the presence of the different species present in solution over a pH range from 2-11 for Cu-GLH, Cu-Sar-LH, Cu-GFH and Cu-Sar-FH. Using the potentiometric speciation diagrams (Figures 3.15-3.18), at pH 5 there is an overlap of the MLH, MLH_{-1} and MLH_{-2} species for Cu-GLH; there is an overlap of the MLH, ML and MLH_{-2} species for Cu-Sar-LH; there is an overlap of the MLH and MLH_{-2} species for Cu-GFH and there is an overlap of the MLH and MLH_{-2} species for Cu-Sar-FH. At pH 11 only the MLH_{-2} species is present for all complexes. Therefore, by adjusting the solution to pH 5 and to pH 11, all the species can be identified for all the complexes. Even though the MLH_{-2} species is present at pH 5 and so analysing the solution at pH 11 might seem redundant, it is good to reconfirm the presence of the MLH_{-2} species at pH 11. At pH 5 the species could overlap one another and so identifying them could be challenging, but because the MLH_{-2} species at pH 11 is the only species present, it is much easier to identify.

7.2 Experimental

Copper(II) complexes for each of the four ligands were prepared as a 1:1 copper(II) ligand ratio in 10 ml of Milli-Q water (18.2 MΩ.cm). The concentration of the ligands was 1 mM and the concentration of copper(II) was adjusted to a slightly lower concentration of 0.7 mM to prevent precipitation. The solution of each complex was divided into two samples so that the pH of the one was set to pH 5 and the other to pH 11. The pH was adjusted using NaOH and HCl. ESI-MS measurement samples were analysed by direct infusion using the sample solvent as a carrier. The apparatus was a Thermo TSQ quadrupole with a HESI ion source type and analysed with MS1 over a scan range of 100-600 m/z in both the positive and negative mode. The data was viewed using the commercial software, Thermos Qual Browser. The capillary temperature

was 270 °C and nitrogen was used as a nebulizing gas. The conditions for electrospray ionisation are as follows: the spray voltage was set to 3500 V, the flow rate to 5 µl/min, the vaporizing temperature to 100 °C, the auxiliary gas pressure to 10 (arbitrary units) and the sheath gas pressure to 5 (arbitrary units).

7.3 Results and Discussion

The MLH_{-2} species is the dominant species for all ligands and therefore the identification of this species on the ESI-MS spectrum was expected to be easily visible. This was found for all ligands at both pH 5 and pH 11 (section 7.3.1-7.3.4). However, the MLH, ML species of Cu-Sar-LH and the MLH_{-1} species of Cu-GLH have lower concentrations and so the identification of these species were thought to be more challenging. This proved true for the MLH species of all ligands, as well as the ML species of Cu-Sar-LH, since they could not be found. But for the MLH_{-1} species of Cu-GLH, a series of peaks could have represented either MLH_{-1} or MLH_{-2} and so the identification of the MLH_{-1} species (section 7.3.1) was unconfirmed.

7.3.1 GLH

The proposed structures for the ESI-MS analysis of Cu-GLH at pH 5 and pH 11 can be seen in Table 7.1 along with their corresponding base peaks.

At pH 5, the MLH, MLH_{-1} and MLH_{-2} species are expected to be present in solution, as well as the uncomplexed ligand. In solution the expected form of the uncomplexed ligand at pH 5 is the LH_2 species, where both the amine-N and imidazole-N are protonated. But during the electrospray ionization process the ligand may lose and gain protons, which will result in forms of the ligand that might not be present in solution at a particular pH. Additionally, the negatively charged carboxyl-O is the first expected site of protonation due to the negative charge, and so in the following analysis this group is always protonated first.

In the positive mode spectrum (Figure 7.2), the base peaks at 326.24 m/z and 348.08 m/z represent the uncomplexed ligand in the form of $(LH+H)^{1+}$ and $(LH+Na)^{1+}$ respectively.

There are four peaks between 370.06 - 373.07 m/z, which were originally thought to have been the complex species. But due to the isotopic pattern, it is more likely to be two sets of uncomplexed ligand peaks with a charge of +1 and a difference of one mass unit between them. The proposed structure for the base peak at 370.06 m/z is therefore $(L+2Na)^{1+}$, while the proposed structure for the base peak at 371.04 m/z is unclear. This is because it is not possible for $(L+2Na)^{1+}$ to gain a hydrogen ion and remain with a +1 charge.

The peaks between 387.07 - 391.13 m/z look as if two complex species with a +1 charge and one mass unit apart are overlapping one another. This was originally thought to show the MLH_{-1} and MLH_{-2} species, but for both species to obtain a +1 charge, means that they will have an equal mass and be displayed within the same set of peaks. Therefore, since there is the presence of two sets of complex groups, and since it is not possible for the difference in one mass unit to come from the ligand while it retains a charge of +1, this suggests that the copper(II) ion is undergoing reduction and becoming copper(I). This phenomenon is seen in literature where the relative proportion of copper(II) peptide complexes is a 1:1 ratio for Cu(I)- and Cu(II)- peptides, and was produced by the electrospray ionization of copper(II) sulphate and Gly-His-Lys.[15] This phenomenon has also been reported for the electrospray ionisation of copper(II)-glycine and glycylglycine[16], as well as with other electrospray ionisation studies[17–19]. This reduction observation can be explained by collision-induced processes in the medium vacuum area of the source, which causes "inner-sphere" ligand to metal electron transfer, as well as the decoordination of odd-electron species.[15,20] For simplicity, when copper(II) gets reduced to copper(I), the symbol "M" in the complex species will be labelled as M^{I}, while copper(II) will remain as "M". It is therefore reasonable to suggest that the base peak at 387.07 m/z could represent either the MLH_{-1} or MLH_{-2} species, or that the peak is a combination of the two species in the form of $(MLH_{-1}+H)^{1+}$ and $(MLH_{-2}+2H)^{1+}$ respectively. Then similarly, the base peak at 388.05 m/z could represent either the MLH_{-1} or MLH_{-2} species, or again a combination of both species in the form of $M^{I}LH_{-1}+2H)^{1+}$ and $(M^{I}LH_{-2}+3H)^{1+}$ respectively. Note in Table 7.1 the coordination mode for the MLH_{-1} species has been randomly selected from the three possible modes.

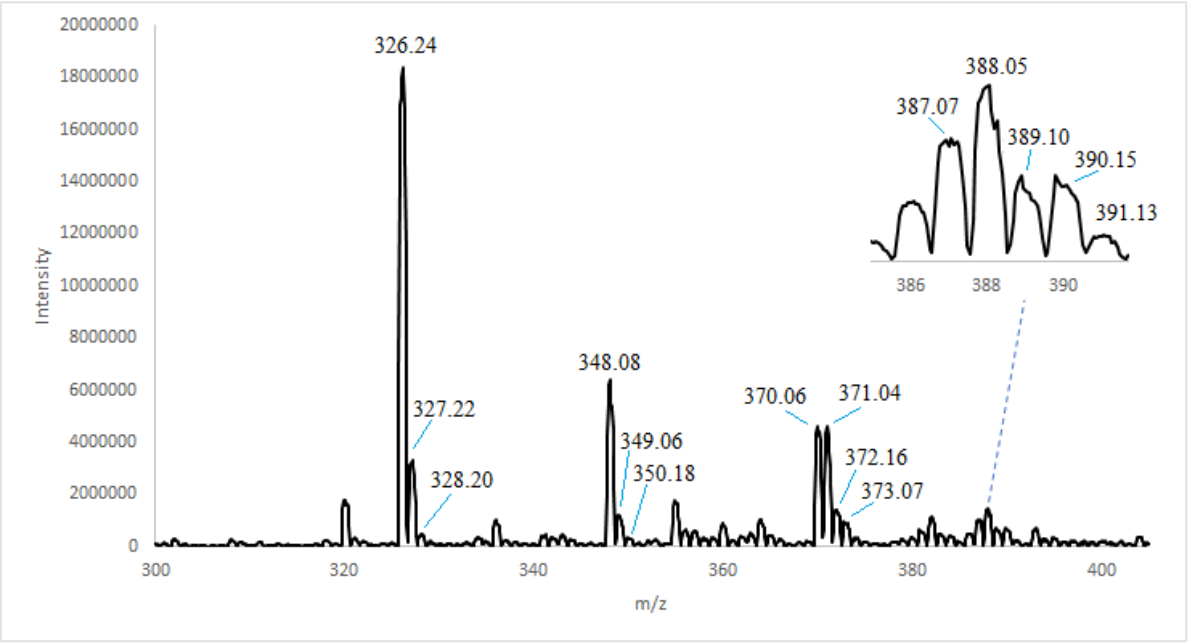

Figure 7.2: Section of the ESI-MS spectrum (positive mode) for the Cu-GLH complex at a ratio of 1:1 and concentration of 1 mM for GLH and 0.7 mM for copper(II) in aqueous solution at pH 5.

At pH 11, the only complex species that is expected to be present is the MLH_{-2} species. The uncomplexed ligand is also predicted to be present since the copper(II) concentration was slightly less than the ligand concentration to avoid precipitation. In the negative mode spectrum (Figure 7.3), the presence of MLH_{-2} species is confirmed by the base peak at 385.11 m/z, which represents the MLH_{-2} species in the form of $(MLH_{-2})^{1-}$. The species already had a charge of -1, which was retained during the ESI-MS ionisation process and therefore could be observed in the negative mode spectrum. This is unlike the MLH_{-2} species of the other ligands, (analysed in sections 7.3.2, 7.3.3 and 7.3.4), which could only be viewed in the positive mode spectrum after hydrogen ions had been added to the species. The other large base peaks at 112.81 m/z and 219.28 m/z represent an isotopic pattern of an uncomplexed ligand and so they are most likely a result of fragmentation.

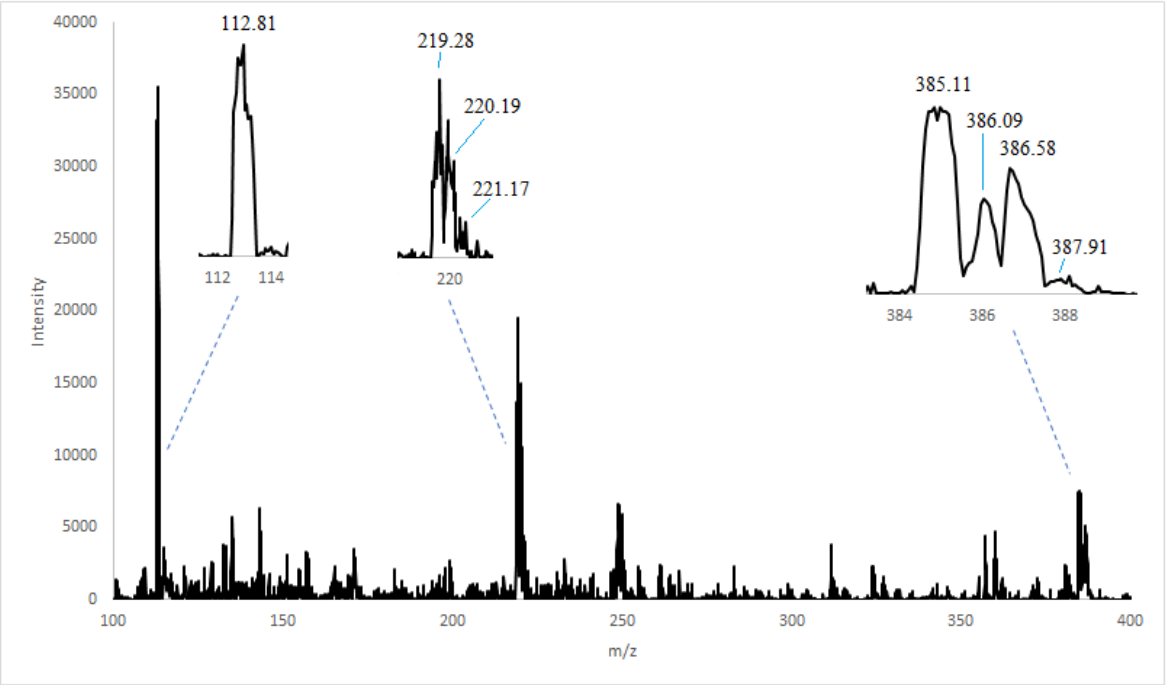

Figure 7.3: Section of the ESI-MS spectrum (negative mode) for the Cu-GLH complex at a ratio of 1:1 and concentration of 1 mM for GLH and 0.7 mM for copper(II) in aqueous solution at pH 11.

Table 7.1: Structural assignments of m/z base peaks that were found in the ESI-MS spectrum for Cu-GLH at pH 5 (positive mode) and pH 11 (negative mode) with a 1:1 ratio and concentration of 1 mM for GLH and 0.7 mM for copper(II) in aqueous solution.

m/z	**pH prevalence**	**Assignment**	**Structure**
326.24	pH 5	$(LH+H)^{1+}$	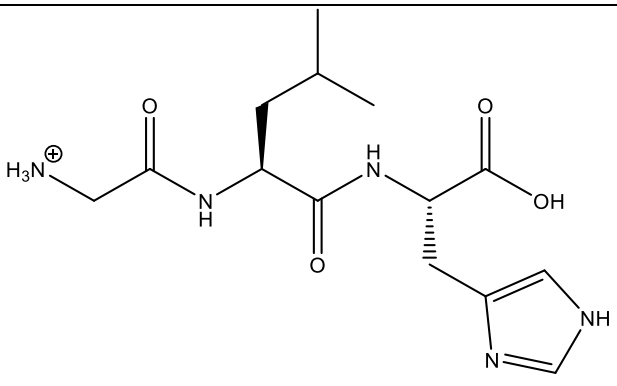 Exact Mass: 326,18

348.08	pH 5	$(LH+Na)^{1+}$	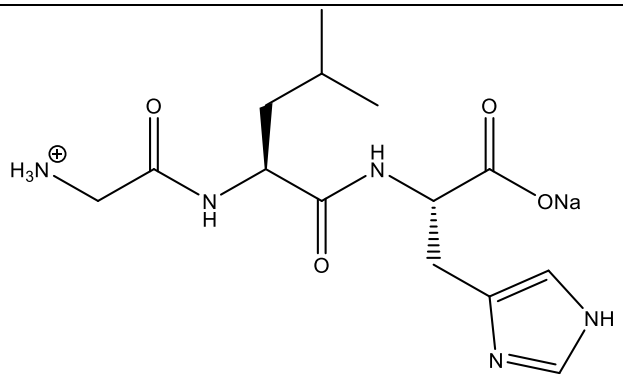 Exact Mass: 348,16
370.06	pH 5	$(L+2Na)^{1+}$	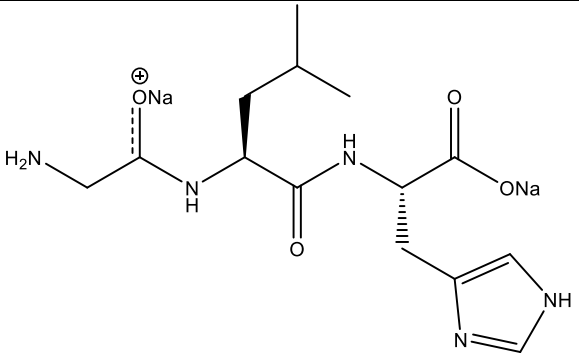 Exact Mass: 370,15
371.04	pH 5	uncomplexed ligand	unclear
387.07	pH 5	$(MLH_{-2}+2H)^{1+}$	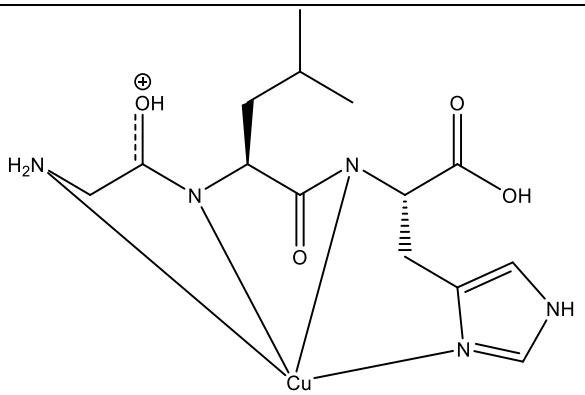 Exact Mass: 387,10
		$(MLH_{-1}+H)^{1+}$	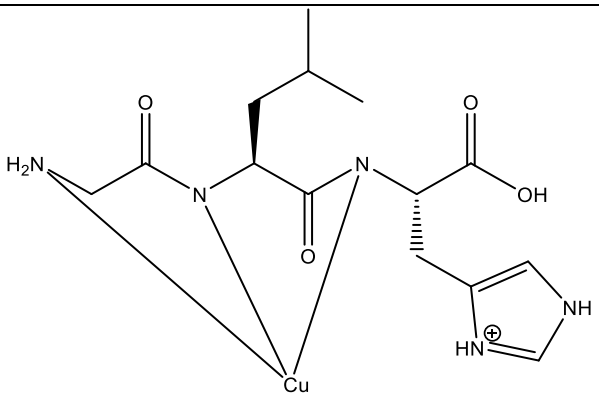 Exact Mass: 387,10

388.05	pH 5	$(M^{I}LH_{-2}+3H)^{1+}$	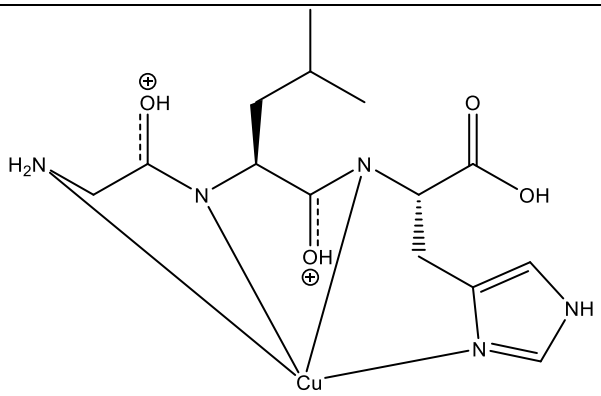 Exact Mass: 388,10
		$(M^{I}LH_{-1}+2H)^{1+}$	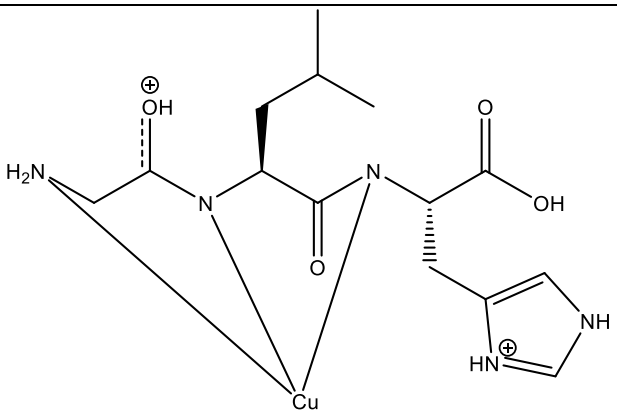 Exact Mass: 388,10
385.11	pH 11	$(MLH_{-2})^{1-}$	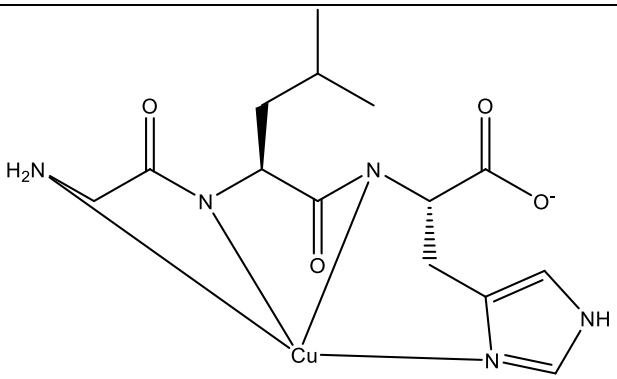 Exact Mass: 385,08
112.81	pH 11	fragmented uncomplexed ligand	unclear
219.28	pH 11	fragmented uncomplexed ligand	unclear

7.3.2 Sar-LH

The proposed structures for the ESI-MS analysis of Cu-Sar-LH at pH 5 and pH 11 can be seen in Table 7.2 along with their corresponding base peaks.

At pH 5, the MLH, ML and MLH_{-2} species of Cu-Sar-LH, as well as the uncomplexed ligand, are expected to be present in solution. In the positive mode spectrum (Figure 7.4), the base peaks 340.10 m/z, 362.08 m/z and 378.11 m/z represent the uncomplexed ligand in the form of $(LH+H)^{1+}$, $(LH+Na)^{1+}$ and $(LH+K)^{1+}$ respectively. K^+ ions were not added during the preparation of the complex and so they most likely come from residual salts in the injector or tubing of the mass spectrometer. The 4N coordination of the MLH_{-2} species is verified by the peaks between 401.00 - 405.13 m/z. These peaks represent the overlap of the two different forms of the MLH_{-2} species, namely where copper is in the Cu(II) form and where it gets reduced from Cu(II)→Cu(I). The base peak at 401.00 m/z represents the MLH_{-2} species in the $(MLH_{-2}+2H)^{1+}$ form and the base peak at 402.05 m/z represents the $(M^{I}LH_{-2}+3H)^{1+}$ form. The base peak at 355.08 m/z also could represent the MLH_{-2} species, but after it has undergone fragmentation. A suggestion for the fragmentation is, $(MLH_{-2}$ - carboxyl group$)^{1+}$.

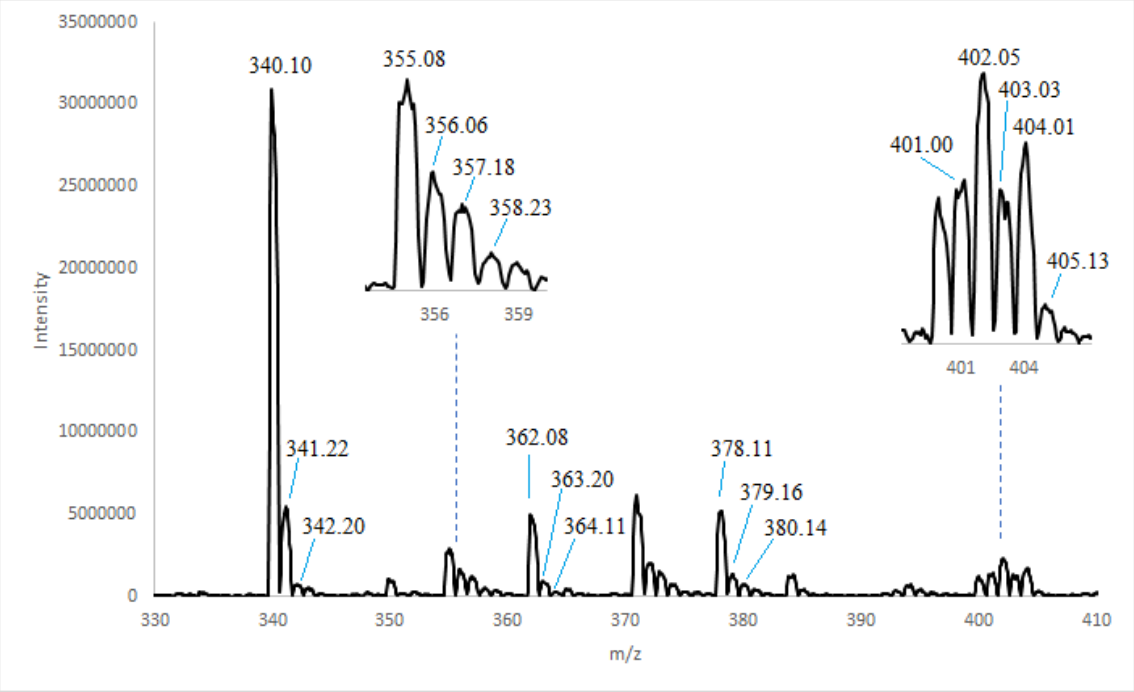

Figure 7.4: Section of the ESI-MS spectrum (positive mode) for the Cu-Sar-LH complex at a ratio of 1:1 and concentration of 1 mM for Sar-LH and 0.7 mM for copper(II) in aqueous solution at pH 5.

At pH 11, the only complex species present in solution is the MLH_{-2} species, but the uncomplexed ligand is also expected to be present. The presence of the MLH_{-2} species was verified in the positive mode spectrum (Figure 7.5), since the base peaks at 400.93 m/z and 423.05 m/z represent this species in the form of $(MLH_{-2}+2H)^{1+}$ and $(MLH_{-2}+H+Na)^{1+}$ respectively. The presence of the uncomplexed ligand was seen in the base peaks at 340.17 m/z, 362.15 m/z, 378.04 m/z and 383.99 m/z, which represent the uncomplexed ligand in the form of $(LH+H)^{1+}$, $(LH+Na)^{1+}$, $(LH+K)^{1+}$ and $(L+2Na)^{1+}$ respectively.

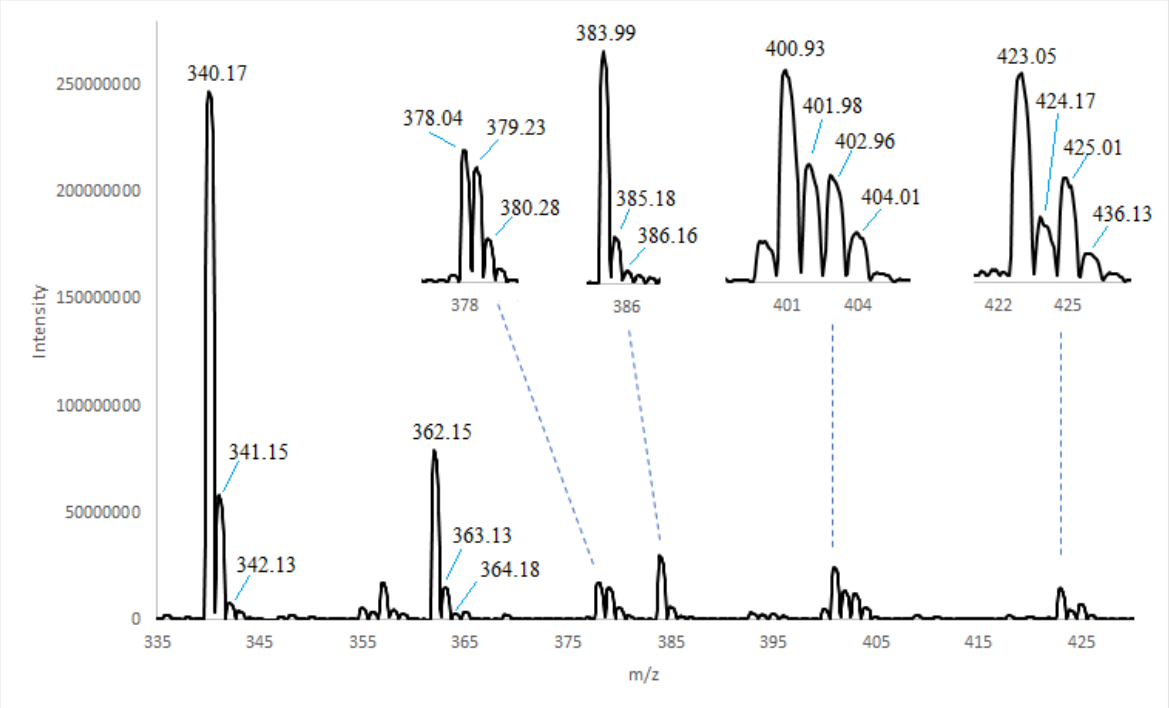

Figure 7.5: Section of the ESI-MS spectrum (positive mode) for the Cu-Sar-LH complex at a ratio of 1:1 and concentration of 1 mM for Sar-LH and 0.7 mM for copper(II) in aqueous solution at pH 11.

Table 7.2: Structural assignments of m/z base peaks that were found in the ESI-MS spectrum for Cu-Sar-LH at pH 5 (positive mode) and pH 11 (positive mode) with a 1:1 ratio and concentration of 1 mM for Sar-LH and 0.7 mM for copper(II) in aqueous solution.

m/z	pH prevalence	Assignment	Structure
340.10	pH 5	$(LH+H)^{1+}$	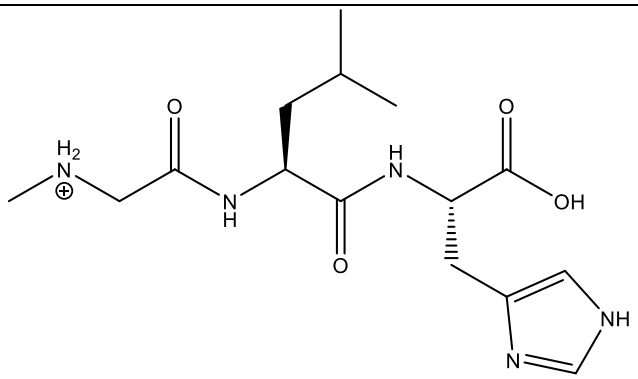 Exact Mass: 340,20
340.17	pH 11		
355.08	pH 5	$(MLH_{-2}$ - carboxyl group$)^{1+}$	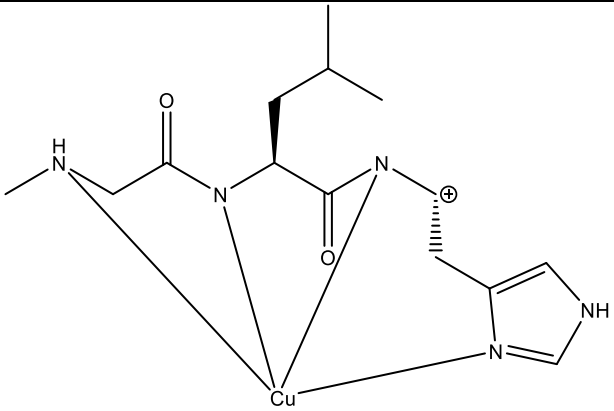 Exact Mass: 355,11
362.08	pH 5	$(LH+Na)^{1+}$	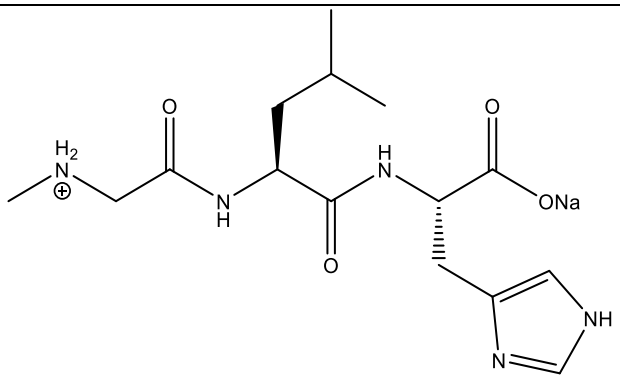 Exact Mass: 362,18
362.15	pH 11		

378.11 378.04	pH 5 pH 11	$(LH+K)^{1+}$	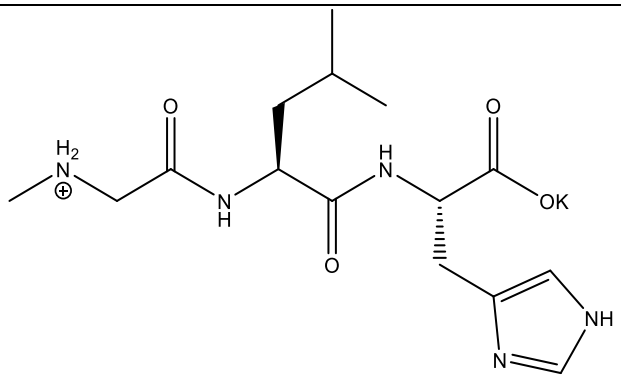 Exact Mass: 378,15
383.99	pH 11	$(L+2Na)^{1+}$	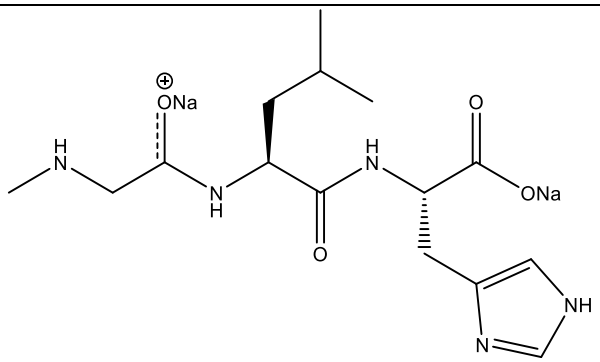 Exact Mass: 384,16
401.00 400.93	pH 5 pH 11	$(MLH_{-2}+2H)^{1+}$	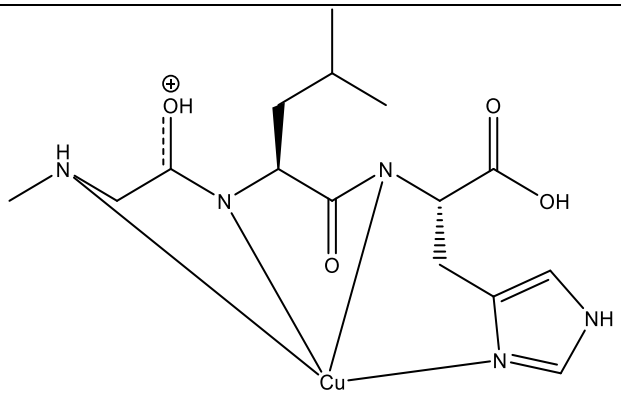 Exact Mass: 401,11
402.05	pH 5	$(M^{I}LH_{-2}+3H)^{1+}$	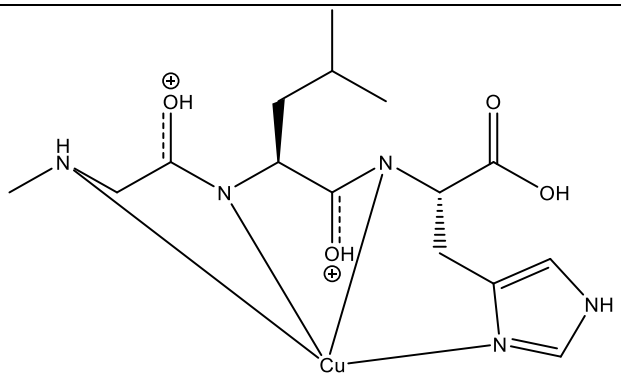 Exact Mass: 402,12

423.05	pH 11	$(MLH_{-2}+H+Na)^{1+}$	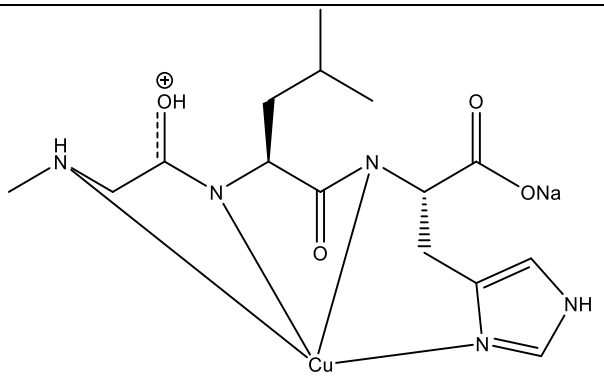 Exact Mass: 423,09

7.3.3 GFH

The proposed structures for the ESI-MS analysis of Cu-GFH at pH 5 and pH 11 can be seen in Table 7.3 along with their corresponding base peaks.

At pH 5, the MLH and MLH_{-2} species, as well as the uncomplexed ligand, are expected to be present in solution. In the positive mode spectrum (Figure 7.6), the base peaks at 360.19 m/z, 382.10 m/z and 404.15 m/z represent the uncomplexed ligand in the form of $(LH+H)^{1+}$, $(LH+Na)^{1+}$ and $(L+2Na)^{1+}$ respectively. The peaks between 421.02 - 424.17 m/z represent the overlap of two different forms of the MLH_{-2} species, namely where copper is Cu(II) and where copper gets reduced from Cu(II)→Cu(I). The base peak at 421.02 m/z represents the $(MLH_{-2}+2H)^{1+}$ form and the base peak at 422.07 m/z represents the $(M^{I}LH_{-2}+3H)^{1+}$ form. The spectrum also displays base peaks at 354.94 m/z and 370.97 m/z which could first represent the fragmentation of the imidazole group, $(MLH_{-2}+H\text{-imidazole})^{1+}$, and then the addition of water, $(MLH_{-2}+H\text{-imidazole}+H_2O)^{1+}$.

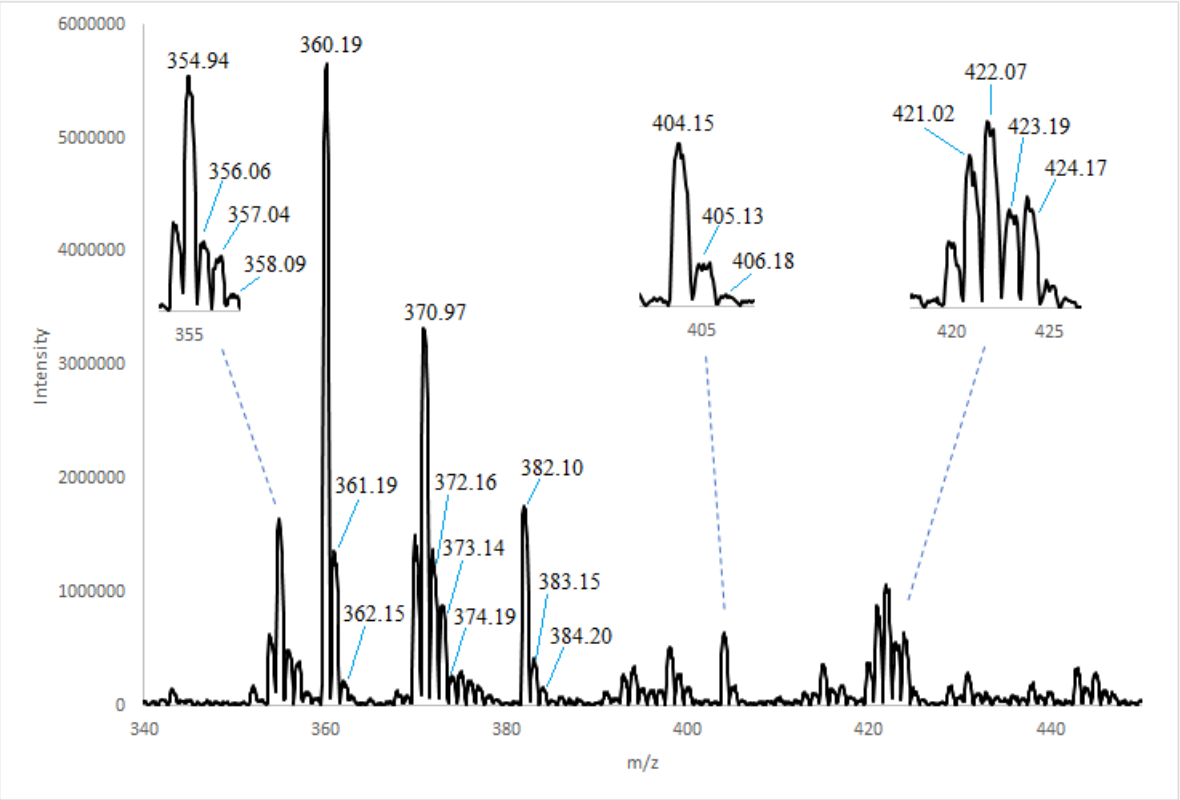

Figure 7.6: Section of the ESI-MS spectrum (positive mode) for the Cu-GFH complex at a ratio of 1:1 and concentration of 1 mM for GFH and 0.7 mM for copper(II) in aqueous solution at pH 5.

At pH 11, the only complex species present in solution is the MLH_{-2} species, but the uncomplexed ligand is also expected to be present. Looking at the positive mode spectrum (Figure 7.7), the MLH_{-2} species is verified by the presence of the base peak at 465.12 m/z, which represents the $(MLH_{-2}+2Na)^{1+}$ form. Besides this peak, the other peaks representing this species show fragmentation. The base peaks at 355.01 m/z and 371.04 m/z could be due to the loss of the imidazole group, $(MLH_{-2}+H\text{-imidazole})^{1+}$, and then the subsequent gain of a water molecule, $(MLH_{-2}+H\text{-imidazole}+H_2O)^{1+}$, respectively. At high m/z values there is what appears to be the presence of the complex species with a base peak at 523.08 m/z, but the exact form of the species could not be identified. This is also observed for what appears to be the uncomplexed ligand with a base peak at 540.16 m/z. The largest base peak at 404.08 m/z is the result of the uncomplexed ligand gaining two Na^+ ions in the form of $(L+2Na)^{1+}$.

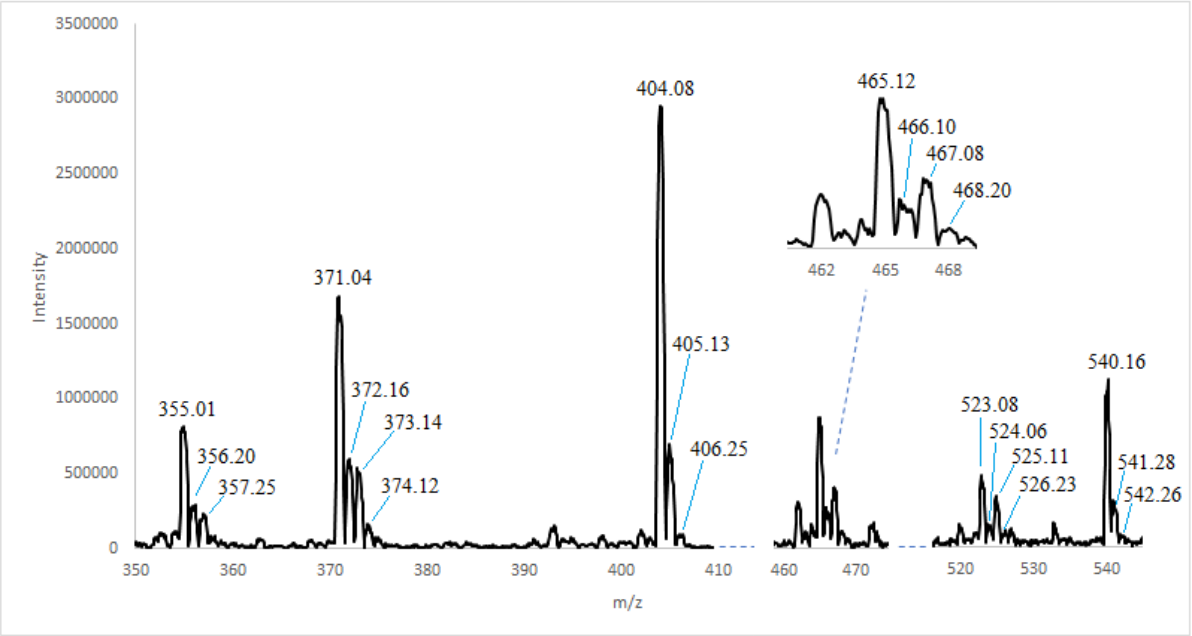

Figure 7.7: Section of the ESI-MS spectrum (positive mode) for the Cu-GFH complex at a ratio of 1:1 and concentration of 1 mM for GFH and 0.7 mM for copper(II) in aqueous solution at pH 11.

Table 7.3: Structural assignments of m/z base peaks that were found in the ESI-MS spectrum for Cu-GFH at pH 5 (positive mode) and pH 11 (positive mode) with a 1:1 ratio and concentration of 1 mM for GFH and 0.7 mM for copper(II) in aqueous solution.

m/z	pH prevalence	Assignment	Structure
354.94	pH 5	$(MLH_{-2}+H\text{-imidazole})^{1+}$	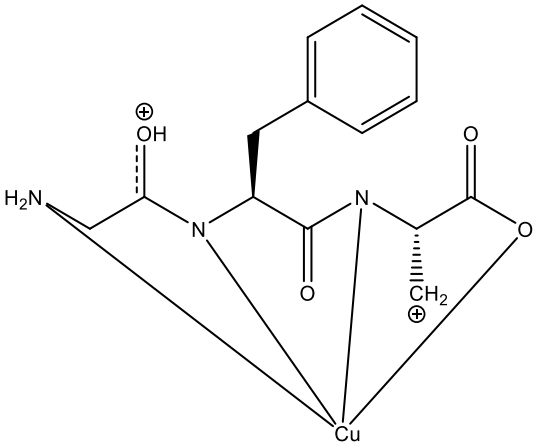 Exact Mass: 353,04
355.01	pH 11		

360.19	pH 5	$(LH+H)^{1+}$	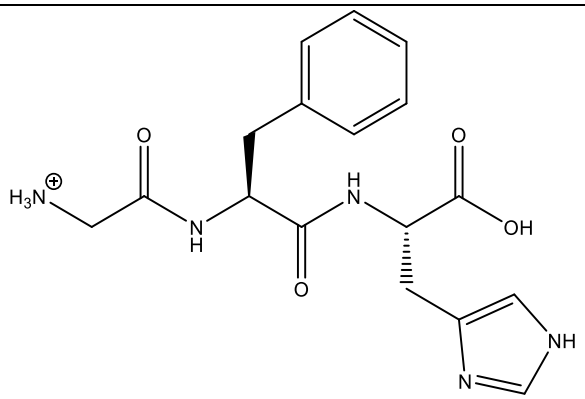 Exact Mass: 360,17
370.97	pH 5	$(MLH_{-2}+H\text{-imidazole}+H_2O)^{1+}$	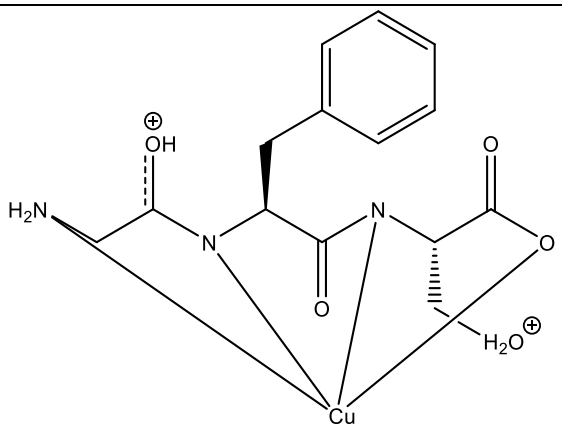 Exact Mass: 371,05
371.04	pH 11		
382.10	pH 5	$(LH+Na)^{1+}$	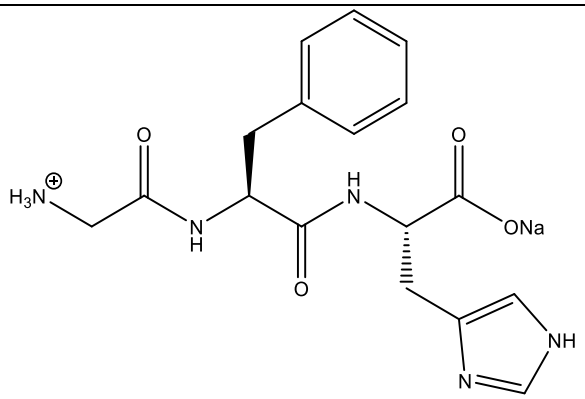 Exact Mass: 382,15
404.15	pH 5	$(L+2Na)^{1+}$	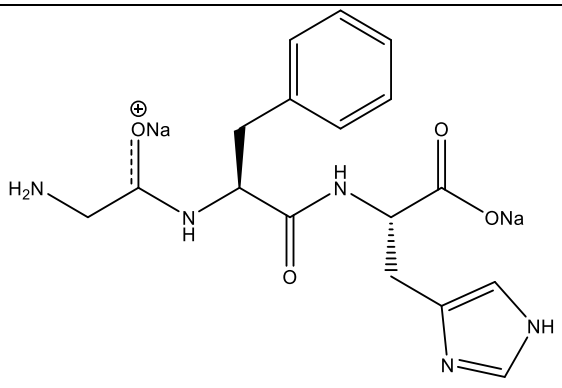 Exact Mass: 404,13
404.08	pH 11		

421.02	pH 5	$(MLH_{-2}+2H)^{1+}$	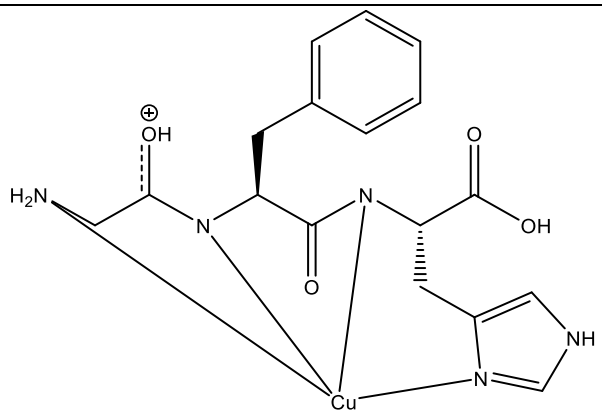 Exact Mass: 421,08
422.07	pH 5	$(M^{I}LH_{-2}+3H)^{1+}$	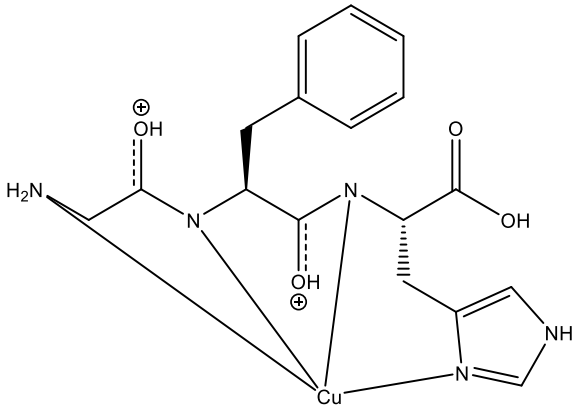 Exact Mass: 422,09
465.12	pH 11	$(MLH_{-2}+2Na)^{1+}$	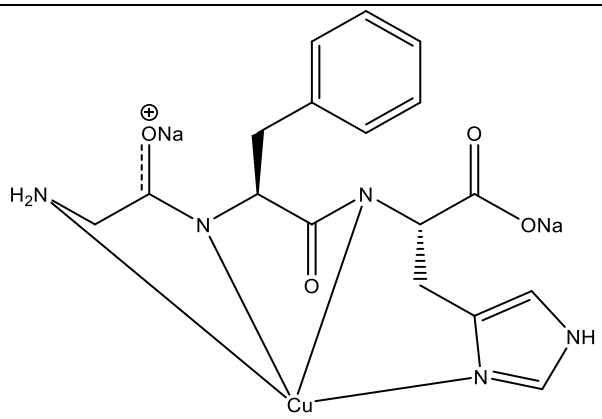 Exact Mass: 465,04
523.08	pH 11	complex	unclear
540.16	pH 11	uncomplexed ligand	unclear

7.3.4 Sar-FH

The proposed structures for the ESI-MS analysis of Cu-Sar-FH at pH 5 and pH 11 can be seen in Table 7.4 along with their corresponding base peaks.

At pH 5, the MLH and MLH_{-2} species, as well as the uncomplexed ligand, are expected to be present in solution. In the positive mode (Figure 7.8), the base peaks representing the uncomplexed ligand dominate the spectrum, whereby 374.12 m/z, 396.10 m/z and 418.22 m/z represent $(LH+H)^{1+}$, $(LH+Na)^{1+}$ and $(L+2Na)^{1+}$ respectively. The base peak at 368.03 m/z also represents the uncomplexed ligand, but after it has undergone fragmentation. A suggestion for how the ligand has undergone fragmentation involves the decomposition of the benzene ring. The decomposition of the benzene ring has been seen in literature where tropone first loses CO to yield a benzene cation radical, which then leads on to the decomposition of the benzene structure.[21] The presence of the MLH_{-2} species is verified by the peaks between 435.02 - 439.01 m/z. These peaks represent the overlap of two different forms of the MLH_{-2} species, namely where copper is Cu(II) and where copper gets reduced from Cu(II)→Cu(I). The base peak at 435.02 m/z represents the $(MLH_{-2}+2H)^{1+}$ form and the base peak at 436.07 m/z represents the $(M^{I}LH_{-2}+3H)^{1+}$ form. The base peaks at 408.00 m/z and 430.12 m/z also represent the complex after it has undergone fragmentation, as well as a reduction from Cu(II)→Cu(I). The fragmentation again is suggested to be the decomposition of the benzene ring, and so the suggested forms of the complex are $(M^{I}LH_{-2}+2H\text{-benzene ring decomposition})^{1+}$ and $(M^{I}LH_{-2}+H+Na\text{-benzene ring decomposition})^{1+}$ respectively.

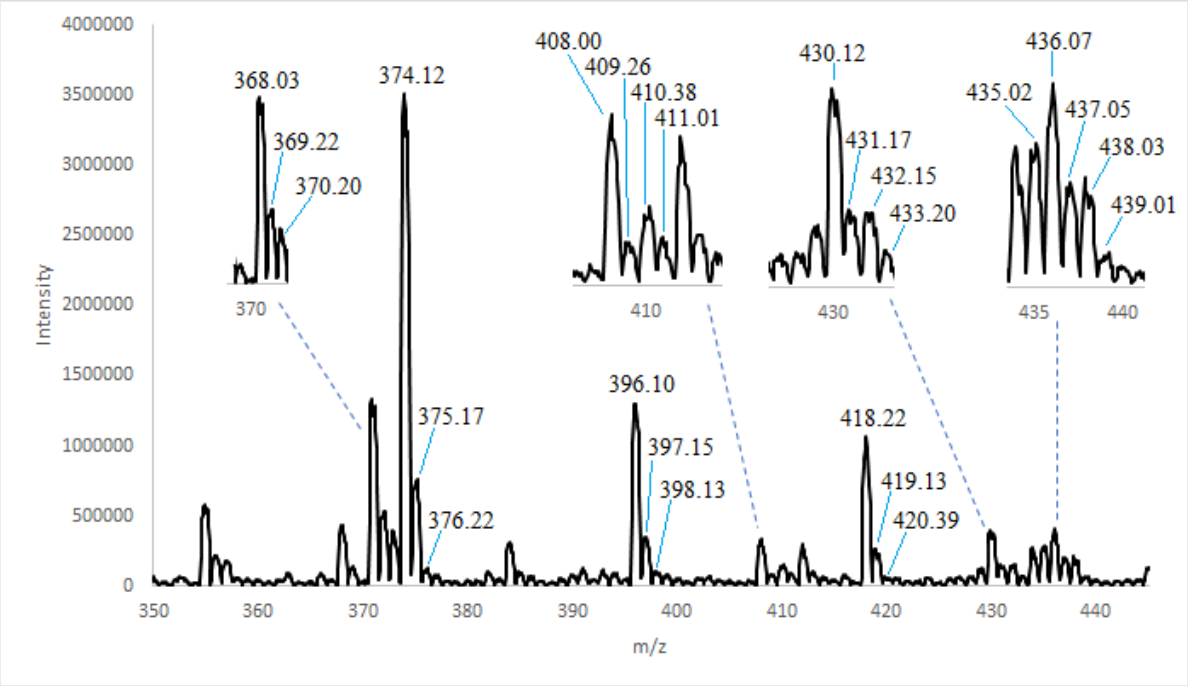

Figure 7.8: Section of the ESI-MS spectrum (positive mode) for the Cu-Sar-FH complex at a ratio of 1:1 and concentration of 1 mM for Sar-LH and 0.7 mM for copper(II) in aqueous solution at pH 5.

At pH 11, the MLH_{-2} species, as well as the uncomplexed ligand, are expected to be present. The MLH_{-2} species is verified in the positive mode spectrum (Figure 7.9), since the base peaks at 434.95 m/z and 457.07 m/z represent this species in the form of $(MLH_{-2}+2H)^{1+}$ and $(MLH_{-2}+H+Na)^{1+}$ respectively. The uncomplexed ligand dominates the spectrum with the presence of the base peaks at 187.64 m/z, 374.05 m/z and 396.03 m/z, which represent the ligand in the form of $(LH_2+H)^{2+}$, $(LH+H)^{1+}$ and $(LH+Na)^{1+}$ respectively. The base peak at 303.07 m/z also represents the uncomplexed ligand after it has fragmented. A suggestion for the fragmentation is the loss of sarcosine during the cleavage of the amide bond.

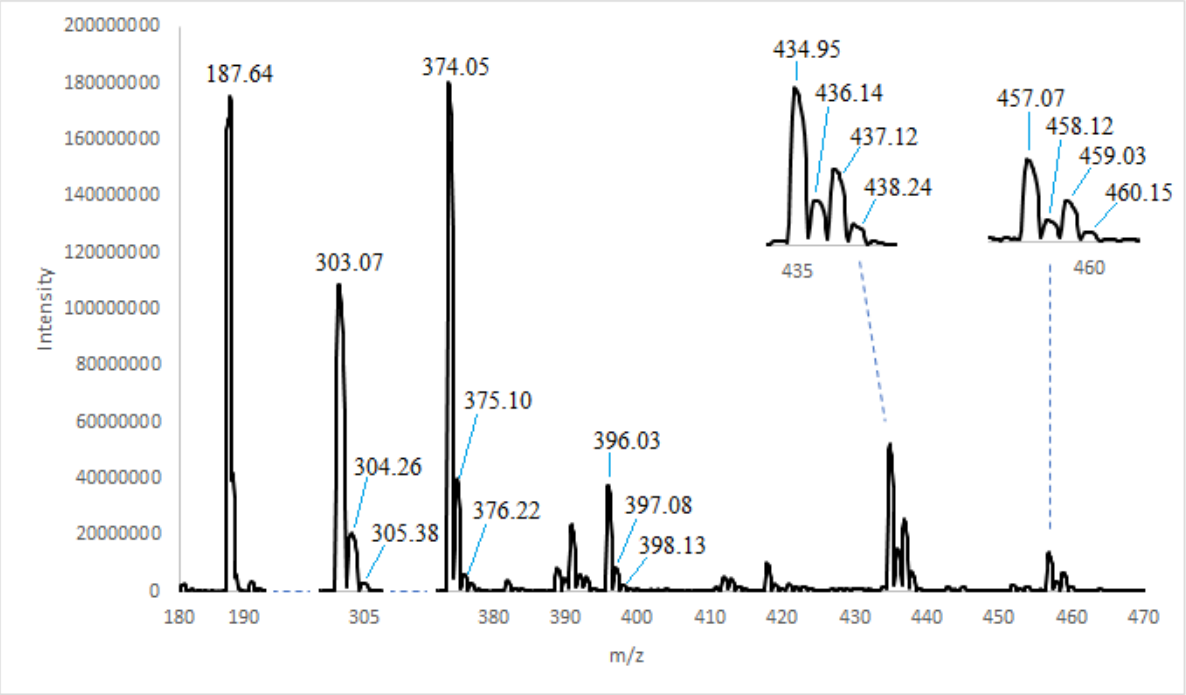

Figure 7.9: Sections of the ESI-MS spectrum (positive mode) for the Cu-Sar-FH complex at a ratio of 1:1 and concentration of 1 mM for Sar-FH and 0.7 mM for copper(II) in aqueous solution at pH 11.

Table 7.4: Structural assignments of m/z base peaks that were found in the ESI-MS spectrum for Cu-Sar-FH at pH 5 (positive mode) and pH 11 (positive mode) with a 1:1 ratio and concentration of 1 mM for Sar-FH and 0.7 mM for copper(II) in aqueous solution.

m/z	pH prevalence	Assignment	Structure
187.64	pH 11	$(LH_2+H)^{2+}$	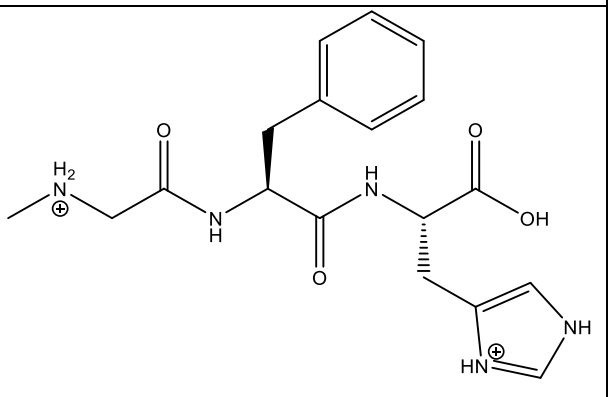 Exact Mass: 375,19

303.07	pH 11	(uncomplexed ligand fragmentation)$^{1+}$	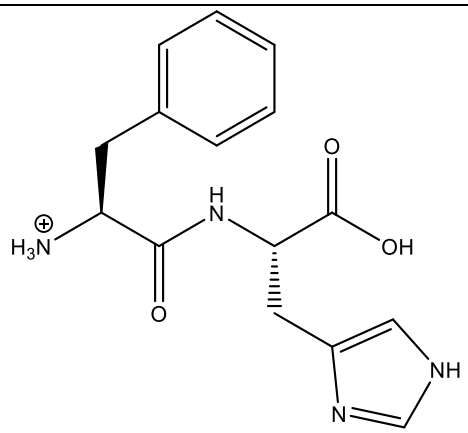 Exact Mass: 303,15
368.03	pH 5	(L+Na-benzene ring decomposition)$^{1+}$	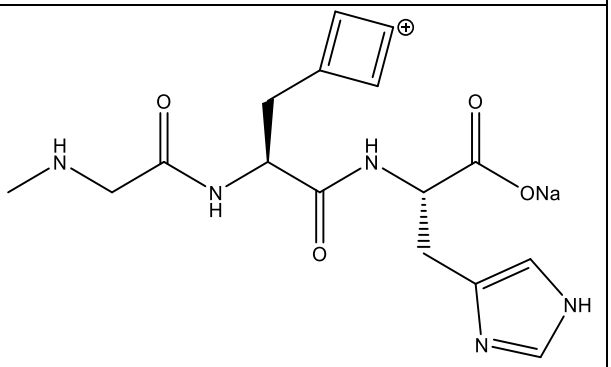 Exact Mass: 368,13
374.12	pH 5	(LH+H)$^{1+}$	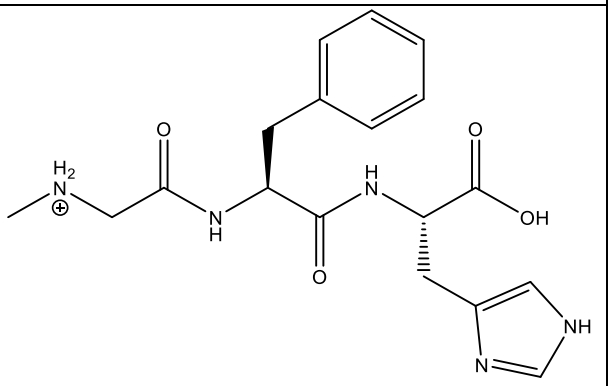 Exact Mass: 374,18
374.05	pH 11		
396.10	pH 5	(LH+Na)$^{1+}$	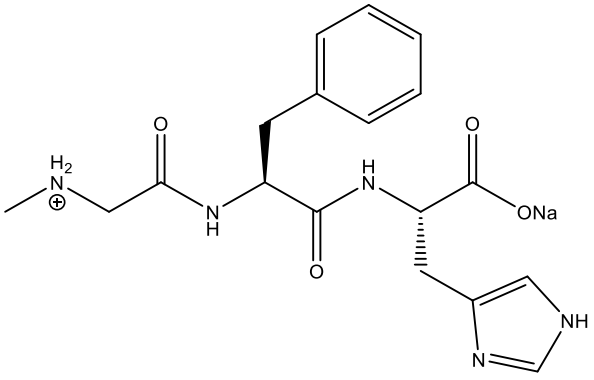 Exact Mass: 396,16
396.03	pH 11		

408.00	pH 5	($M^{I}LH_{-2}$+2H-benzene ring decomposition)$^{1+}$	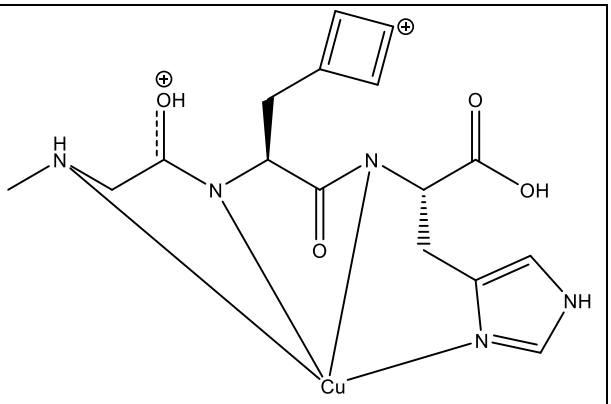 Exact Mass: 408,07
418.22	pH 5	$(L+2Na)^{1+}$	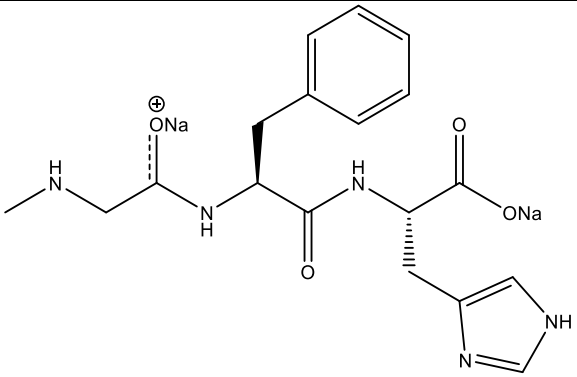 Exact Mass: 418,15
430.12	pH 5	($M^{I}LH_{-2}$+H+Na-benzene ring decomposition)$^{1+}$	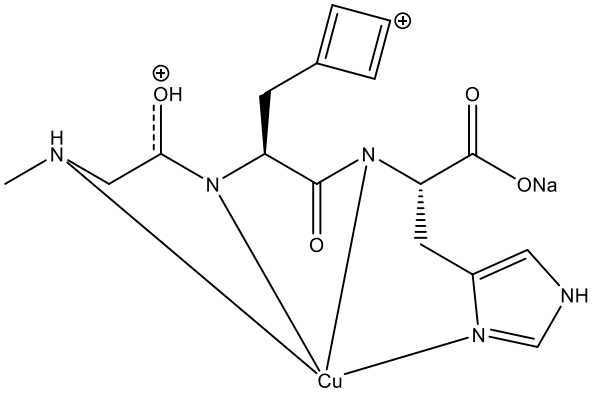 Exact Mass: 430,05
435.02	pH 5	$(MLH_{-2}+2H)^{1+}$	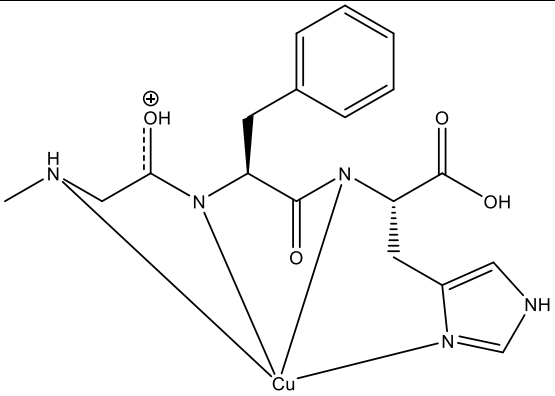 Exact Mass: 435,10
434.95	pH 11		

436.07	pH 5	$(M^{I}LH_{-2}+3H)^{1+}$	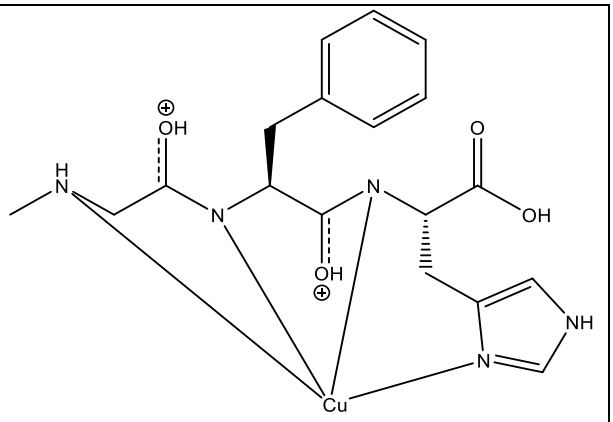 Exact Mass: 436,10
457.07	pH 11	$(MLH_{-2}+H+Na)^{1+}$	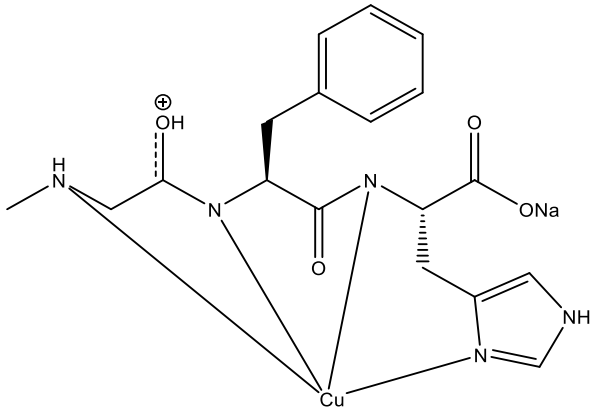 Exact Mass: 457,08

7.4 Conclusion

The identification of the MLH_{-2} species was found for all ligand complexes at both pH 5 and 11, which verifies the existence of the species. Due to the nature of electrospray ionisation, the MLH_{-2} species was mainly found in the form of $(MLH_{-2}+2H)^{1+}$ for the positive mode and $(MLH_{-2})^{1-}$ for the negative mode, but other ionised adducts were also found. These ionised adducts allow an intact complex to be analysed. Collision-induced processes also occurred, which caused the complex to become fragmented at varying regions of the ligands. They also caused the reduction of Cu(II)→Cu(I). For all the ligands, the MLH species was not identified due to its low concentration. Similarly, the ML species of Cu-Sar-LH, could not be found. The MLH_{-1} species of Cu-GLH was speculated to overlap with the peaks of MLH_{-2}, which prevented the confirmation of the MLH_{-1} species.

7.5 References

1 C. S. Ho, C. W. K. Lam, M. H. M. Chan, R. C. K. Cheung, L. K. Law, L. C. W. Lit, K. F. Ng, M. W. M. Suen and H. L. Tai, Electrospray ionisation mass spectrometry: principles and clinical applications., *Clin. Biochem. Rev.*, 2003, **24**, 3–12.

2 A. El-Aneed, A. Cohen and J. Banoub, Mass Spectrometry, Review of the Basics: Electrospray, MALDI, and Commonly Used Mass Analyzers, *Appl. Spectrosc. Rev.*, 2009, **44**, 210–230.

3 J. Fenn, M. Mann, C. Meng, S. Wong and C. Whitehouse, Electrospray ionization for mass spectrometry of large biomolecules, *Science (80-.).*, 1989, **246**, 64–71.

4 S. Banerjee and S. Mazumdar, Electrospray Ionization Mass Spectrometry: A Technique to Access the Information beyond the Molecular Weight of the Analyte, *Int. J. Anal. Chem.*, 2012, **2012**, 1–40.

5 M. Przybylski and M. O. Glocker, Electrospray Mass Spectrometry of Biomacromolecular Complexes with Noncovalent Interactions—New Analytical Perspectives for Supramolecular Chemistry and Molecular Recognition Processes, *Angew. Chemie Int. Ed. English*, 1996, **35**, 806–826.

6 E. Farkas, E. Csapó, P. Buglyó, C. A. Damante and G. Di Natale, Metal-binding ability of histidine-containing peptidehydroxamic acids: Imidazole versus hydroxamate coordination, *Inorganica Chim. Acta*, 2009, **362**, 753–762.

7 P. Gizzi, B. Henry, P. Rubini, S. Giroux and E. Wenger, A multi-approach study of the interaction of the Cu(II) and Ni(II) ions with alanylglycylhistamine, a mimicking pseudopeptide of the serum albumine N-terminal residue, *J. Inorg. Biochem.*, 2005, **99**, 1182–1192.

8 A. R. S. Ross and S. L. Luettgen, Speciation of cyclo(Pro-Gly)3 and its divalent metal-ion complexes by electrospray ionization mass spectrometry, *J. Am. Soc. Mass Spectrom.*, 2005, **16**, 1536–1544.

9 D. P. Demarque, A. E. M. Crotti, R. Vessecchi, J. L. C. Lopes and N. P. Lopes, Fragmentation reactions using electrospray ionization mass spectrometry: an important tool for the structural elucidation and characterization of synthetic and natural products, *Nat. Prod. Rep.*, 2016, **33**, 432–455.

10 A. Steckel and G. Schlosser, An Organic Chemist's Guide to Electrospray Mass Spectrometric Structure Elucidation, *Molecules*, 2019, **24**, 611.

11 E. P. L. Hunter and S. G. Lias, Evaluated Gas Phase Basicities and Proton Affinities of Molecules: An Update, *J. Phys. Chem. Ref. Data*, 1998, **27**, 413–656.

12 F.-F. Hsu and J. Turk, Structural characterization of triacylglycerols as lithiated adducts by electrospray ionization mass spectrometry using low-energy collisionally activated dissociation on a triple stage quadrupole instrument, *J. Am. Soc. Mass Spectrom.*, 1999, **10**, 587–599.

13 E. Bayer, P. Gfrörer and C. Rentel, Coordination-Ionspray-MS (CIS-MS), a Universal Detection and Characterization Method for Direct Coupling with Separation Techniques, *Angew. Chemie Int. Ed.*, 1999, **38**, 992–995.

14 J. S. McIndoe and K. L. Vikse, Assigning the ESI mass spectra of organometallic and coordination compounds, *J. Mass Spectrom.*, 2019, **54**, 466–479.

15 H. Lavanant, H. Virelizier and Y. Hoppilliard, Reduction of copper(II) complexes by electron capture in an electrospray ionization source, *J. Am. Soc. Mass Spectrom.*, 1998, **9**, 1217–1221.

16 Y. Xu, X. Zhang and A. L. Yergeycor, Electrospray ionization of copper—glycine solutions, *J. Am. Soc. Mass Spectrom.*, 1996, **7**, 25–29.

17 C. L. Gatlin, F. Turecek and T. Vaisar, Determination of Soluble Cu(I) and Cu(II) Species in Jet Fuel by Electrospray Ionization Mass Spectrometry, *Anal. Chem.*, 1994, **66**, 3950–3958.

18 T. Vaisar, C. L. Gatlin and F. Tureček, Oxidation of Peptide−Copper Complexes by Alkali Metal Cations in the Gas Phase, *J. Am. Chem. Soc.*, 1996, **118**, 5314–5315.

19 A. Tintaru, L. Charles, P. Milko, J. Roithová and D. Schröder, Redox reactions of copper(II) upon electrospray ionization in the presence of acridine ligands with an amide side chain, *J. Phys. Org. Chem.*, 2009, **22**, 229–233.

20 H. Lavanant, E. Hecquet and Y. Hoppilliard, Complexes of l-histidine with Fe2+, Co2+, Ni2+, Cu2+, Zn2+ studied by electrospray ionization mass spectrometry, *Int. J. Mass Spectrom.*, 1999, **185**–**187**, 11–23.

21 A. Ishiwata, S. Yamabe, T. Minato and T. Machiguchi, Norcaradiene intermediates in mass spectral fragmentations of tropone and tropothione., *J. Chem. Soc. Perkin Trans. 2*, 2001, 2202–2210.

8. Molecular Modelling

8.1 Introduction

Computational chemistry/molecular modelling has three broad classes that use different techniques to investigate chemical problems at molecular levels: molecular mechanics (MM), quantum mechanics (QM), and molecular dynamics (MD). QM can be split into three more methods, which are ab initio (Hartree–Fock and Post-Hartree–Fock methods) calculations, semi-empirical (SE) calculations and density functional theory (DFT). A brief explanation of the theory behind each of these methods is given below.

1. MM calculations uses a balls-and-springs system to model molecules. By knowing the spring lengths and angles between them, as well as the energy it takes to bend and stretch the springs, the energy of the whole system can then be calculated. MM is a fast method, whereby a desktop computer can optimize a large molecule, like a steroid, in seconds.

2. Ab initio calculations solve the Schrödinger equation for a molecule to give the molecule wavefunction and energy. However, approximations must be made because the equation cannot be solved exactly for a molecule that has more than one electron. These calculations are relatively slow, where a steroid molecule could take weeks on a Pentium-type machine.

3. SE calculations are also based on the Schrödinger equation, but more approximations are made to solve it. It also makes use of parameterization, which plugs experimental values into a mathematical procedure to get the best calculated values. This mixing of theory and experimental values is why it is called “semi-empirical”. SE calculations are about 100 times slower than MM, but about 100-1000 times faster than ab initio calculations.

4. DFT calculations are also based on the Schrödinger equation, but unlike the ab initio and SE calculations, DFT does not calculate a wavefunction. Instead, it derives the electron distribution directly. In terms of the speed, these calculations are faster than ab initio, but slower than SE.

5. MD calculations simulate the motion of molecules, as they change shape by applying the laws of motion.[1]

Due to limitations of computational resources in the past, many PhD theses[2–5], as well as journals[6,7] which have studied copper(II) peptide complexes, have used an MM approach. This approach can only provide details on the molecular structure (bond length, bond angle etc) and atomic charges. Presently, an MM approach is only used in the modelling of large systems such as proteins, oligosaccharides and polymers, since QM modelling is more computationally intensive for these systems. For smaller systems, higher QM techniques i.e. SE, HF, and DFT provide more accurate electronic properties since the transition states, excited states and electronic contributions are all included into the calculations, all of which are not included into MM.[8–11]

Among QM modelling, DFT is one of the most commonly and successfully used QM methods to calculate the electronic structure of atoms and molecules in gas, solution and solids states.[12–15] One of the biggest attractions is the favourable price/performance ratio compared to electron-correlated wave function-based methods. This meant that larger molecular systems could be studied with adequate accuracy, and is computationally simpler.[14,15] For this reason, as well as its ability to calculate the electronic transition within the molecule, DFT was the chosen method to study the copper(II) complexes (Cu-GLH, Cu-Sar-LH, Cu-GFH and Cu-Sar-FH).

The theory behind DFT is that the energy of an electronic system can be defined in terms of its electron probability density, F. If a system has n number of electrons, then F(r) is the total electron density at a point in space, r. From the DFT formalism, there is a one-to-one correspondence between the electron density and the energy of a system, such that the energy E is considered as the functional of the electron density $E(F)$. This means that for a given function $F(r)$, it parallels as a single energy. This advantage can be illustrated by considering a system which has n electrons. The wave function would have three coordinates for every electron, plus another coordinate for each electron to include the spin, and thus would have a total of $4n$ coordinates. In comparison, electron density only depends on three coordinates and is independent of the number of electrons that make up the system. Therefore, as the wave function complexity increases with the increasing number of electrons, the number of variables for the electron density remains the same.[12] Thus, determining the electron density functional will give the total energy of the system.

There are many types of functionals in DFT simulations that determine the total energy of the system. The approaches range from using a pure method, which uses only the electron density (local methods), or the electron density combined with the gradients (gradient corrected methods), to a hybrid method which mixes DFT and Hartree-Fock exchange energies. The idea behind hybrid functionals is that the performance improves when the exchange energies are mixed. B3LYP is the most commonly used hybrid density functional due to the good compromise between the computational cost, coverage and accuracy of results.[12,16,17] The (B3)[18,19] term is Becke's three-parameter hybrid functional, which is a combination of local and nonlocal treatments of exchange and correlation with Hartree–Fock exchange. The (LYP)[20] term is the Lee Yang and Parr correlation functional; the combination between the (B3) scheme and the (LYP) functional led to the a hybrid function which had more accurate results compared to using only a pure (B) function.[21,22] As a result of the popularity and reported accuracy, this hybrid functional was chosen to perform the calculations of the four complexes in this study.

When choosing the basis set for the ligands, which are a set of functions that describe the shape of atomic orbitals, the basis set that other studies have used when working with copper(II) complexes was considered. A study which looked at transition metals and amide side chains with the B3LYP method, specifically used the basis set, 6-31G, for the first and second row of atoms on the periodic table, as well as for the first row of transition metals.[23] Another study[24], which also focused on copper(II) complexes with the B3LYP method, also used the 6-31G basis set and it is for this reason that the copper(II) complexes of this study used the 6-31G basis set.

Once the basis set was chosen, the polarization and diffuse functions were also added. Adding these functions helps to improve the accuracy of the results. The polarization function allows the orbitals to change shape by adding orbitals with angular momentum to atoms. This addition of orbitals goes beyond what is described for their ground state, which means that for an atom like carbon the polarized basis set adds a d function. The notation is a * or (d) to symbolise a d-type polarization function on heavy atoms or f-type polarization on transition metals; and a ** or (d,p) to symbolise an additional polarization function on hydrogen. The diffuse functions are larger versions of s- and p-type functions regarding size, in comparison to the standard valence functions. This gives more space for the orbitals to occupy and is crucial for molecules that have lone pairs, anions, negative charges, excited states or any system where the electrons

are relatively far from the nucleus. The notation is a + for the diffuse function on all atoms except hydrogens (i.e. heavy atoms) and a ++ for an additional diffuse function on hydrogen atoms. In general, the higher the polarization and diffuse functions are, the more accurate the results. However, there is usually very little significant difference between + and ++.[25] For this study the functions, ++ and ** were used. These functions are not the highest, but in terms of accuracy and the timeframe for the calculations, they were adequate to be compared with the experimental data.

The procedure for finding the minimum energy of a molecule is called geometry optimization. This involves the calculation of the wave function and energy at a starting geometry and then searching to find a new geometry with a lower energy. This process is repeated until the geometry with the lowest energy is found. To achieve this, the force on each atom is calculated by finding the gradient of the energy with respect to the atomic positions. Then for each subsequent step, algorithms are used to select a new geometry with the aim of converging the structure to the lowest energy. As soon as convergence occurs, the calculation stops. The force on each atom at the final, minimum energy geometry will be zero. If the system is stable, then the energy will either be a local or global minimum. If the system is not stable, then the energy will be a saddle point. To check the stability, the frequency of each structure can be evaluated. If negative frequencies are present, then the structure has reached a saddle point and is unstable. If all the frequencies are positive, then this indicates that the structure is stable and has reached a local or global minimum.[26]

Computational methods have been used in this study for multiple reasons. The first is to verify the coordination modes of the MLH_{-2} and MLH species of Cu-GLH, Cu-Sar-LH, Cu-GFH and Cu-Sar-FH. The second is to help determine the correct coordination mode for the ML species of Cu-Sar-LH and the MLH_{-1} species of Cu-GLH. Another reason is DFT calculations can calculate the electron transition of the complexes, which is used to explain why the MLH, ML and MLH_{-1} species did not produce an observed UV-Vis absorption band.

8.2 Methodology

All calculations were performed using facilities provided by the University of Cape Town's High-Performance Computing team (hpc.uct.ac.za) using Gaussian 09 software.[27] The coordination modes for the MLH, ML, MLH_{-1} and MLH_{-2} species of Cu-GLH, Cu-Sar-LH, Cu-GFH and Cu-Sar-FH were built using the trial GaussView 6.0.16[28] software with the appropriate multiplicity and charge of each structure. The starting geometry of copper(II) was also realigned to an octahedral geometry. The multiplicity for all structures is a doublet, since copper(II) has an unpaired electron, and the charge for the MLH, ML, MLH_{-1} and MLH_{-2} species is +2, +1, 0 and -1 respectively. Each structure was then optimized at a B3LYP/6-31++G** level using water as a solvent. The solvent effect was implemented using the Solvation Model Density (SMD).[29] All optimised structures were found to be a minima with no imaginary frequency and were viewed in the demo Chemcraft program[30]. Time dependent density functional theory (TD-DFT) calculations were conducted at the same level and solvent to obtain the electronic transitions of the copper(II) complexes. Only the first three excited states were considered for these calculations.

8.3 Results and Discussion

For simplicity, the amine-N, amide-N of leucine/phenylalanine, amide-N of histidine and the imidazole-N will be referred to as N1, N2, N3 and N4 respectively. Similarly, the carbonyl-O of glycine/sarcosine, the carbonyl-O of leucine/phenylalanine and the carboxyl-O will be referred to as O1, O2 and O3 respectively. The selected labelling is illustrated in Figure 8.1; GLH was randomly chosen, but it is applicable to all ligands.

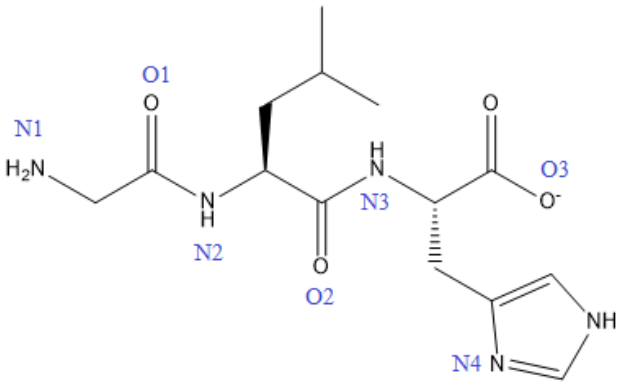

Figure 8.1: Labelling specifications for bonding sites of copper(II). GLH was randomly chosen.

8.3.1 The MLH_{-2} species

Throughout all the structure determining techniques, (potentiometry, UV-Vis, EPR, ^{1}H NMR and mass spectrometry) the MLH_{-2} species for all ligands was confirmed to be present at high pH values. UV-Vis, EPR and mass spectrometry then suggested that copper(II) coordinated as a CuN_4 chromophore to the amine (N1), two amide-Ns (N2, N3) and the imidazole-N (N4). Molecular modelling using DFT was used to validate this structure. The starting structure had copper(II) coordinate in an octahedral manner, where axial bonds were water molecules. After optimization, the axial waters were lost, and all four complexes became square planar. The resulting structures became a benchmark for an additional optimization, so that the structures could be optimized with no water molecules present. These results can be seen in Figure 8.2. A square planar complex was suggested by UV-Vis and EPR spectroscopy. The high extinction coefficient, the low $g_{\|}$ and high $A_{\|}$, as well as the high value of the superhyperfine nitrogen constant, are all in agreement with the outcome of this molecular modelling.

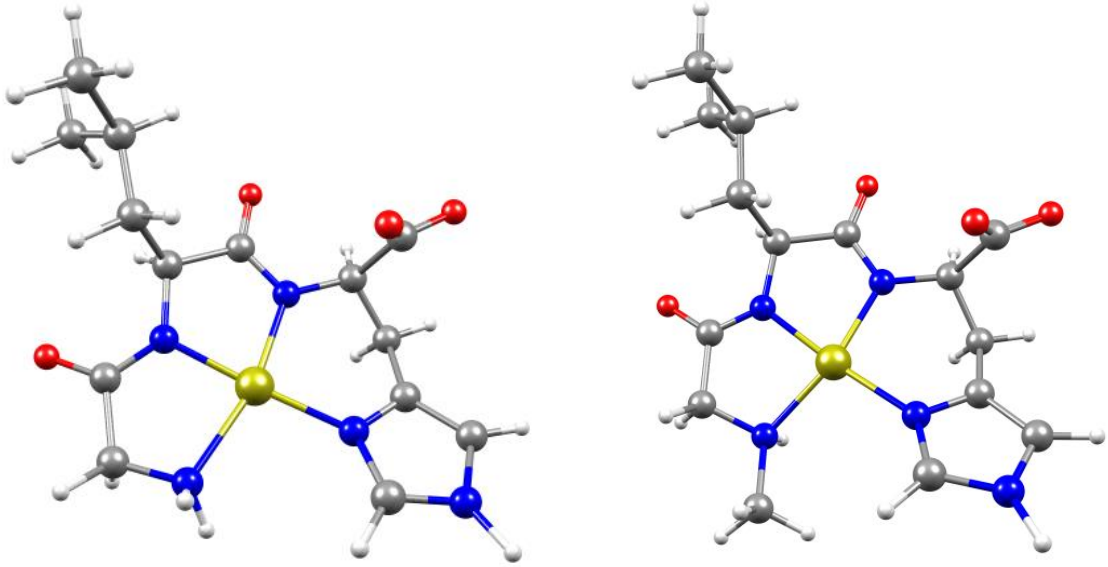

(a) (b)

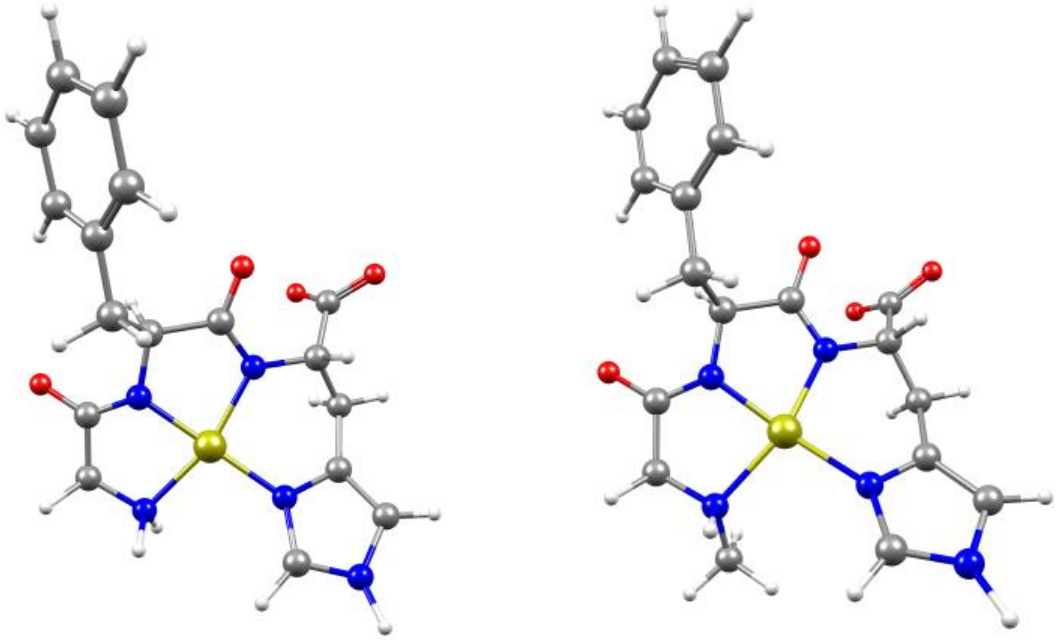

(c) (d)

Figure 8.2: Optimized structures of the MLH_{-2} species of (a) Cu-GLH, (b) Cu-Sar-LH, (c) Cu-GFH and (d) Cu-Sar-FH at B3LYP/6-31++G**.

TD-DFT is able to report the electron transition of the complexes, so that the λ_{max} associated with the complex can be calculated. Since the MLH_{-2} species is the only species in this study where the experimental λ_{max} values are known, this species was used mainly to verify that the correct DFT levels of theory and solvent effect were chosen. The rationale is that if the correct choice is made for the MLH_{-2} species, then it should be the correct choice for the MLH, ML and MLH_{-1} species. The calculated and experimental λ_{max} of MLH_{-2} can be compared to verify

that they agree with one another and this comparison can be seen in Table 8.1. The difference between the calculated and experimental λ_{max} is 2-18 nm, which is close enough to verify that the two values agree with one another and therefore signify that the selected DFT levels (B3LYP/6-31++G**) and solvent effect (SMD) are valid for this system.

Table 8.1: The calculated and experimental λ_{max} of the MLH_{-2} species from Cu-GLH, Cu-Sar-LH, Cu-GFH and Cu-Sar-FH.

Complex	**λ_{max} (nm)**	
	B3LYP/6-31++G**	**experimental**
Cu-GLH	516	518
Cu-Sar-LH	541	523
Cu-GFH	527	517
Cu-Sar-FH	534	521

To verify the validity of the DFT outputs, the obtained bond lengths and bond angles for the MLH_{-2} species were compared to the previously reported X-ray structures of similar complexes and can be seen in Table 8.2 and Table 8.3 respectively.

Table 8.2: Bond lengths from the MLH_{-2} coordination mode of Cu-GLH, Cu-Sar-LH, Cu-GFH and Cu-Sar-FH.

Labelled bond length	**Complex**	**Bond length (Å) B3LYP/6-31++G****	**Bond length (Å) literature**
Cu-N1	Cu-GLH Cu-Sar-LH Cu-GFH Cu-Sar-FH	2.086 2.136 2.092 2.109	1.883 - 2.043[31–34]
Cu-N2	Cu-GLH Cu-Sar-LH Cu-GFH Cu-Sar-FH	1.933 1.932 1.931 1.932	1.907 - 2.05[31,33,35,36]
Cu-N3	Cu-GLH Cu-Sar-LH Cu-GFH Cu-Sar-FH	1.991 2.000 2.000 1.997	
Cu-N4	Cu-GLH Cu-Sar-LH Cu-GFH Cu-Sar-FH	1.991 1.997 1.991 2.000	1.883 - 2.00[31–33]

Table 8.3: Bond angles from the MLH_{-2} coordination mode of Cu-GLH, Cu-Sar-LH, Cu-GFH and Cu-Sar-FH.

Labelled bond angle	Complex	Bond angle (°), B3LYP/6-31++G**	Bond angle (°) literature
N1-Cu-N2	Cu-GLH Cu-Sar-LH Cu-GFH Cu-Sar-FH	82.0 82.0 82.2 82.4	80.8 - 99.6[32,33,37–39]
N2-Cu-N3	Cu-GLH Cu-Sar-LH Cu-GFH Cu-Sar-FH	82.5 82.4 82.6 82.6	
N3-Cu-N4	Cu-GLH Cu-Sar-LH Cu-GFH Cu-Sar-FH	95.1 94.0 95.3 94.6	
N4-Cu-N1	Cu-GLH Cu-Sar-LH Cu-GFH Cu-Sar-FH	100.5 103.8 101.0 101.7	
N1-Cu-N3	Cu-GLH Cu-Sar-LH Cu-GFH Cu-Sar-FH	164.3 156.1 163.0 163.3	164.2 - 177.5[32,33,37–39]
N2-Cu-N4	Cu-GLH Cu-Sar-LH Cu-GFH Cu-Sar-FH	176.3 171.2 169.9 166.1	

The bond lengths of Cu-N1 were found to be the longest for each ligand complex and were slightly longer than literature values, which means that this bond is experiencing slight torsional strain. The Cu-N2 bonds were found to be the shortest for each ligand complex, which means that this bond type experiences the least amount of torsional strain. The Cu-N3 bonds are of a similar length to the Cu-N4 bonds. The Cu-N2, Cu-N3 and Cu-N4 bond lengths are within literature values.

For the bond angles, the MLH_{-2} species has four main angles that should be close to 90°; the N1-Cu-N2 angle, the N2-Cu-N3 angle, the N3-Cu-N4 angle and the N4-Cu-N1 angle. For all the MLH_{-2} species these angles deviated from the optimum angle as a result of torsional strain, which makes the square planar geometry slightly distorted. The N4-Cu-N1 angle was found to be the most strained. The deviations are either within the literature range, or in the case of the N4-Cu-N1 angle, slightly larger but still comparable. Another factor to consider for planar complexes, is to check if the structure is indeed planar. The bond angles that will verify the planar aspect of the complex is the angle between N1-Cu-N3, as well as the angle between N2-

Cu-N4. These angles ideally should be 180°, but all the MLH_{-2} species were found to deviate from this angle. The deviation of the N1-Cu-N3 angle is more significant and the angle is slightly smaller than the literature values, while the deviation of N2-Cu-N4 is within literature values. The planar aspect can also be checked by measuring the dihedral angle of the plane created from N1-N2-N3-N4 (Table 8.4). For a planar geometry the dihedral angle should be 0°, so looking at Table 8.4, all the complexes deviate from planarity with the Cu-GLH deviating the least and Cu-Sar-LH deviating the most. Additionally, the methyl group on the amine reduces the planarity of the complex by 15.834° when comparing Cu-GLH and Cu-Sar-LH, and by 2.512° when comparing Cu-GFH and Cu-Sar-FH.

Table 8.4: Dihedral angles from the MLH_{-2} coordination mode of Cu-GLH, Cu-Sar-LH, Cu-GFH and Cu-Sar-FH.

Complex	**N1-N2-N3-N4 dihedral angle, B3LYP/6-31++G****
Cu-GLH	-4.102
Cu-Sar-LH	-19.936
Cu-GFH	-12.698
Cu-Sar-FH	-15.210

Overall, all the bond angle deviations are comparable to literature and along with the bond lengths, also verify that the B3LYP/6-31++G** level is valid for this system.

8.3.2 The MLH species

^{1}H-NMR was the main contributing structure determining technique that identified the MLH species for all ligands. EPR also found the MLH species, but only for the Sar-LH ligand. ^{1}H-NMR identified that copper(II) coordinates to each ligand at two different locations to form the MLH species. The one location is on the amine (N1) and neighbouring carbonyl-O (O1) with the imidazole-N protonated, and the other location is on the imidazole-N (N4) and carboxyl-O (O3) with the amine protonated. Molecular modelling using DFT was used to validate these coordination modes and then obtain the λ_{max} values from the DFT output. By obtaining the λ_{max} values a reason can be proposed as to why this species could not be detected on the UV-Vis spectra.

Each structure started with copper(II) in an octahedral environment with water molecules taking up vacant sites. After optimization, all coordination modes, except for coordination mode (b) of GLH and coordination mode (b) of Sar-LH, lost an axially coordinated water molecule and became square pyramidal. Coordination mode (b) of GLH and Sar-LH became tetragonally distorted octahedral. The square pyramidal geometries became a starting point for an additional optimization without the non-bonding water molecule. The optimized structures with their relative energy differences can be seen in Figures 8.3-8.6. Each coordination mode has been represented in both a face down view (Figures 8.3-8.6 (i)), as well as a side view (Figures 8.3-8.6 (ii)). The face down view shows the coordination sites, as well as the overall structure of the species, while the side view shows the square pyramidal or tetragonally distorted octahedral geometry. The axial water molecules were omitted from the face down view so that they did not obstruct the view of the coordination bonds. When comparing the ground state energy difference between coordination modes (a) and (b) for each ligand, coordination mode (b) of GLH and Sar-LH have one more water molecule than their respective coordination mode (a) structures. Therefore, to compare the energy of these structures the ground state energy of water under the same conditions (B3LYP/6-31++G**) was added to the energy of coordination mode (a). Note that in these calculations, entropy changes were not taken into account. The energy difference between the two coordination modes for all ligands is between 1.79-10.86 kJ/mol. This small energy difference means that there is an almost equal probability of both coordination modes forming, which agrees with the proposal that two coordination modes for MLH occur simultaneously.

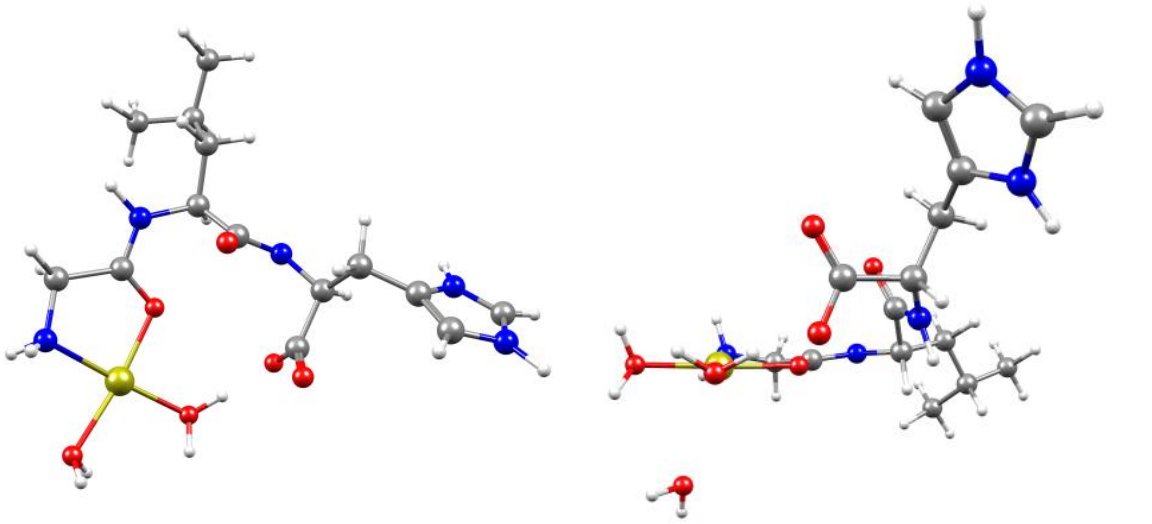

(i) (ii)

(a)
0.00 kJ/mol

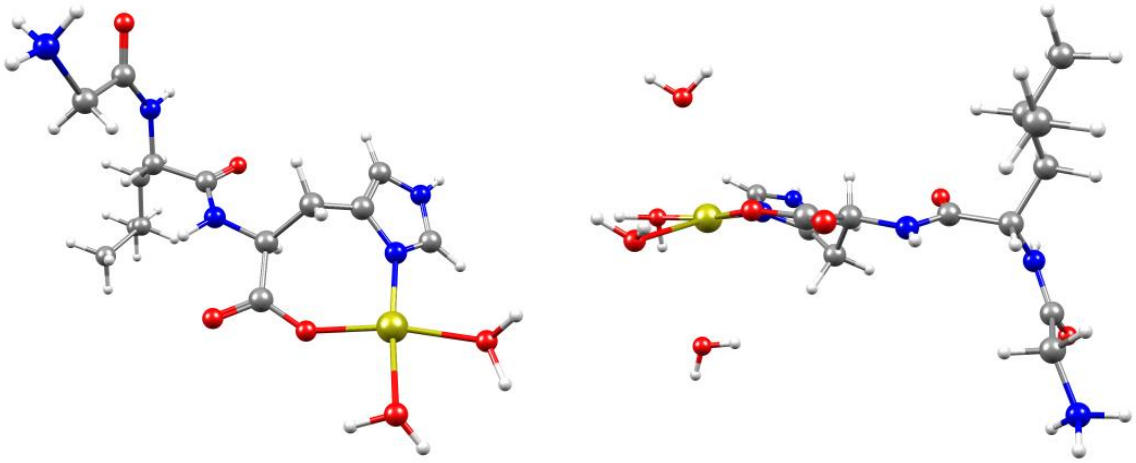

(i) (ii)

(b)
1.79 kJ/mol

Figure 8.3: Optimized structures of the MLH species from Cu-GLH at B3LYP/6-31++G**. Coordination mode (a) has an amine (N1) and neighbouring carbonyl-O (O1) coordination and coordination mode (b) has an imidazole-N (N4) and carboxyl-O (O3) coordination. (ai) and (bi) represent the coordination modes at a face down angle with removed axial water bonds, and (aii) and (bii) represent the coordination modes at a side angle.

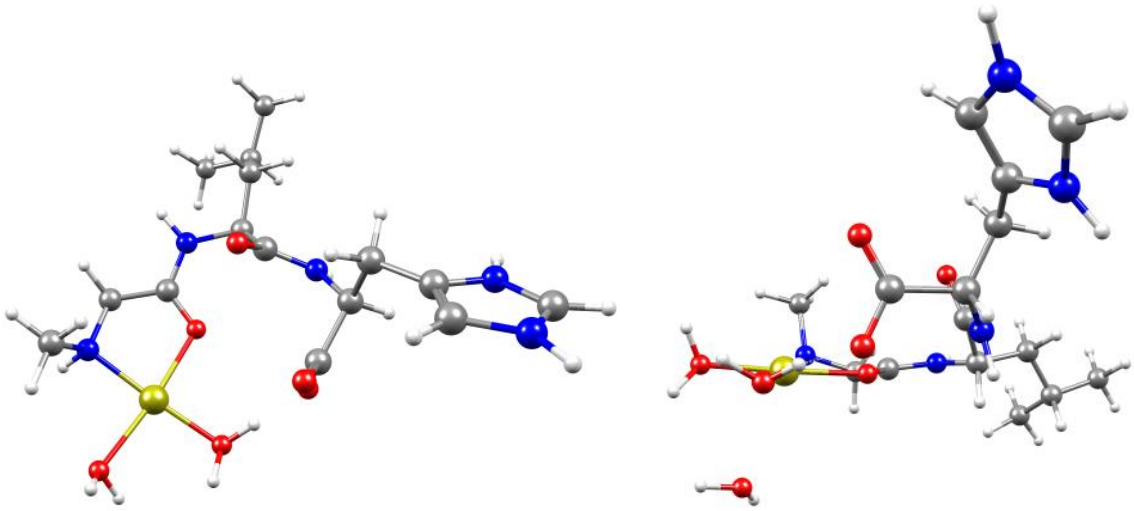

(i) (ii)

(a)
4.74 kJ/mol

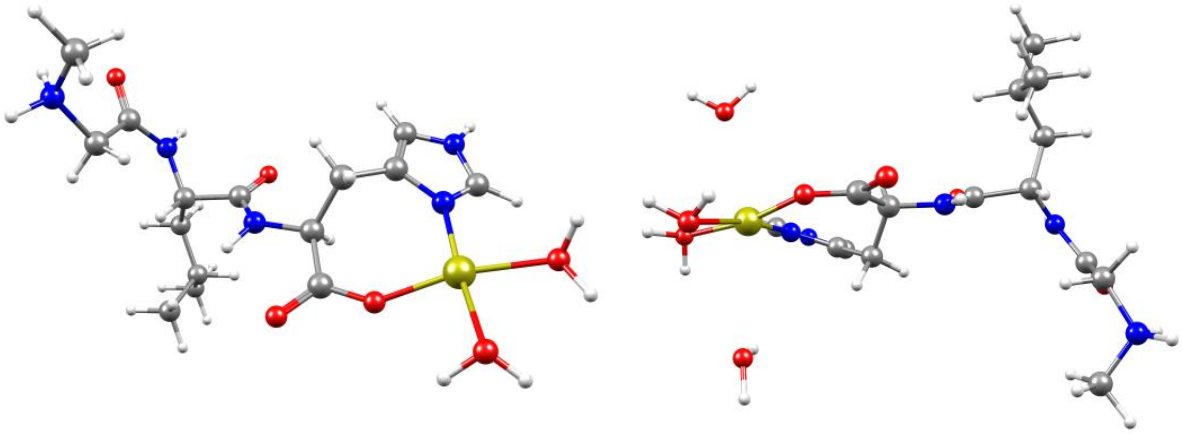

(i) (ii)

(b)
0.00 kJ/mol

Figure 8.4: Optimized structures of the MLH species from Cu-Sar-LH at B3LYP/6-31++G**. Coordination mode (a) has an amine (N1) and neighbouring carbonyl-O (O1) coordination and coordination mode (b) has an imidazole-N (N4) and carboxyl-O (O3) coordination. (ai) and (bi) represent the coordination modes at a face down angle with removed axial water bonds, and (aii) and (bii) represent the coordination modes at a side angle.

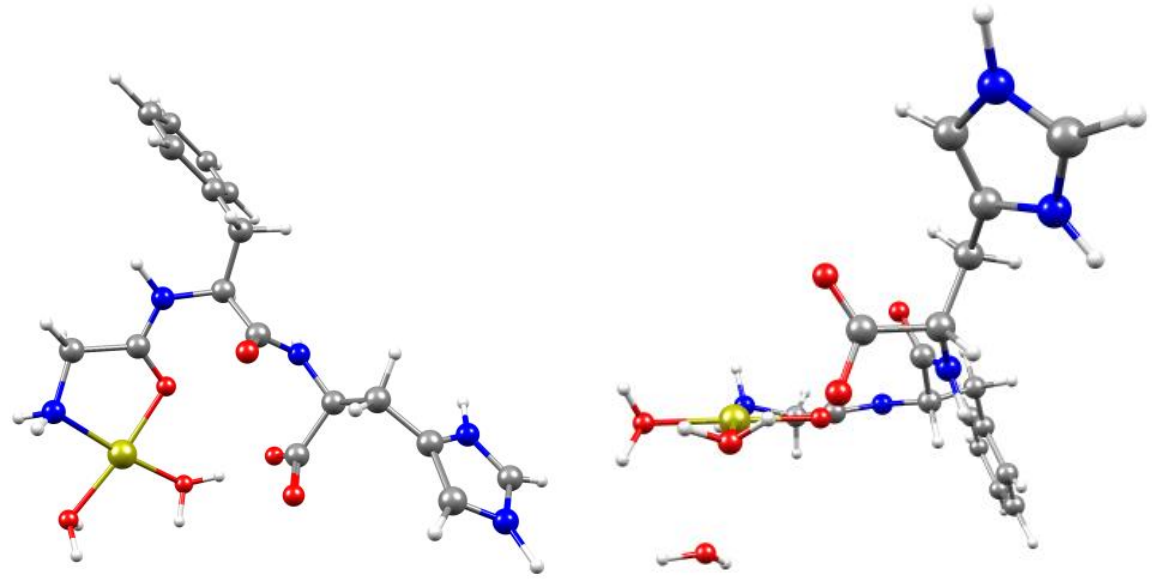

(i) (ii)

(a)
0.00 kJ/mol

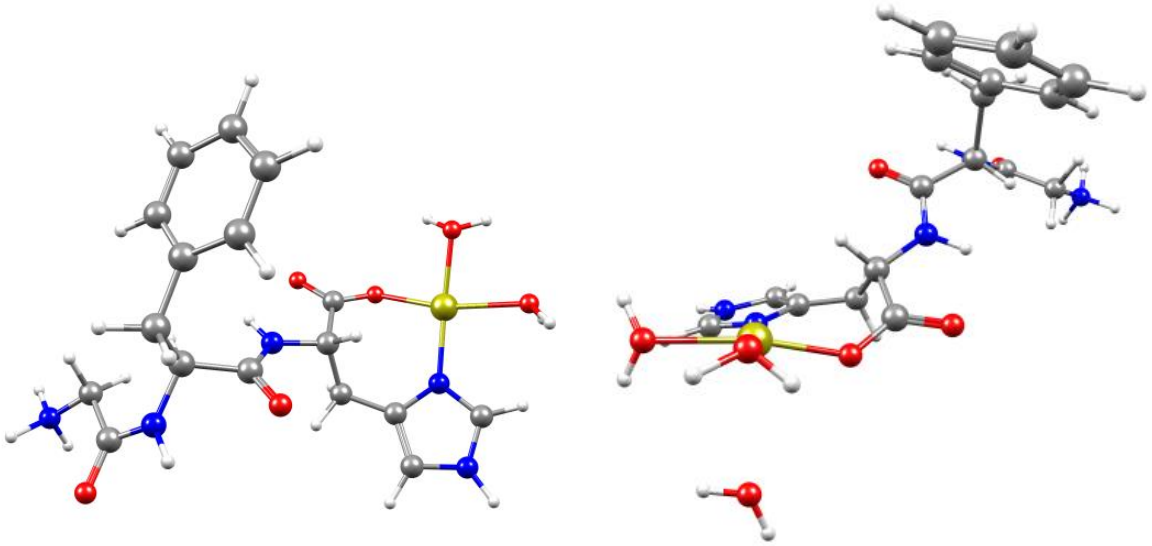

(i) (ii)

(b)
10.86 kJ/mol

Figure 8.5: Optimized structures of the MLH species from Cu-GFH at B3LYP/6-31++G**. Coordination mode (a) has an amine (N1) and neighbouring carbonyl-O (O1) coordination and coordination mode (b) has an imidazole-N (N4) and carboxyl-O (O3) coordination. (ai) and (bi) represent the coordination modes at a face down angle with removed axial water bonds, and (aii) and (bii) represent the coordination modes at a side angle.

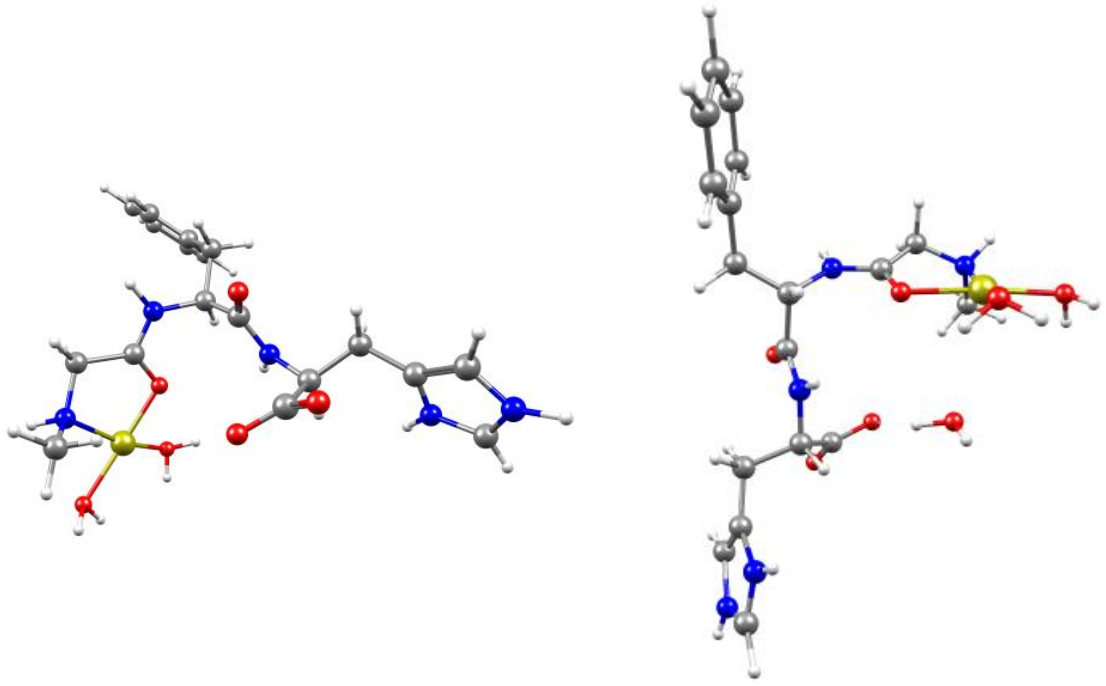

(i) (ii)

(a)
7.10 kJ/mol

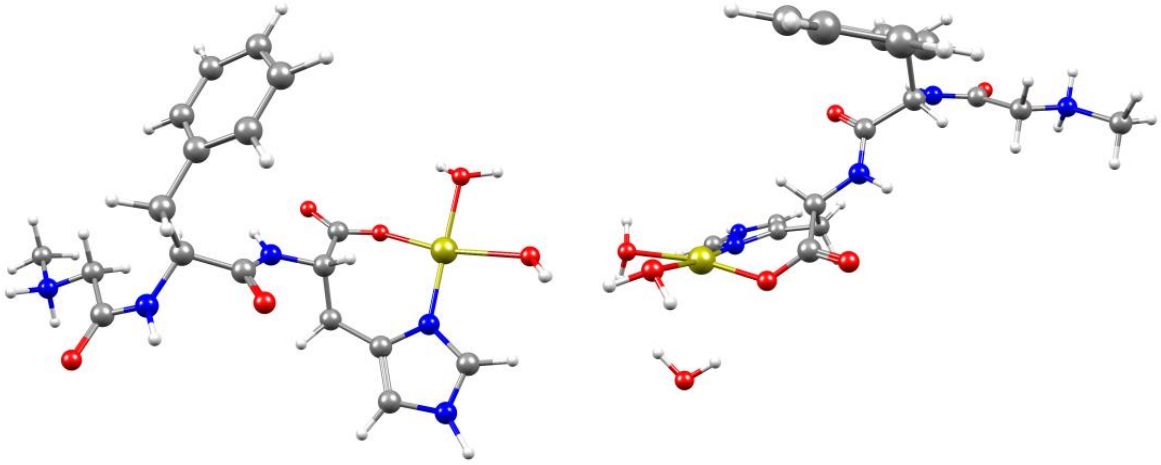

(i) (ii)

(b)
0.00 kJ/mol

Figure 8.6: Optimized structures of the MLH species from Cu-Sar-FH at B3LYP/6-31++G**. Coordination mode (a) has an amine (N1) and neighbouring carbonyl-O (O1) coordination and coordination mode (b) has an imidazole-N (N4) and carboxyl-O (O3) coordination. (ai) and (bi) represent the coordination modes at a face down angle with removed axial water bonds, and (aii) and (bii) represent the coordination modes at a side angle.

The resulting structures produced electronic transitions with calculated λ_{max} values to be between 699-889 nm (Table 8.5). The measured range of the experimental UV-Vis spectrum is 200-800 nm, and so the coordination modes that have experimental λ_{max} values above this range, means that the spectrophotometer will not be able to detect them, since they will appear in the near-infrared region. Nevertheless, besides the spectrophotometer not being able to detect the λ_{max} values above 800 nm, $Cu(H_2O)_6$ produces a broad absorption band with a λ_{max} value at 800 nm. This means that any compound with a λ_{max} occurring at approximately 700-800 nm, will overlap with the absorption band of $Cu(H_2O)_6$. It also means that the λ_{max} values occurring just beyond the measured range will also overlap, since the $Cu(H_2O)_6$ absorption band extends into the near-infrared region. Therefore, since the MLH species have a low concentration prevalence (according to the potentiometric speciation diagrams), the MLH absorption band for all the coordination modes will be concealed by the absorption band of $Cu(H_2O)_6$. This provides a plausible explanation for why the MLH species could not be detected on the UV-Vis spectrum. It also agrees with the suggestion made in the UV-Vis section that the MLH species is being hidden by the absorption band of $Cu(H_2O)_6$.

Table 8.5: The calculated λ_{max} at B3LYP/6-31++G** of coordination modes (a) and (b) of the MLH species from Cu-GLH, Cu-Sar-LH, Cu-GFH and Cu-Sar-FH.

Complex	**Coordination mode**	**Calculated λ_{max} (nm)**
Cu-GLH	(a)	710
	(b)	882
Cu-Sar-LH	(a)	699
	(b)	889
Cu-GFH	(a)	837
	(b)	875
Cu-Sar-FH	(a)	707
	(b)	868

Again, to verify the DFT calculations, the bond lengths and bond angles of MLH were compared to literature and can be seen in Table 8.6 and Table 8.7 respectively. Since there are water molecules bonded in each species, the labelling for each atom of interest in both coordination modes (a) and (b) can be seen in Figure 8.7. The random selection of coordination mode (a) from GLH was chosen to represent the labelling for all coordination mode (a) species. For the coordination mode (b) species, GLH was randomly chosen to represent the labelling of the tetragonally distorted octahedral geometries and GFH was randomly chosen to represent the square pyramidal geometries.

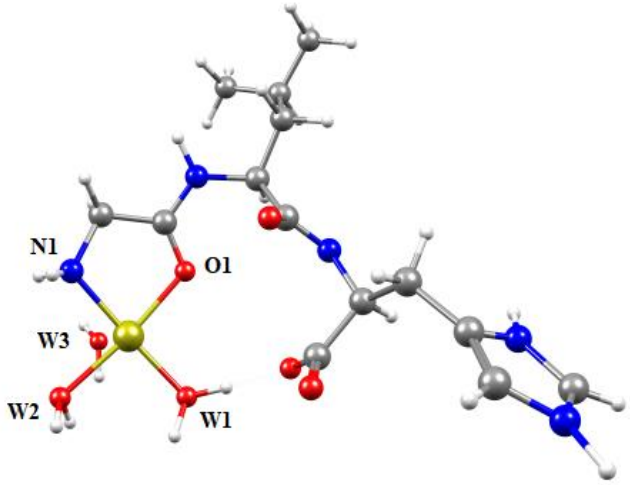

(a)

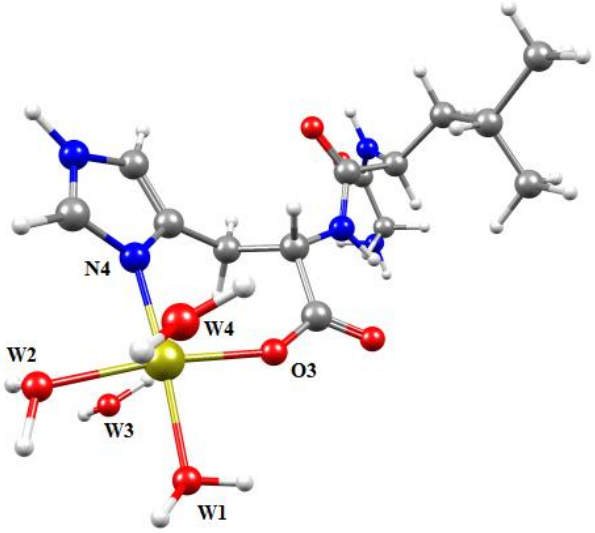

(bi)

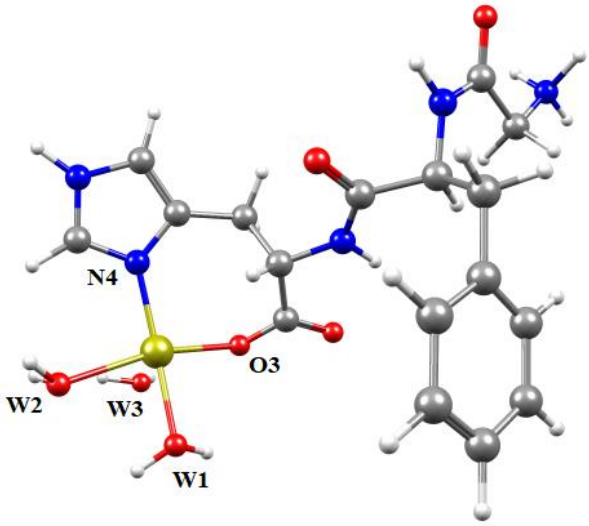

(bii)

Figure 8.7: Labelling specifications for MLH coordination mode (a), where GLH was randomly chosen. Labelling specifications for MLH coordination mode (b), where GLH was randomly chosen to represent the tetragonally distorted octahedral geometries (bi) and GFH was randomly chosen to represent the square pyramidal geometries (bii).

Table 8.6: Bond lengths of coordination modes (a) and (b) for the MLH species of Cu-GLH, Cu-Sar-LH, Cu-GFH and Cu-Sar-FH.

Coordination mode	**Labelled bond length**	**Complex**	**Bond length (Å) B3LYP/6-31++G****	**Bond length (Å) literature**
(a)	Cu-N1	Cu-GLH Cu-Sar-LH Cu-GFH Cu-Sar-FH	2.027 2.038 2.022 2.031	1.883 - 2.043[31–34]
	Cu-O1	Cu-GLH Cu-Sar-LH Cu-GFH Cu-Sar-FH	2.002 2.007 2.006 1.997	1.902 - 1.974[39]
	Cu-W1	Cu-GLH Cu-Sar-LH Cu-GFH Cu-Sar-FH	2.003 2.007 1.985 2.038	1.95 - 1.98[34,40]
	Cu-W2	Cu-GLH Cu-Sar-LH Cu-GFH Cu-Sar-FH	2.054 2.053 2.052 2.038	
	Cu-W3	Cu-GLH Cu-Sar-LH Cu-GFH Cu-Sar-FH	3.061 3.059 3.242 3.405	2.225 - 2.943[31,34,41,42]
(b)	Cu-N4	Cu-GLH Cu-Sar-LH Cu-GFH Cu-Sar-FH	1.978 1.979 2.011 2.011	1.883 - 2.00[31–33]
	Cu-O3	Cu-GLH Cu-Sar-LH Cu-GFH Cu-Sar-FH	1.969 1.969 1.958 1.959	1.902 - 1.974[39]
	Cu-W1	Cu-GLH Cu-Sar-LH Cu-GFH Cu-Sar-FH	2.074 2.074 2.047 2.049	1.95 - 1.98[34,40]
	Cu-W2	Cu-GLH Cu-Sar-LH Cu-GFH Cu-Sar-FH	2.080 2.086 2.071 2.070	
	Cu-W3	Cu-GLH Cu-Sar-LH Cu-GFH Cu-Sar-FH	3.068 3.417 3.068 3.082	2.225 - 2.943[31,34,41,42]
	Cu-W4	Cu-GLH Cu-Sar-LH Cu-GFH Cu-Sar-FH	3.401 3.368 - -	

Table 8.7: Bond angles of coordination modes (a) and (b) for the MLH species of Cu-GLH, Cu-Sar-LH, Cu-GFH and Cu-Sar-FH.

Coordination mode	Labelled bond angle	Complex	Bond angle (°), B3LYP/6-31++G**	Bond angle (°) literature
(a)	N1-Cu-O1	Cu-GLH Cu-Sar-LH Cu-GFH Cu-Sar-FH	82.9 82.9 82.7 83.0	80.8° - 99.6°[32,33,37–39]
	O1-Cu-W1	Cu-GLH Cu-Sar-LH Cu-GFH Cu-Sar-FH	94.4 93.9 92.4 91.3	
	W1-Cu-W2	Cu-GLH Cu-Sar-LH Cu-GFH Cu-Sar-FH	92.9 92.8 93.8 94.9	
	W2-Cu-N1	Cu-GLH Cu-Sar-LH Cu-GFH Cu-Sar-FH	89.8 90.2 91.0 92.2	
	N1-Cu-W1	Cu-GLH Cu-Sar-LH Cu-GFH Cu-Sar-FH	174.2 173.8 174.7 164.7	164.2° - 177.5°[32,33,37–39]
	O1-Cu-W2	Cu-GLH Cu-Sar-LH Cu-GFH Cu-Sar-FH	172.7 173.0 173.4 172.0	
	N1-Cu-W3	Cu-GLH Cu-Sar-LH Cu-GFH Cu-Sar-FH	93.6 94.0 87.8 102.9	84.7° - 111.2°[32,34,41]
	O1-Cu-W3	Cu-GLH Cu-Sar-LH Cu-GFH Cu-Sar-FH	105.5 107.1 101.7 77.3	
	W1-Cu-W3	Cu-GLH Cu-Sar-LH Cu-GFH Cu-Sar-FH	92.1 92.1 91.2 89.6	
	W2-Cu-W3	Cu-GLH Cu-Sar-LH Cu-GFH Cu-Sar-FH	75.0 74.3 76.3 97.6	
(b)	N4-Cu-O3	Cu-GLH Cu-Sar-LH Cu-GFH Cu-Sar-FH	101.1 101.6 98.2 97.6	80.8° - 99.6°[32,33,37–39]
	O3-Cu-W1	Cu-GLH Cu-Sar-LH Cu-GFH Cu-Sar-FH	82.6 82.1 85.0 85.5	
	W1-Cu-W2	Cu-GLH Cu-Sar-LH Cu-GFH Cu-Sar-FH	89.2 88.9 82.0 82.2	

	W2-Cu-N4	Cu-GLH Cu-Sar-LH Cu-GFH Cu-Sar-FH	88.4 88.6 95.7 95.4	
	N4-Cu-W1	Cu-GLH Cu-Sar-LH Cu-GFH Cu-Sar-FH	170.4 170.9 172.8 173.3	164.2° - 177.5°[32,33,37–39]
	O3-Cu-W2	Cu-GLH Cu-Sar-LH Cu-GFH Cu-Sar-FH	168.5 167.8 164.5 165.8	
	N1-Cu-W3	Cu-GLH Cu-Sar-LH Cu-GFH Cu-Sar-FH	89.2 87.2 101.9 99.8	84.7° - 111.2°[32,34,41]
	O1-Cu-W3	Cu-GLH Cu-Sar-LH Cu-GFH Cu-Sar-FH	105.7 105.4 81.9 83.7	
	W1-Cu-W3	Cu-GLH Cu-Sar-LH Cu-GFH Cu-Sar-FH	81.3 83.8 84.9 86.4	
	W2-Cu-W3	Cu-GLH Cu-Sar-LH Cu-GFH Cu-Sar-FH	80.8 81.7 88.5 88.4	
	N1-Cu-W4	Cu-GLH Cu-Sar-LH Cu-GFH Cu-Sar-FH	93.9 93.6 - -	
	O1-Cu-W4	Cu-GLH Cu-Sar-LH Cu-GFH Cu-Sar-FH	90.6 90.3 - -	
	W1-Cu-W4	Cu-GLH Cu-Sar-LH Cu-GFH Cu-Sar-FH	94.9 94.8 - -	
	W2-Cu-W4	Cu-GLH Cu-Sar-LH Cu-GFH Cu-Sar-FH	82.1 82.2 - -	

Looking at Table 8.6, the bond lengths of the equatorial bonds in coordination mode (a) are all relatively the same magnitude, which means that all the bonds are experiencing a similar or symmetrical torsional strain. While in coordination mode (b), for GLH and Sar-LH, N4-Cu and Cu-O3 are the shortest equatorial bond lengths and Cu-W1 and Cu-W2 the longest; and for GFH and Sar-FH, Cu-O3 is the shortest equatorial bond length and Cu-W1 and Cu-W2 are the longest. This means that the bonds coordinating copper(II) to the ligand are experiencing less strain than the bonds between copper(II) and water. All the equatorial bond lengths from both coordination modes (a) and (b) are comparable to literature. The axial bonds, Cu-W3 and Cu-

W4, are recorded to be relatively longer than literature values for both coordination mode (a) and (b). This raised the question regarding whether the bond is present or not and resulted in the bond being removed and the structures reoptimized. The resultant λ_{max} values for these reoptimized structures were still between approximately 700-850 nm. Since these reoptimized structures were then square planar, a λ_{max} value of 700-850 nm is not possible as square planar geometries have λ_{max} values of about 526 nm[43]. This therefore showed that the axial bond was significant and should be included. $Cu(H_2O)_6$ was optimised under the same conditions (B3LYP/6-31++G**) as the complexes, so that the axial bond lengths could be measured. The two axial bond lengths were recorded to be 3.048 Å and 3.129 Å. These bond lengths are also relatively long compared to literature and so justifies that the axial water bonds in a complex are expected to be of a similar length or slightly longer, which is what is seen in the MLH coordination modes.

All the bond angles in a square pyramidal or octahedral geometry should be close to 90° and the planar aspect should be close to 180°. Looking at Table 8.7, the equatorial bond angles of coordination mode (a) are all relatively close to the optimum 90° and fall within literature ranges. The N1-Cu-O1 angle deviates the most, while the other three angles are approximately equal in magnitude and are only a few degrees deviated from the optimum 90°. This is expected, since these three angles are formed from non-bound water molecules and therefore the water molecules can form angles close to the optimum angle more easily than bite angles. For the planar aspect, both N1-Cu-W1 and O1-Cu-W2 deviated by a similar amount for GLH, Sar-LH and GFH and all values are less than 10° away from the optimum 180°. For Sar-FH, N1-Cu-W1 deviated slightly more than O1-Cu-W2, but is still within literature ranges and only deviated 15.3° away from the optimum 180°. The axial water bonds should also have an angle of 90° with respect to the N1-O1-W1-W2 plane. The deviation of the axial bonds is greater compared to the deviation of the equatorial bonds, but these deviations are still comparable to literature.

Similarly, the bond angles of coordination mode (b) are also all relatively close to the optimum 90° and comparable to literature values, except for N4-Cu-O3 and O1-Cu-W3 of GLH and Sar-LH which have deviated to a larger degree compared to the other angles. Nevertheless, all these angles are still close to the optimum angle. For the planar aspect, O3-Cu-W2 deviated more from 180° than N4-Cu-W1, but again all angles representing the planar aspect of the ligands

are within literature ranges and the biggest deviation is 15.5°. Similarly, the deviation of axial bonds in coordination mode (b) are also higher than the deviation of the equatorial bonds, but again they are still comparable to literature.

The similar bond lengths and similar deviated bond angles between coordination mode (a) and coordination mode (b) of each ligand show why the two coordination modes have similar ground state energies. To verify this further, the dihedral angles that are created from the plane of N1-O1-W1-W2 in coordination mode (a) and the plane of N4-O3-W1-W2 in coordination mode (b) were compared and can be seen in Table 8.8. The deviation from planarity is relatively similar and therefore adds to the verification of the similar ground state energies.

Table 8.8: Dihedral angles from the MLH species of Cu-GLH, Cu-Sar-LH, Cu-GFH and Cu-Sar-FH.

Complex	**N1-O1-W1-W2 dihedral angle, B3LYP/6-31++G** Coordination mode (a)**	**N4-O3-W1-W2 dihedral angle, B3LYP/6-31++G** Coordination mode (b)**
Cu-GLH	3.351	-11.421
Cu-Sar-LH	2.852	-11.290
Cu-GFH	-0.243	10.729
Cu-Sar-FH	-14.182	9.417

Overall, the bond lengths and slight deviations from the optimum angles in the equatorial plane for coordination modes (a) and (b) also verify that the coordination modes are experiencing minimal strain. The deviation of the axial bonds adds a slight distortion to the geometry, but still reflects a geometry of a typical tetragonally distorted octahedral or square pyramidal coordination. This verifies that the selected DFT levels (B3LYP/6-31++G**) are valid for this system.

8.3.3 The MLH_{-1} species

The MLH_{-1} species from Cu-GLH has three different possible coordination modes that were proposed in the potentiometric section. The first is to the amine (N1) and two amide-Ns (N2, N3) with a protonated imidazole-N; the second is to the amine (N1), neighbouring amide-N (N2) and to the imidazole-N (N4); and the third is to the amine (N1), two amide-Ns (N2, N3) and the carboxyl-O (O3) with a protonated imidazole-N. Potentiometry suggested that the third coordination mode is the most likely to form because it forms three stable 5-membered chelate

rings. In comparison, the first and second coordination modes only form two and one 5-membered chelate rings respectively. Molecular modelling using DFT can firstly help to determine which of these coordination modes is most likely to form by comparing the ground state energies. Secondly, DFT can calculate the λ_{max} of each complex, which will help to explain why an absorption band for this complex species cannot be detected on the UV-Vis spectrum.

Similarly, the starting structure for each coordination mode placed copper(II) in an octahedral environment and then each structure was optimized. Coordination modes (a) and (c) resulted in a square planar geometry, whereas coordination mode (b) resulted in a distorted square pyramidal geometry with an elongated axial water bond. These three coordination modes then became a benchmark for an additional optimization which excluded non-bonding water molecules. Similarly, the energy difference between the coordination modes is taken relative to the most stable coordination mode. These three coordination modes with their relative energy differences can be seen in Figure 8.8. Coordination mode (b) has been represented in both a face down view in Figure 8.8 (b)(i) and a side view in Figure 8.8 (b)(ii). The face down view shows the coordination sites and overall structure of the species, while the side view shows the distorted square pyramidal geometry. Coordination mode (b) has one more water molecule than coordination mode (a) and two more water molecules than coordination mode (c). Therefore, to compare the ground state energies, the ground state energy of water under the same conditions (B3LYP/6-31++G**) was added to the ground state energy of coordination mode (a) and added twice to the ground state energy of coordination mode (c). Note that in these calculations, entropy changes were not taken into account. The biggest difference in energy between the three coordination modes is 37.40 kJ/mol, which is not significant enough to say that the one coordination mode will form more likely in solution over the other. Therefore, in terms of energy, all three coordination modes could potentially be found in solution.

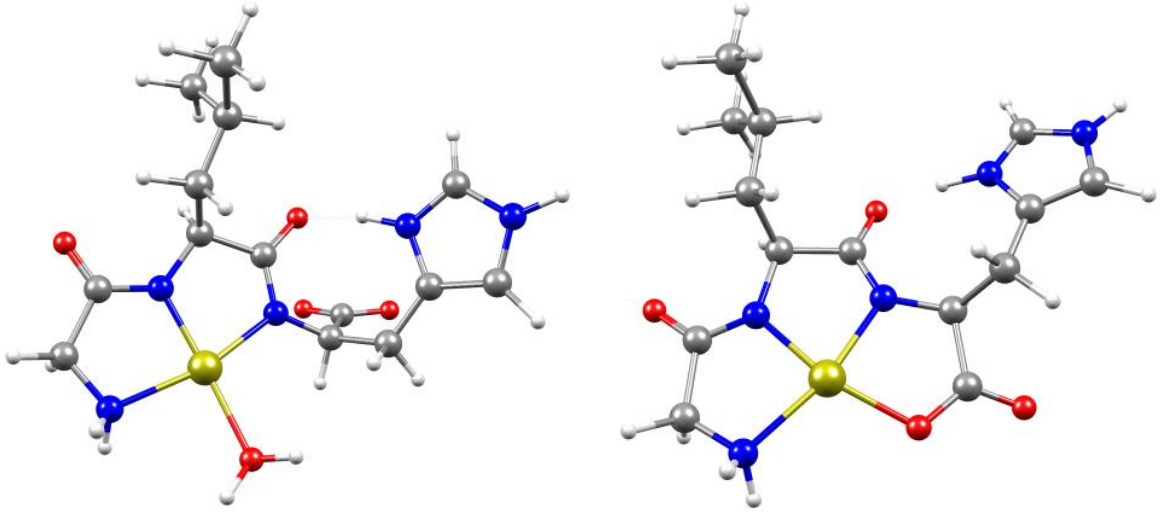

(a)
37.40 kJ/mol

(c)
0.00 kJ/mol

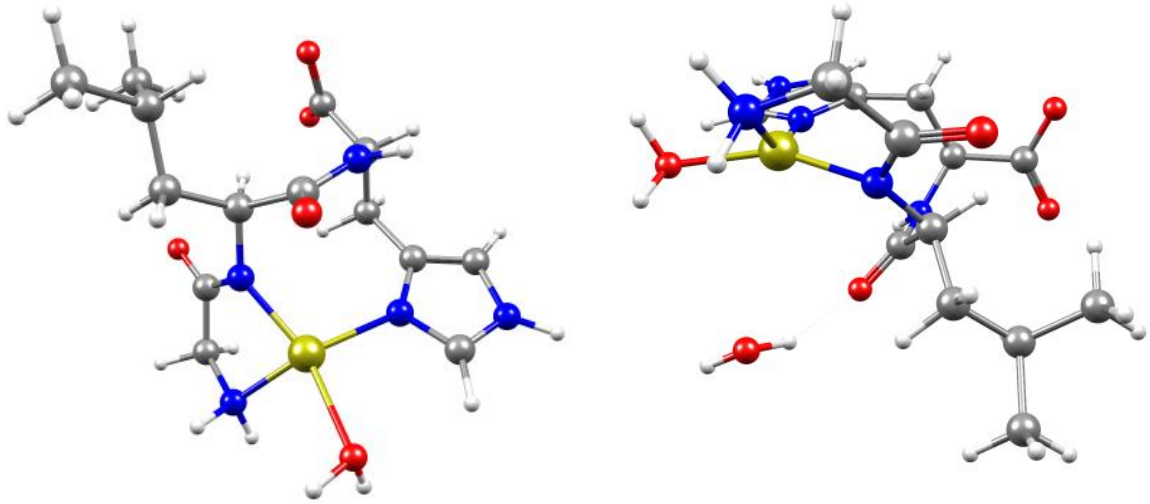

(i)

(ii)

(b)
27.75 kJ/mol

Figure 8.8: Proposed structures of the MLH_{-1} species of Cu-GLH. Coordination mode (a) has an amine (N1) and two amide-Ns (N2, N3) coordination; coordination mode (b) has an amine (N1), neighbouring amide-N (N2) and imidazole-N (N4) coordination; and coordination mode (c) has an amine (N1), two amide-Ns (N2, N3) and a carboxyl-O (O3) coordination. (bi) represents coordination mode (b) at a face down angle with a removed axial water bond and (bii) represents coordination mode (b) at a side angle.

The calculated λ_{max} values of all three coordination modes can be seen in Table 8.9. Coordination modes (a) and (c) produce electronic transitions which correspond to a calculated λ_{max} of 569 nm and 592 nm respectively. The λ_{max} of the MLH_{-2} species occurs between 517-

523 nm for all ligands, which means that the λ_{max} of coordination modes (a) and (c) will be hidden by the large absorption band of the MLH_{-2} species. According to the potentiometry speciation diagrams, the concentration of the MLH_{-1} species is low in comparison to the MLH_{-2} species and therefore even though the λ_{max} values do not overlap exactly, they are still close enough for the absorption band of MLH_{-2} to dominate over the absorption band of coordination modes (a) and (c). Coordination mode (b) produces an electronic transition which corresponds to a calculated λ_{max} of 763 nm. Similar to the MLH species, the λ_{max} of coordination mode (b) overlaps with the broad absorption band of $Cu(H_2O)_{6,}$ and since the concentration of the MLH_{-1} species is low, the absorption of coordination mode (b) will be hidden. This provides a credible explanation for why the absorption band for the MLH_{-1} species was not seen. It also suggests that coordination modes (a) and (c) contribute to the violet-pink colour change of the complex solution as the pH is increased from 2-11. Interestingly, UV-Vis suggested that coordination mode (b) should also be hidden by the MLH_{-2} absorption band as a result of calculating the λ_{max} values using Sigel and Martin's[44] parameters. This suggests that because the calculated (TD-DFT calculations) λ_{max} value from coordination mode (b) is much higher than the λ_{max} value (595 nm) using Sigel and Martin's[44] parameters, the distortion of the square pyramidal geometry is significant and results in the vast difference.

Table 8.9: The calculated λ_{max} of the coordination modes (a), (b) and (c) of the MLH_{-1} species from Cu-GLH.

Coordination mode	**λ_{max} (nm) calculated**
(a)	569
(b)	763
(c)	592

The bond lengths and bond angles of coordination modes (a), (b) and (c) can be seen in Table 8.10 and 8.11 respectively. The labelling for each atom of interest can be seen in Figure 8.9. Looking at Table 8.10, the bond lengths of the equatorial bonds for all the coordination modes are all comparable to literature. For all coordination modes, the Cu-N2 bond length is the shortest and least strained. The Cu-W1 bond is the longest and most strained bond for coordination modes (a) and (b), while the Cu-N1 bond is the longest and most strained bond for coordination mode (c). Similar to the MLH species, the Cu-W2 axial bond of coordination mode (b) is relatively long, but still significant.

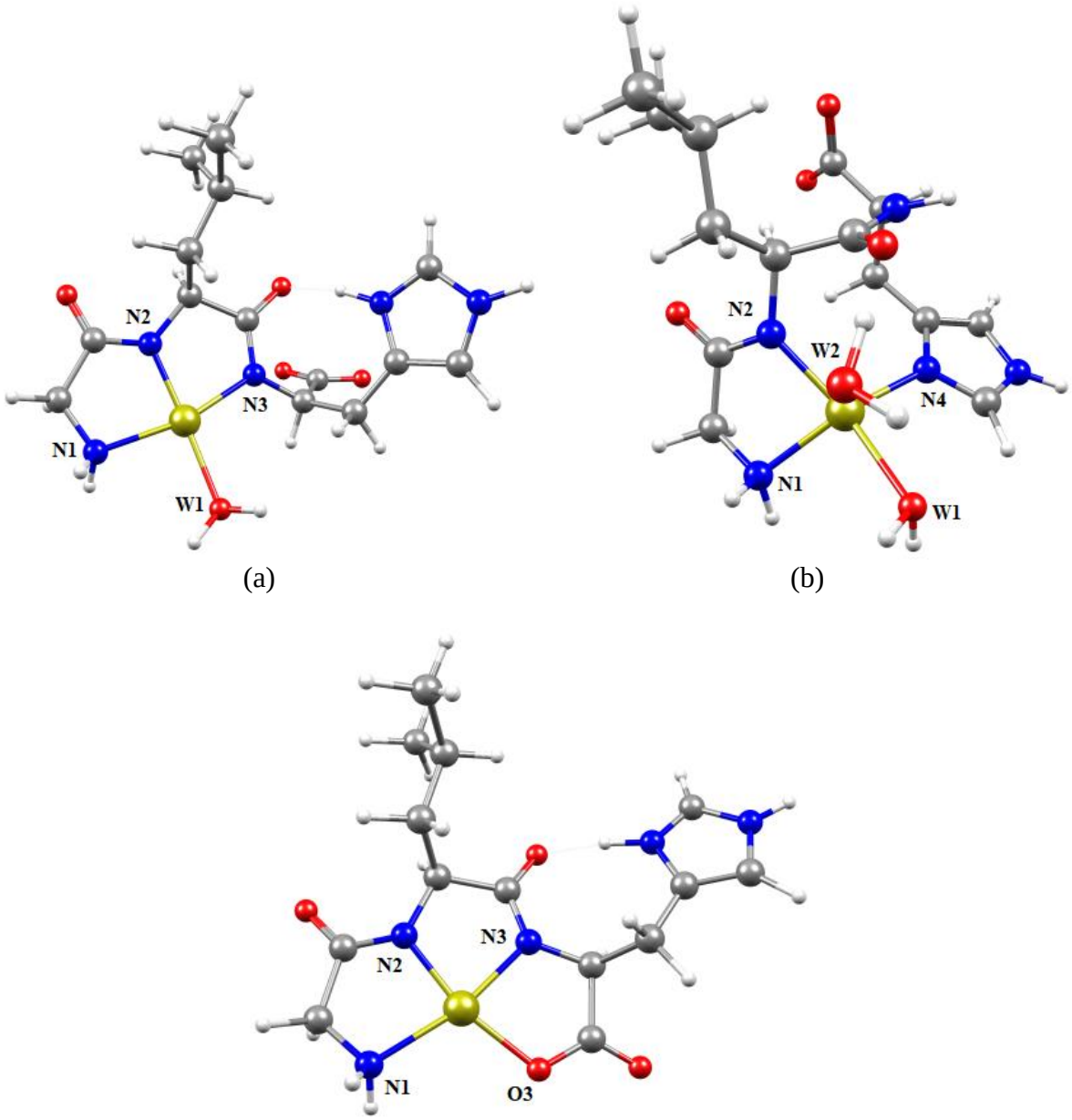

Figure 8.9: Labelling specifications for the MLH_{-1} coordination modes (a), (b) and (c) of Cu-GLH.

A square planar and square pyramidal geometry should have bond angles close to 90° and the planar aspect should be close to 180°. For coordination mode (a), all the angles are close to the optimum 90° and comparable to literature. For the planar aspect, N1-Cu-N3 deviates more from the optimum 180° than N2-Cu-W1, but the deviation is still within literature ranges. The planar dihedral angle that is produced from the plane created from N1-N2-N3-W1, is -8.325°, and shows that the planar aspect is indeed planar.

For coordination mode (c) the O3-Cu-N1 angle has deviated quite significantly from the optimum 90°, but this is due to the formation of a three 5-membered chelate ring system, which causes the greatest strain in the non-bite angle. The bite angles are all close to the optimum 90° and the angles that measure the planar aspect deviate away from the optimum 180° to a similar degree. These angles are also within literature ranges. The planar dihedral angle that is produced from the plane created from N1-N2-N3-O3, is 6.948°, and again shows that the planar aspect is planar.

Since coordination mode (b) was found to have a distorted square pyramidal geometry, these angles are expected to deviate significantly. The bond angles, N4-Cu-W1 and W1-Cu-N1 were found to be the closest angles to 90° and this is due to the ability of the water molecule to freely move and find an optimum position in space. The N1-Cu-N2 angle is also relatively close to 90° and falls within the literature range, but the N2-Cu-N4 angle has significantly deviated and falls outside of the literature range. For the planar aspect, both the N1-Cu-N4 and N2-Cu-W1 angles have significantly deviated to an extent that the angles could represent a geometry that is between a planar and a tetrahedral angle (tetrahedral angles are typically 109.5°). This deviation is also confirmed with the planar dihedral angle that is produced from the plane created from N1-N2-N4-W1, which is -39.646°. The axial water bond should also have an optimum angle of 90° with respect to the plane of N1-N2-N4-W1, but since the plane is distorted, the axial bond will also deviate from the ideal angle. The deviation from angles N1-Cu-W2 and N2-Cu-W2 is within the literature range, while the deviation from angles N4-Cu-W2 and W1-Cu-W2 is outside of the literature range. All these deviations therefore confirm that coordination mode (b) is experiencing high distortion.

Nevertheless, the bond lengths and bond angles of all three coordination modes are reasonable and verify that the selected DFT levels (B3LYP/6-31++G**) are valid for this system.

Table 8.10: Bond lengths from the MLH_{-1} coordination modes (a), (b) and (c) of Cu-GLH.

Coordination mode	Labelled bond length	Bond length (Å) B3LYP/6-31++ G**	Bond length (Å) literature
(a)	Cu-N1	2.064	1.883 - 2.043[31–34]
	Cu-N2	1.921	1.907 - 2.05[31,33,35,36]
	Cu-N3	1.992	
	Cu-W1	2.087	1.95 - 1.98[34,40]
(b)	Cu-N1	2.032	1.883 - 2.043[31–34]
	Cu-N2	1.990	1.907 - 2.05[31,33,35,36]
	Cu-N4	2.066	1.883 - 2.00[31–33]
	Cu-W1	2.101	1.95 - 1.98[34,40]
	Cu-W2	3.700	2.225 - 2.943[31,34,41,42]
(c)	Cu-N1	2.067	1.883 - 2.043[31–34]
	Cu-N2	1.934	1.907 - 2.05[31,33,35,36]
	Cu-N3	1.956	
	Cu-O3	2.012	1.902 - 1.974[39]

Table 8.11: Bond angles from the MLH_{-1} coordination modes (a), (b) and (c) of Cu-GLH.

Coordination mode	Labelled bond angle	Bond angle (°), B3LYP/6-31++ G**	Bond angle (°) literature
(a)	N1-Cu-N2	83.0	80.8° - 99.6°[32,33,37–39]
	N2-Cu-N3	83.0	
	N3-Cu-W1	100.2	
	W1-Cu-N1	94.3	
	N1-Cu-N3	164.5	164.2° - 177.5°[32,33,37–39]
	N2-Cu-W1	174.4	
(b)	N1-Cu-N2	82.0	80.8° - 99.6°[32,33,37–39]
	N2-Cu-N4	108.2	
	N4-Cu-W1	91.4	
	W1-Cu-N1	92.8	
	N1-Cu-N4	144.4	164.2° - 177.5°[32,33,37–39]
	N2-Cu-W1	153.1	
	N1-Cu-W2	100.4	84.7° - 111.2°[32,34,41]
	N2-Cu-W2	80.8	
	N4-Cu-W2	114.7	
	W1-Cu-W2	74.2	
(c)	N1-Cu-N2	83.3	80.8° - 99.6°[32,33,37–39]
	N2-Cu-N3	83.3	
	N3-Cu-O3	82.9	
	O3-Cu-N1	110.6	
	N1-Cu-N3	166.5	164.2° - 177.5°[32,33,37–39]
	N2-Cu-O3	164.3	

8.3.4 The ML species

The ML species of Cu-Sar-LH has two possible coordination modes that were proposed in the potentiometric section. The one (coordination mode (a)), is coordinated to the amine (N1), neighbouring amide-N (N2) and the carbonyl-O (O2) of leucine with the imidazole-N protonated. The other (coordination mode (b)), is coordinated to the amine (N1) and neighbouring amide-N (N2) with the imidazole-N protonated. DFT calculations were used to determine which one is more likely to form and then propose a reason why the species was not visible in the UV-Vis spectrum.

Both coordination modes were set to have copper(II) in an octahedral environment. The resultant geometry for coordination modes (a) and (b) is square planar and tetragonally distorted octahedral respectively. The non-bonding water molecule in coordination mode (a) was then removed and this resultant structure was benchmarked for an additional optimization. Both coordination modes can be seen in Figure 8.10. The energy difference between the coordination modes is taken relative to the most stable coordination mode. Coordination mode (b) has been represented in both a face down view in Figure 8.10 (b)(i) and a side view in Figure 8.10 (b)(ii). The face down view shows the coordination sites and overall structure of the species, while the side view shows the tetragonally distorted octahedral geometry. Coordination mode (a) has three less water molecules than coordination mode (b) and so when comparing the ground state energies, the ground state energy of a water molecule under the same conditions (B3LYP/6-31++G**) was added thrice to the energy of coordination mode (a). Note that in these calculations, entropy changes were not taken into account. By comparing the energies, coordination mode (b) is only 22.84 kJ/mol more stable than coordination mode (a) and therefore both coordination modes have the potential to form in solution.

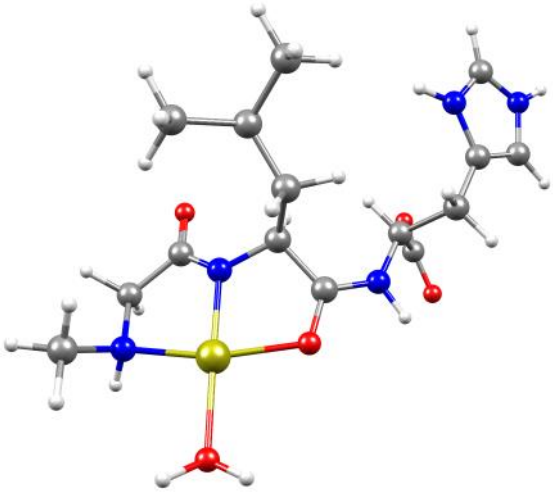

(a)
22.84 kJ/mol

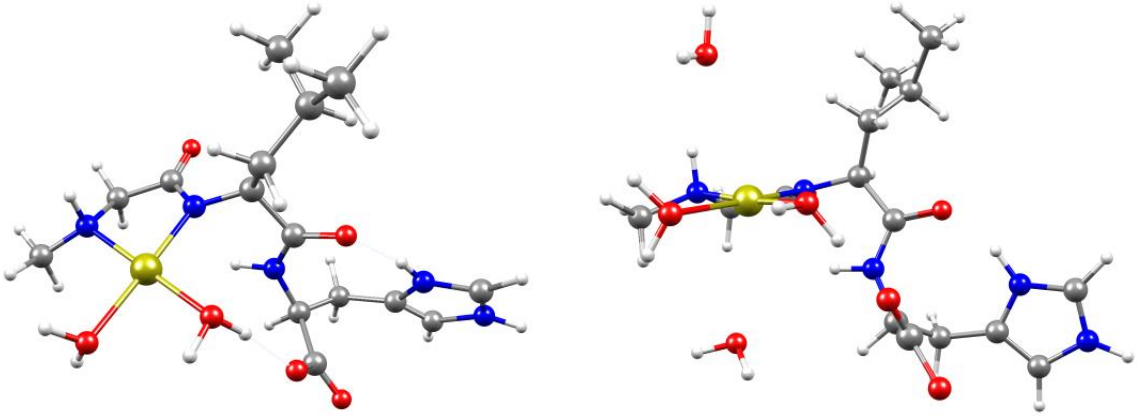

(i) (ii)

(b)
0.00 kJ/mol

Figure 8.10: Proposed structures of the ML species of Cu-Sar-LH. Coordination mode (a) has an amine (N1), neighbouring amide-N (N2) and carbonyl-O (O2) of leucine coordination and coordination mode (b) has an amine (N1) and neighbouring amide-N (N2) coordination. (bi) represents coordination mode (b) at a face down angle with a removed axial water bond and (bii) represents coordination mode (b) at a side angle.

A table containing the calculated λ_{max} values can be seen in Table 8.12. Coordination mode (a) produces an electronic transition which corresponds to a λ_{max} of 586 nm and coordination mode (b) produces an electronic transition which corresponds to a λ_{max} of 719 nm. This means that the absorption band of coordination mode (a) will overlap with the large absorption band of the MLH_{-2} species (λ_{max} = 517-523 nm) and coordination mode (b) will overlap with the broad

absorption band of $Cu(H_2O)_6$ (λ_{max} = 800 nm). Since both species have a low concentration, they will be hidden by either the MLH_{-2} or $Cu(H_2O)_6$ absorption band. This also suggests that coordination mode (a) could contribute towards the violet-pink colour change of the complex solution as the pH is increased from 2-11.

This outcome for the ML species is consistent with the room temperature EPR superhyperfine lines that suggested a CuN_2O_2 chromophore. Coordination mode (b) agrees with UV-Vis, since it was suggested that a possible reason for not detecting the ML species is because the ML absorption band is hidden by the $Cu(H_2O)_6$ absorption band. In potentiometry, literature suggested that the coordination for the ML species will tend towards the more stable tridentate formation (coordination mode (a)). Therefore, the outcome from DFT calculations agrees that coordination mode (a) will form, but does not agree that it is the more stable form.

Table 8.12: The calculated λ_{max} of the coordination modes (a) and (b) of the ML species from Cu-Sar-LH.

Coordination mode	λmax (nm) calculated
(a)	586
(b)	719

The labelling for each atom of interest in each coordination mode can be seen in Figure 8.11.

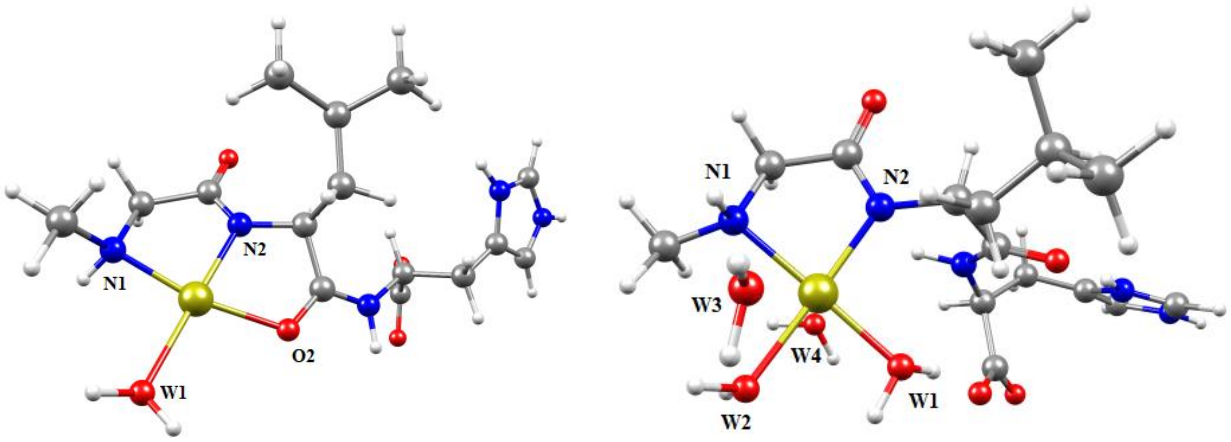

(a) (b)

Figure 8.11: Labelling specifications for ML coordination modes (a) and (b) of Cu-Sar-LH.

When looking at the equatorial bond lengths in Table 8.13, Cu-N2 is the shortest in both coordination modes and therefore the least strained, while the other bond lengths in both coordination modes are longer, and all have similar values to one another. All these equatorial bond lengths are comparable to literature. In comparison, the axial water bonds for coordination mode (b) are substantially longer than literature values, but as mentioned previously, the bonds are still significant.

As stated before, the optimum bond angles for square planar or octahedral geometries are 90°. When looking at Table 8.14, for coordination mode (a), all the bond angles deviate away from the optimum 90° to a similar degree and are within literature ranges. For the planar aspect, N1-Cu-O2 deviated more from the optimum 180° than N2-Cu-W1, but the deviation is still comparable to literature. The dihedral angle that is produced as a result of the plane created from N1-N2-O2-W1 is -5.658, which shows the geometry is typically square planar.

For coordination mode (b) all the bond angles for both the plane and the angles for the axial water molecule are all close to 90° and comparable with literature. When checking the planar aspect of the geometry, both N1-Cu-W1 and N2-Cu-W2 are firstly close in value and secondly close to the optimum 180°. The dihedral angle that is produced as a result of the plane created from N1-N2-W1-W2 is 3.075. This slight deviation, as well as the relatively small deviations from the optimum angles, verifies that overall the coordination mode is experiencing minimal strain, except for the axial bond lengths. This therefore reflects a typical tetragonally distorted octahedral geometry, which along with the bond lengths and angles of coordination mode (a), verifies that the selected DFT levels (B3LYP/6-31++G**) are valid for this system.

Table 8.13: Bond lengths from the ML coordination modes (a) and (b) of Cu-Sar-LH.

Coordination mode	**Labelled bond length**	**Bond length (Å) B3LYP/6-31++ G****	**Bond length (Å) literature**
(a)	Cu-N1	2.050	1.883 - 2.043[31–34]
	Cu-N2	1.923	1.907 - 2.05[31,33,35,36]
	Cu-O2	2.040	1.902 - 1.974[39]
	Cu-W1	2.038	1.95 - 1.98[34,40]
(b)	Cu-N1	2.047	1.883 - 2.043[31–34]
	Cu-N2	1.983	1.907 - 2.05[31,33,35,36]
	Cu-W1	2.039	1.95 - 1.98[34,40]
	Cu-W2	2.093	
	Cu-W3	3.336	2.225 - 2.943[31,34,41,42]
	Cu-W4	3.379	

Table 8.14: Bond angles from the ML coordination modes (a) and (b) of Cu-Sar-LH.

Coordination mode	Labelled bond angle	Bond angle (°), B3LYP/6-31++ G**	Bond angle (°) literature
(a)	N1-Cu-N2	84.0	80.8° - 99.6°[32,33,37–39]
	N2-Cu-O2	81.9	
	O2-Cu-W1	97.5	
	W1-Cu-N1	96.5	
	N1-Cu-O2	163.6	164.2° - 177.5°[32,33,37–39]
	N2-Cu-W1	178.7	
(b)	N1-Cu-N2	82.8	80.8° - 99.6°[32,33,37–39]
	N2-Cu-W1	98.4	
	W1-Cu-W2	83.0	
	W2-Cu-N1	95.8	
	N1-Cu-W1	175.2	164.2° - 177.5°[32,33,37–39]
	N2-Cu-W2	178.5	
	N1-Cu-W3	84.4	84.7° - 111.2°[32,34,41]
	N2-Cu-W3	101.1	
	W1-Cu-W3	90.8	
	W2-Cu-W3	78.2	
	N1-Cu-W4	89.2	
	N2-Cu-W4	97.9	
	W1-Cu-W4	95.3	
	W2-Cu-W4	82.6	

8.4 Conclusion

The coordination modes and square planar geometry of the MLH_{-2} species for all ligands were verified with DFT calculations. The two MLH coordination modes for each ligand were already known, but the geometry was unknown. DFT verified these coordination modes, where coordination mode (a) has an amine and neighbouring carbonyl-O coordination with a protonated imidazole-N, and coordination mode (b) has an imidazole-N and carboxyl-O coordination with a protonated amine. DFT also found the geometry to be square pyramidal for coordination modes (a) and (b) of GFH and Sar-FH, as well as coordination mode (a) of GLH and Sar-LH. Coordination mode (b) of GLH and Sar-LH was found to be tetragonally distorted octahedral.

From three possible coordination modes for the MLH_{-1} species of Cu-GLH, all three coordination modes have the same potential to form in solution. Coordination mode (a), where copper(II) coordinates to the amine and two amide-Ns with a protonated imidazole-N, and coordination mode (c), where copper(II) coordinates to the amine, two amide-Ns and a carboxyl-O with a protonated imidazole-N, were both found to be square planar. Coordination

mode (b), where copper(II) coordinates to the amine, the neighbouring amide-N and the imidazole-N, was found to be a distorted square pyramid.

The two possible coordination modes for the ML species of Cu-Sar-LH were both found to have the same potential for forming in solution. Coordination mode (a), where copper(II) has coordinated to the amine, neighbouring amide-N and the carbonyl-O of leucine with the imidazole-N protonated, was found to be square planar. Coordination mode (b), where copper(II) has coordinated to the amine and neighbouring amide-N with the imidazole-N protonated, was found to be a tetragonally distorted octahedral geometry.

DFT calculations also provided a reason for the lack of a visible UV-Vis absorption peak in the experimental UV-Vis section for the MLH, ML and MLH_{-1} species. The absorption band for both the coordination modes of the MLH species is concealed behind the broad absorption band of $Cu(H_2O)_6$. For the MLH_{-1} species of Cu-GLH, coordination modes (a) and (c) are concealed behind the large absorption band of the MLH_{-2} species and coordination mode (b) is concealed behind the broad absorption band of $Cu(H_2O)_6$. For the ML species of Cu-Sar-LH, coordination mode (a) is concealed behind the large absorption band of the MLH_{-2} species and coordination mode (b) is concealed behind the broad absorption band of $Cu(H_2O)_6$.

8.5 References

1 E. G. Lewars, in *Computational Chemistry: Introduction to the Theory and Applications of Molecular and Quantum mechanics*, Kluwer Academic Publishers, Massachusetts, 2003, pp. 385–394.

2 F. M. A. Elmagbari, Synthesis and design of ligand copper complexes as anti-inflammatory drugs, PhD Thesis, University of Cape Town, 2015.

3 M. Mohajane, Dipeptides as potential anti-flammatory drugs for rheumatoid arthritis, PhD Thesis, University of Cape Town, 2013.

4 A. N. Hammouda, Development of copper peptide complexes as anti-Inflammatory drugs, PhD Thesis, University of Cape Town, 2015.

5 J. N. Zvimba, Copper chelating anti-inflammatory agents of pseudo-mimics of Human Serum Albumin (HSA): copper and rheumatoid arthritis, PhD Thesis, University of Cape Town, 2005.

6 J. N. Zvimba and G. E. Jackson, Solution equilibria of copper(II) complexation with N,N′-(2,2′-azanediylbis(ethane-2,1-diyl))dipicolinamide: A bio-distribution and dermal absorption study, *J. Inorg. Biochem.*, 2007, **101**, 1120–1128.

7 S. Odisitse and G. E. Jackson, In vitro and in vivo studies of N,N′-bis[2(2-pyridyl)-methyl]pyridine-2,6-dicarboxamide–copper(II) and rheumatoid arthritis, *Polyhedron*, 2008, **27**, 453–464.

8 J. C. A. Boeyens and P. Comba, Molecular mechanics: theoretical basis, rules, scope and limits, *Coord. Chem. Rev.*, 2001, **212**, 3–10.

9 A. K. Rappé, C. J. Casewit, K. S. Colwell, W. A. Goddard and W. M. Skiff, UFF, a Full Periodic Table Force Field for Molecular Mechanics and Molecular Dynamics Simulations, *J. Am. Chem. Soc.*, 1992, **114**, 10024–10035.

10 T. A. Halgren, Merck molecular force field. I. Basis, form, scope, parameterization, and performance of MMFF94, *J. Comput. Chem.*, 1996, **17**, 490–519.

11 F. K. Winkler and J. D. Dunitz, The non-planar amide group, *J. Mol. Biol.*, 1971, **59**, 169–182.

12 S. F. Sousa, P. A. Fernandes and M. J. Ramos, General Performance of Density Functionals, *J. Phys. Chem. A*, 2007, **111**, 10439–10452.

13 K. Capelle, A bird's-eye view of density-functional theory, *Brazilian J. Phys.*, 2002, **36**, 1318–1343.

14 T. van Mourik, M. Bühl and M.-P. Gaigeot, Density functional theory across chemistry, physics and biology, *Philos. Trans. R. Soc. A Math. Phys. Eng. Sci.*, 2014, **372**, 20120488.

15 N. Argaman and G. Makov, Density functional theory: An introduction, *Am. J. Phys.*, 2000, **68**, 69–79.

16 N. M. Harrison, in *Computational materials science*, eds. R. Catlow and E. Kotomin, IOS Press, Berlin, 2003, pp. 45–70.

17 J. Tirado-Rives and W. L. Jorgensen, Performance of B3LYP Density Functional Methods for a Large Set of Organic Molecules, *J. Chem. Theory Comput.*, 2008, **4**, 297–306.

18 A. D. Becke, A new mixing of Hartree–Fock and local density-functional theories, *J. Chem. Phys.*, 1993, **98**, 1372–1377.

19 A. D. Becke, Density-functional thermochemistry. IV. A new dynamical correlation functional and implications for exact-exchange mixing, *J. Chem. Phys.*, 1996, **104**, 1040–1046.

20 C. Lee, W. Yang and R. G. Parr, Development of the Colle-Salvetti correlation-energy formula into a functional of the electron density, *Phys. Rev. B*, 1988, **37**, 785–789.

21 F. Abu-Awwad and P. Politzer, Variation of parameters in Becke-3 hybrid exchange-correlation functional, *J. Comput. Chem.*, 2000, **21**, 227–238.

22 A. V. Arbuznikov, Hybrid exchange correlation functionals and potentials: Concept elaboration, *J. Struct. Chem.*, 2007, **48**, S1–S31.

23 L. Rulíšek and Z. Havlas, Theoretical Studies of Metal Ion Selectivity. 1. DFT Calculations of Interaction Energies of Amino Acid Side Chains with Selected Transition Metal Ions (Co 2+ , Ni 2+ , Cu 2+ , Zn 2+ , Cd 2+ , and Hg 2+), *J. Am. Chem. Soc.*, 2000, **122**, 10428–10439.

24 A. Robertazzi, A. Magistrato, P. de Hoog, P. Carloni and J. Reedijk, Density Functional Theory Studies on Copper Phenanthroline Complexes, *Inorg. Chem.*, 2007, **46**, 5873–5881.

25 J. B. Foresman and Æ. Frisch, *Exploring Chemistry with Electronic Structure Methods*, Gaussian, Inc, Pittsburgh, PA, 2nd edn., 1996.

26 A. Tomberg, Gaussian 09W Tutorial: An Introduction to Computational Chemistry using G09W and Avogadro Software, https://barrett-group.mcgill.ca/tutorials/Gaussian tutorial.pdf, (accessed 23 January 2020).

27 M. J. Frisch, G. W. Trucks, H. B. Schlegel, G. E. Scuseria, M. A. Robb, J. R.

Cheeseman, G. Scalmani, V. Barone, B. Mennucci, G. A. Petersson, H. Nakatsuji, M. Caricato, X. Li, H. P. Hratchian, A. F. Izmaylov, J. Bloino, G. Zheng, J. L. Sonnenberg, M. Hada, M. Ehara, K. Toyota, R. Fukuda, J. Hasegawa, M. Ishida, T. Nakajima, Y. Honda, O. Kitao, H. Nakai, T. Vreven, J. A. Montgomery, J. E. Peralta, F. Ogliaro, M. Bearpark, J. J. Heyd, E. Brothers, K. N. Kudin, V. N. Staroverov, T. Keith, R. Kobayashi, J. Normand, K. Raghavachari, A. Rendell, J. C. Burant, S. S. Iyengar, J. Tomasi, M. Cossi, N. Rega, J. M. Millam, M. Klene, J. E. Knox, J. B. Cross, V. Bakken, C. Adamo, J. Jaramillo, R. Gomperts, R. E. Stratmann, O. Yazyev, A. J. Austin, R. Cammi, C. Pomelli, J. W. Ochterski, R. L. Martin, K. Morokuma, V. G. Zakrzewski, G. A. Voth, P. Salvador, J. J. Dannenberg, S. Dapprich, A. D. Daniels, O. Farkas, J. B. Foresman, J. V Ortiz, J. Cioslowski and D. J. Fox, Gaussian, Inc., Wallingford CT, 2010.

28 R. Dennington, T. A. Keith and J. M. Millam, 2016.

29 A. V. Marenich, C. J. Cramer and D. G. Truhlar, Universal Solvation Model Based on Solute Electron Density and on a Continuum Model of the Solvent Defined by the Bulk Dielectric Constant and Atomic Surface Tensions, *J. Phys. Chem. B*, 2009, **113**, 6378–6396.

30 Chemcraft - graphical software for visualization of quantum chemistry computations, https://www.chemcraftprog.com, (accessed 2 February 2020).

31 J. F. Blount, K. A. Fraser, H. C. Freeman, J. T. Szymanski, C. -h. Wang and F. R. N. Gurd, Model Compounds for Metal-Protein Interaction. The Crystal Structure of the Copper(11) Complex of Glycyl-L-histidine, *Chem. Commun. (London)*, 1966, 23–24.

32 A. García-Raso, J. J. Fiol, B. Adrover, E. Molins and C. Miravitlles, X-ray diffraction structure of a ternary copper(II) peptide complex (benzimidazole) (glycylglycinato) copper(II) trihydrate, *Polyhedron*, 1996, **15**, 1829–1834.

33 P. De Meester and D. J. Hodgson, Oxidative decarboxylation of glycylglycyl-L-histidine by copper(II) hydroxide: x-ray structural characterization of .alpha.,.beta.-didehydroglycylglycylhistaminatocopper(II) dihydrate, *Inorg. Chem.*, 1978, **17**, 440–444.

34 J. F. Blount, K. A. Fraser, H. C. Freeman, J. T. Szymanski and C. H. Wang, Crystallographic studies of metal peptide complexes. IV. (Glycyl-L-histidinato)copper(II) sesquihydrate, *Acta Crystallogr.*, 1967, **22**, 396–405.

35 Q. Wang, C.-F. Bi, D.-Q. Wang and Y.-H. Fan, Dichlorido{ N -[1-(2-pyridyl)ethylidene]ethane-1,2-diamine}copper(II), *Acta Crystallogr. Sect. E Struct.*

Reports Online, 2009, **65**, m439–m439.

36 A. Garcia-Raso, A. Terron, J. J. Fiol, E. Molins and C. Miravitlles, X-ray crystal structure of a ternary copper(II) peptide creatinine complex, (Aquo)(Creatinine)(Glycylglycinato) copper(II) sesquihydrate, *Polyhedron*, 1995, **14**, 2537–2545.

37 Á. García-Raso, J. J. Fiol, B. Adrover, P. Tauler, A. Pons, I. Mata, E. Espinosa and E. Molins, Reactivity of copper(II) peptide complexes with bioligands (benzimidazole and creatinine), *Polyhedron*, 2003, **22**, 3255–3264.

38 M. B. Hursthouse, S. A. A. Jayaweera, H. Milburn and A. Quick, Crystal structure of aqua(glycyl)-L-tryptophanatocopper(II) dihydrate, *J. Chem. Soc. Dalt. Trans.*, 1975, 2569.

39 P. F. Lee, C.-T. Yang, D. Fan, J. J. Vittal and J. D. Ranford, Synthesis, characterization and physicochemical properties of copper(II) complexes containing salicylaldehyde semicarbazone, *Polyhedron*, 2003, **22**, 2781–2786.

40 P. Frank, M. Benfatto, R. K. Szilagyi, P. D'Angelo, S. Della Longa and K. O. Hodgson, The Solution Structure of [Cu(aq)] 2+ and Its Implications for Rack-Induced Bonding in Blue Copper Protein Active Sites, *Inorg. Chem.*, 2005, **44**, 1922–1933.

41 N. Camerman, J. K. Fawcett, T. P. A. Kruck, B. Sarkar and A. Camerman, Copper(II)-histidine stereochemistry. Structure of L-histidinato-D-histidinatodiaquocopper(II) tetrahydrate, *J. Am. Chem. Soc.*, 1978, **100**, 2690–2693.

42 A. W. Addison, T. N. Rao, J. Reedijk, J. van Rijn and G. C. Verschoor, Synthesis, structure, and spectroscopic properties of copper(II) compounds containing nitrogen–sulphur donor ligands; the crystal and molecular structure of aqua[1,7-bis(N-methylbenzimidazol-2′-yl)-2,6-dithiaheptane]copper(II) perchlorate, *J. Chem. Soc., Dalt. Trans.*, 1984, 1349–1356.

43 S. Nigam and H. Mohabey, Electronic Spectra of Mixed Ligand Complexes of Copper(II) with Different Amino Acids., *Aisan J. Chem.*, 2001, **13**, 107–110.

44 H. Sigel and R. B. Martin, Coordinating properties of the amide bond. Stability and structure of metal ion complexes of peptides and related ligands, *Chem. Rev.*, 1982, **82**, 385–426.

9. Dermal Absorption

9.1 Introduction

The administration of copper(II) into the body has two convenient routes; via an oral or a transdermal route. A third route is via subcutaneous/parenteral administration.[1,2] However, a subcutaneous administration means that patients have to seek professional help to administer the copper(II) and irritation can occur at the site of the injection, so this route is not favoured.[3] Parenteral administration has been beneficial in showing that simple copper(II) salts, such as copper(II) chloride, do reduce inflammation by an amount that is proportional to the amount of copper(II) injected.[1] Jackson *et al*.[1] also found that once *in vivo*, the copper(II) complexes will protect against oedema, which is also proportional to the amount administered.

For oral administration, the copper(II) complex has to withstand low stomach pH and be absorbed through a variety of body compartments. The normal dietary intake of copper(II) is 2.5-5.0 mg, of which only approximately 30% is absorbed by the small intestine. Copper(II) is also naturally absorbed as low molecular weight complexes, which are monomeric, acidic amino acids in the L-configuration. However, this absorption is suppressed by other metals and ligands like Ca^{2+} and PO_4^{3-}.[1,2] Non-absorbed copper(II) salts are irritants which cause ulceration and oedema.[4] Therefore administering copper(II) orally could be harmful. Additionally, if absorption does occur, copper(II) will be exposed to protein binding in the plasma and this will decrease the bioavailability of copper(II) even further.[1,2] Thus an oral administrative pathway is also not favoured.

The transdermal absorption route requires the copper(II) complex to diffuse passively across the skin barrier and enter the blood plasma. This route is limited by the diffusion ability of the copper(II) complex, which is essentially governed by its lipophilicity and protein binding properties.[5,6] Besides the limitations associated with the dermal permeability of the copper(II) complex, this route is nonharmful and convenient for patients. Therefore, it is the aim of this study to develop a copper(II) complex that can be administered topically.

Skin is a multi-layered organ that consists of three layers, namely the epidermis, the dermis and the subcutis. The epidermis is the outermost layer which is separated into five layers, with the stratum corneum being the outermost layer of the epidermis and therefore of the skin.[7] It is the stratum corneum that can be considered as the rate-limiting barrier for skin permeation of drugs.[8,9] It is usually 15-20 μm thick and consists of two alternating amorphous lipophilic and hydrophilic layers.[10] The hydrophilic layer has keratinized corneocytes and in between these cells is the lipophilic lipid layer, called the lamellar membrane. The lamellar membrane is arranged in bilayers and essentially fills the space between the hydrophilic keratinized corneocytes.[7,11–13] Permeation of drugs through the skin is a passive diffusion process, which can be defined by Fick's first law of diffusion.[14,15] Depending on the nature of the chemicals, there are three pathways for drugs to pass through the stratum corneum. The major pathway is an intercellular pathway that goes through the lipid bilayer. The second pathway is an intracellular route through the corneocytes and a smaller portion of the lipid bilayer when travelling from cell to cell.[16,17] The third pathway is through the skin appendages, which includes sweat and sebaceous glands, and hair follicles. However, the total flux through these appendages is 0.1-1 % for total skin coverage and so this is not a favourable route.[7,11,18] A diagram that shows the layers of the skin, the structure of the stratum corneum and the three different pathways for drug penetration through the skin can be seen in Figure 9.1.

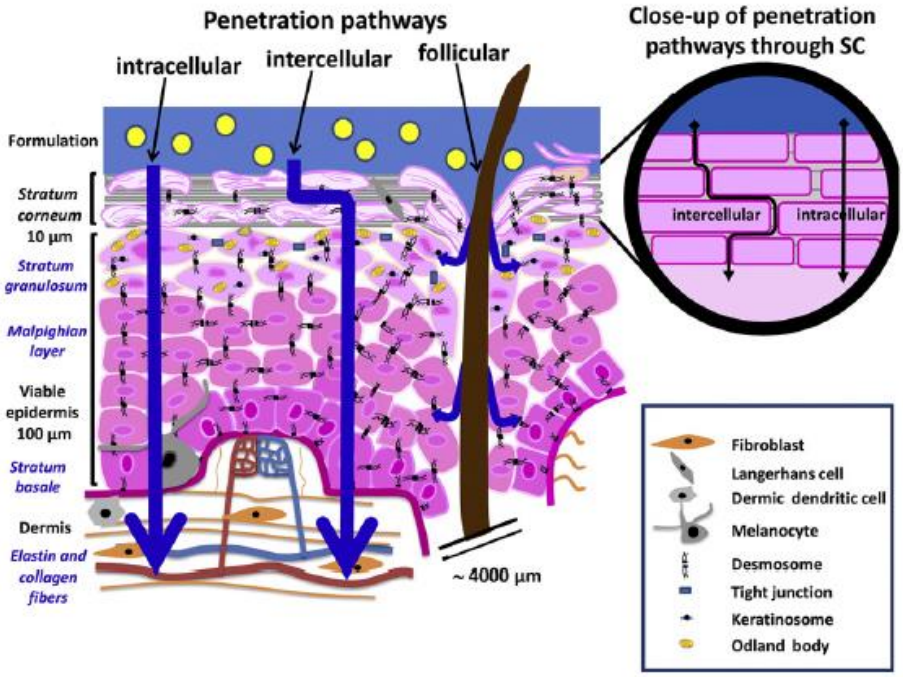

Figure 9.1: An illustration showing the different layers of the skin, the structure of the stratum corneum and the different pathways a drug can take to diffuse through the skin.[17]

The major intercellular pathway is the ideal route for the copper(II) complexes and therefore to pass through a lipophilic layer, they essentially need to be non-polar and lipophilic themselves. However, assuming a lipophilic complex is found, once diffused through the stratum corneum, the complex will have to enter an aqueous medium. If the lipophilic complex is too lipophilic, it will remain in the stratum corneum and so a balance between lipophilicity and hydrophilicity has to be achieved.[7]

Other factors that affect the permeability of a drug are the molecular size and hydrogen bonding. Molecule size could affect the pathway the drug takes, while hydrogen bonding can affect non-covalent interactions with proteins in the skin.[7] Once the complexes have diffused through the stratum corneum and the other layers of the epidermis, they will diffuse through the dermis and enter blood capillaries. The dermis consists of collagen and elastin that has been embedded in a mix of mucopolysaccharides.[7] It also consists of mast cells, macrophages, lymphocytes and melanocytes, as well as blood vessels, nerves and skin appendages. Due to the structural composition, the dermis is less of a diffusion barrier compared to the stratum corneum, but lipophilic drugs may experience a reduction in permeation.[19] Since blood capillaries are situated in the dermis layer, the complexes will not reach the subcutis layer.[7,11]

To determine how effective the copper(II) complexes are at undergoing transdermal absorption, two methods were used. The one is the Flask Shake method, which gives the partition coefficients and the second is the Franz cell diffusion method, which gives the permeability coefficients.

9.2 Octanol/Water Partition Coefficient

9.2.1 Flask Shake method

Octanol/water partition coefficients are seen as a reference parameter for lipophilicity, which can give an estimation for the transdermal transport of a drug. The most common method of measuring octanol/water partition coefficients is using the Flask Shake method, which adds a known concentration of analyte to water. An organic solvent is then added which extracts the analyte. The amount of analyte in the organic solvent and the amount of analyte remaining in the water is measured and the ratio is used to determine the partition coefficient. For metal complexes the partition coefficient is defined as:

$$\log P_{oct/aq} = \log \left(\frac{[Cu(II)]_{oct}}{[Cu(II)]_{aq}} \right) \quad (9.1)$$

where $[Cu(II)]_{oct}$ is the copper(II) concentration that is extracted into the organic phase and $[Cu(II)]_{aq}$ is the copper(II) concentration that remains in the aqueous phase.[7] The separation of the two phases is assumed to be complete when two distinct layers can be seen.

9.2.2 Experimental

Each complex was prepared with a 1:1 copper(II) ligand ratio in 50 ml of HCl (0.01 M) and background electrolyte (0.15 M). The concentration of the ligands was 0.004 M and the concentration of copper(II) was adjusted to be slightly lower at 0.0035 M to prevent the precipitation of $Cu(OH)_2$, but still maintain an approximate 1:1 ratio. 1.4 ml of copper(II) ligand solution was added to 20 glass vials for each ligand. The pH was adjusted using NaOH, so that it was increased in increments of 0.3-0.5, starting at pH 2 and ending at pH 11. After this, 5 ml of water-saturated 1-octanol solution was added to each glass vial. The glass vials where then shaken for 1 min and then left to stand for another 10 min to allow the two phases to separate.

1 ml of organic layer from each vial was withdrawn and placed into separate vials. 7 ml of 5 % HNO_3 was added to each withdrawn organic phase. The vials were again shaken for 1 min and left to stand for 10 min. This allows the copper(II) to extract back into the aqueous phase. 5 ml of the 5 % HNO_3 solution, containing the aqueous phase, was withdrawn and placed into another vial. These vials were then used to determine the copper(II) concentration of the organic phase.

For the aqueous phase, 0.5 ml was extracted from each vial after the two phases had separated and placed into separate vials. Then 24.9 ml of 5 % HNO_3 solution was added into each vial so that a total volume of 25.4 ml was obtained. From this, 5 ml of aqueous solution was withdrawn from each vial and placed into another vial, so that the copper(II) concentration of the aqueous phase could be determined. These volumes were specifically calculated because a final copper(II) concentration of between 1-2 ppm for the aqueous phase was required.

The copper(II) concentrations were analysed using an Agilent 4100 Microwave Plasma Atomic Emission Spectrometer (4100 MP-AES) from Agilent technologies and the data were analysed using MP Expert, Microwave Plasma Instrument software, version 1.1.1.45895. For the organic phase, standard solutions of 0.02, 0.05, 0.2, 0.5, 0.8, 1, 1.6, 2, 3, and 5 ppm were prepared using 5 % HNO_3. For the aqueous phase, standard solutions of 0.5, 1, 2, 2.5, 3, 4, 5 ppm were prepared using 5 % HNO_3 solution. The MP-AES was set to a wavelength of 324.795 nm.

A flow diagram that outlines the method can be seen in Figure 9.2.

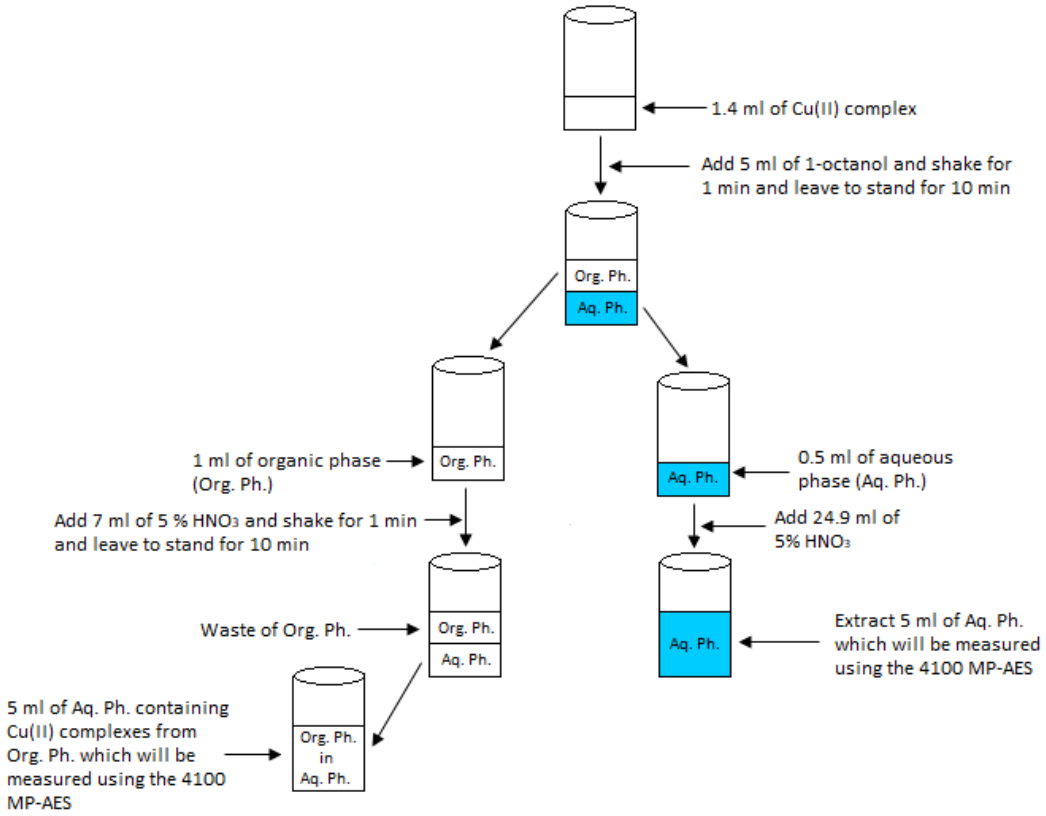

Figure 9.2: Flow diagram that depicts the flask shake method.

9.2.3 Results and Discussion

The partition coefficients (log $P_{oct/aq}$) were plotted against pH for each copper(II) complex and then overlaid onto the corresponding speciation diagrams, so that it is easy to identify which species are contributing to the trends seen in the partition coefficient curves. These overlaid graphs can be seen in Figures 9.3-9.6. A general similarity for Figures 9.3-9.6 is that over the pH range from 2-11, all the partition coefficient values are negative. At low pH values, only hydrated copper(II), $[Cu(OH_2)_6]^{2+}$, is present, which means the log $P_{oct/aq}$ values of -3.30 to -3.45, are due to hydrated copper(II). Other studies from literature have also found that before complexation occurs, in the acidic region, the low partition coefficient values are due to hydrated copper(II).[5,30–32] For all graphs, as the pH increases, the partition coefficient curves increase to reach a peak between approximately pH 4.6-5.5, after which they decrease and plateau with log $P_{oct/aq}$ values of approximately -3.10 to -3.27. By overlaying the partition coefficient values with the corresponding speciation diagram, it shows that the MLH and MLH_{-1} species for Cu-GLH, the MLH and ML species for Cu-Sar-LH and the MLH species for both Cu-GFH and Cu-Sar-FH, are responsible for the peak in each partition coefficient curve.

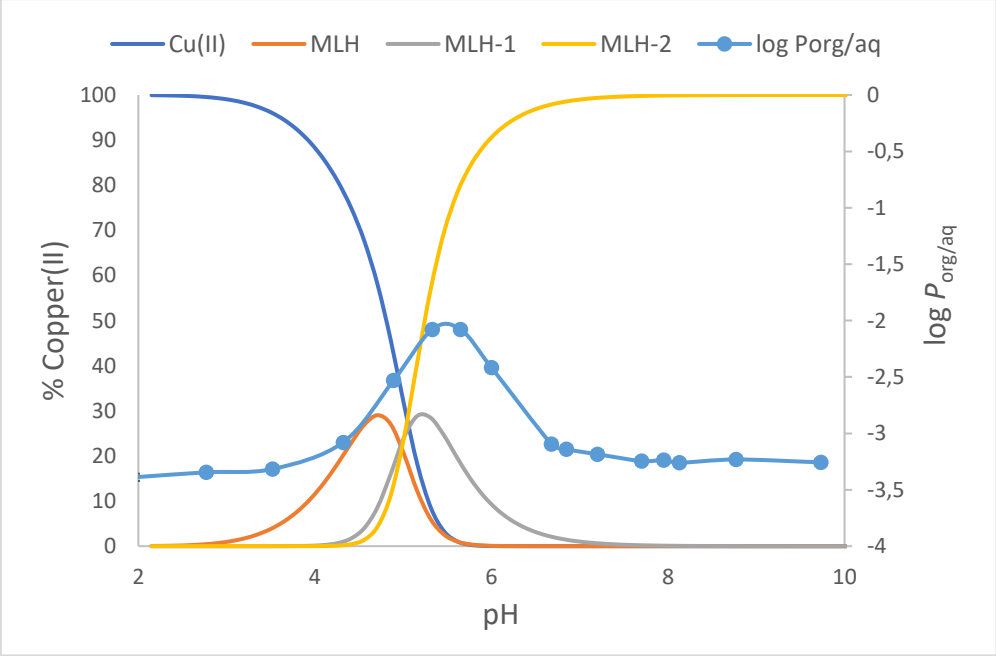

Figure 9.3: Species distribution curve for Cu-GLH at 25 °C in 0.15 mol.dm^{-3} of NaCl overlaid with the partition coefficient values of Cu-GLH (1:1) over a pH range from 2-10. Error bars have been included, but they are small and hidden behind the data points.

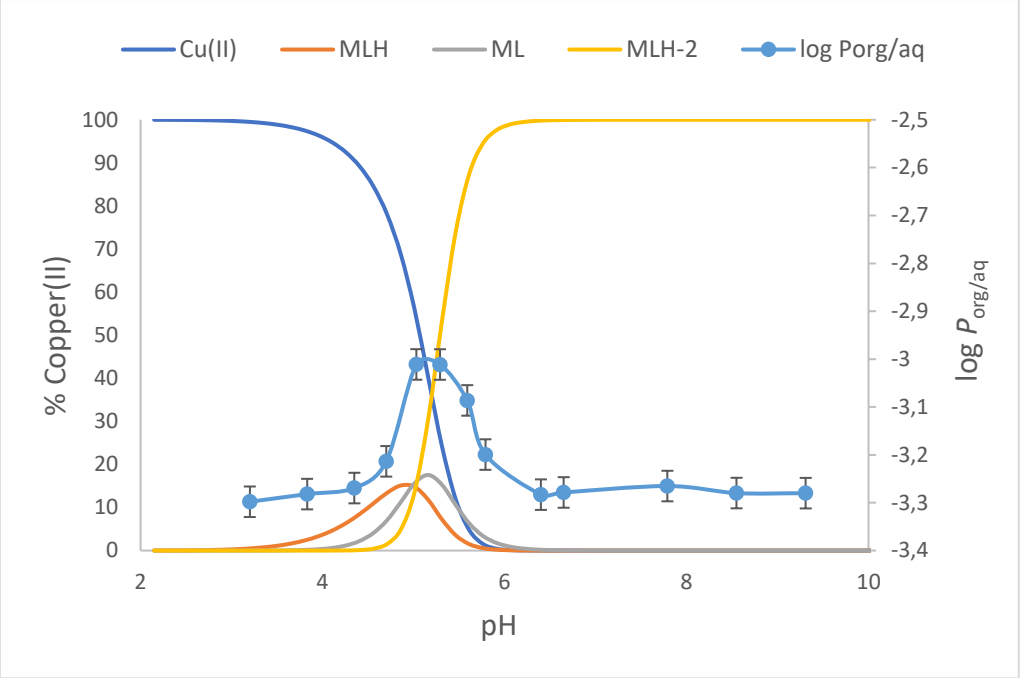

Figure 9.4: Species distribution curve for Cu-Sar-LH at 25 °C in 0.15 mol.dm^{-3} of NaCl overlaid with the partition coefficient values of Cu-Sar-LH (1:1) over a pH range from 2-10.

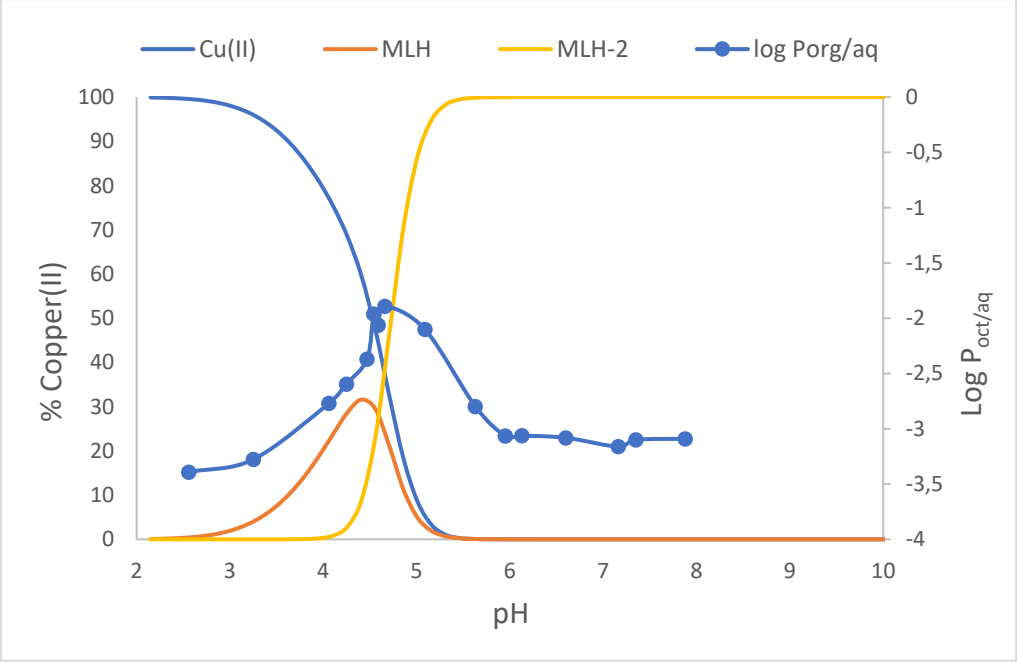

Figure 9.5: Species distribution curve for Cu-GFH at 25 °C in 0.15 mol.dm^{-3} of NaCl overlaid with the partition coefficient values of Cu-GFH (1:1) over a pH range from 2-10. Error bars have been included, but they are small and hidden behind the data points.

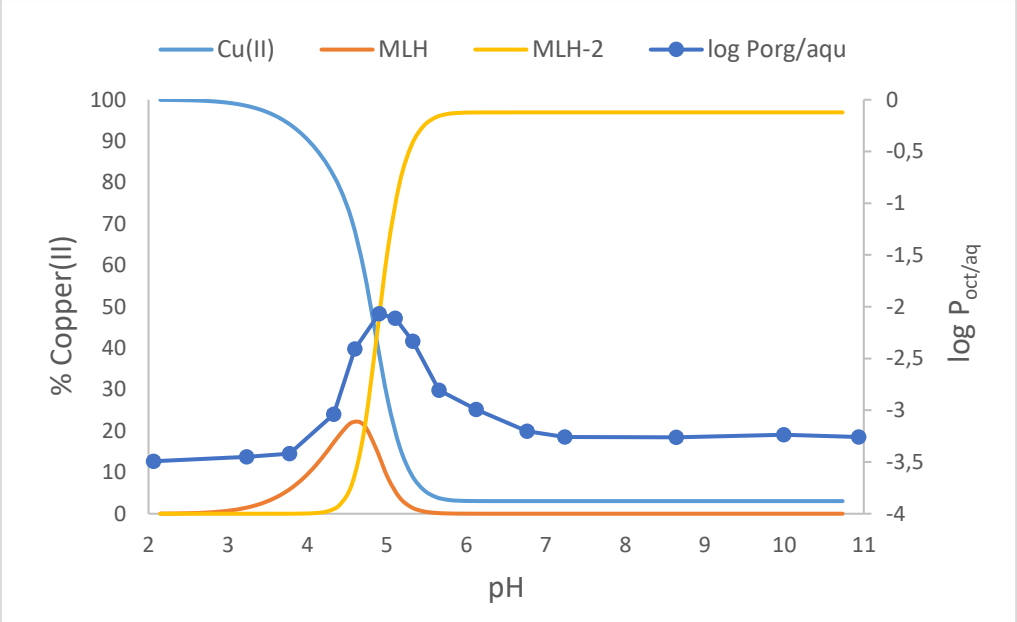

Figure 9.6: Species distribution curve for Cu-Sar-FH at 25 °C in 0.15 mol.dm^{-3} of NaCl overlaid with the partition coefficient values of Cu-Sar-FH (1:1) over a pH range from 2-10. Error bars have been included, but they are small and hidden behind the data points.

Octanol is an aliphatic alcohol, and so the more lipophilic a compound is, the more soluble it will be in the octanol phase. The lipophilicity of a complex or drug can be separated into four distinct areas. log $P_{oct\backslash aq}$ = 0-2.5 is a low lipophilicity, log $P_{oct\backslash aq}$ = 2.5-5 is an intermediate lipophilicity, log $P_{oct\backslash aq}$ = 5-7 is a high lipophilicity and log $P_{oct\backslash aq} \geq 7$ is a very high lipophilicity.[33] However, for transdermal absorption, a drug can be too lipophilic and instead of being absorbed through the skin, it gets trapped in the dermal layer.[34] Therefore, Zvimba *et al*.[35] suggests that for transdermal absorption to take place, the lipophilicity of a drug needs to be log $P_{oct\backslash aq}$ = 0.6. Following these definitions, the negative partition coefficients found in all four copper(II) complexes make them hydrophilic. However, as can be seen in Figures 9.3-9.6, the different species for each copper(II) complex have varying degrees of hydrophilicity and therefore depending on the pH, each complex has some lipophilic character. This makes a particular species able to dissolve into the octanol phase more readily than another species at a specific pH.

The types of species found between the four copper(II) complexes are the $[MLH]^{2+}$, $[ML]^{+}$ $[MLH_{-1}]$ and $[MLH_{-2}]^{-}$ species, each of which has a different charge. The charge of a complex affects its ability to move into the octanol phase, since the less charged a complex is, the more lipophilic it is and thus the more easily it can dissolve into the octanol phase. This is because

in the aqueous phase, the polar nature of water stabilizes the charge which causes the charged complex to preferentially remain in the aqueous phase. Other factors that also contribute to the hydrophilicity of the complexes are the formation of hydrogen bonds between the carbonyl and water molecules, as well as the bonding between charged groups within each species and NaCl. To calculate the charge of each complex, the ligands GLH, Sar-LH, GFH and Sar-FH are viewed in the state where the carboxyl group has lost a hydrogen, and the amine and imidazole groups are not protonated; this gives an overall ligand charge of -1. Copper(II) has a charge of +2, and therefore the MLH species has a charge of +2, the ML species has a charge of +1, the MLH_{-1} species has a charge of 0 and the MLH_{-2} species has a charge of -1. Thus, the expected order of lipophilicity is $MLH_{-1} > ML = MLH_{-2} > MLH$.

A physiological pH of 7.4 only refers to the blood plasma. The surface of the skin has a fine film called the mantle, which is slightly acidic with an average pH of 4.5-6.7. This mantle is a natural protection against infectious pathogens and therefore topical creams should be within this pH range or be pH-neutral (7) so that the mantle is not disrupted.[36] As a result of this pH requirement, the partition coefficient results will be analysed at the physiological pH of 7.4, as well as between pH 4.6-5.5.

At pH 7.4, the MLH_{-2} species is the only species present for all four copper(II) complexes and so the partition coefficient value at this pH is solely due to MLH_{-2}. The pH range of 4.6-5.5 firstly falls within the pH requirement for topical skin products and secondly it is where there is a maximum peak for all the partition coefficient curves. Specifically, the maximum peak for Cu-GLH, Cu-Sar-LH, Cu-GFH and Cu-Sar-FH occurs at approximately pH 5.5, pH 5.2, pH 4.6 and pH 4.9 respectively. These log $P_{oct\backslash aq}$ values, as well as the log $P_{oct\backslash aq}$ values for copper(II) chloride at pH 3 have been tabulated in Table 9.1. It is noted that at pH 7.4, the log $P_{oct\backslash aq}$ values are essentially the same as the log $P_{oct\backslash aq}$ values for copper(II) chloride. Furthermore, the amount of copper(II) that has been extracted into the octanol phase, is only 0.06%, 0.05%, 0.08% and 0.05% for Cu-GLH, Cu-Sar-LH, Cu-GFH and Cu-Sar-FH respectively, which is negligible. Since the copper(II) complexes have similar partition coefficient results to copper(II) chloride at pH 7.4, it is expected that the permeability of the complexes and thus their effectiveness to undergo transdermal absorption, will be similar to copper(II) chloride. Conversely, between pH 4.6-5.5 the complexes form an MLH and MLH_{-1} species for Cu-GLH, an MLH and ML species for Cu-Sar-LH and an MLH species for Cu-GFH and Cu-Sar-FH, which cause the complexes to become more lipophilic than copper(II)

chloride. It is interesting to note that even though the MLH species and the ML species are expected to be less or equal to the lipophilicity of the MLH_{-2} species, they both appear to be more lipophilic than the MLH_{-2} species. The copper(II) extraction into the octanol phase at the maximum of each curve, between pH 4.6-5.5, is 1%, 0.1%, 1.2% and 0.8% for Cu-GLH, Cu-Sar-LH, Cu-GFH and Cu-Sar-FH respectively.

Table 9.1: Comparison of the partition coefficient values at pH 7.4, pH 4.6-5.5 and pH 3.0 for Cu-GLH, Cu-Sar-LH, Cu-GFH and Cu-Sar-FH. The experimental error was calculated using the method outlined by Gardiner.[37]

Complex	**log $P_{oct\backslash aq}$ at pH 7.4**	**log $P_{oct\backslash aq}$ at pH 4.6-5.5**	**log $P_{oct\backslash aq}$ at pH 3.0**
Cu-GLH	-3.25 ± 0.03	-2.08 ± 0.03	-3.33 ± 0.03
Cu-Sar-LH	-3.27 ± 0.03	-3.01 ± 0.03	-3.30 ± 0.03
Cu-GFH	-3.10 ± 0.03	-1.89 ± 0.03	-3.32 ± 0.03
Cu-Sar-FH	-3.26 ± 0.04	-2.07 ± 0.04	-3.45 ± 0.04

A Student's t-test was performed to compare the complex partition coefficient values at a particular pH in order to determine how similar they are to one another. In the Student's t-test, each complex was paired with another and the resulting t-values can be seen in Table 9.2.

Table 9.2: Student's t-test of a two-tailed t-distribution performed between copper(II) complexes at pH 7.4, pH 4.6-5.5 and pH 3.0 with a significance level, α = 0.05, 4 degrees of freedom and a critical value ($t_{1-\alpha/2,\nu}$) = 2.776.

Copper(II) Complex Pair	**pH 7.4**	**pH 4.6-5.5**	**pH 3.0**
Cu-GLH and Cu-Sar-LH	0.82	37.97	-1.22
Cu-GLH and Cu-GFH	-6.12	-7.76	-0.41
Cu-GLH and Cu-Sar-FH	0.35	-0.35	4.16
Cu-Sar-LH and Cu-GFH	-6.94	-45.72	0.82
Cu-Sar-LH and Cu-Sar-FH	-0.35	-32.56	5.20
Cu-GFH and Cu-Sar-FH	5.54	6.24	4.50

When comparing the maximum recorded log $P_{oct\backslash aq}$ values between each complex at pH 4.6-5.5 (Table 9.1), the non-N-methylated groups appear to be more lipophilic than the N-methylated groups. The difference between the N-methylated and non-N-methylated complexes was confirmed to be significant by comparing the t-values in Table 9.2, which were found to be larger than the critical value. It was initially thought that since N-methylated groups would be more lipophilic than non-N-methylated groups, the complexes which have sarcosine would have higher partition coefficient values. However, Vicatos[38] found that there was no

difference between the lipophilicity between the non-N-methylated and N-methylated groups of Gly-Leu-Phe and Sar-Leu-Phe (t-value < critical value). As a result, this study was structured to verify this finding. Since this study also found a deviation from the expected result, there must be other factors that affect the lipophilicity of the complex. A possible factor could be similar to the factor that caused the non-N-methylated complexes to be unexpectedly more stable than the N-methylated complexes. If the amine groups preferentially form hydrogen bonds with water, which causes the stability of the complexes with sarcosine to decrease in comparison to the complexes with glycine, then it is possible that the redistribution of charge causes the complexes with sarcosine to become more polar and thus decreases their lipophilic nature. Additionally, when comparing the complexes with leucine to the complexes with phenylalanine, the complexes with phenylalanine are more lipophilic. Similarly, the difference was found to be significant when looking at the t-values in Table 9.2. Both leucine and phenylalanine are lipophilic groups with either an isobutyl or benzyl group respectively. A possible reason for the complexes with phenylalanine being more lipophilic, could be due to the same suggestion for why the phenylalanine complexes were found to be more stable than the leucine complexes. This again is possibly due to the preferential bonding of the amine groups with water, and the subsequent redistribution of charge.

At pH 7.4, as mentioned previously, the only species present in solution is MLH_{-2} and even though the partition coefficient values of all complexes were found to be similar to copper(II) chloride, an analysis to determine if methylation has an effect on the partition coefficient can be carried out. Looking at Table 9.1, when comparing the N-methylated to non-N-methylated complexes, there is no consistency in the results to suggest that methylation contributes to the lipophilicity. The same conclusion can be drawn when comparing the complexes with leucine to the complexes with phenylalanine. The t-values in Table 9.2 confirm that there is no consistency in either of the comparisons. Moreover, the partition coefficient values of GLH, Sar-LH and Sar-FH appear to have similar values to one another, while GFH appears to be significantly more lipophilic. This is confirmed with the t-values in Table 9.2.

At pH 3.0, it is expected that all the complex partition coefficient values will be similar because complexation is minimal at pH 3.0, and so the partition coefficient will be due to copper(II) chloride. When comparing the partition coefficient values, GLH, Sar-LH and GFH all appear to have similar values, while Sar-FH appears to deviate significantly from expected values. The t-values in Table 9.2 confirm this.

The design of the ligands GLH, Sar-LH, GFH and Sar-FH were based on the results from Vicatos[38] and Hammouda[34,39]. Vicatos[38] found the complexes Cu-Gly-Leu-Phe and Cu-Sar-Leu-Phe produced the highest transdermal absorption rates for tripeptides and the main contributing factors were the lipophilic leucine and phenylalanine amino acids. It was mainly because of these permeability results that leucine and phenylalanine were incorporated into GLH, Sar-LH, GFH and Sar-FH. The complexes studied by Hammouda[34,39] did not have as high transdermal absorption rates. But the complexes did have good mobilizing capacities, where the histidine amino acid was the main contributing factor and so histidine was also incorporated into the design. Therefore, because these literature studies are so closely linked to the design of GLH, Sar-LH, GFH and Sar-FH, a comparison between the partition coefficient values can be made to determine any similarities (Table 9.3). To make the comparison, the log $P_{oct\backslash aq}$ value at pH 7.4 was used to compare the complexes of this study to literature complexes. The pH range of 4.6-5.5 represents the maximum log $P_{oct\backslash aq}$ value of Cu-GLH, Cu-Sar-LH, Cu-GFH and Cu-Sar-FH at pH 5.5, pH 5.2, pH 4.6 and pH 4.9 respectively. Therefore, for simplicity, when comparing the complexes of this study to the complexes of literature, the log $P_{oct\backslash aq}$ value at pH 5.0 for each literature complex will be used. Similarly, a Student's t-test (Table 9.4) was done to assess if there is a significant difference between the complexes of this study and the literature complexes at pH 7.4 and pH 4.6-5.5. The outcome of this Student's t-test is that every comparison at each pH is significantly different.

Table 9.3: Comparison of the partition coefficient values at pH 7.4 and pH 4.6-5.5 between the complexes, Cu-GLH, Cu-Sar-LH, Cu-GFH, Cu-Sar-FH and literature.[34,38,39] Literature log $P_{oct\backslash aq}$ values have been taken at pH 5.0 for the comparison at pH 4.6-5.5. The experimental error was calculated using the method outlined by Gardiner.[37]

Complex	**log $P_{oct\backslash aq}$ at pH 7.4**	**log $P_{oct\backslash aq}$ at pH 4.6-5.5**
Cu-GLH	-3.25 ± 0.03	-2.08 ± 0.03
Cu-Sar-LH	-3.27 ± 0.03	-3.01 ± 0.03
Cu-GFH	-3.10 ± 0.03	-1.89 ± 0.03
Cu-Sar-FH	-3.26 ± 0.04	-2.07 ± 0.04
Cu-Sar-His-Lys[34,39]	-3.02 ± 0.01	-3.30 ± 0.05
Cu-Sar-Lys-His[34,39]	-2.05 ± 0.01	-2.40 ± 0.05
Cu-Sar-His-His[34,39]	-2.96 ± 0.01	-2.90 ± 0.05
Cu-Sar-Lys-Lys[34,39]	-2.63 ± 0.01	-3.60 ± 0.05
Cu-Sar-Gly-His[34,39]	-2.40 ± 0.01	-3.20 ± 0.05
Cu-Gly-Leu-Phe[38]	-1.79 ± 0.05	-2.25 ± 0.05
Cu-Sar-Leu-Phe[38]	-1.72 ± 0.05	-2.75 ± 0.05

Table 9.4: Student's t-test of a two-tailed t-distribution performed between the copper(II) complexes, Cu-GLH, Cu-Sar-LH, Cu-GFH, Cu-Sar-FH and literature[34,38,39], at pH 7.4 and pH 4.6-5.5 with a significance level, a = 0.05, 4 degrees of freedom and a critical value ($t_{1-a/2,v}$) = 2.776.

Copper(II) Complex Pair		**pH 7.4**	**pH 4.6-5.5**
Cu-GLH	Cu-Sar-His-Lys[34,39]	-12.60	36.24
	Cu-Sar-Lys-His[34,39]	-65.73	9.51
	Cu-Sar-His-His[34,39]	-15.88	24.36
	Cu-Sar-Lys-Lys[34,39]	-33.96	45.15
	Cu-Sar-Gly-His[34,39]	-46.56	33.27
	Cu-Gly-Leu-Phe[38]	-43.37	5.05
	Cu-Sar-Leu-Phe[38]	-45.45	18.12
Cu-Sar-LH	Cu-Sar-His-Lys[34,39]	-13.69	8.61
	Cu-Sar-Lys-His[34,39]	-66.82	-18.12
	Cu-Sar-His-His[34,39]	-16.98	-3.27
	Cu-Sar-Lys-Lys[34,39]	-35.05	17.53
	Cu-Sar-Gly-His[34,39]	-47.65	5.64
	Cu-Gly-Leu-Phe[38]	-43.96	-22.58
	Cu-Sar-Leu-Phe[38]	-45.74	-7.72
Cu-GFH	Cu-Sar-His-Lys[34,39]	-4.38	41.88
	Cu-Sar-Lys-His[34,39]	-57.51	15.15
	Cu-Sar-His-His[34,39]	-7.67	30.00
	Cu-Sar-Lys-Lys[34,39]	-25.74	50.79
	Cu-Sar-Gly-His[34,39]	-38.34	38.91
	Cu-Gly-Leu-Phe[38]	-38.91	10.69
	Cu-Sar-Leu-Phe[38]	-40.99	25.55
Cu-Sar-FH	Cu-Sar-His-Lys[34,39]	-10.08	33.27
	Cu-Sar-Lys-His[34,39]	-50.83	8.93
	Cu-Sar-His-His[34,39]	-12.60	22.45
	Cu-Sar-Lys-Lys[34,39]	-26.47	41.39
	Cu-Sar-Gly-His[34,39]	-36.13	30.57
	Cu-Gly-Leu-Phe[38]	-39.76	4.87
	Cu-Sar-Leu-Phe[38]	-41.66	18.39

Looking at Table 9.3, the partition coefficient values of this study's complexes at pH 7.4 are closer to the partition coefficient values of Hammouda[34,39] in comparison to the partition coefficient values of Vicatos[38]. This could be due to the presence of the histidine amino acid. But it could also be due to the types of species and their varying charges present at pH 7.4. To make a proper comparison, the contribution of the MLH_{-2} species towards the partition coefficient values, must be compared. However, this is not possible, since the log $P_{oct\backslash aq}$ values from Hammouda[34,39] and Vicatos[38] are a result from a combination of species, while the values from Cu-GLH, Cu-Sar-LH, Cu-GFH and Cu-Sar-FH are a result from only MLH_{-2}. In the pH range of 4.6-5.5, the peak partition coefficient values of Cu-GLH, Cu-Sar-LH, Cu-GFH and Cu-Sar-FH are neither closer to the partition coefficient values of Vicatos[38] nor of Hammouda[34,39].

Other studies which analysed the partition coefficient values of copper(II) complexes for the purpose of transdermal absorption have found log $P_{oct\backslash aq}$ values in the range of -1.65 to 0.08.[5,30–32,35] These values are higher than the values found for Cu-GLH, Cu-Sar-LH, Cu-GFH and Cu-Sar-FH, but the partition coefficient peak values (pH 4.6-5.5) are closer to the bottom value of this range. Therefore, the four ligands should be adjusted to this pH range to allow for transdermal absorption to occur.

9.2.4 Conclusion

The partition coefficients for the copper(II) complexes were found to be hydrophilic over the pH range from 2-10, but had varying degrees of hydrophilicity depending on the species present. For all copper(II) complexes, at pH 7.4, the only species present was the MLH_{-2} species. This species gave partition coefficient values that were similar to the partition coefficient values of copper(II) chloride, which meant that only 0.05-0.08 % of copper(II) was extracted into the octanol phase. The most lipophilic value over the pH range from 2-10, for each copper(II) complex, occurred between pH 4.6-5.5 and caused 0.8-1.2 % of copper(II) to be extracted into the octanol phase. The species that were responsible for bringing about this peak in partition coefficients, were the MLH and MLH_{-1} species for Cu-GLH, the MLH and ML species for Cu-Sar-LH and the MLH species for both Cu-GFH and Cu-Sar-FH. For the partition coefficient values between pH 4.6-5.5, the non-N-methylated ligands were found to be more lipophilic than the N-methylated ligands, and the ligands with phenylalanine were found to be more lipophilic than the ligands with leucine. Overall, the pH range of 4.6-5.5 is within the pH requirement for topical skin creams and it is also the range where the complexes, Cu-GLH, Cu-Sar-LH, Cu-GFH and Cu-Sar-FH have a peak log $P_{oct\backslash aq}$ value. This means that the pH of the ligands needs to be adjusted to this pH range when undergoing transdermal absorption.

9.3 Modified Franz Cell: Permeability Coefficient

9.3.1 Franz cell diffusion method

While the octanol/water partition coefficient values predict the lipophilicity of complexes, the permeability coefficient values physically measure how well complexes can undergo transdermal absorption via the intercellular pathway of the stratum corneum.[20,21] To measure the permeability coefficients, a modified Franz cell can be used.[22] This apparatus is essentially two chambers which are separated by a membrane. In this case it is an artificial membrane. Copper(II) diffuses passively from the one chamber into the other through the membrane, and by monitoring this movement, the permeability coefficients can be calculated.[14] A diagram of the modified Franz cell setup can be seen in Figure 9.7.

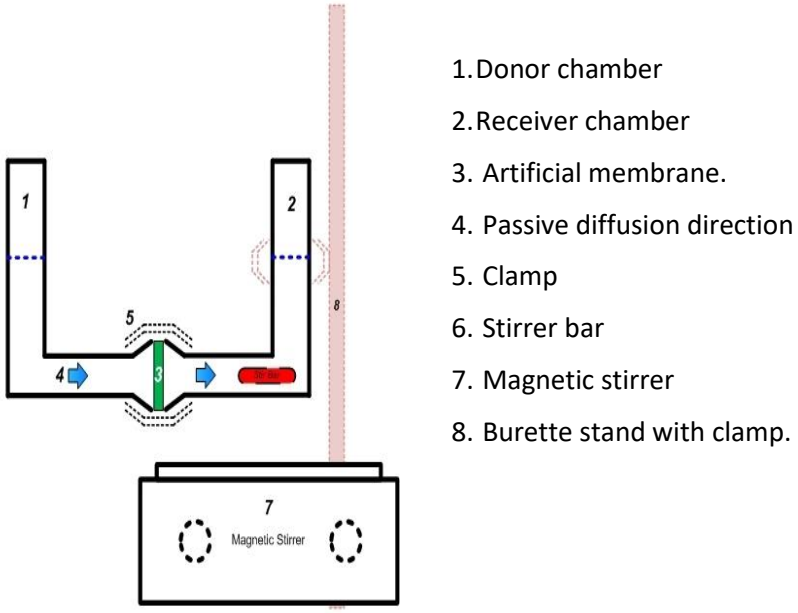

Figure 9.7: Diagram of a modified Franz cell.[23]

The permeability coefficient is related to the steady state of flux of the copper(II) complexes as they passively diffuse through the membrane via the equation:

$$K_{\mathrm{p}} = \frac{J}{c_i} \tag{9.2}$$

where, K_p is the permeability coefficient (cm/h), J is the steady state of flux, which is the mass that crosses through a unit area of the membrane in a unit time (mg/cm^{2}h), and C_i is the initial concentration of the solution in the donor chamber.[13,22] The relationship between the permeability and the steady state of flux is possible because of Fick's first law, which relates the flux (J) to the concentration gradient of a solute.[24,25] (equation 9.3)

$$J = - D \frac{dC}{dX} \tag{9.3}$$

where, D is the diffusion coefficient of the solute (cm^2/h), dC is the change in concentration of the solute (mg/cm^3) and dX is the change in position of the solute (cm). The negative sign shows that the flux is positive when the movement of the solute is down the gradient.
When mass is involved, the steady state of flux, J, can also be expressed as:

$$J = \frac{1}{S}\frac{dM}{dt} \tag{9.4}$$

where, dM is the change in mass (mg), dt is the change in time (h) and S (cm^2) is the surface area available for the mass to move through.[10,24,26] In this case, S is the surface area of the artificial membrane.

From equation 9.4, the steady state of flux can thus be calculated when the gradient of the linear region, in an accumulative diffusion-time curve, is divided by the surface area of the artificial membrane. From equation 9.2, the permeability coefficient can then be calculated when the steady state of flux is divided by the initial concentration of copper(II) in the donor chamber.[27,28]

At the beginning of an accumulative diffusion-time curve, the diffusion rate is not constant and therefore the system has not yet achieved a steady state of flux. The time the system takes to reach a steady state of flux is called the lag time and it is a result of the solutes reaching an equilibrium between the solution in the donor phase and the membrane. Translated to an *in vivo* environment, the lag time is a function of how long it takes for the drug to enter the stratum corneum and dermis, the thickness of the skin and the diffusivity. The lag time (τ) can be expressed as:

$$\tau = \frac{x^2}{6D} \tag{9.5}$$

where, x is the thickness of the membrane and *D* is the diffusion coefficient.[25,29]

9.3.2 Experimental

Each copper(II) complex was prepared as a 1:1 copper(II) ligand ratio in 20 ml of Milli-Q water (18.2 MΩ.cm) and set to the physiological pH of 7.4. Each copper(II) complex was again prepared as a 1:1 copper(II) ligand ratio in 20 ml of Milli-Q water, except with a different pH setting. Cu-GLH was set to pH 5.5, Cu-Sar-LH was set to pH 5.2, Cu-GFH was set to pH 4.6 and Cu-Sar-FH was set to pH 4.9. These pH values correspond to the pH where the maximum partition coefficient occurred for each ligand (pH 4.6-5.5). The concentration of the ligands was 0.005 M and the concentration of copper(II) was adjusted to be slightly lower at 0.004 M to prevent the precipitation of $Cu(OH)_2$, but still maintain an approximate 1:1 ratio. A copper(II) chloride solution with the same concentration as the copper(II) added to the ligands, was prepared in 20 ml of Milli-Q water and set to a pH of 4.2. The adjusted lower pH was to prevent the precipitation of $Cu(OH)_2$. All solutions were prepared with no background electrolyte. The experiment was set up into two groups; the first group measured the permeability at pH 7.4 and the second group measured the permeability at the pH where each ligand showed a maximum partition coefficient (pH 4.6-5.5). The diameter opening for each chamber was measured and the available area where diffusion can take place for the first group (pH 7.4) was measured to be 0.617, 0.570, 0.617, 0.570 and 0.570 cm^2 for Cu-GFH, Cu-Sar-LH, Cu-GLH, Cu-Sar-FH and copper(II) chloride respectively. For the second group (pH 4.6-5.5), the available area was measured to be 0.617 cm^2 for all ligands. The artificial membrane was made using Whatman International Ltd filter paper, which has a thickness of 0.0012 cm and a diffusion area of 0.709 cm^2. The lipid membrane solution was prepared by mixing 70 % silicone and 30 % isopropyl myristate (IPM)[40]. The filter paper was then soaked in the lipid membrane solution and any excess solution was shaken off. The amount of lipid absorbed by the filter paper was determined by the mass difference between the lipid-absorbed filter paper and the non-lipid-absorbed filter paper. This was between 0.026-0.037 g for all setups.

Each of the nine solutions was added to the donor chamber of the Franz cells and 20 ml of Milli-Q water was added simultaneously to the receiver chamber of the Franz cells. Before the Milli-Q water was added to the receiver chambers, the Milli-Q water that was paired with the complex solutions was adjusted to mimic the pH in the donor phase and the Milli-Q water that was paired with the copper(II) chloride solution was adjusted to pH 4.2. Magnetic stirrer bars were added to each chamber and the whole Franz cell setup was kept in a temperature-controlled environment of 25 °C. The opening of each chamber was covered to help minimise evaporation. At time zero and after every subsequent reading, 0.5 ml samples were extracted from both the donor and receiver chambers. The intervals between each reading were kept to 1-1.5 hourly intervals for the first 10 hours and then randomly thereafter until approximately 35-50 hours had passed. 4.5 ml of 5 % nitric acid solution was added to each collected receiver phase sample to make a total volume of 5 ml. 84 ml of 5 % nitric acid solution was added to the first donor phase sample (0 h), so that the concentration became approximately 2 ppm. The copper(II) concentrations from each sample were analysed using an Agilent 4100 Microwave Plasma Atomic Emission Spectrometer (4100 MP-AES) from Agilent technologies and the data were analysed using MP Expert, Microwave Plasma Instrument software, version 1.1.1.45895. Standard solutions of 0.5, 1, 2, 4, 6, 8 and 10 ppm of copper(II) were prepared using 5 % nitric acid solution. The MP-AES was set to a wavelength of 324.795 nm.

9.3.3 Results and Discussion

Before performing the Franz cell diffusion experiments, the validity of the membrane first had to be verified. This was done by repeating an experiment from literature with the aim of reproducing a similar permeability coefficient. This was achieved by reproducing the permeability coefficient of salicylic acid, which experimentally was found to have a permeability coefficient of -4.03, while in literature it is -4.26.[40] This similarity meant that the Franz cell experiments would give accurate results.

The concentration of copper(II) measured in the receiver phase for all the complexes at pH 7.4, as well as for copper(II) chloride can be seen in Table 9.5. The time intervals for Cu-GLH and Cu-Sar-FH are slightly different to the time intervals for Cu-Sar-LH, Cu-GFH and $CuCl_2.2H_2O$. This is due to having a limited number of Franz cell apparatuses and having to repeat the process twice.

Table 9.5: Copper(II) concentration measured in the receiver phase as a function of time after each copper(II) complex (pH 7.4) and copper(II) chloride (4.2) had diffused through the artificial membrane. The experimental errors were calculated by following the method outlined by Gardiner.[37]

Time (h)	Cu-GLH (ppm)	Cu-Sar-FH (ppm)	Time (h)	Cu-GFH (ppm)	Cu-Sar-LH (ppm)	$CuCl_2.2H_2O$ (ppm)
0.0	0.14 ± 0.05	0.08 ± 0.05	0.0	0.00 ± 0.04	0.00 ± 0.04	0.00 ± 0.04
1.0	0.19 ± 0.05	0.22 ± 0.05	1.0	0.13 ± 0.04	0.04 ± 0.04	0.22 ± 0.04
2.0	0.41 ± 0.05	0.27 ± 0.05	2.0	0.41 ± 0.04	0.17 ± 0.04	0.65 ± 0.04
3.0	0.64 ± 0.05	0.42 ± 0.05	3.0	0.56 ± 0.04	0.33 ± 0.04	1.09 ± 0.04
4.0	1.33 ± 0.05	0.55 ± 0.05	4.3	0.78 ± 0.04	0.38 ± 0.04	1.49 ± 0.04
5.0	1.08 ± 0.05	0.70 ± 0.05	5.3	0.94 ± 0.04	0.69 ± 0.04	1.76 ± 0.04
6.0	1.30 ± 0.05	0.88 ± 0.05	6.6	1.17 ± 0.04	1.03 ± 0.04	2.16 ± 0.04
8.0	1.51 ± 0.05	1.07 ± 0.05	7.8	1.36 ± 0.04	1.28 ± 0.04	2.42 ± 0.04
9.0	1.76 ± 0.05	1.22 ± 0.05	9.3	1.63 ± 0.04	1.39 ± 0.04	2.73 ± 0.04
10.3	2.29 ± 0.04	1.60 ± 0.05	11.1	1.98 ± 0.04	1.47 ± 0.04	3.39 ± 0.04
13.1	2.64 ± 0.04	2.00 ± 0.05	14.2	2.37 ± 0.04	1.77 ± 0.04	3.93 ± 0.04
16.1	3.27 ± 0.04	2.43 ± 0.04	16.8	2.87 ± 0.04	2.71 ± 0.04	4.64 ± 0.04
23.3	4.51 ± 0.04	3.36 ± 0.04	19.1	3.21 ± 0.04	3.09 ± 0.04	5.01 ± 0.04
25.9	4.83 ± 0.04	3.66 ± 0.04	26.7	4.10 ± 0.04	4.38 ± 0.04	6.50 ± 0.04
28.1	6.37 ± 0.05	4.00 ± 0.04	29.5	4.76 ± 0.04	4.64 ± 0.04	7.03 ± 0.04
29.9	5.26 ± 0.04	4.10 ± 0.04	32.1	5.07 ± 0.04	4.94 ± 0.04	7.27 ± 0.04
32.2	5.55 ± 0.04	5.28 ± 0.04	33.9	5.65 ± 0.04	5.47 ± 0.04	7.82 ± 0.04
34.9	5.84 ± 0.05	4.72 ± 0.04	36.7	5.93 ± 0.04	5.87 ± 0.04	8.16 ± 0.04
38.0	6.41 ± 0.05	5.21 ± 0.04	39.2	6.27 ± 0.04	6.26 ± 0.04	8.61 ± 0.05
40.3	6.70 ± 0.05	5.58 ± 0.04	41.5	6.57 ± 0.04	6.09 ± 0.04	8.87 ± 0.05
49.3	7.54 ± 0.05	6.50 ± 0.05	43.8	6.87 ± 0.04	6.93 ± 0.04	9.22 ± 0.05
52.1	7.84 ± 0.05	5.81 ± 0.05	54.3	8.17 ± 0.04	8.01 ± 0.04	10.14 ± 0.05

A graphical representation of Table 9.5 is plotted in Figure 9.8 and shows the measured copper(II) concentration found in the receiver cells over time. For the first two hours (0-2 hr), the system seems to be establishing an equilibrium between the solutions and the membrane. Another equilibrium is reached between the solutes of the donor phase and the receiver phase after approximately 20.0 hours for Cu-Sar-LH and Cu-GFH, 24.0 hours for Cu-GLH and Cu-Sar-FH, and 30.0 hours for $CuCl_2.2H_2O$. A steady state of flux can therefore be seen in the linear regions between 2.0-19.1 hours, 2.0-23.3 hours and 2.0-30.0 hours respectively.

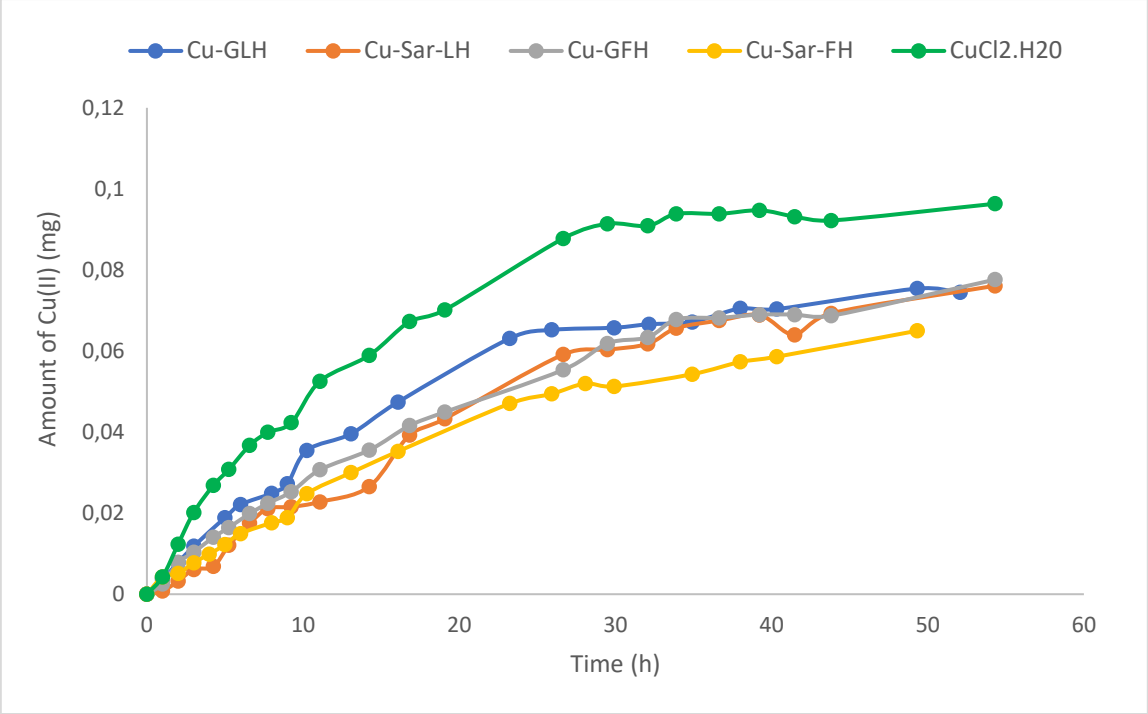

Figure 9.8: Graphical representation of the copper(II) concentration measured in the receiver phase as a function of time after each copper(II) complex (pH 7.4) and copper(II) chloride (pH 4.2) had diffused through the artificial membrane. Also known as the accumulative absorption-time curve. Error bars ranging from ± 0.0004-0.001 mg of copper(II) were omitted for simplicity.

By calculating the gradient of the linear portion in the accumulative absorption-time curve in Figure 9.8, the steady state of flux, *J*, can be calculated using equation 9.4 and then the permeability coefficients, K_p, can be calculated from equation 9.2. Figure 9.9 shows the gradients of each linear portion, which is 0.0026, 0.0022, 0.0022, 0.002 and 0.0024 for Cu-GLH, Cu-Sar-LH, Cu-GFH, Cu-Sar-FH and $CuCl_2.H_2O$ respectively. The calculated steady states of flux, *J*, and the permeability coefficients, K_p, can be seen in Table 9.6.

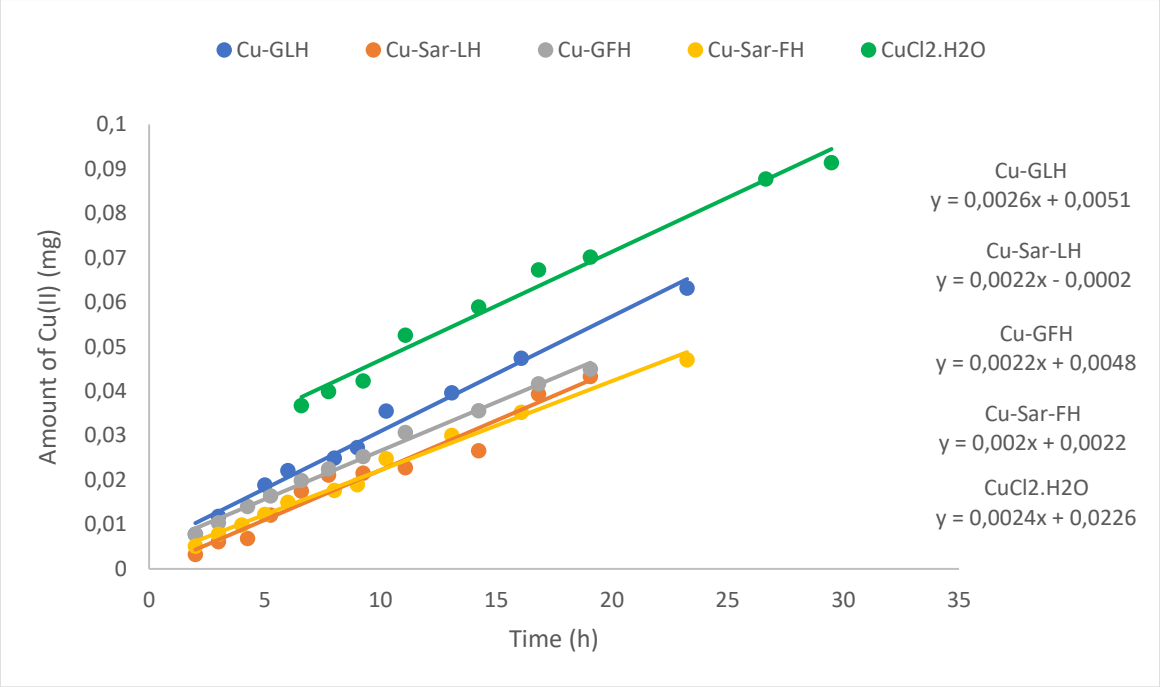

Figure 9.9: The calculated gradients from the linear region in the accumulative absorption-time curve for the measured copper(II) concentration in each receiver phase at pH 7.4.

Table 9.6: The calculated steady state of flux, *J*, and permeability coefficient, K_p for copper(II) complexes at pH 7.4 and copper(II) chloride at pH 4.2 after each had diffused through the artificial membrane. The experimental errors were calculated by following the method outlined by Gardiner.[37]

Complexes	***J* (mg/cm^2 h)**	**K_p (cm/h)**
Cu-GLH	0.0042 ± 0.0003	0.0162 ± 0.0003
Cu-Sar-LH	0.0035 ± 0.0003	0.0136 ± 0.0003
Cu-GFH	0.0035 ± 0.0002	0.0135 ± 0.0003
Cu-Sar-FH	0.0035 ± 0.0002	0.0152 ± 0.0003
$CuCl_2.H_2O$	0.0042 ± 0.0003	0.0146 ± 0.0003

Looking at the steady states of flux and permeability coefficients (Table 9.6), the values for all the complexes, as well as for copper(II) chloride, are essentially the same, since they are within or close to the experimental error of each other. The initial thought is that the membrane of the Franz cell is not able to differentiate between the complexes and copper(II) chloride. However, it can differentiate, because firstly the validity of the membrane was verified and secondly, the partition coefficients suggested that the permeability of the copper(II) complexes and copper(II) chloride would be similar, since the partition coefficient values were similar.

Therefore, following the results from the flask shake method, the partition coefficient values of each ligand were at a maximum between pH 4.6-5.5, and so for the Franz cell, each ligand was set to a pH that corresponded to their maximum partition coefficient value. For Cu-GLH this is pH 5.5, for Cu-Sar-LH this is pH 5.2, for Cu-GFH this is pH 4.6 and for Cu-Sar-FH this is pH 4.9. The concentration of copper(II) measured in the receiver phase for all the ligands between pH 4.6-5.5 can be seen in Table 9.7. Additionally, as mentioned before, at the surface of the skin, the mantle is slightly acidic with a pH of 4.5-6.7 and so the optimum goal is to develop a topical cream that has a pH range within 4.5-6.7 or a neutral pH (7), so that the mantle is not disrupted.[36] Conveniently the pH where the maximum partition coefficient values occur, is also within the optimum pH range to develop a topical cream, so obtaining the permeability of the ligands between pH 4.5-6.7 is ideal from all aspects.

Table 9.7: Copper(II) concentration measured in the receiver phase as a function of time after each copper(II) complex (pH 4.6-5.5) had diffused through the artificial membrane. The experimental errors were calculated by following the method outlined by Gardiner.[37]

Time (h)	**Cu-GLH (ppm)**	**Time (h)**	**Cu-Sar-LH (ppm)**	**Time (h)**	**Cu-GFH (ppm)**	**Time (h)**	**Cu-Sar-FH (ppm)**
0.0	-0.06 ± 0.07	0.0	0.00 ± 0.05	0.0	0.14 ± 0.04	0.0	-0.01 ± 0.05
1.0	0.06 ± 0.07	1.0	0.17 ± 0.04	1.0	0.45 ± 0.04	1.0	0.09 ± 0.05
3.0	0.20 ± 0.07	2.1	0.34 ± 0.04	2.0	0.61 ± 0.04	2.0	0.15 ± 0.04
4.0	0.42 ± 0.07	3.1	0.55 ± 0.04	3.0	0.85 ± 0.04	3.3	0.27 ± 0.04
5.0	0.71 ± 0.07	4.1	0.93 ± 0.04	4.0	1.09 ± 0.04	4.3	0.29 ± 0.04
6.0	0.84 ± 0.07	5.1	0.76 ± 0.04	5.0	1.34 ± 0.04	5.3	0.43 ± 0.04
7.0	1.07 ± 0.07	6.3	1.22 ± 0.04	6.0	1.51 ± 0.04	6.0	0.64 ± 0.04
8.0	1.55 ± 0.06	7.4	1.46 ± 0.04	7.0	1.96 ± 0.04	7.1	0.84 ± 0.04
9.0	1.81 ± 0.06	8.5	1.67 ± 0.04	8.0	2.19 ± 0.04	8.1	1.24 ± 0.04
10.1	1.97 ± 0.06	10.3	1.91 ± 0.04	10.0	2.41 ± 0.04	9.1	1.52 ± 0.04
11.0	2.33 ± 0.06	12.5	2.28 ± 0.04	12.0	2.83 ± 0.04	10.1	1.96 ± 0.04
13.0	2.62 ± 0.06	14.5	2.61 ± 0.04	14.0	3.41 ± 0.04	12.2	2.19 ± 0.04
14.9	2.99 ± 0.06	16.5	2.72 ± 0.04	16.0	3.78 ± 0.04	14.0	2.47 ± 0.04
16.3	3.38 ± 0.06	20.9	3.36 ± 0.04	18.3	4.34 ± 0.04	15.9	2.84 ± 0.04
20.3	4.05 ± 0.06	23.0	3.70 ± 0.04	22.0	4.81 ± 0.04	17.3	3.16 ± 0.04
23.0	4.52 ± 0.06	24.5	3.84 ± 0.04	24.0	5.42 ± 0.04	18.9	3.63 ± 0.04
25.1	5.00 ± 0.06	27.5	4.41 ± 0.04	28.0	6.00 ± 0.04	22.3	4.34 ± 0.04
26.0	5.28 ± 0.06	30.5	4.97 ± 0.04	30.2	6.40 ± 0.04	25.5	4.95 ± 0.04
28.1	5.57 ± 0.06	33.3	5.37 ± 0.04	33.2	6.81 ± 0.04	27.5	5.38 ± 0.04
30.5	5.93 ± 0.06	36.0	5.76 ± 0.04			30.8	6.01 ± 0.04
33.1	6.41 ± 0.06					33.8	6.20 ± 0.04
35.0	6.68 ± 0.06					37.0	7.09 ± 0.04

Similarly, a graphical representation of Table 9.7 is plotted in Figure 9.10. The graph of copper(II) chloride used in Figure 9.8 has been added as well. Unlike Figure 9.8, these complexes take up to 10 hours to establish an equilibrium between the solutions and the

membrane. Another difference is that they do not reach an equilibrium between the solutes of the donor phase and the receiver phase in the time lapse of the experiment. A steady state of flux for the complexes can therefore be seen between approximately 10-35 hours.

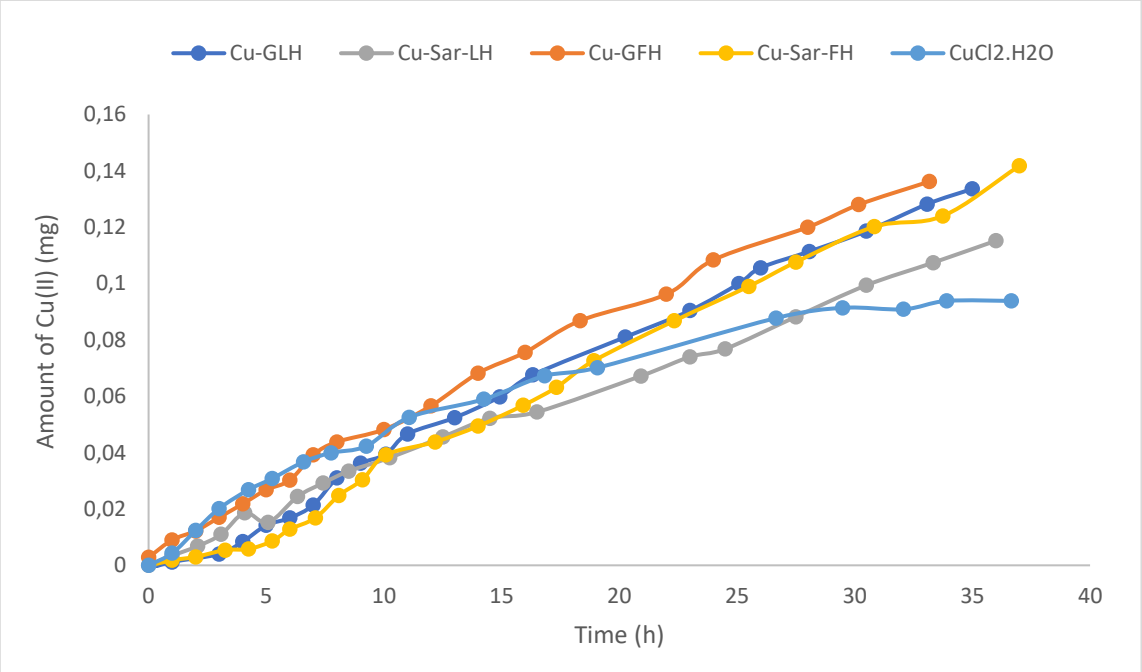

Figure 9.10: Graphical representation of the copper(II) concentration measured in the receiver phase as a function of time after each copper(II) complex (pH 4.6-5.5) and copper(II) chloride (pH 4.2) had diffused through the artificial membrane. Error bars ranging from ± 0.0004-0.001 mg of copper(II) were omitted for simplicity.

Similarly, the gradient of the linear portion in the accumulative absorption-time curve in Figure 9.10 was used to calculate the steady state of flux, J, and then the permeability coefficients, K_p, which can be seen in Table 9.8. Figure 9.11 shows the gradients of the linear portions, which are 0.0039, 0.0030, 0.0040, 0.0041 and 0.0024 for Cu-GLH, Cu-Sar-LH, Cu-GFH, Cu-Sar-FH and $CuCl_2.H_2O$ respectively.

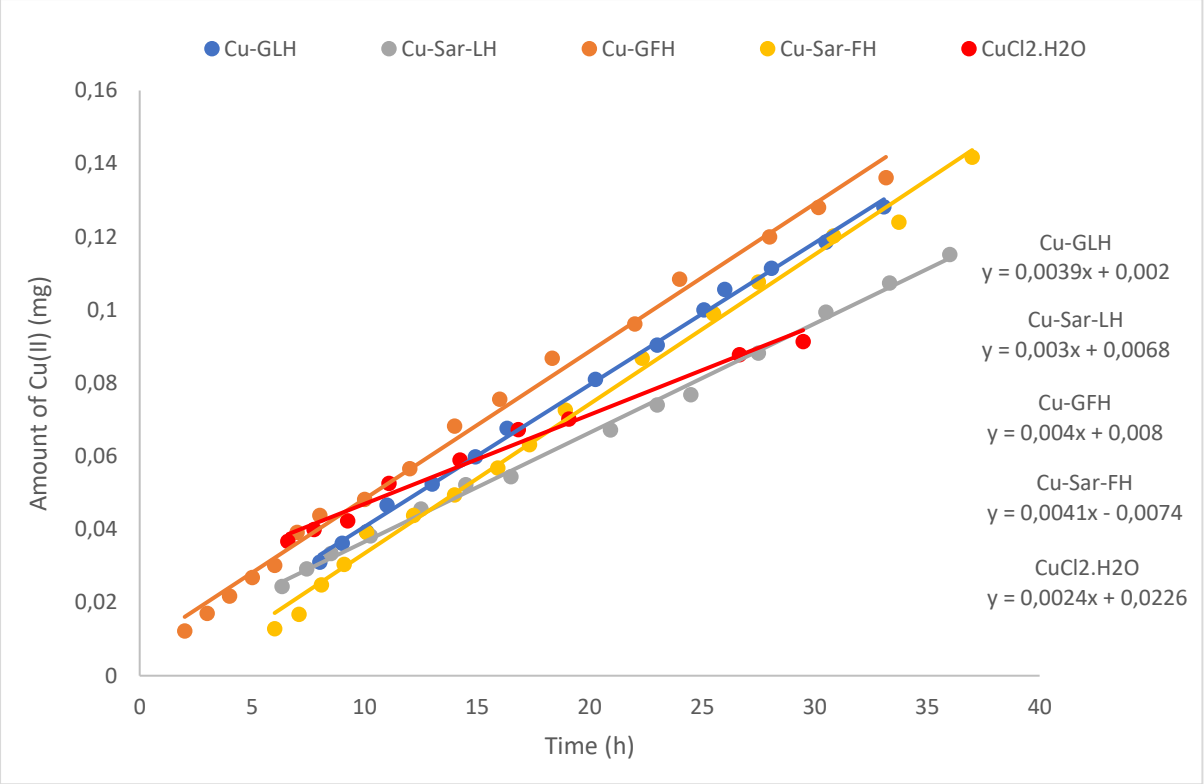

Figure 9.11: The calculated gradients from the linear region in the accumulative absorption-time curve for the measured copper(II) concentration in each receiver phase at pH 4.6-5.5.

Table 9.8: The calculated steady state of flux, J, and permeability coefficient, K_p, for copper(II) complexes at pH 4.6-5.5 and copper(II) chloride at pH 4.2 after each had diffused through the artificial membrane. The experimental errors were calculated by following the method outlined by Gardiner.[37]

Complexes	***J* (mg/cm^2 h)**	***K_p* (cm/h)**
Cu-GLH	0.0063 ± 0.0003	0.0253 ± 0.0005
Cu-Sar-LH	0.0049 ± 0.0004	0.0203 ± 0.0004
Cu-GFH	0.0065 ± 0.0003	0.0276 ± 0.0006
Cu-Sar-FH	0.0067 ± 0.0003	0.0287 ± 0.0006
$CuCl_2.H_2O$	0.0042 ± 0.0003	0.0146 ± 0.0003

Table 9.8, as well as Figures 9.10 and 9.11, show that the copper(II) complexes between a pH of 4.6-5.5 have a higher steady state of flux and permeability coefficient than copper(II) chloride. This observation corresponds to the results from the partition coefficient values, where it was expected that the ligands would have a higher permeability coefficient than copper(II) chloride at pH values between 4.6-5.5. It also shows that out of the four ligands, Sar-LH has the lowest permeability coefficient, which corresponds to Sar-LH having the lowest partition coefficient at approximately pH 5.2. Additionally, no increase in permeability

coefficients was found for the non-N-methylated ligands or for the ligands with phenylalanine, even though an increase was found in their lipophilicity.

This means that the aim of finding a ligand that can increase the permeation rate of copper(II) by forming a complex with copper(II) and undergoing transdermal absorption, particularly via a passive diffusion through the stratum corneum, has been achieved with Cu-GLH, Cu-Sar-LH, Cu-GFH and Cu-Sar-FH. These ligands can therefore be considered as therapeutic drugs for rheumatoid arthritis.

For the purpose of comparison, it is interesting to see the permeability results of other drugs, which have been designed for anti-inflammatory purposes. To compare permeability results between different studies, the direct values of K_p cannot be used. This is because the permeability coefficient is dependent on the concentration and because the concentration has an influence on the liquid compounds in percutaneous absorption, which cannot be quantified.[28] Thus, to compare the permeability between complexes, each copper(II) complex permeability result will first be calculated as a percentage of copper(II) that permeates through the membrane per $cm.h^{-1}$. Then the percentage of permeated copper(II) chloride will be subtracted from the percentage of permeated copper(II) complex from the same study. These resultant values can then be seen as the effective percentage per $cm.h^{-1}$ of copper(II) that permeates through the artificial membrane as a result of complexation. A table comparing the ability of literature tripeptides to permeate through an artificial membrane, compared to Cu-GLH, Cu-Sar-LH, Cu-GFH and Cu-Sar-FH, can be seen in Table 9.9.

Table 9.9: A comparison between the permeability of Cu-GLH, Cu-Sar-LH, Cu-GFH and Cu-Sar-FH with the copper(II) tripeptide complexes from Hammouda[39], Vicatos[38] and Mazurowska and Mojski[10] is done by calculating the effective amount of permeated copper(II) as a result of the complex.

Complex	**% of permeated copper(II) chloride per cm.h^{-1}**	**% of permeated copper(II) complex per cm.h^{-1}**	**Effective amount of permeated copper(II) as a result of the complex (% per cm.h^{-1})**
Cu-GLH	1.5 %	2.5 %	1.0 %
Cu-Sar-LH	1.5 %	2.0 %	0.5 %
Cu-GFH	1.5 %	2.8 %	1.3 %
Cu-Sar-FH	1.5 %	2.9 %	1.4 %
Cu-Gly-Leu-Phe[38]	13.7 %	22.5 %	8.8 %
Cu-Sar-Leu-Phe[38]	13.7 %	20.6 %	6.9 %
Cu-Gly-His-Lys[10]	0.1 %	2.2 %	1.3 %
Cu-Sar-His-Lys[39]	2.8 %	4.9 %	2.1 %
Cu-Sar-Lys-His[39]	2.8 %	4.7 %	1.9 %
Cu-Sar-His-His[39]	2.8 %	4.1 %	1.3 %
Cu-Sar-Lys-Lys[39]	2.8 %	3.8 %	1.0 %
Cu-Sar-Gly-His[39]	2.8 %	6.1 %	3.3 %

From Table 9.9, it can be seen that Cu-GLH, Cu-Sar-LH, Cu-GFH and Cu-Sar-FH are comparable to the tripeptides studied by Hammouda[39], as well as by Mazurowska and Mojski[10], since they have similar permeated percentage values. The tripeptides Gly-Leu-Phe and Sar-Leu-Phe[38] have significantly higher permeated percentage values. This high permeability was suggested[38] to be due to the amino acids, leucine and phenylalanine, which have non-polar side chains, and thus make the overall tripeptides lipophilic. In comparison, histidine and lysine have polar functional groups which create an overall hydrophilic effect. The initial thought in creating the tripeptides, GLH, Sar-LH, GFH and Sar-FH was that by adding either leucine or phenylalanine together with histidine, leucine and phenylalanine will combat the polar effect of histidine to a degree. However, since the permeability of the four tripeptides in this study are similar in value to the tripeptides studied by Hammouda[39] and by Mazurowska and Mojski[10], it suggests that the polar effect of the imidazole functional group in histidine is stronger than the non-polar effect of leucine or phenylalanine.

The artificial membrane of the Franz cell represents the intercellular pathway through the lipid bilayer. It does not consider the intracellular pathway which goes primarily through the corneocytes and a smaller portion of the lipid bilayer when travelling from cell to cell. Since only polar, hydrophilic substances can diffuse through the corneocytes, this route could also be a potential pathway for the copper(II) complexes.[7,11,16] The other possible pathway that needs

to be considered is through the hair follicle appendages. Even though the exact process of how particles pass through the hair follicles is not well understood,[16,41] it seems to be the main route for hydrophilic drugs and therefore could also be a potential pathway for Cu-GLH, Cu-Sar-LH, Cu-GFH and Cu-Sar-FH.[18,42] However, the 0.1-1 %[11,17] prevalence of follicles on total skin coverage area is not favourable. Needless to say, these alternative considerations and pathways could also increase the amount of drug that undergoes transdermal absorption.

9.3.4 Conclusion

The permeability coefficients at pH 7.4, for all the copper(II) complexes were the same as that of copper(II) chloride. This means that these complexes, at pH 7.4, cannot increase the bioavailable pool of copper(II) *in vivo* by using exogenous sources and undergoing an intercellular route. However, the permeability of the copper(II) complexes was increased when the pH was set to correspond to each ligand's maximum partition coefficient value, between pH 4.6-5.5. In this pH range the permeation rate of copper(II) increased by 1.0 % for Cu-GLH, 0.5 % for Cu-Sar-LH, 1.3 % for Cu-GFH and 1.4 % for Cu-Sar-FH. This pH range also conveniently overlaps with the optimum pH range of topical cream. This, as well as the increased permeation rates, signifies that between pH 4.6-5.5, the copper(II) complexes can be considered as a possible therapeutic drug for rheumatoid arthritis.

9.4 References

1 G. E. Jackson, P. M. May and D. R. Williams, Metal-ligand complexes involved in rheumatoid arthritis—I, *J. Inorg. Nucl. Chem.*, 1978, **40**, 1189–1194.

2 G. E. Jackson, P. M. May and D. R. Williams, Metal-ligand complexes involved in rheumatoid arthritis—VI, *J. Inorg. Nucl. Chem.*, 1978, **40**, 1227–1234.

3 K. D. Rainsford and M. W. Whitehouse, Concerning the merits of copper aspirin as a potential anti-inflammatory drug, *J. Pharm. Pharmacol.*, 1976, **28**, 83–86.

4 J. R. J. Sorenson, Copper Chelates as Possible Active Forms of the Antiarthritic Agents, *J. Med. Chem.*, 1976, **19**, 135–148.

5 S. Odisitse and G. E. Jackson, In vitro and in vivo studies of N,N′-bis[2(2-pyridyl)-methyl]pyridine-2,6-dicarboxamide-copper(II) and rheumatoid arthritis, *Polyhedron*, 2008, **27**, 453–464.

6 S. Odisitse and G. E. Jackson, In vitro and in vivo studies of the dermally absorbed Cu(II) complexes of N5O2 donor ligands - Potential anti-inflammatory drugs, *Inorganica Chim. Acta*, 2009, **362**, 125–135.

7 G. P. Moss, J. C. Dearden, H. Patel and M. T. D. Cronin, Quantitative structure–permeability relationships (QSPRs) for percutaneous absorption, *Toxicol. Vitr.*, 2002, **16**, 299–317.

8 R. J. Scheuplein and I. H. Blank, Permeability of the skin, *Physiol. Rev.*, 1971, **51**, 702–747.

9 R. J. Scheuplein, Mechanism of Percutaneous Adsorption, *J. Invest. Dermatol.*, 1965, **45**, 334–346.

10 L. Mazurowska and M. Mojski, ESI-MS study of the mechanism of glycyl-l-histidyl-l-lysine-Cu(II) complex transport through model membrane of stratum corneum, *Talanta*, 2007, **72**, 650–654.

11 M. Rauma and G. Johanson, Comparison of the thermogravimetric analysis (TGA) and Franz cell methods to assess dermal diffusion of volatile chemicals, *Toxicol. Vitr.*, 2009, **23**, 919–926.

12 P. H. Lee, R. Conradi and V. Shanmugasundaram, Development of an in silico model for human skin permeation based on a Franz cell skin permeability assay, *Bioorg. Med. Chem. Lett.*, 2010, **20**, 69–73.

13 R. O. Potts and R. H. Guy, Predicting skin permeability., *Pharm. Res.*, 1992, **9**, 663–9.

14 J. J. Hostynek, Factors determining percutaneous metal absorption, *Food Chem. Toxicol.*, 2003, **41**, 327–345.

15 R. J. Feldmann, Penetration of 14C Hydrocortisone Through Normal Skin, *Arch. Dermatol.*, 1965, **91**, 661.

16 O. G. Jepps, Y. Dancik, Y. G. Anissimov and M. S. Roberts, Modeling the human skin barrier — Towards a better understanding of dermal absorption, *Adv. Drug Deliv. Rev.*, 2013, **65**, 152–168.

17 M.-A. Bolzinger, S. Briançon, J. Pelletier and Y. Chevalier, Penetration of drugs through skin, a complex rate-controlling membrane, *Curr. Opin. Colloid Interface Sci.*, 2012, **17**, 156–165.

18 F. Knorr, J. Lademann, A. Patzelt, W. Sterry, U. Blume-Peytavi and A. Vogt, Follicular transport route – Research progress and future perspectives, *Eur. J. Pharm. Biopharm.*, 2009, **71**, 173–180.

19 T. Haque and M. M. U. Talukder, Chemical Enhancer: A Simplistic Way to Modulate Barrier Function of the Stratum Corneum, *Adv. Pharm. Bull.*, 2018, **8**, 169–179.

20 T. Hatanaka, M. Inuma, K. Sugibayashi and Y. Morimoto, Prediction of skin permeability of drugs. I. Comparison with artificial membrane., *Chem. Pharm. Bull. (Tokyo).*, 1990, **38**, 3452–3459.

21 K. Matsyzaki, T. Imaoka, M. Asano and K. Miyajima, Development of a Model Membrane System Using Stratum Corneum Lipids for Estimation of Drug Skin Permeability., *Chem. Pharm. Bull. (Tokyo).*, 1993, **41**, 575–579.

22 L. Mazurowska, K. Nowak-Buciak and M. Mojski, ESI–MS method for in vitro investigation of skin penetration by copper–amino acid complexes: from an emulsion through a model membrane, *Anal. Bioanal. Chem.*, 2007, **388**, 1157–1163.

23 E. U. Tsumbu, Evaluation of tissue permeability of novel copper based anti-arthritic drugs, MSc Thesis, University of Cape Town, 2010.

24 H. J. V. Tyrrell, The origin and present status of Fick's diffusion law, *J. Chem. Educ.*, 1964, **41**, 397.

25 L. Bartosova and J. Bajgar, Transdermal Drug Delivery In Vitro Using Diffusion Cells, *Curr. Med. Chem.*, 2012, **19**, 4671–4677.

26 S. Ebnesajjad, Ed., *Handbook of Biopolymers and Biodegradable Plastics: Properties, Processing and applications*, William Andrew, UK/USA, 2013.

27 S. Wilkinson and F. Williams, Effects of experimental conditions on absorption of glycol ethers through human skin in vitro, *Int. Arch. Occup. Environ. Health*, 2002, **75**,

519–527.

28 G. Korinth, K. H. Schaller and H. Drexler, Is the permeability coefficient Kp a reliable tool in percutaneous absorption studies?, *Arch. Toxicol.*, 2005, **79**, 155–159.

29 H. L. Frisch, The Time Lag in Diffusion, *J. Phys. Chem.*, 1957, **61**, 93–95.

30 J. N. Zvimba and G. E. Jackson, Solution equilibria of copper(II) complexation with N,N′-(2,2′-azanediylbis(ethane-2,1-diyl))dipicolinamide: A bio-distribution and dermal absorption study, *J. Inorg. Biochem.*, 2007, **101**, 1120–1128.

31 J. N. Zvimba and G. E. Jackson, Copper chelating anti-inflammatory agents; N1-(2-aminoethyl)-N2-(pyridin-2-ylmethyl)-ethane-1,2-diamine and N-(2-(2-aminoethylamino)ethyl)picolinamide: An in vitro and in vivo study, *J. Inorg. Biochem.*, 2007, **101**, 148–158.

32 S. Odisitse, G. E. Jackson, T. Govender, H. G. Kruger and A. Singh, Chemical speciation of copper(II) diaminediamide derivative of pentacycloundecane - A potential anti-inflammatory agent, *Dalt. Trans.*, 2007, 1140–1149.

33 M. Gertz, P. J. Kilford, J. B. Houston and A. Galetin, Drug Lipophilicity and Microsomal Protein Concentration as Determinants in the Prediction of the Fraction Unbound in Microsomal Incubations, *Drug Metab. Dispos.*, 2008, **36**, 535–542.

34 G. E. Jackson, A. N. Hammouda, F. M. Elmagbari and R. P. Bonomo, In vitro studies of dermally absorbed Cu(II) tripeptide complexes as potential anti-inflammatory drugs, *Polyhedron*, 2017, **123**, 23–32.

35 J. N. Zvimba and G. E. Jackson, Thermodynamic and spectroscopic study of the interaction of Cu(II), Ni(II), Zn(II) and Ca(II) ions with 2-amino-N-(2-oxo-2-(2-(pyridin-2-yl)ethyl amino)ethyl)acetamide, a pseudo-mimic of human serum albumin, *Polyhedron*, 2007, **26**, 2395–2404.

36 J. Buscemi, We asked experts about the importance of pH in skin care, and proceeded to test all of our products, https://hellogiggles.com/beauty/ph-skincare-explainer/, (accessed 25 October 2019).

37 W. P. Gardiner, *Statistical Analysis Methods for Chemists: A Software Based Approach*, The Royal Society of Chemistry, UK, 1997.

38 G. M. Vicatos, In vitro studies of dermally absorbed Cu(II) tripeptide complexes as potential anti-inflammatory drugs, MSc Thesis, University of Cape Town, 2016.

39 A. N. Hammouda, Development of copper peptide complexes as anti-Inflammatory drugs, PhD Thesis, University of Cape Town, 2015.

40 G. Ottaviani, S. Martel and P.-A. Carrupt, Parallel Artificial Membrane Permeability

Assay: A New Membrane for the Fast Prediction of Passive Human Skin Permeability, *J. Med. Chem.*, 2006, **49**, 3948–3954.

41 K. Wilke, R. Wepf, F. J. Keil, K.-P. Wittern, H. Wenck and S. S. Biel, Are Sweat Glands an Alternate Penetration Pathway? Understanding the Morphological Complexity of the Axillary Sweat Gland Apparatus, *Skin Pharmacol. Physiol.*, 2006, **19**, 38–49.

42 B. . Barry, Drug delivery routes in skin: a novel approach, *Adv. Drug Deliv. Rev.*, 2002, **54**, S31–S40.

10. Blood Plasma Model

10.1 Introduction

In the blood plasma, copper(II) exists as a metal that is bound to a variety of species and the exact ratio of how copper(II) is divided up between the variety of species varies within literature.[1,2] For instance, one report says that 65% of copper(II) is bound irreversibly to caeruloplasmin, 15% to the N-terminal end of serum albumin, 15% to transcuprein and 5% to low molecular mass complexes.[3] Another report says that 71% of copper(II) is bound to caeruloplasmin, 19% to serum albumin, 7% to transcuprein, and 2% to amino acids.[4] Overlooking the slight discrepancies, what is commonly evident is that a large portion of endogenous copper(II) is not available, as it is irreversibly bound to caeruloplasmin. The exchangeable copper(II), which is the copper(II) that is bound to the other species, is less prevalent, but can become mobile if needed.

Therefore, the secondary aim of this study is to design a drug that, once in the blood plasma, will increase the concentration of low molecular mass complexes. In doing so, it will increase the bioavailable pool of copper(II), provided that the homeostasis of the other endogenous metal ions is not affected. The rationale behind this attempt is led by a shift in the equilibrium of free vs bound endogenous copper(II), i.e. the ligand will form a complex with free copper(II), which in turn will cause proteins such as albumin to release copper(II) so that a new equilibrium is established. This was achieved with the ligands 3,6,9,12-tetra-azatetradecanedioic acid (ttda) and 3,6,9-triazaundecanedioate (dtda).[5,6] However, they were such powerful chelators of copper(II) that their complexes became biologically inactive and were excreted, unchanged in the urine.[6,7] Thus, the aim is to develop a ligand that is selective for copper(II), but less competitive than serum albumin.

A computer model can be used to analyse all the low molar mass complexes of the blood plasma along with the ligands GLH, Sar-LH, GFH and Sar-FH, provided that there is the assumption that all components of the blood are at equilibrium. The program, Evaluation of Constituent Concentrations in Large Equilibrium Systems, (ECCLES) was used to perform the analysis.[8] This program has a list of metals and ligands that are found in the blood plasma, as

well as a list of the complex species, with their stability constants, that are formed between the metals and ligands. From these lists, the program generates 5000 complexes that are found in the blood plasma from 7 metal ions and 40 ligands. The program is then able to calculate the speciation of the metals and ligands, which includes the competition from other species, as well as estimates the equilibrium concentration of individual species.[8–12]

The results are presented in terms of a plasma mobilizing index (P.M.I), which represents the movement of metal ions from a protein bound form to a low molar mass complex. A definition for the P.M.I is the increase in the total concentration of low molecular weight complexes of a specific metal ion, which is caused by a ligand. The better the ligands are at specifically binding to endogenous copper(II), the higher the P.M.I value is. The value of P.M.I is calculated using equation 10.1.[11,13]

$$\text{P.M.I} = \frac{\text{Total concentration of low molecular weight metal complex species in plasma in presence of the ligand}}{\text{Total concentration of low molecular weight metal complex species in normal plasma}} \quad (10.1)$$

However, as mentioned previously, a very high P.M.I will indicate a biologically inactive complex, which will not be beneficial as a treatment for rheumatoid arthritis. Therefore a P.M.I value that is not too large (relative to previous literature values[5]) and which is produced from a ligand with a low, biologically suitable concentration, is required.

In the blood plasma, copper(II) has to compete with other metal ions to form a complex with the ligands. In particular, zinc(II), nickel(II) and calcium(II) are of concern, since they have higher concentrations than copper(II) and therefore could interfere with the complexation of copper(II). The concentration of free zinc(II), nickel(II) and calcium ions is 10^{-11}-10^{-8} mol.dm^{-3}, 10^{-11} mol.dm^{-3} and 10^{-3} mol.dm^{-3} respectively, while the concentration of free copper(II) ions is 10^{-18}-10^{-11} mol.dm^{-3}.[8,14,15] This means that the ligands have to preferentially bind to copper(II) to overcome the higher concentration of the other metal ions. The stability constants of nickel(II) and zinc(II) were determined during the potentiometric titrations and so these values can be inserted into ECCLES. However, the stability constants for calcium(II) were not determined during the potentiometric titrations, but they can be estimated from a linear free energy relationship.[16,17] A graph showing the linear free energy relationship between copper(II) and calcium(II) was constructed by Hammouda[18] and can be seen in Figure 10.1. From the

equation of the graph, the stability constants for the ML and MLH species of calcium(II) were found. The MLH_{-1} and MLH_{-2} species were not calculated, since calcium(II) only coordinates to the oxygen donors of peptides.[19,20]

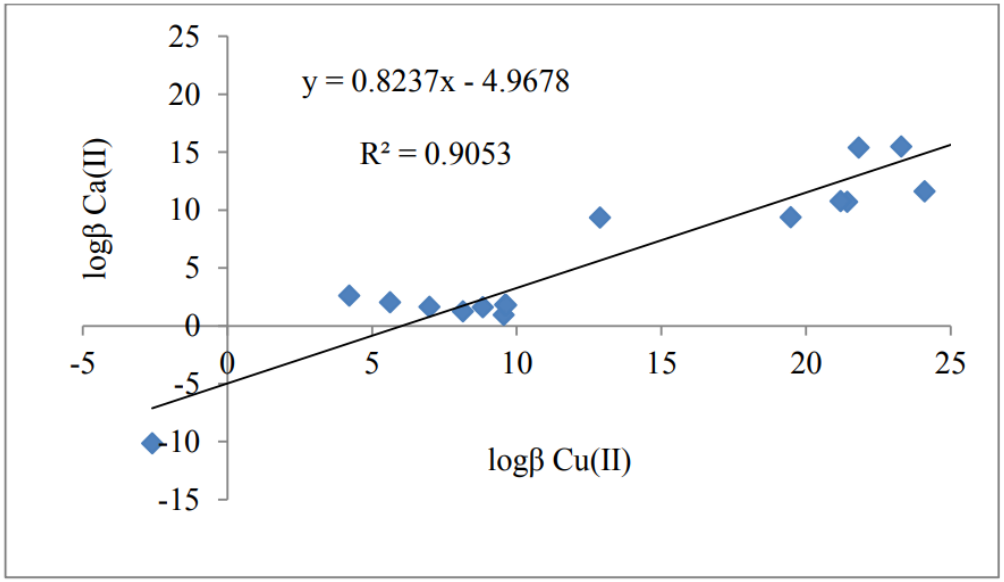

Figure 10.1: The linear free energy relationship between log β Cu(II) and log β Ca(II) constructed from amino acid and peptide complex species which have the same ionic strength and temperature.[18]

10.2 Methodology

The program ECCLES was used to model the speciation of copper(II), nickel(II), zinc(II) and calcium(II) with GLH, Sar-LH, GFH and Sar-FH in the blood plasma. The protonation and stability constants that were determined in the potentiometric titration section for copper(II), nickel(II) and zinc(II) were inserted into ECCLES. These protonation and stability constants can be seen in Table 10.1 and Table 10.2 respectively. The calculated stability constants for calcium(II) that were obtained from the linear free energy relationship between log β Cu(II) and log β Ca(II) in Figure 10.1, were also inserted into ECCLES. From this, ECCLES was able to calculate the P.M.I indices. The comparison between the P.M.I indices of copper(II) with nickel(II), zinc(II) and calcium(II) can determine whether the complexes can favour binding specifically to copper(II) in the presence of free nickel(II), zinc(II) and calcium(II).

Table 10.1: Potentiometric protonation constants that were used to calculate the P.M.I indices.

Ligand	Protonation		
	LH	**LH_2**	**LH_3**
GLH	8.21	15.10	17.88
Sar-LH	8.45	15.32	18.05
GFH	7.95	14.82	17.65
Sar-FH	8.22	15.09	17.96

Table 10.2: Potentiometric stability constants that were used to calculate the P.M.I indices.

Metal	Ligand	Species			
		MLH	**ML**	**MLH_{-1}**	**MLH_{-2}**
Copper(II)	GLH	12.71		2.77	-2.24
	Sar-LH	12.37	7.38		-2.70
	GFH	12.76			-1.03
	Sar-FH	12.66			-1.51
Nickel(II)	GLH	11.34		-1.78	-9.20
	Sar-LH	11.52		-2.79	-9.86
	GFH	11.32		-1.84	-8.53
	Sar-FH	11.40		-2.88	-9.48
Zinc(II)	GLH		4.51	-3.71	-13.62
	Sar-LH	10.66	3.70	-4.13	-13.47
	GFH		4.23	-3.34	-13.44
	Sar-FH		3.52	-3.82	-13.35
Calcium(II)	GLH	5.50			
	Sar-LH	5.22	1.11		
	GFH	5.54			
	Sar-FH	5.46			

10.3 Results

Figures 10.2-10.5 show the P.M.I curves for copper(II), nickel(II), zinc(II) and calcium(II) as a function of ligand concentration. For all complexes, nickel(II), zinc(II) and calcium(II) are not competitors against copper(II) and thus the ligands can effectively mobilise copper(II) in the blood plasma. For topical application, a realistic ligand concentration would be 0.1 mM. If this concentration is used, then the increase in low molecular mass metal species would be 2.4 times for GLH, 1.3 times for Sar-LH, 40.7 times for GFH and 8.7 times for Sar-FH.

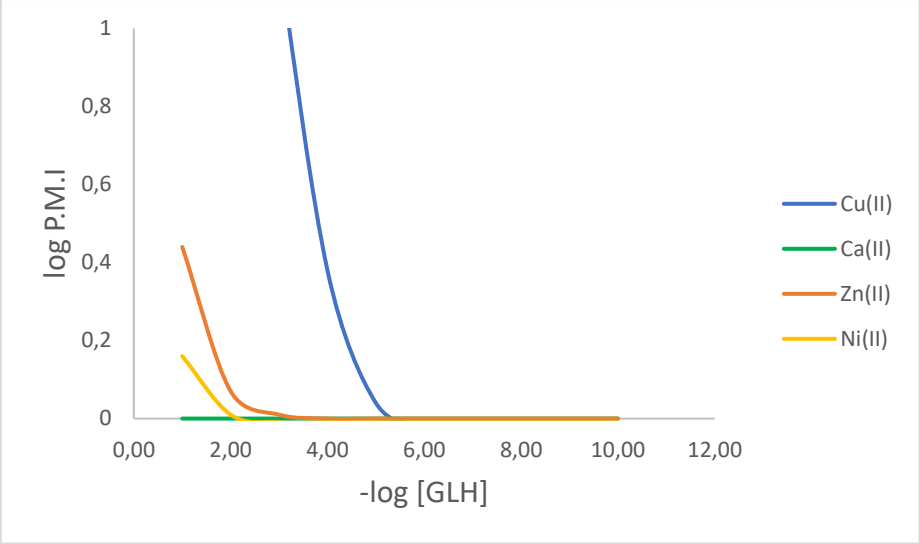

Figure 10.2: The log P.M.I curves for copper(II), calcium(II), zinc(II) and nickel(II) with GLH and plotted against –log[GLH].

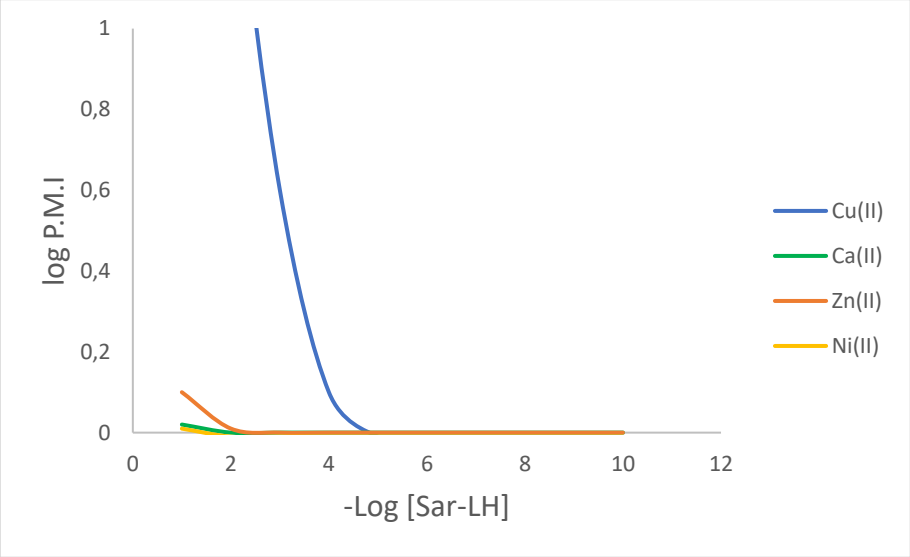

Figure 10.3: The log P.M.I curves for copper(II), calcium(II), zinc(II) and nickel(II) with Sar-LH and plotted against –log[Sar-LH].

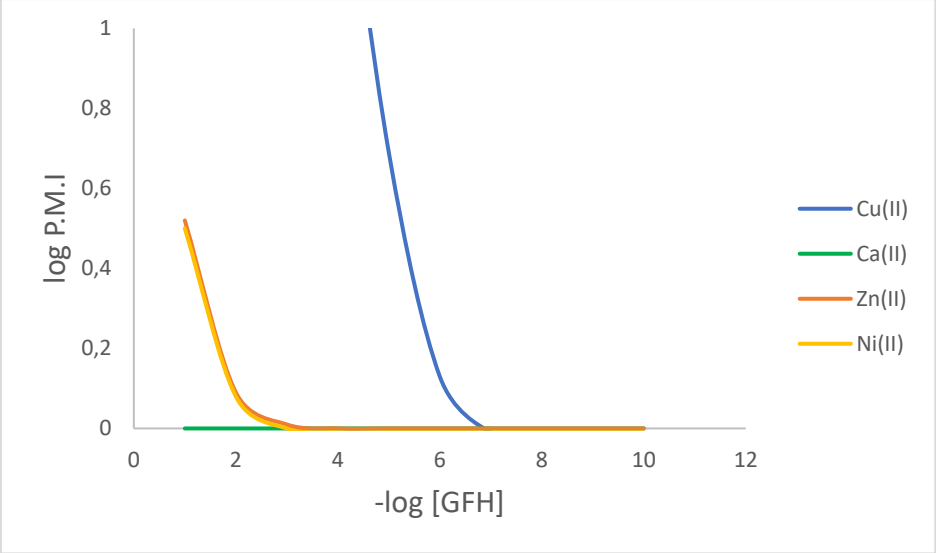

Figure 10.4: The log P.M.I curves for copper(II), calcium(II), zinc(II) and nickel(II) with GFH and plotted against –log[GFH].

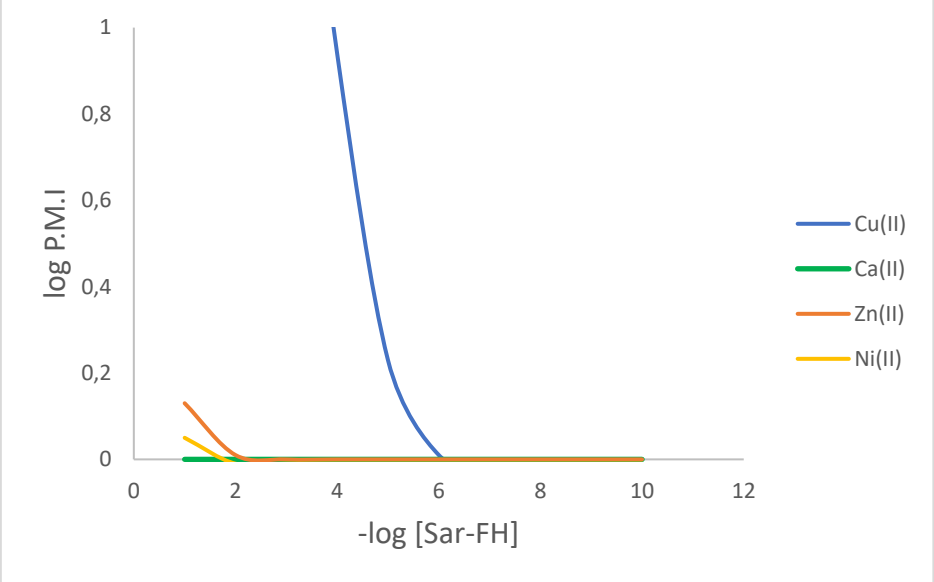

Figure 10.5: The log P.M.I curves for copper(II), calcium(II), zinc(II) and nickel(II) with Sar-FH and plotted against –log[Sar-FH].

10.4 Discussion

The ligand order for the mobilising of copper(II) is GFH > Sar-FH > GLH > Sar-LH. Figure 10.6 visually compares the mobilizing efficiency of copper(II) between these ligands. Two patterns have emerged from this order. The first is that the ligands with phenylalanine have

higher mobilizing capacities than the ligands with leucine, and the second is that the ligands with glycine are higher than the ligands with sarcosine. Notably, Jackson *et al.*[10] found that the ligands with a methyl group increased the mobilizing efficiency by 10-fold and this was rationalized as a result from an inductive effect, but in this case the non-methylated tripeptides are more efficient.

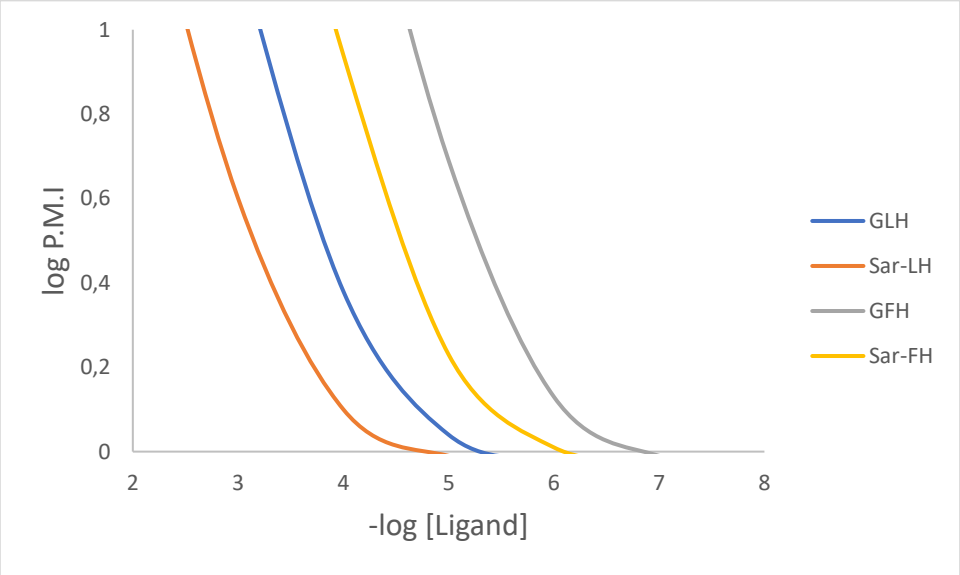

Figure 10.6: A comparison of the mobilizing efficiency of copper(II) between GLH, Sar-LH, GFH and Sar-FH.

Hammouda[18] found that despite a report[10] which says that ligands containing histidine are not good at mobilising copper(II) *in vivo*, tripeptides with histidine actually do help to increase the mobilization of copper(II). More specifically, histidine in the third position of the tripeptide increased the mobilizing capacity more than if it were in the second position. It was for this reason that all the ligands, GLH, Sar-LH, GFH and Sar-FH, contained histidine in the third position. In comparison, the mobilizing capacities of GLH, Sar-LH, GFH and Sar-FH are in general much better than the ligands studied by Hammouda[18]. This is due to the amino acids, leucine and phenylalanine. Like histidine, leucine and phenylalanine were specifically chosen because Mohajane[21] studied a series of dipeptides and found that Gly-Phe and Gly-Leu had the highest mobilizing capacities.

When comparing the P.M.I values of other drugs that have been designed for anti-inflammatory purposes, GLH, Sar-LH, GFH and Sar-FH tend to fall within a middling range. For example, relative to the mobilizing capacities of the four ligands at ligand concentrations where a 10-fold

increase in low molecular mass metal species is obtained, N^1-(2-aminoethyl)-N^2-(pyridine-2-ylmethyl)ethane-1,2-diamine[11] ((555)-N) is 2.5-4.5 orders of magnitude better at mobilizing copper(II); ttda and dtda[5,6] are approximately 2-4 orders of magnitude better at mobilizing copper(II); and *N*-(2-(2-aminoethylamino)ethyl)picolinamide[11] (H(555)-N) is 0.5-2.5 orders of magnitude better at mobilizing copper(II). Then there are other anti-inflammatory drugs where GLH, Sar-LH, GFH and Sar-FH are much better at mobilizing copper(II) *in vivo*. This includes *N*,*N*′-(2,2′-azanediylbis(ethane-2,1-diyl))dipicolinamide ([H_2(5555)-N])[22] and [H_2(556)-N][22], which are both less efficient at mobilizing copper(II) by approximately 1-3 orders of magnitude and by approximately 0.5-2.5 orders of magnitude respectively. A graph visually showing how the ligand with the highest copper(II) mobilizing capacity (GFH) compares to literature, can be seen in Figure 10.7.

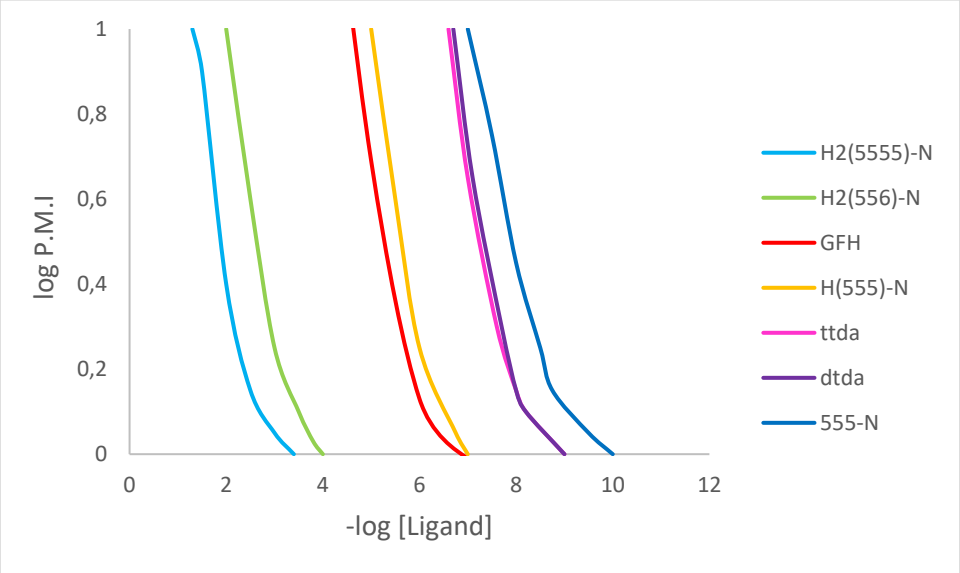

Figure 10.7: A comparison of the P.M.I curves between literature and GFH.

These results show that GLH, Sar-LH, GFH and Sar-FH all satisfy the aim of being able to increase the concentration of low molecular mass complexes of copper(II) at realistic ligand concentrations of 0.1 mM. At the same time, they are very selective for copper(II), so they do not disrupt the homeostasis of other metal ions such as nickel(II), zinc(II) or calcium(II). This is unlike EDTA, which was found to form strong complexes with zinc(II) and calcium(II) and therefore rendered as ineffective at copper(II) plasma mobilization.[6] Additionally, the fact that the mobilizing capacities of GLH, Sar-LH, GFH and Sar-FH are not equivalent to the mobilizing capacities of ttda and dtda[5], means that the ligands are not as powerful chelators of copper(II) as ttda and dtda, and therefore should be biologically active.

10.5 Conclusion

The ligands, GLH, Sar-LH, GFH and Sar-FH can mobilize copper(II) *in vivo* in the presence of nickel(II), zinc(II) and calcium(II) at realistic ligand concentrations of 0.1 mM. The ligand order for the mobilising of copper(II) is GFH > Sar-FH > GLH > Sar-LH. GFH has the highest ability to increase low molecular mass metal species by 40.7 times at 0.1 mM and Sar-LH has the lowest ability to cause an increase, by only a factor of 1.3 times at 0.1 mM. These results show that all the ligands, and especially GFH, will be realistic drugs to use as a therapeutic treatment for rheumatoid arthritis once the complexes are *in vivo*.

10.6 References

1 V. Lopez-Avila, O. Sharpe and W. H. Robinson, Determination of ceruloplasmin in human serum by SEC-ICPMS, *Anal. Bioanal. Chem.*, 2006, **386**, 180–187.

2 S. Catalani, M. Paganelli, M. E. Gilberti, L. Rozzini, F. Lanfranchi, A. Padovani and P. Apostoli, Free copper in serum: An analytical challenge and its possible applications, *J. Trace Elem. Med. Biol.*, 2018, **45**, 176–180.

3 D. M. Templeton, Trace element speciation in toxicology and clinical sciences, *Analusis*, 1998, **26**, 68–71.

4 L. Barrow and M. S. Tanner, Copper distribution among serum proteins in paediatric liver disorders and malignancies, *Eur. J. Clin. Invest.*, 1988, **18**, 555–560.

5 G. E. Jackson and M. J. Kelly, Copper anti-inflammatory drugs in rheumatoid arthritis. Part 2. A potentiometric and spectroscopic study of copper(II) polyaminodicarboxylate complexes, *J. Chem. Soc. Dalt. Trans.*, 1989, 2429–2433.

6 M. Kelly, Metal ion equilibria in biofluids-Copper and rheumatoid arthritis, PhD Thesis, University of Cape Town, 1998.

7 G. E. Jackson, L. Mkhonta-Gama, A. Voyé and M. Kelly, Design of copper-based anti-inflammatory drugs, *J. Inorg. Biochem.*, 2000, **79**, 147–152.

8 P. M. May, P. W. Linder and D. R. Williams, Computer simulation of metal-ion equilibria in biofluids: models for the low-molecular-weight complex distribution of calcium(II), magnesium(II), manganese(II), iron(III), copper(II), zinc(II), and lead(II) ions in human blood plasma, *J. Chem. Soc. Dalt. Trans.*, 1977, 588.

9 E. T. Nomkoko, G. E. Jackson and B. S. Nakani, In vitro and in vivo stability investigations of Cu (ii), Zn (ii), Ca (ii) and Gd (iii) complexes with N, N′-bis (2-hydroxyiminopropionyl) propane-1, 3-diamine, *Dalt. Trans.*, 2004, 1432–1440.

10 G. E. Jackson and M. J. Kelly, Copper anti-inflammatory drugs in rheumatoid arthritis. Part 1. Computer aided drug design, *Inorganica Chim. Acta*, 1988, **152**, 215–217.

11 J. N. Zvimba and G. E. Jackson, Copper chelating anti-inflammatory agents; N1-(2-aminoethyl)-N2-(pyridin-2-ylmethyl)-ethane-1,2-diamine and N-(2-(2-aminoethylamino)ethyl)picolinamide: An in vitro and in vivo study, *J. Inorg. Biochem.*, 2007, **101**, 148–158.

12 S. Odisitse and G. E. Jackson, In vitro and in vivo studies of the dermally absorbed Cu(II) complexes of N5O2 donor ligands - Potential anti-inflammatory drugs,

Inorganica Chim. Acta, 2009, **362**, 125–135.

13 S. Odisitse, G. E. Jackson, T. Govender, H. G. Kruger and A. Singh, Chemical speciation of copper(II) diaminediamide derivative of pentacycloundecane - A potential anti-inflammatory agent, *Dalt. Trans.*, 2007, 1140–1149.

14 M. J. Dreyer, Serum total calcium, ionised calcium and corrected total calcium concentrations in Kwashiorkor and nephrotic syndrome patients, *Med. Technol. SA*, 2011, **25**, 29–32.

15 P. Djurdjevic, I. Jakovljevic, L. Joksovic, N. Ivanovic and M. Jelikic-Stankov, The Effect of Some Fluoroquinolone Family Members on Biospeciation of Copper(II), Nickel(II) and Zinc(II) Ions in Human Plasma, *Molecules*, 2014, **19**, 12194–12223.

16 D. Vlassopoulos, S. A. Wood and A. Mucci, Gold speciation in natural waters: II. The importance of organic complexing—Experiments with some simple model ligands, *Geochim. Cosmochim. Acta*, 1990, **54**, 1575–1586.

17 T. D. Matthews and D. R. Williams, Solubility products for aminocarboxylate ligands: determination, validation and speciation uses, *Anal. Chim. Acta*, 2003, **480**, 119–122.

18 A. N. Hammouda, Development of copper peptide complexes as anti-Inflammatory drugs, PhD Thesis, University of Cape Town, 2015.

19 E. J. Baran, Metal Complexes of Carnosine, *Biochem.*, 2000, **65**, 789–797.

20 E. Gaggelli and G. Valensin, 1 H and 13 C NMR relaxation investigation of the calcium complex of β-alanyl- L -histidine (carnosine) in aqueous solution, *J. Chem. Soc., Perkin Trans. 2*, 1990, 401–406.

21 M. Mohajane, Dipeptides as potential anti-flammatory drugs for rheumatoid arthritis, PhD Thesis, University of Cape Town, 2013.

22 J. N. Zvimba and G. E. Jackson, Solution equilibria of copper(II) complexation with N,N′-(2,2′-azanediylbis(ethane-2,1-diyl))dipicolinamide: A bio-distribution and dermal absorption study, *J. Inorg. Biochem.*, 2007, **101**, 1120–1128.

11. General Concluding Remarks

The aim of this study was to develop a drug that will help treat the inflammation associated with rheumatoid arthritis. To do this, the drug had to increase the bioavailable pool of copper(II) *in vivo* using exogenous and/or endogenous sources. At the same time the drug must not disrupt the homeostasis of endogenous metal ions. The preferred route of administration is via dermal absorption and so the drug had to be designed specifically to be able to form a stable complex with copper(II) and then be lipophilic enough to undergo transdermal absorption. Once in the blood plasma, the design of the drug had to have a high enough mobility in order to mobilize copper(II) from endogenous sources.

The design of the drug resembles the structure of human serum albumin (HSA), where HSA binds copper(II) to an amine, two amide-N donors and an imidazole-N. HSA is a primary, reversable carrier for copper(II) in the body in the form of Asp-Ala-His, so basing the structure on this protein was ideal.[1,2] The drug for this study was therefore made up of three amino acids and the combination of amino acids was based on the research from Hammouda[3] and Vicatos[4]. Hammouda[3] found that histidine in the third position increased the mobility of the ligand, while Vicatos[4] found that leucine and phenylalanine increased the lipophilicity of the complex due to the non-polar side chains. These three amino acids and their positions were the main important factors in the design of the drugs. Vicatos[4] also unexpectedly found no difference in the lipophilicity between glycine and sarcosine and so these two amino acids were also used to verify this claim. Therefore, four ligands were designed to incorporate these amino acids, namely, GLH, Sar-LH, GFH and Sar-FH.

To determine how well the copper(II) complexes could undergo transdermal absorption, two methods were used. The first was the Flask Shake method, which determined the octanol/water partition coefficient values and the second was the Franz cell which determined the permeability coefficients. Specifically, the partition coefficients measure the lipophilicity of the complex, and the permeability coefficients physically measure how well the copper(II) complexes can undergo transdermal absorption. For both methods, the initial thought was that pH 7.4 is important, since it is the physiological pH, and that as a result these complexes should be analysed at this pH. However, on the skin surface, the pH is slightly acidic with an average

range of pH 4.5-6.7. Therefore, the complexes should ideally be analysed within this pH range or at a neutral pH 7, so that a topical cream containing these complexes can be applied to the skin, and due to their adjusted pH, not disrupt the mantel.[5] As a result, an analysis for the partition and permeability coefficients were analysed at both the physiological pH and within the pH range of 4.5-6.7. The outcome from these methods showed that at the physiological pH, the copper(II) complexes did not display any increase in lipophilicity or permeability when compared to the control (copper(II) chloride), and therefore were deemed unable to increase the bioavailable pool of copper(II) *in vivo* using external sources at pH 7.4. However, when analysing the results between pH 4.6-5.5, there was an increase in both the lipophilicity and permeability compared to the control, and thus in this pH range these copper(II) complexes can undergo dermal absorption and satisfy the aim.

In particular, even though an increase in the lipophilicity was found between pH 4.6-5.5, overall the partition coefficient values were negative over the pH range from 2-11, which means the species are inherently hydrophilic. The varying degrees of lipophilicity were attributed to the different species present in solution at particular pH values. The MLH_{-2} species, which occurred at high pH values, had a similar partition coefficient value to copper(II) chloride, which meant that only 0.05-0.08 % of copper(II) was extracted into the octanol phase. The increase in lipophilicity between pH 4.6-5.5 was due to the MLH and MLH_{-1} species for Cu-GLH, the MLH and ML species for Cu-Sar-LH and the MLH species for both Cu-GFH and Cu-Sar-FH. These species caused 0.1-1.2 % of copper(II) to be extracted into the octanol phase. Therefore, even though these species are fundamentally hydrophilic, this increase in percentage of extracted copper(II) qualitatively shows how much copper(II) is expected to undergo dermal absorption. Additionally, the non-N-methylated groups (GLH, GFH), instead of the expected N-methylated groups (Sar-LH, Sar-FH), appeared to be more lipophilic. Therefore, since this study and the study by Vicatos[4] found a deviation from the norm, other factors such as hydrogen bonding and the redistribution of charge could affect the lipophilicity of the complex. A similar suggestion can be made for why the ligands with phenylalanine (GFH, Sar-FH) were found to be more lipophilic than the ligands with leucine (GLH, Sar-LH).

The permeability coefficients correlated with the outcome of the partition coefficient values. At a pH of 7.4, where only the MLH_{-2} species is present in solution, like the partition coefficient values, the permeability of the complex was the same as that of copper(II) chloride. But when the pH was set to correspond to each ligand's maximum partition coefficient value, the

permeation rate increased. With respect to the permeation rate of copper(II) chloride, the permeation rate of Cu-GLH, Cu-Sar-LH, Cu-GFH and Cu-Sar-FH was respectively 1%, 0.5 %, 1.3 % and 1.4 % more than the permeation rate of copper(II) chloride. Since these ligands incorporated amino acids from both Vicatos[4] and Hammouda[3], and since the amino acids taken from Vicatos[4] have non-polar side chains while the amino acid taken from Hammouda[3] has a polar side chain, it is logical to expect that the permeability results from GLH, Sar-LH, GFH and Sar-FH should be in between the results from Hammouda[3] and Vicatos[4]. However, the results were found to be closer to the results from Hammouda[3], which suggests that the polar effect of histidine is stronger than the non-polar effect of leucine and phenylalanine. An illustration of this comparison between the effective permeation rates as a result of the complex can be seen in Figure 11.1. (The effective permeation rate was calculated by subtracting the percentage of permeated copper(II) chloride from the percentage of permeated copper(II) complex from the same study)

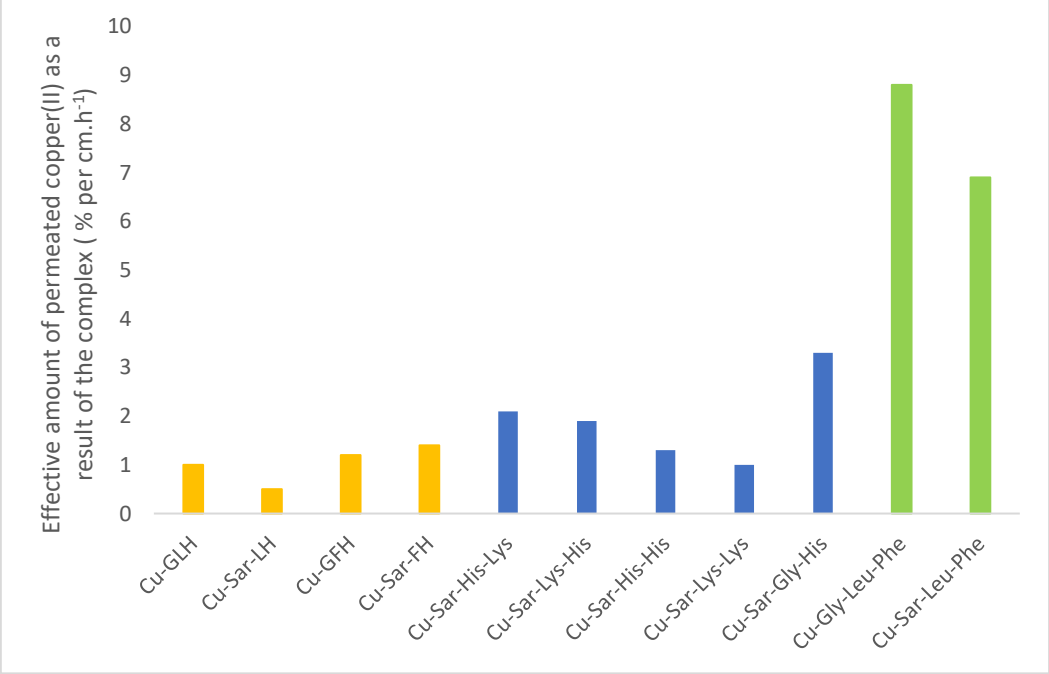

Figure 11.1: An illustrated comparison on the effective permeated rate of copper(II) as a result of the complex between the ligands in this study (orange) with the ligands of Hammouda[3] (blue) and Vicatos[4] (green).

The expected increase in the lipophilicity and permeability rates for the methyl group on the complexes with sarcosine, compared to the complexes with glycine, was not seen. This suggests that for future research, instead of including glycine or sarcosine as the first position

amino acid, it might be more beneficial to add another amino acid that has a non-polar side chain. This could then have an accumulative effect on the overall lipophilicity of the complex, since there will be at least two amino acids instead of one that will have non-polar side chains to help overcome the polar effect of the imidazole group in histidine.

As indicated above, depending on the pH of the solution, the speciation of each ligand changes. To determine the species present in solution over a pH range from 2-11, glass electrode potentiometry was used to study the thermodynamics of the copper(II) complexes at 25 °C and 0.15 M ionic strength (NaCl). From this an issue arose where potentiometry identified multiple models for each ligand instead of identifying only one. The reason for this was that the potentiometric titrations could not distinguish between the different models when it measured the release of protons. Each of these models had a different set of possible species and the challenge going forward was to identify which of these models was the correct one. In order to do this a series of structure determining techniques were carried out, which included UV-Vis, EPR, ^{1}H NMR, mass spectrometry and molecular modelling. X-ray crystallography was also attempted as a structure determining technique.

The first clue was a visual observation where, as the pH of the solution increased, a colour change from clear to violet-pink occurred. The violet-pink colour occurs in the pH range where the MLH_{-2} species predominates. Thus, the violet-pink λ_{max} value is assigned to this species. All the ligands had λ_{max} values between 517-523 nm, which is typical of a square planar geometry with a CuN_4 chromophore. No other species could be identified using the UV-Vis technique, but there was the speculation that they were hidden behind the MLH_{-2} and/or $Cu(H_2O)_6$ absorption bands. EPR was also able to identify and confirm the presence of an MLH_{-2} species for all ligands, and that this species had a CuN_4 chromophore and occurred from pH 7. EPR also managed to resolve the Cu-Sar-LH system, which consisted of an MLH species, an ML species with a CuN_2O_2 chromophore and an MLH_{-2} species. As a result, the correct model with its corresponding stability constants for Cu-Sar-LH was selected in potentiometry. ^{1}H NMR identified the MLH species for all ligands. ^{1}H NMR also showed that the MLH species has two different coordination modes, one where the coordination is to the amine-N and neighbouring carbonyl-O with a protonated imidazole-N, and the other where the imidazole-N and carboxyl-O are coordinated and the amine-N is protonated. As a result of identifying the MLH species in all ligands, as well as combining it with the information from

UV-Vis and EPR spectroscopy, the model choice for Sar-FH and Sar-LH was identified, while the models for GLH and GFH were narrowed down. The model choice for GLH and GFH was chosen by using the standard deviations, Hamilton *R*-factors and observing the "best fit" between the theoretical and experimental functions from potentiometry.

The model choices for each ligand consisted of the following species: GLH (MLH, MLH_{-1}, MLH_{-2}), Sar-LH (MLH, ML, MLH_{-2}), GFH (MLH, MLH_{-2}), Sar-FH (MLH, MLH_{-2}). The formation of these species is a result of the loss of protons. Mass spectrometry was used to try and identify all the species present in solution. However, again only the MLH_{-2} species was confirmed to be present for all ligands. An interesting discovery, while analysing the mass spectrometry data was that copper was found in both the II and I oxidation state. The conclusion for not identifying the other species was that their concentrations were too low for detection. A summary of the process that took place to determine the correct model for each ligand, can be seen in Table 11.1. Only the structure determining techniques which contributed information that narrowed down the selection for each ligand, are displayed.

Table 11.1: Summary of process to determine correct model for each ligand.

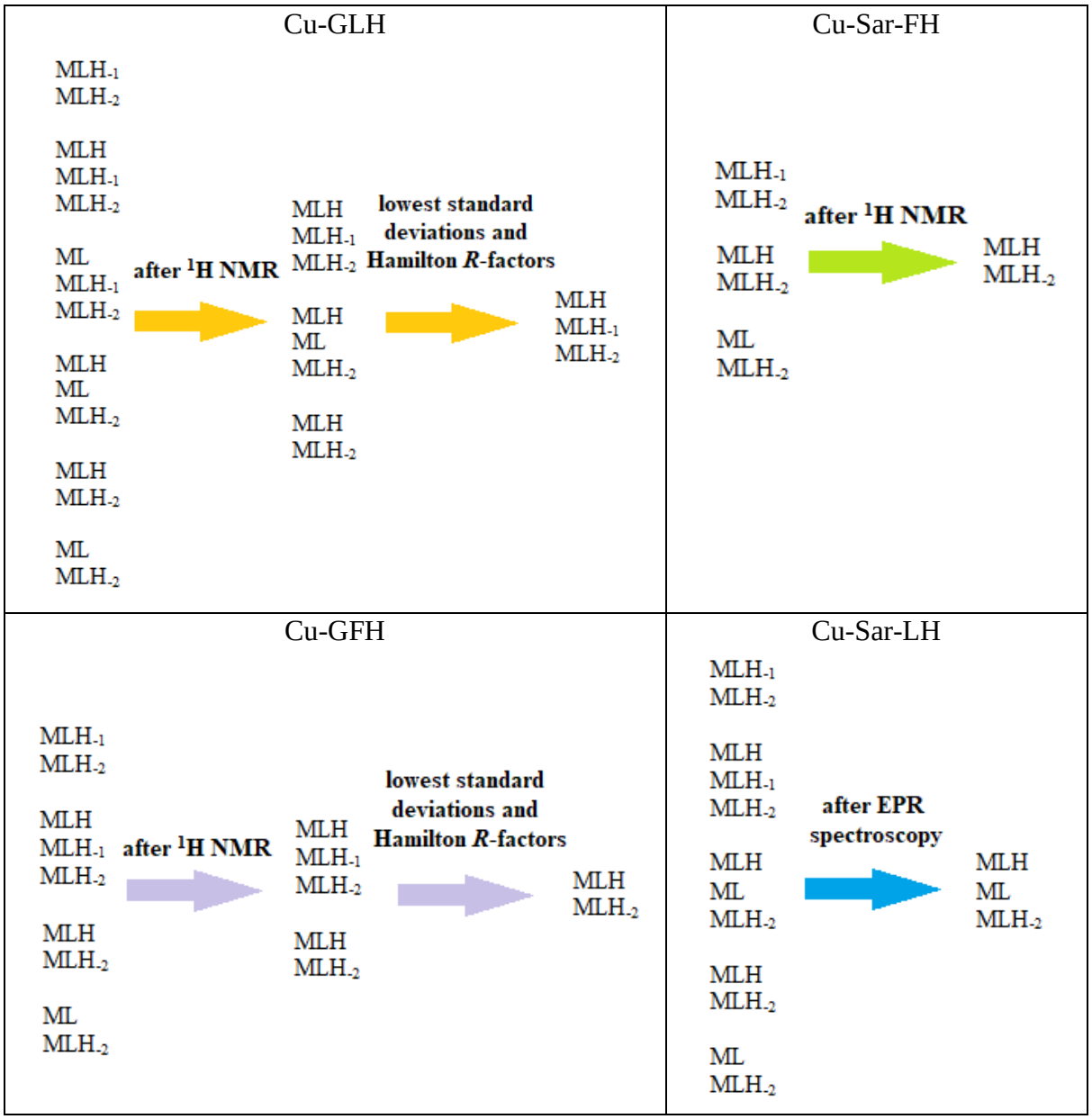

Another structure determining technique that was attempted, was to use single-crystal X-ray diffraction. X-ray crystallography can be used for studying the structures of copper(II)-peptide complexes, because it gives precise structural information at the atomic resolution level.[6,7] However, the most challenging step, particularly for peptides, is growing a crystal that is able to diffract at a high resolution. This is because peptides are sensitive to changes in the crystal growing environment and therefore finding the correct combination to create a viable environment is difficult.[7] Despite having attempted multiple methods to crystallise the complexes, which included slow evaporation and vapour diffusion methods as described in literature[8–12], a crystal with diffracting properties was not attained. As a result of not obtaining

a single crystal, powder X-ray diffraction (PXRD) was performed to identify whether the four ligands had crystalline properties (Figure 11.2). All the crystallographic experimental methodologies that were used can be seen in Section 1 of the appendix.

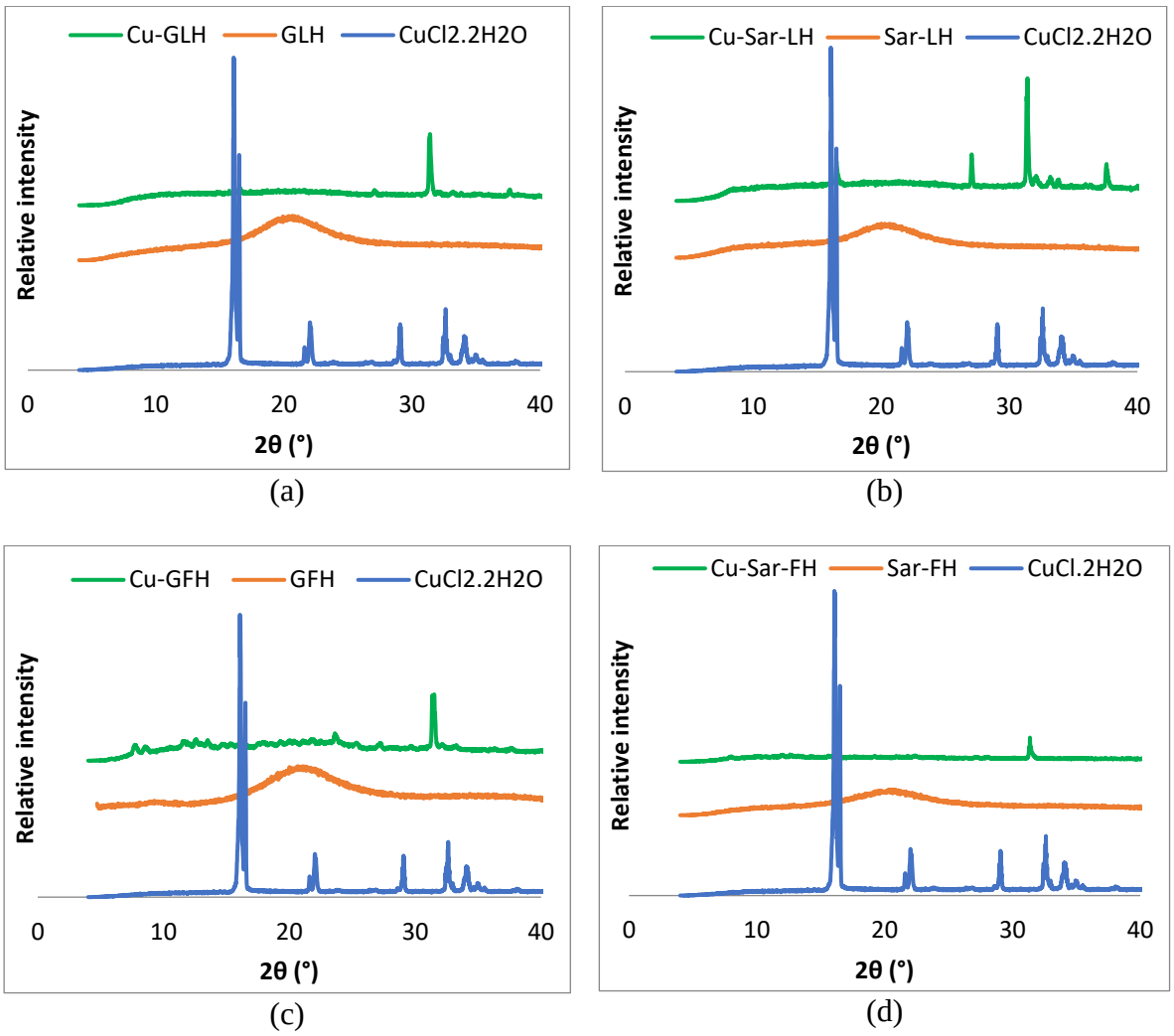

Figure 11.2: PXRD patterns of the complexes (green) and their starting materials, $CuCl_2.2H_2O$ (blue) and ligands (orange), for the ligands (a) GLH, (b) Sar-LH, (c) GFH and (d) Sar-FH.

Figure 11.2 shows that all of the ligands used were amorphous. When complexed to copper(II), the resulting complexes were also amorphous, with very little long-range order, or crystallinity. This may provide an explanation for the difficulty in preparing large enough single crystals for full structural elucidation.

Molecular modelling using DFT calculations was beneficial for two reasons. The first was that it validated the proposed structures for the MLH_{-2} and MLH species, as well as indicated which coordination modes would most likely form in solution for the MLH, ML and MLH_{-1} species. The second was that by using DFT to calculate the λ_{max} of species, a suggestion was made for why the absorption bands of the MLH, ML and MLH_{-1} species were not visible in the UV-Vis spectrum. Interestingly, all the possible coordination modes for each MLH, ML and MLH_{-1} species were found to have similar ground state energies and therefore, all coordination modes have an equal probability of forming in solution. Therefore, all coordination modes for each species have been proposed as final structures. The visual representation of the final proposed optimized structures for each coordination mode of each species can be seen in Table 11.2. Additionally, a summary regarding the geometry, DFT calculated λ_{max} values, experimental λ_{max} values for the MLH_{-2} species and a suggestion for why the MLH, ML and MLH_{-1} species did not appear in the UV-Vis spectrum, has also been included.

Table 11.2: Visual representation of the proposed final structures for the MLH, ML, MLH_{-1} and MLH_{-2} species, as well as a summary of their geometry, DFT calculated λ_{max}, experimental λ_{max} for the MLH_{-2} species and a suggestion for why the MLH, ML and MLH_{-1} species did not appear in the UV-Vis spectrum.

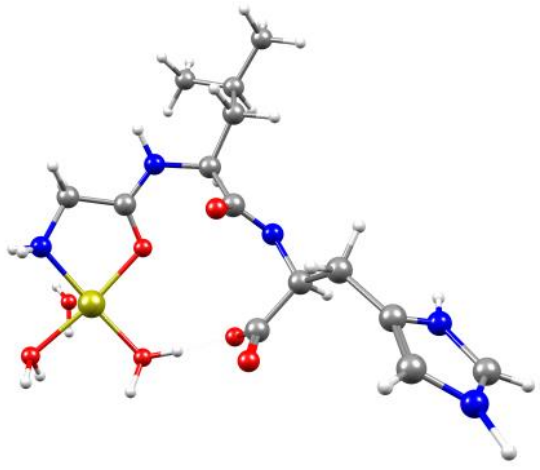 Ligand: GLH Species: MLH Coordination mode (a) Geometry: square pyramidal B3LYP/6-31++G** λ_{max} : 710 Experimental λ_{max}: not seen due to concealment from broad absorption band of $Cu(H_2O)_6$	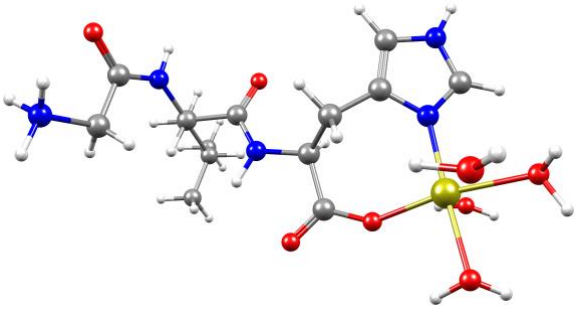 Ligand: GLH Species: MLH Coordination mode (b) Geometry: tetragonally distorted octahedral B3LYP/6-31++G** λ_{max} : 882 Experimental λ_{max}: not seen due to concealment from broad absorption band of $Cu(H_2O)_6$

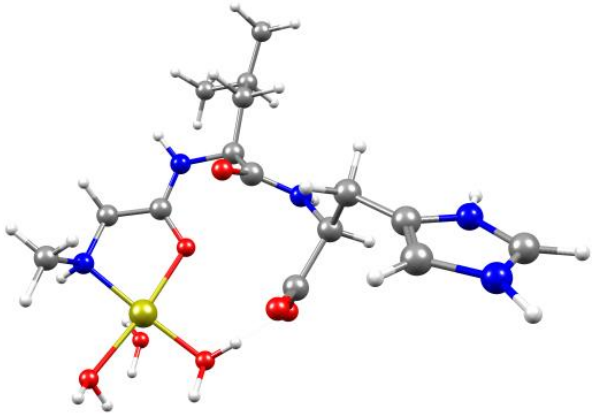

Ligand: Sar-LH
Species: MLH
Coordination mode (a)
Geometry: square pyramidal
B3LYP/6-31++G** λ_{max} : 699
Experimental λ_{max}: not seen due to concealment from broad absorption band of $Cu(H_2O)_6$

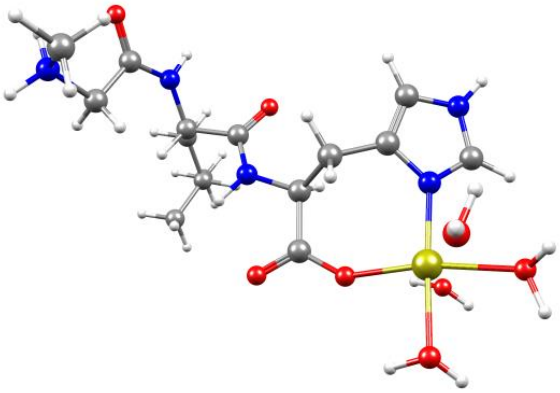

Ligand: Sar-LH
Species: MLH
Coordination mode (b)
Geometry: tetragonally distorted octahedral
B3LYP/6-31++G** λ_{max} : 889
Experimental λ_{max}: not seen due to concealment from broad absorption band of $Cu(H_2O)_6$

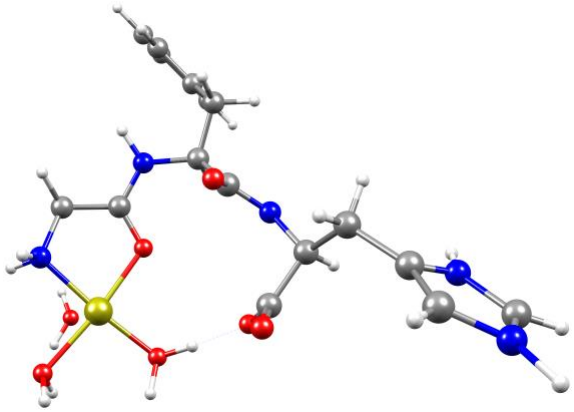

Ligand: GFH
Species: MLH
Coordination mode (a)
Geometry: square pyramidal
B3LYP/6-31++G** λ_{max} : 837
Experimental λ_{max}: not seen due to concealment from broad absorption band of $Cu(H_2O)_6$

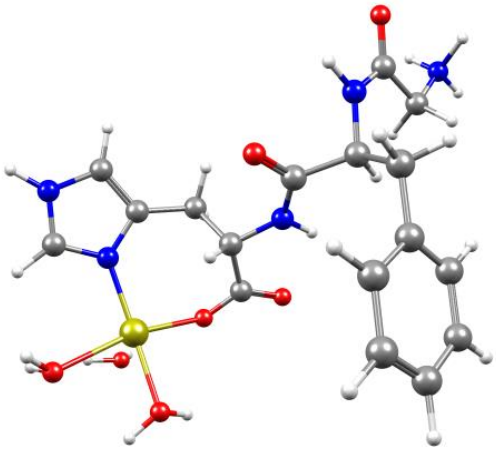

Ligand: GFH
Species: MLH
Coordination mode (b)
Geometry: square pyramidal
B3LYP/6-31++G** λ_{max} : 875
Experimental λ_{max}: not seen due to concealment from broad absorption band of $Cu(H_2O)_6$

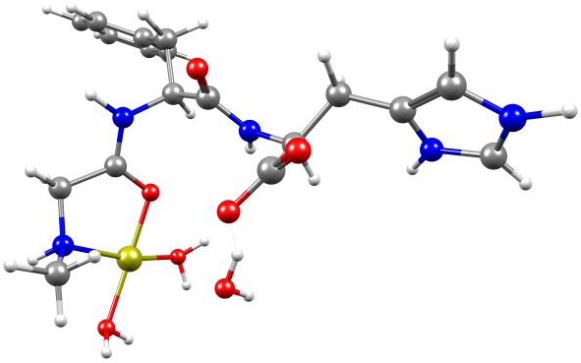

Ligand: Sar-FH
Species: MLH
Coordination mode (a)
Geometry: square pyramidal
B3LYP/6-31++G** λ_{max} : 707
Experimental λ_{max}: not seen due to concealment from broad absorption band of $Cu(H_2O)_6$

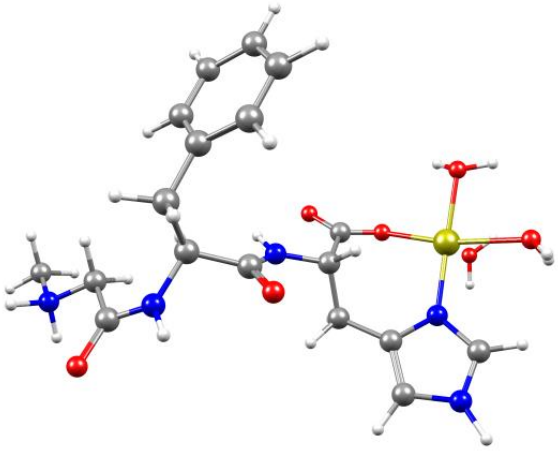

Ligand: Sar-FH
Species: MLH
Coordination mode (b)
Geometry: square pyramidal
B3LYP/6-31++G** λ_{max} : 868
Experimental λ_{max}: not seen due to concealment from broad absorption band of $Cu(H_2O)_6$

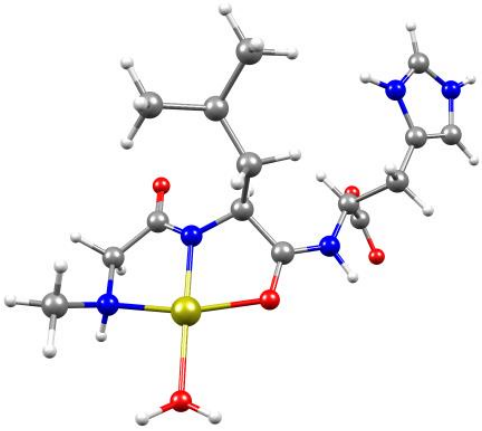

Ligand: Sar-LH
Species: ML
Coordination mode (a)
Geometry: square planar
B3LYP/6-31++G** λ_{max} : 586
Experimental λ_{max}: not seen due to concealment from large absorption band of the MLH_{-2} species

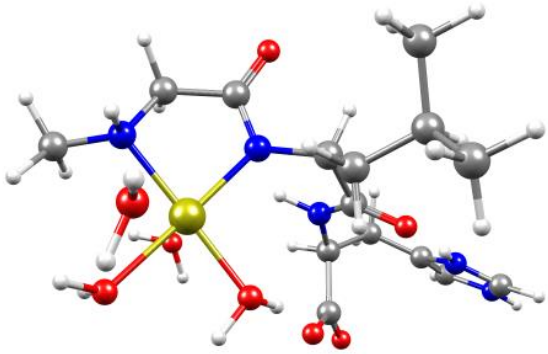

Ligand: Sar-LH
Species: ML
Coordination mode (b)
Geometry: tetragonally distorted octahedral
B3LYP/6-31++G** λ_{max} : 719
Experimental λ_{max}: not seen due to concealment from broad absorption band of $Cu(H_2O)_6$

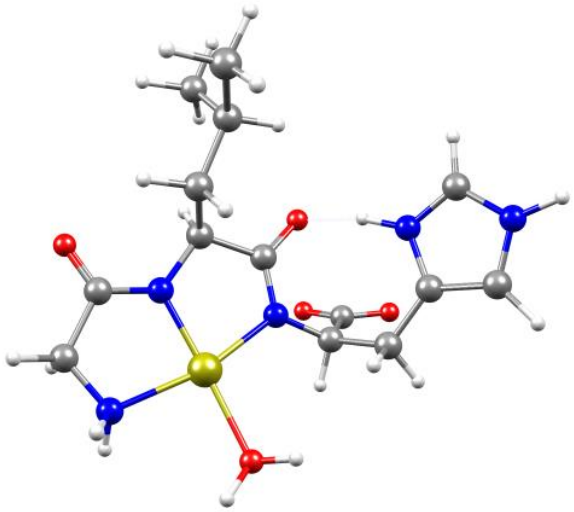

Ligand: GLH
Species: MLH_{-1}
Coordination mode (a)
Geometry: square planar
B3LYP/6-31++G** λ_{max} : 569
Experimental λ_{max}: not seen due to concealment from large absorption band of the MLH_{-2} species

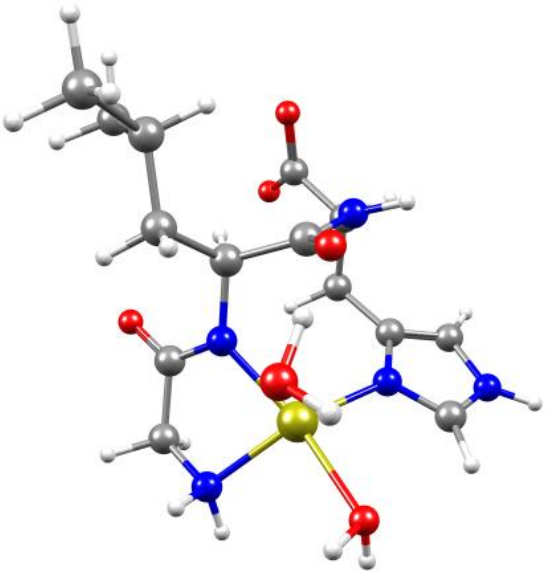

Ligand: GLH
Species: MLH_{-1}
Coordination mode (b)
Geometry: distorted square pyramidal
B3LYP/6-31++G** λ_{max} : 763
Experimental λ_{max}: not seen due to concealment from broad absorption band of $Cu(H_2O)_6$

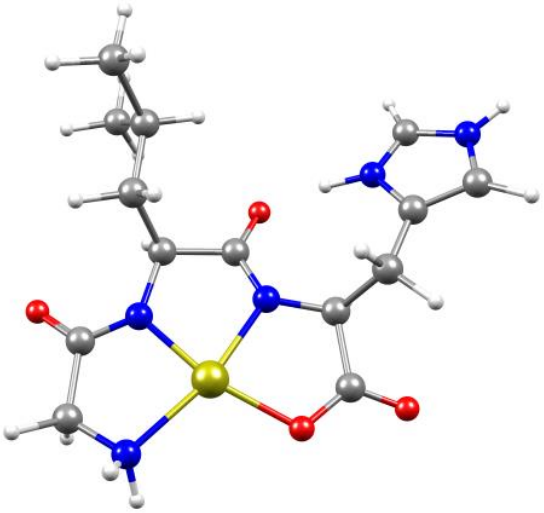

Ligand: GLH
Species: MLH_{-1}
Coordination mode (c)
Geometry: square planar
B3LYP/6-31++G** λ_{max} : 592
Experimental λ_{max}: not seen due to concealment from large absorption band of the MLH_{-2} species

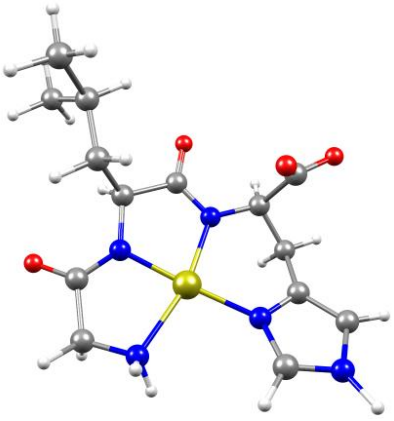 Ligand:GLH Species: MLH_{-2} Geometry: square planar B3LYP/6-31++G** λ_{max} : 516 Experimental λ_{max}: 518	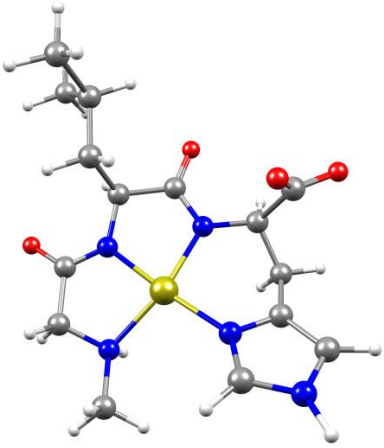 Ligand:Sar-LH Species: MLH_{-2} Geometry: square planar B3LYP/6-31++G** λ_{max} : 541 Experimental λ_{max}: 523
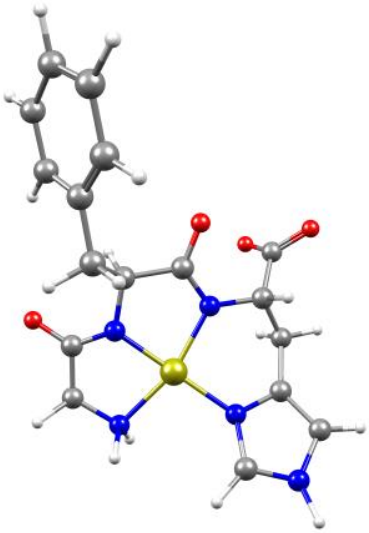 Ligand: GFH Species: MLH_{-2} Geometry: square planar B3LYP/6-31++G** λ_{max} : 527 Experimental λ_{max}: 517	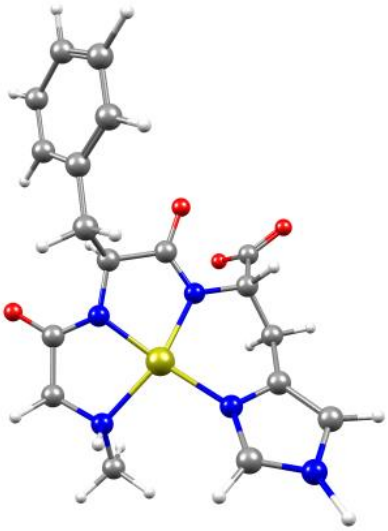 Ligand: Sar-FH Species: MLH_{-2} Geometry: square planar B3LYP/6-31++G** λ_{max} : 534 Experimental λ_{max}: 521

Having established the species present in solution for each copper(II) ligand complex and having determined the coordination modes for each species, it is evident that stable species form. However, the question that arises is whether these complex species will be biologically active *in vivo*. It is possible that the stability of the complex is too high, as seen with 3,6,9,12-tetra-azatetradecanedioic acid (ttda) and 3,6,9-triazaundecanedioic acid (dtda), which resulted in their copper(II) complexes being excreted, unchanged, in the urine.[13–15] Therefore, by comparing the stability constants of Cu-GLH, Cu-Sar-LH, Cu-GFH and Cu-Sar-FH with the

stability constants of Cu-ttda and Cu-dtda, it can give an indication whether the ligands are likely to be excreted, intact or not. The comparison can be seen in Table 11.3.

Table 11.3: Comparison of the complex stability constants between Cu-GLH, Cu-Sar-LH, Cu-GFH and Cu-Sar-FH with Cu-ttda and Cu-dtda.[13]

Species type	**ligands**	**log β**
MLH	Cu-GLH	12.71
	Cu-Sar-LH	12.37
	Cu-GFH	12.76
	Cu-Sar-FH	12.66
	Cu-ttda	24.92
	Cu-dtda	21.35
ML	Cu-Sar-LH	7.38
	Cu-ttda	21.34
	Cu-dtda	19.16
MLH_{-1}	Cu-GLH	2.77
	Cu-dtda	8.24
MLH_{-2}	Cu-GLH	-2.24
	Cu-Sar-LH	-2.70
	Cu-GFH	-1.03
	Cu-Sar-FH	-1.51
MLH_2	Cu-ttda	26.67

It can be seen from Table 11.3 that the stability constants of Cu-ttda and Cu-dtda are considerably larger than the stability constants of Cu-GLH, Cu-Sar-LH, Cu-GFH and Cu-Sar-FH. This large difference suggests that the four ligands are a lot less stable and thus will be able to release copper(II) *in vivo* and not get excreted. The main structural difference between the four ligands and ttda/dtda that accounts for the difference in the stability constants is due to the number of amine nitrogens. In ttda, copper(II) binds to four amine nitrogens and in dtda to three, while in GLH, Sar-LH, GFH and Sar-FH, copper(II) only binds to one. Additionally, for GLH, Sar-LH, GFH and Sar-FH, besides the one amine coordination, copper(II) is also bound to amide-Ns, which upon complexation have to deprotonate, which in turn helps to lower the stability of the complex.[15] Copper(II) also binds to O-donor groups, which as a result of their higher electronegativity, generally form less stable bonds to copper(II) compared to N-donor groups, and so help to lower the stability of the complex in relation to ttda and dtda. When comparing the stability between the ligands, the expected increase in stability for the complexes with the methyl group from sarcosine compared to glycine, as well as the complexes with leucine compared to phenylalanine, was not seen.

The ligands have demonstrated that even though they are still overall hydrophilic, they will undergo dermal absorption and satisfy the aim of increasing the bioavailable pool of copper(II) from exogenous sources. The secondary aim for the ligands to mobilise and release copper(II) from endogenous sources was achieved by using the program, Evaluation of Constituent Concentrations in Large Equilibrium Systems (ECCLES) to determine the mobility capacity of copper(II) complexes *in vivo*. The results showed that all four ligands in the order of GFH > Sar-FH > GLH > Sar-LH were able to mobilize copper(II) *in vivo* at realistic ligand concentrations of 0.1 mM, while not disrupting the homeostasis of nickel(II), zinc(II) and calcium(II). GFH was found to have the highest mobilizing capacity, which increased the low molecular mass metal species by 40.7 times at 0.1 mM, and was thus proposed as the best choice to use as a therapeutic treatment once the complexes are *in vivo*. Since the mobilizing capacity of ttda and dtda were so high[13–15], they became a marker to indicate whether the mobilising capacities of GLH, Sar-LH, GFH and Sar-FH were low enough to warrant biological activity. Since the four ligands were found to be 2-4 orders of magnitude less effective at mobilising copper(II) than ttda and dtda, it suggests that these ligands could be biologically active *in vivo.*

The suggestion by Hammouda[3] to place histidine in the third position to increase the mobilizing capacity evidently was a success. For future work, the ligand should keep histidine in the third position, but as mentioned before, to improve the overall lipophilicity of the complex, two amino acids with non-polar side chains should also be used. A suggestion could be to use both leucine and phenylalanine in the same tripeptide, so that the two possibilities are Leu-Phe-His and Phe-Leu-His.

Overall, the ligands GLH, Sar-LH, GFH and Sar-FH have been shown to be successful transporters of copper(II), which are able to increase the bioavailable pool of copper(II) from both exogenous and endogenous sources without disrupting the homeostasis of other endogenous metal ions. As a result, these ligands should undergo animal testing where the bio-distribution is studied. The complex ligand will be radio-labelled using ^{64}Cu(II) as a radiotracer. The bio-distribution study will trace the efficiency of the ligands to transport copper(II) through the body and deliver copper(II) to the sites of inflammation. This will also determine the stability of the complexes *in vivo*. The ideal form of treatment would be in the form of a topical cream, but intravenous and percutaneous administration methods can both be used to compare the ability of the ligands to undergo dermal absorption. Additionally, further animal studies

can be done to determine the anti-inflammatory activity by topically applying the radio-labelled complex. In previous research, copper(II) concentrations of 1 mmol.dm^{-3} were prepared in sterile saline solutions of pH 7.4.[15,16] Therefore, a copper(II) ligand solution containing this concentration can be prepared for both the intravenous and percutaneous administration methods.

11.1 References

1 L. Perrone, E. Mothes, M. Vignes, A. Mockel, C. Figueroa, M.-C. Miquel, M.-L. Maddelein and P. Faller, Copper Transfer from Cu-Aβ to Human Serum Albumin Inhibits Aggregation, Radical Production and Reduces Aβ Toxicity, *ChemBioChem*, 2009, **11**, 110–118.

2 J. E. Weder, C. T. Dillon, T. W. Hambley, B. J. Kennedy, P. A. Lay, J. R. Biffin, H. L. Regtop and N. M. Davies, Copper complexes of non-steroidal anti-inflammatory drugs: an opportunity yet to be realized, *Coord. Chem. Rev.*, 2002, **232**, 95–126.

3 A. N. Hammouda, Development of copper peptide complexes as anti-Inflammatory drugs, PhD Thesis, University of Cape Town, 2015.

4 G. M. Vicatos, In vitro studies of dermally absorbed Cu(II) tripeptide complexes as potential anti-inflammatory drugs, MSc Thesis, University of Cape Town, 2016.

5 J. Buscemi, We asked experts about the importance of pH in skin care, and proceeded to test all of our products, https://hellogiggles.com/beauty/ph-skincare-explainer/, (accessed 25 October 2019).

6 B. Rupp and K. Katherine, *Biomolecular Crystallography: Principles, Practice, and Application to Structural Biology*, Garland Science, New York/London, 2010.

7 R. K. Spencer and J. S. Nowick, A Newcomer′s Guide to Peptide Crystallography, *Isr. J. Chem.*, 2015, **55**, 698–710.

8 P. Deschamps, P. P. Kulkarni and B. Sarkar, X-ray Structure of Physiological Copper(II)−Bis(l-histidinato) Complex, *Inorg. Chem.*, 2004, **43**, 3338–3340.

9 P. Deschamps, P. P. Kulkarni and B. Sarkar, The Crystal Structure of a Novel Copper(II) Complex with Asymmetric Ligand Derived from L-Histidine, *Inorg. Chem.*, 2003, **42**, 7366–7368.

10 O. Yamauchi, T. Sakurai and A. Nakahara, Histidine-containing ternary amino acid-copper(II) complexes. Syntheses and properties, *J. Am. Chem. Soc.*, 1979, **101**, 4164–4172.

11 T. Ono, H. Shimanouchi, Y. Sasada, T. Sakurai, O. Yamauchi and A. Nakahara, Crystal Structures of Mixed Ligand Copper(II) Complexes Containing L-Amino Acids. I. L-Asparaginato-L-histidinato-copper(II) and Its Hydrate, *Bull. Chem. Soc. Jpn.*, 1979, **52**, 2229–2234.

12 N.-H. Dung, B. Viossat, A. Busnot, A. G. Sicilia Zafra, J. M. Gonzalez Perez and J.

Niclos Gutierrez, New mixed-ligand copper(II) complex with iminodiacetate and imidazole: Bis[bis(imidazole)(iminodiacetato)copper(II)] dihydrate, *Inorganica Chim. Acta*, 1990, **169**, 9–12.

13 G. E. Jackson and M. J. Kelly, Copper anti-inflammatory drugs in rheumatoid arthritis. Part 2. A potentiometric and spectroscopic study of copper(II) polyaminodicarboxylate complexes, *J. Chem. Soc. Dalt. Trans.*, 1989, 2429–2433.

14 M. Kelly, Metal ion equilibria in biofluids-Copper and rheumatoid arthritis, PhD Thesis, University of Cape Town, 1998.

15 G. E. Jackson, L. Mkhonta-Gama, A. Voyé and M. Kelly, Design of copper-based anti-inflammatory drugs, *J. Inorg. Biochem.*, 2000, **79**, 147–152.

16 S. Odisitse and G. E. Jackson, In vitro and in vivo studies of N,N′-bis[2(2-pyridyl)-methyl]pyridine-2,6-dicarboxamide–copper(II) and rheumatoid arthritis, *Polyhedron*, 2008, **27**, 453–464.

Appendix

Section 1

1.1 Crystallographic experimental

1.1.1 Solution preparation

An aqueous solution that contained a 1:1 copper(II) ligand ratio was prepared for each of the four ligands, GLH, Sar-LH, GFH and Sar-FH. The concentration of the ligands was 0.1 M and the concentration of $CuCl_2 \cdot 2H_2O$ was adjusted lower at 0.08 M to prevent the precipitation of $Cu(OH)_2$, but still maintain an approximate 1:1 ratio. The pH of each solution was adjusted to pH 11 using NaOH and filtered into a vial with a nylon 0.45 μm microfilter.

1.1.2 Slow diffusion

Slow diffusion was used as a crystal growth method and two types of setups were used. The first used 0.5 ml of each ligand solution mixed with 0.5 ml of dimethylformamide (DMF) to make a 50/50 vol/vol DMF/water solution. The solution was kept under an enclosed ethanol atmosphere at room temperature for three weeks, but no crystals formed. The second setup used 0.5 ml of each ligand solution and mixed with 0.5 ml of aqueous ethanol to make a 50/50 vol/vol ethanol/water solution. This mixture was kept under an enclosed acetone atmosphere at room temperature and after 7 days small clusters of blue block-like crystals formed.

1.1.3 Slow evaporation

For the slow evaporation method, all the following mixtures were left to dry in a vial in the open air at room temperature: 0.25 ml of each ligand solution mixed with 0.25 ml of aqueous ethanol; 0.25 ml of each ligand solution mixed with 0.25 ml of DMF; 0.25 ml of each ligand solution mixed with 0.25 ml of ethanol, as well as 0.25 ml of chloroform; and 0.25 ml of each ligand solution only. The solution that contained only 0.25 ml of ligand solution produced small clusters of blue crystals.

1.1.4 Single Crystal X-ray Diffraction (SCXRD)

Crystals that formed from the slow diffusion and slow evaporation methods were analysed using a single crystal four-circle X-ray diffractometer to determine the structural properties of the crystals. These crystals were extracted from their immediate environment and coated in Paratone oil[1] to prevent the loss of water molecules that could be included in the crystal structure. The crystals were separated from their clusters and placed in the diffractometer. The resulting diffraction was not sufficient for further SCXRD to take place.

1.1.5 Powder X-ray Diffraction (PXRD)

PXRD patterns were recorded for the starting materials (GLH, Sar-LH, GFH, Sar-FH and $CuCl_2 \cdot 2H_2O$) and the resulting copper(II) ligand complexes. This analysis was performed at room temperature using a Bruker D2 Phaser diffractometer (Bruker, United States) using Cu$K\alpha_1$ radiation (λ = 1.5406 Å) with an X-ray generator set at 30 kV and 50 mA. The sample preparation involved co-grinding the products from an evaporated sample that contained only 0.25 ml of copper(II) ligand solution to minimise the effect of preferred orientation. $CuCl_2 \cdot 2H_2O$ was also co-ground, but the ligands were hydroscopic and so these were added to the PXRD without co-grinding. All these samples were separately placed onto a silicon zero background sample holder, where the scanning range was 4^o – 40^o 2θ with a step size of 0.0164^o and a primary beam path slit of 0.6 mm.

1.2 Reference

1 *Paratone N oil*, Exxon Chemical Co., Texas, USA.